MAR 16 1998

ORNL-6931

ornl

OAK RIDGE NATIONAL LABORATORY

LOCKHEED MARTIN

Durability-Based Design Criteria for an Automotive Structural Composite: Part 2. Background Data and Models

J. M. Corum
R. L. Battiste
C. R. Brinkman
W. Ren
M. B. Ruggles
Y. J. Weitsman
G. T. Yahr

MANAGED AND OPERATED BY
LOCKHEED MARTIN ENERGY RESEARCH CORPORATION
FOR THE UNITED STATES
DEPARTMENT OF ENERGY

ORNL-27 (3-96)

This report has been reproduced directly from the best available copy.

Available to DOE and DOE contractors from the Office of Scientific and Technical Information, P.O. Box 62, Oak Ridge, TN 37831; prices available from (423) 576-8401.

Available to the public from the National Technical Information Service, U.S. Department of Commerce, 5285 Port Royal Rd., Springfield, VA 22161.

This report was prepared as an account of work sponsored by an agency of the United States Government. Neither the United States Government nor any agency thereof, nor any of their employees, makes any warranty, express or implied, or assumes any legal liability or responsibility for the accuracy, completeness, or usefulness of any information, apparatus, product, or process disclosed, or represents that its use would not infringe privately owned rights. Reference herein to any specific commercial product, process, or service by trade name, trademark, manufacturer, or otherwise, does not necessarily constitute or imply its endorsement, recommendation, or favoring by the United States Government or any agency thereof. The views and opinions of authors expressed herein do not necessarily state or reflect those of the United States Government or any agency thereof.

ORNL-6931

Engineering Technology Division

DURABILITY-BASED DESIGN CRITERIA FOR AN AUTOMOTIVE STRUCTURAL COMPOSITE: PART 2. BACKGROUND DATA AND MODELS

J. M. Corum
R. L. Battiste
C. R. Brinkman
W. Ren
M. B. Ruggles
Y. J. Weitsman
G. T. Yahr

February 1998

Prepared by the
OAK RIDGE NATIONAL LABORATORY
Oak Ridge, Tennessee 37831-6285
managed by
LOCKHEED MARTIN ENERGY RESEARCH CORP.
for the
U.S. DEPARTMENT OF ENERGY
under contract DE-AC05-96OR22464

CONTENTS

PART 1: DESIGN RULES

	Page
LIST OF FIGURES	ix
LIST OF TABLES	xi
ABSTRACT	1-1
1. INTRODUCTION	1-1
1.1 GENERAL	1-1
1.2 REFERENCE MATERIAL	1-2
1.3 LOADINGS AND ENVIRONMENTS	1-2
1.4 DESIGN APPROACH	1-2
1.5 DEFINITIONS	1-3
2. DEFORMATION AND STIFFNESS PROPERTIES FOR DESIGN ANALYSES	2-1
2.1 GENERAL	2-1
2.2 ELASTIC CONSTANTS FOR DESIGN	2-1
2.2.1 Basic Values	2-1
2.2.2 Environmental Effects	2-2
2.2.3 Prior Loading Effects	2-3
2.3 CREEP BEHAVIOR FOR DESIGN	2-3
2.3.1 Basic Creep Equation	2-3
2.3.2 Isochronous Stress-Strain Curves	2-6
2.3.3 Environmental Effects	2-6
3. MULTIAXIAL STRENGTH CRITERION — EQUIVALENT STRESS	3-1
4. DESIGN ALLOWABLES FOR STATIC LOADINGS	4-1
4.1 SHORT-TIME ALLOWABLE STRESS INTENSITY, S_0	4-1
4.2 TIME-DEPENDENT ALLOWABLE STRESS INTENSITY, S_t	4-2
4.3 TREATMENT OF INCREMENTS OF SUSTAINED LOADS	4-6
5. DESIGN LIMITS FOR CYCLIC LOADINGS	5-1
5.1 BASIC FATIGUE DESIGN CURVES	5-1
5.2 TREATMENT OF MEAN STRESSES	5-2
5.3 ENVIRONMENTAL EFFECTS	5-2
5.4 TREATMENT OF VARYING STRESS AMPLITUDES	5-4
5.5 FATIGUE EVALUATION PROCEDURE	5-4
6. DAMAGE TOLERANCE DESIGN FOR LOW-ENERGY IMPACTS AND OTHER DEFECTS	6-1
6.1 GENERAL REQUIREMENTS	6-1
6.2 DETERMINATION OF DAMAGE AREA	6-1
6.3 DETERMINATION OF STRENGTH AND STIFFNESS DEGRADATION	6-1
7. SUMMARY—SIMPLIFIED CRITERIA	7-1
7.1 STIFFNESS AND CREEP PROPERTIES FOR DESIGN ANALYSES	7-1
7.2 MULTIAXIAL STRENGTH THEORY	7-2
7.3 ALLOWABLE STRESSES FOR STATIC LOADINGS	7-2
7.4 LIMITS FOR CYCLIC LOADINGS	7-3
7.5 DAMAGE TOLERANCE EVALUATION	7-4

CONTENTS

PART 2: BACKGROUND DATA AND MODELS

	Page
LIST OF FIGURES	ix
LIST OF TABLES	xiii
ABSTRACT	1-1
1. INTRODUCTION	1-1
1.1 BACKGROUND	1-1
1.2 REFERENCE COMPOSITE	1-2
1.3 OVERVIEW OF PART 1 RULES	1-2
1.4 OVERVIEW OF PART 2	1-2
2. ELASTIC ANALYSIS	2-1
3. TENSILE, COMPRESSIVE, AND FLEXURAL ELASTIC CONSTANTS AND STRENGTH PROPERTIES	3-1
3.1 IN-AIR ELASTIC CONSTANTS AND STRENGTH PROPERTIES AS A FUNCTION OF TEMPERATURE	3-1
3.1.1 Tensile Elastic Constants and Strength Properties	3-1
3.1.2 Compressive Elastic Constants and Strength Properties	3-5
3.1.3 Flexural Elastic Constants and Strength Properties	3-6
3.2 PROPORTIONAL LIMIT, STRENGTH VALUES, AND DAMAGE DEVELOPMENT IN TENSILE LOADING	3-6
3.3 EFFECT OF STRAIN RATE	3-8
4. IN-PLANE AND INTERLAMINAR SHEAR PROPERTIES	4-1
4.1 IN-PLANE SHEAR MODULUS AND STRENGTH	4-1
4.2 INTERLAMINAR SHEAR	4-1
4.3 ENVIRONMENTAL DEGRADATION	4-3
4.4 OBSERVATIONS AND RECOMMENDATIONS	4-3
5. ENVIRONMENTAL DEGRADATION OF STRENGTH AND STIFFNESS	5-1
5.1 CORRELATIONS OF EFFECTS OF MOISTURE EXPOSURE ON STRENGTH AND STIFFNESS	5-1
5.2 FACTORS FOR OTHER FLUIDS	5-7
6. MULTIAXIAL STRENGTH CRITERION	6-1
7. REPRESENTATION OF CREEP UNDER VARIOUS STRESS, TEMPERATURE, AND ENVIRONMENTAL CONDITIONS	7-1
7.1 INTRODUCTION	7-1
7.2 REFERENCE CREEP EQUATION	7-1
7.3 TEMPERATURE DEPENDENCE	7-4
7.4 EFFECT OF DISTILLED WATER ON CREEP (ROOM TEMPERATURE)	7-10
7.5 EFFECTS OF OTHER ENVIRONMENTS ON CREEP	7-13
APPENDIX 7.A	7-15
APPENDIX 7.B	7-17
APPENDIX 7.C	7-19
8. DEVELOPMENT OF CREEP-RUPTURE CORRELATIONS AND DESIGN CURVES IN VARIOUS ENVIRONMENTS	8-1
8.1 INTRODUCTION	8-1
8.2 CREEP-RUPTURE CURVES AND EQUATIONS FOR VARIOUS TEMPERATURES IN AIR/50% RH	8-1
8.3 TABLE OF TIME/TEMPERATURE VALUES	8-12

8.4 DESIGN CURVES AND TABLE 8-12
8.4.1 In Air 8-12
8.4.2 In Distilled Water 8-15
8.4.3 Superimposed Motor Vibration and Low-Frequency Impulse Load Cycling on Creep-Rupture Strength 8-19
8.4.4 In Water-Based Fluids 8-22
8.4.5 In Oil-Based Fluids 8-23
8.4.6 In Sulfuric Acid Environment 8-23
8.5 ENVIRONMENTAL KNOCK-DOWN FACTORS 8-27
8.6 PROCEDURES FOR DEVELOPING CREEP-RUPTURE CURVES AND ALLOWABLE STRESSES 8-29
8.6.1 General Procedures and Precaution for Applications 8-29
8.6.2 Some Details in Developing the Maximum Design-Allowable Stress Curves 8-30
8.7 APPLICABILITY OF TIME FRACTIONS FOR CREEP-RUPTURE 8-32
9. ENVIRONMENTAL EFFECTS ON CREEP DEFORMATION AND RUPTURE DESIGN CURVES OF THE CSM ISOCYANURATE COMPOSITE FOR COMPRESSIVE LOADINGS 9-1
9.1 INTRODUCTION 9-1
9.2 CREEP DEFORMATION CURVES FOR AIR/50% RH AND DISTILLED WATER 9-1
9.2.1 Creep Deformation in Air/50% RH 9-1
9.2.2 Creep Deformation in Distilled Water 9-1
9.2.3 Loading Deformation 9-1
9.3 COMPRESSIVE CREEP-RUPTURE AND DESIGN CURVES IN AIR/50% RH AND WATER 9-11
9.3.1 Creep-Rupture Life and Creep-Rupture Strain 9-11
9.3.2 Creep Rupture and Design Curves and Equations 9-11
10. BASIC FATIGUE BEHAVIOR AND CORRELATIONS 10-1
10.1 INTRODUCTION 10-1
10.2 FATIGUE S-N CURVES 10-1
10.3 CYCLIC DAMAGE 10-3
10.4 DESIGN MARGINS 10-12
10.5 CONCLUSIONS 10-12
11. RECOMMENDED FATIGUE DESIGN 11-1
11.1 INTRODUCTION 11-1
11.2 FATIGUE DESIGN CURVES 11-1
11.3 ENVIRONMENTAL EFFECTS 11-1
11.4 TREATMENT OF MEAN STRESSES 11-6
11.5 TREATMENT OF CYCLES OF VARYING AMPLITUDES 11-8
11.6 SUMMARY 11-9
12. EFFECTS OF PRIOR STATIC, CYCLIC, AND SUSTAINED LOADINGS 12-1
12.1 INTRODUCTION 12-1
12.2 EFFECT OF PRIOR STATIC LOADING 12-1
12.3 EFFECT OF PRIOR FATIGUE CYCLES ON TENSILE PROPERTIES 12-1
12.4 EFFECT OF PRIOR FATIGUE CYCLES ON CREEP-RUPTURE STRENGTH 12-4
12.5 EFFECT OF PRIOR CREEP ON TENSILE STRENGTH AND STIFFNESS 12-6
12.6 SUMMARY 12-7
13. DAMAGE TOLERANCE DESIGN FOR IMPACTS 13-1
13.1 INTRODUCTION 13-1
13.2 BASIC IMPACT TESTS AND RESULTS 13-1
13.3 EFFECT ON TENSILE, COMPRESSIVE, AND FATIGUE PROPERTIES 13-3
13.4 BRICK-DROP TESTS 13-6
13.5 RECOMMENDED DESIGN APPROACH 13-7

14. SENSITIVITY TO STRESS CONCENTRATIONS—HOLES 14-1
14.1 INTRODUCTION 14-1
14.2 FINITE-ELEMENT ANALYSES 14-1
14.3 TENSILE TESTS 14-1
14.4 FATIGUE TESTS 14-1
14.5 CREEP-RUPTURE TESTS 14-4
14.6 SUMMARY 14-4
15. HAT SECTION FRACTURE TESTS—IMPLICATIONS FOR DESIGN CRITERIA 15-1
15.1 INTRODUCTION 15-1
15.2 MONOTONIC TESTS 15-1
15.3 APPLICATION OF DESIGN GUIDE 15-4
15.4 FATIGUE TESTS 15-4
15.5 SUMMARY 15-8
16. PREDICTIVE MODEL FOR TIME-DEPENDENT DEFORMATION 16-1
16.1 GENERAL 16-1
16.2 DATA AND MODEL 16-1
16.2.1 Linear Range ($0 \leq \sigma < 5.2$ ksi) 16-1
16.2.2 Nonlinear Range ($\sigma > 5.2$ ksi) 16-1
16.2.3 Temperature Effects 16-2
16.2.4 Effects of Distilled Water 16-2
16.2.5 Cyclic Loading 16-3
16.2.6 Generalizations 16-3
16.3 ISOCHRONOUS STRESS-STRAIN CURVES 16-4
16.4 DETAILED RESULTS 16-4
17. DAMAGE DEVELOPMENT AND GROWTH 17-1
17.1 INTRODUCTION 17-1
17.2 DAMAGE INITIATION 17-1
17.3 DAMAGE PROPAGATION 17-2
17.4 ENVIRONMENTAL EFFECTS 17-2

LIST OF FIGURES

Figure		Page
1.1	Reference composite plaque with layer of swirl-mat reinforcement	1-3
2.1	Tensile stress-strain behavior for plaques 1–5	2-2
2.2	The stresses acting on a volume element	2-3
3.1	Relation between strength and stiffness	3-4
3.2	Change in stiffness and strength as a function of ambient temperature	3-5
3.3	Percent change in stiffness vs maximum prior tensile load given in terms of percent UTS	3-7
3.4	Effect of strain rate on tensile stress-strain behavior	3-8
3.5	Effect of strain rate on compressive stress-strain behavior	3-9
4.1	None of the three-point bend tests loaded normal to the plaque failed in interlaminar shear as evidenced by them all failing at the same MOR value	4-2
4.2	Effect of battery acid, distilled water, and 180°F demineralized water on the in-plane shear behavior	4-4
4.3	Typical Iosipescu specimens that were tested after being exposed to four different environments	4-5
5.1	Effect of moisture exposure time on strength	5-1
5.2	Effect of moisture exposure time on stiffness	5-2
5.3	Weight gain due to moisture absorption	5-3
5.4	Reduction in strength due to moisture weight gain	5-5
5.5	Reduction in stiffness due to moisture weight gain	5-6
5.6	Effects of 1080 h pre-soak in 180°F demineralized water and room-temperature distilled water on tensile and compressive properties	5-7
5.7	Effects of prior exposure to various automotive fluids on tensile strength and stiffness	5-8
6.1	Candidate failure criteria	6-2
6.2	Finite-element results on bottom of plate	6-3
6.3	Circular disk specimens after being tested	6-4
6.4	Average maximum stresses at failure in the disks compared with five failure criteria	6-5
6.5	Available data indicate maximum shear criterion applies	6-6
7.1	Creep at reference conditions	7-2
7.2	Creep-strain rate at 3000 h vs stress at reference conditions	7-3
7.3	Creep at 710°R (250°F)	7-5
7.4	Creep-strain rate at 3000 h vs stress	7-6
7.5	WLF Eq. (7.5) vs temperature	7-7
7.6	Creep curves for 2–14 ksi at 535°R (75°F)	7-8
7.7	Creep curves for 2–12 ksi at 595°R (135°F)	7-9
7.8	Creep curves for 2–10 ksi at 650°R (190°F)	7-9
7.9	Creep curves for 1–8 ksi at 710°R (250°F)	7-10
7.10	Creep in distilled water at 535°R (75°F)	7-11
7.11	Creep-strain rate at 3000 h vs stress in distilled water at 75°F	7-12
7.12	Distilled water environmental factor K_{DW} vs stress	7-12
7.A.1	Schematic of a log-log plot of creep-strain rate at a given time vs stress	7-15
7.B.1	Extrapolated creep curves for 2–14 ksi at 420°R (–40°F)	7-17
7.C.1	Correlation of Appendix 7.C model (solid lines) with "data" (dashed lines)	7-20
7.C.2	Predicted (lines) and measured (symbols) creep and recovery for 4 ksi to 0 ksi step at 75°F	7-21
7.C.3	Predicted (lines) and measured (symbols) creep of a step test at 4-6-8 ksi and 75°F	7-21
8.1(*a*)	Average, minimum creep-rupture, and maximum design-allowable curves and equations for air/50% RH at 75°F	8-2

8.1(*b*) Average, minimum creep-rupture, and maximum design-allowable curves and equations for air/50% RH at 75°F on the normalized data base 8-3
8.2(*a*) Maximum design-allowable curve and equation for air/50% RH at 75°F are suggested for 20°F 8-4
8.2(*b*) Maximum design-allowable curve and equation for air/50% RH at 75°F are suggested for 20°F on the normalized data base 8-5
8.3(*a*) Maximum design-allowable curve and equation for air/50% RH at 135°F 8-6
8.3(*b*) Maximum design-allowable curve and equation for air/50% RH at 135°F on the normalized data base 8-7
8.4(*a*) Minimum creep-rupture and maximum design-allowable curves and equation for air/50% RH at 190°F 8-8
8.4(*b*) Minimum creep-rupture and maximum design-allowable curves and equation for air/50% RH at 190°F on the normalized data base 8-9
8.5(*a*) Minimum creep-rupture and maximum design-allowable curves and equation for air/50% RH at 250°F 8-10
8.5(*b*) Minimum creep-rupture and maximum design-allowable curves and equation for air/50% RH at 250°F on the normalized data base 8-11
8.6 Minimum creep-rupture and maximum design-allowable curves and equation for air < 10% RH at 75° 8-13
8.7(*a*) Minimum creep-rupture and maximum design-allowable curves and equation for air > 90% RH at 75°F 8-14
8.7(*b*) Minimum creep-rupture and maximum design-allowable curves and equation for air > 90% RH at 75°F on the normalized data base 8-15
8.8 Minimum creep-rupture and maximum design-allowable curves and equation for distilled water at 75°F 8-16
8.9 Minimum creep-rupture and maximum design-allowable curves and equation for distilled water at 135°F 8-17
8.10 Minimum creep-rupture and maximum design-allowable curves and equation for distilled water at 190°F 8-18
8.11 Minimum creep-rupture and maximum design-allowable curves and equation for motor vibration in air/50% RH at 75°F 8-19
8.12 Minimum creep-rupture and maximum design-allowable curves and equation for low-frequency load cycling in air/50% RH at 75°F 8-20
8.13 Minimum creep-rupture and maximum design-allowable curves and equation for low-frequency load cycling in distilled water at 75°F 8-21
8.14 Maximum design-allowable creep-rupture curve and equation for coolant at various temperatures indicated are assumed to be equivalent to that for distilled water at 75°F. 8-22
8.15 Maximum design-allowable creep-rupture curve and equation for two water-based fluids (i.e., saltwater and windshield washing fluid) are assumed to be equivalent to that for distilled water at 75°F 8-23
8.16 Creep-rupture minimum and maximum design-allowable curves and equation for brake fluid at 75° 8-24
8.17 Creep-rupture minimum and maximum design-allowable curves and equation for used motor oil at 75°F 8-25
8.18 Minimum creep-rupture and maximum design-allowable curves and equation for sulfuric acid environments at 75°F 8-26
8.19 Creep-rupture data and curves at various temperatures in air/50% RH 8-30
8.20 Creep-rupture data and curves in air < 10% RH and air > 90% with the average and minimum for air/50% RH at 75°F 8-31
8.21 Creep-rupture data and curves in distilled water at various temperatures 8-32
9.1 Comparison of tensile and compressive creep deformation curves in air/50% RH at 75°F at 11 ksi shows similar deformation behavior 9-2

9.2 Comparison of tensile and compressive creep deformation curves in air/50% RH at 75°F at 12 ksi shows similar deformation behavior 9-3
9.3 Recovery behavior under compressive loading in air/50% RH at 75°F 9-4
9.4 At 75°F in distilled water, compressive and tensile creep deformation at 12 ksi is comparable 9-5
9.5 Compressive creep deformation is comparable to tensile creep deformation at 135°F and 8 ksi in distilled water 9-6
9.6 Data suggest that compressive creep deformation is increased compared to tensile creep deformation at 135°F and 11 ksi in distilled water 9-7
9.7 Data suggest that compressive creep deformation is increased compared to tensile creep deformation at 135°F and 12 ksi in distilled water 9-8
9.8 Compressive loading deformation is comparable to tensile loading deformation at 75°F in air/50% RH 9-9
9.9 Compressive loading deformation is comparable to tensile loading deformation at 75°F in distilled water 9-10
9.10 Compressive loading deformation is comparable to tensile loading deformation at 135°F in distilled water 9-11
9.11 On a creep-rupture strain basis, compressive creep-rupture life in distilled water is comparable to that under tensile loading conditions at 75°F 9-12
9.12 On a creep-rupture strain basis, compressive creep-rupture life in distilled water is slightly shortened relative to that under tensile loading conditions at 135°F 9-13
9.13 Average and minimum creep-rupture curves and equation, and maximum design-allowable curve and equation for air/50% RH at 75°F for tensile loading are assumed to be equivalent to those for compressive loading 9-14
9.14 Minimum creep-rupture and maximum design-allowable curves and equation for distilled water at 75°F for tensile loading are assumed to be equivalent to those for compressive loading 9-15
9.15 Minimum creep-rupture and the maximum design-allowable curves and equation for distilled water at 135°F 9-16
9.16 Minimum creep-rupture and the maximum design-allowable curves and equation for water at 190°F 9-17
9.17 Average creep-rupture curves show that compressive loading tends to decrease creep-rupture life or creep-rupture stress compared to tensile loading in distilled water at 135°F 9-18
9.18 Average creep-rupture curves show that compressive loading tends to decrease creep-rupture life or creep-rupture stress even more at 190°F compared to tensile loading in distilled water at the same temperature 9-19
10.1 Fatigue S-N curves 10-4
10.2 Stress-strain loops for selected tests 10-5
10.3 Stiffness reduction vs life fraction at –40°F 10-6
10.4 Stiffness reduction vs life fraction at room temperature 10-7
10.5 Stiffness reduction vs life fraction at 250°F 10-8
10.6 Maximum strain vs cycles at –40°F 10-9
10.7 Maximum strain vs cycles at room temperature 10-10
10.8 Maximum strain vs cycles at 250°F 10-11
10.9 Slope of initial straight lines in Fig. 10.7 vs maximum stress 10-13
10.10 Possible design margins relative to –40°F data 10-13
10.11 Possible design margins relative to room-temperature data 10-14
10.12 Possible design margins relative to 250°F data 10-14
11.1 Normalized S-N curve showing near-colinearity of 0° and 90° fatigue data 11-2
11.2 Normalized 0° direction fatigue data with average and minimum representations 11-3
11.3 Normalized 0° direction fatigue data with possible design margins 11-4
11.4 Recommended fatigue design curves 11-5

11.5 Distilled water fatigue data and power law fits to data and to corresponding ambient air data 11-6
11.6 Comparison of R = 0 and R = –1 (zero mean stress) fatigue data 11-8
11.7 Compression-compression (R = 0.1) fatigue data compared to tension-tension and fully reversed fatigue data 11-9
12.1 Loss of stiffness due to prior static tensile loadings to indicated levels 12-2
12.2 Reduction in tensile strength vs prior cyclic life fraction 12-3
12.3 Stiffness reduction vs cyclic life fraction 12-4
12.4 Comparison of creep-rupture curves for various amounts of prior fatigue damage 12-5
12.5 Effect of prior creep strain on subsequent tensile strength 12-6
12.6 Effect of prior creep strain on subsequent stiffness 12-7
13.1 Baseline correlation—damage area vs $m^{0.564} \times v$ 13-2
13.2 Comparison of results for other conditions with baseline correlation 13-3
13.3 Typical distributions of tensile properties across impacted specimens 13-4
13.4 Relative tensile, compressive, and 10^6 cycle fatigue strengths vs damage area 13-5
13.5 Relative tensile stiffness vs damage area 13-5
13.6 Comparison of damage areas from brick drops with baseline data 13-6
13.7 Design curve for determining impact damage area 13-7
13.8 Strength degradation as a function of damage area 13-8
13.9 Tensile stiffness degradation as a function of damage area 13-8
13.10 Calculated peak contact force vs damage area 13-9
14.1 Finite-element grid and analysis results 14-2
14.2 Circular hole strength reduction predictions compared with impact strength degradation results 14-3
14.3 Calculated stiffness compared to impact degradation results 14-3
14.4 Fatigue strength (solid line) of specimens with 0.25-in.-diam holes compared to reference fatigue curve (dashed line) 14-4
14.5 Creep-rupture strength of specimens with 0.25-in.-diam holes (solid points, dashed line) compared to reference creep-rupture curve (open points, solid line) 14-5
15.1 Hat section 15-1
15.2 Application of load in the tension and compression hat specimens 15-2
15.3 Hat section torsion specimen 15-2
15.4 Compressive hat section specimen 15-3
15.5 Delamination occurred in the corners when tension was applied to the hat section specimens 15-5
15.6 Hat section torsion specimens broke as shown, starting at the edges 15-6
15.7 Elastic analysis results agreed well with hat section tensile tests beyond the load that produced the maximum allowable stress intensity 15-7
15.8 Elastic analysis agreed well with hat section compressive test results at low loads 15-7
15.9 Range of elastic analysis results for torsion hat section specimens bounds the measured rotations 15-8
16.1 Isochronous stress-strain curves 16-4
16.2 Isochronous curves of recovery strain $\in$ vs previously applied stress 16-5
17.1 C-scan images of a tensile specimen incrementally loaded to 20, 40, 60, and 80% of the UTS 17-1
17.2 Crack propagation through a large void 17-3
17.3 Propagation of a crack across a tensile specimen 17-4
17.4 Progression in observable damage as a function of cycles 17-5
17.5 Fracture surface viewed from the side and top (70x) 17-5
17.6 River patterns on a fracture surface (300x) 17-6
17.7 Fracture surface of a failed creep specimen 17-6
17.8 Schematic of failure mechanism 17-7
17.9 SEM images of creep specimen fracture surfaces 17-8
17.10 SEM images of fatigue specimen fracture surfaces 17-9

LIST OF TABLES

Table		Page
3.1	Tensile properties, 0° direction	3-2
3.2	Tensile properties, 90° direction	3-3
3.3	Tensile properties as a function of temperature	3-4
6.1	Data from tests on circular disks subjected to ring load	6-3
7.1	Estimated creep factor for various conditions	7-13
8.1	Comparison of the R values for power law curve fitting between original and normalized data for air/50% RH	8-11
8.2	Maximum design-allowable stress in air/50% RH for specific no-rupture time limits	8-12
8.3	Maximum design-allowable stress (ksi) in air < 10% RH and air > 90% RH for specific no-rupture time limits	8-14
8.4	Comparison of the R values for power law curve fitting between original and normalized data for air > 90% RH at 75°F	8-15
8.5	Maximum design-allowable stress in distilled water for specific no-rupture time limits	8-18
8.6	Maximum design-allowable stress under motor vibration and low-frequency load cycling for specific no-rupture time limits	8-21
8.7	Maximum design-allowable stress in oil-based fluids for specific no-rupture time limits	8-25
8.8	Maximum design-allowable stress in sulfuric acid and sulfuric acid spot conditions for specific no-rupture time limits	8-26
8.9	Stress reduction factor in air/50% RH for specific no-rupture time limits	8-27
8.10	Stress reduction factor in air < 10% RH and air > 90% RH for specific no-rupture time limits	8-27
8.11	Stress reduction factor in distilled water for specific no-rupture time limits	8-27
8.12	Stress reduction factor under motor vibration in air/50% RH and low-frequency load cycling in air/50% RH and distilled water for specific no-rupture time limits	8-28
8.13	Stress reduction factor in oil-based fluids for specific no-rupture time limits	8-28
8.14	Stress reduction factor under sulfuric acid conditions for specific no-rupture time limits	8-28
8.15	Stress reduction factor under various conditions for specific no-rupture time limits	8-29
9.1	Maximum compressive design-allowable stress in air/50% RH for specific no-rupture time limits	9-19
9.2	Maximum compressive design-allowable stress in distilled water for specific no-rupture time limits	9-20
9.3	Stress reduction factors in air/50% RH for specific no-rupture time limits under compressive loading	9-20
9.4	Stress reduction factors in distilled water for specific no-rupture time limits under compressive loading	9-20
10.1	Plaque P36 tensile properties	10-1
10.2	Plaque P36 fatigue properties	10-2
11.1	Fatigue stress reduction factors for various automotive fluid environments	11-6
11.2	Results of block loading tests	11-10
12.1	Test matrix (number of duplicate specimens) for effect of prior fatigue on tensile properties (P34–0°)	12-2
12.2	Test matrix for effects of prior fatigue on creep-rupture strength (P34–0°)	12-4
12.3	Test matrix (number of duplicate specimens) for effects of prior creep on tensile properties	12-6
13.1	List of impact tests and subsequent mechanical property tests	13-2

CONVERSION FACTORS

U.S. Customary Units to SI Units

Quantity	Multiply	By	To obtain
Length	Inch (in.)	2.54×10^{-2}	Meter (m)
Force	Pound (lb)	4.448	Newton (N)
Mass	Slug $\left(\frac{\text{lb} \cdot \text{s}^2}{\text{ft}}\right)$	14.59	Kilogram (kg)
Stress	Pound/inch^2 (psi)*	6.895×10^6	Pascal (Pa)
Velocity	Foot/second (ft/s)	0.3048	Meter/second (m/s)
Torque	Inch · pound (in. · lb)	0.1130	Newton · meter (N · m)
Temperature	Temperature (°F – 32)	0.5556	Temperature (°C)

*ksi = 10^3 psi; Msi = 10^6 psi.

DURABILITY-BASED DESIGN CRITERIA FOR AN AUTOMOTIVE STRUCTURAL COMPOSITE: PART 2. BACKGROUND DATA AND MODELS

J. M. Corum
R. L. Battiste
C. R. Brinkman
W. Ren
M. B. Ruggles
Y. J. Weitsman
G. T. Yahr

ABSTRACT

This background report is a companion to the document entitled *Durability-Based Design Criteria for an Automotive Structural Composite: Part 1. Design Rules* (ORNL-6930). The rules and the supporting material characterization and modeling efforts described here are the result of a U.S. Department of Energy Advanced Automotive Materials project entitled "Durability of Lightweight Composite Structures." The overall goal of the project is to develop experimentally based, durability-driven design guidelines for automotive structural composites. The project is closely coordinated with the Automotive Composites Consortium (ACC). The initial reference material addressed by the rules and this background report was chosen and supplied by ACC. The material is a structural reaction injection-molded isocyanurate (urethane), reinforced with continuous-strand, swirl-mat, E-glass fibers.

This report consists of 16 position papers, each summarizing the observations and results of a key area of investigation carried out to provide the basis for the durability-based design guide. The durability issues addressed include the effects of cyclic and sustained loadings, temperature, automotive fluids, vibrations, and low-energy impacts (e.g., tool drops and roadway kickups) on deformation, strength, and stiffness. The position papers cover these durability issues. Topics include (1) tensile, compressive, shear, and flexural properties; (2) creep and creep rupture; (3) cyclic fatigue; (4) the effects of temperature, environment, and prior loadings; (5) a multiaxial strength criterion; (6) impact damage and damage tolerance design; (7) stress concentrations; (8) a damage-based predictive model for time-dependent deformations; (9) confirmatory subscale component tests; and (10) damage development and growth observations.

1. INTRODUCTION

1.1 BACKGROUND

This report is a companion to the document entitled *Durability-Based Design Criteria for an Automotive Structural Composite: Part 1. Design Rules* (ORNL-6930) and provides the material characterization and modeling information on which the rules of Part 1 are based. It is the background documentation for the rules.

Both documents—Part 1 and Part 2—are the products of a U.S. Department of Energy (DOE) Advanced Automotive Materials project at Oak Ridge National Laboratory (ORNL) entitled "Durability of Lightweight Composite Structures." The overall goal of the project is to develop experimentally based, durability-driven design guidelines for automotive composite structures and to demonstrate their applicability to lightweight manufacturable structures under realistic loading histories and environments.

Key technical issues are the potentially degrading effects that both cyclic and sustained loadings, various environments, and low-energy impacts can have on the dimensional stability, strength, and stiffness of automotive structural composites. Specific project objectives are thus to (1) characterize and model the synergistic effects of cyclic and creep loadings, temperature, relevant automotive fluid environments, vibrations, and low-energy impacts (e.g., tool drops and roadway kickups) on deformation, strength, and stiffness and (2) develop and validate, through subscale component tests, design guidance to ensure the long-term (15-year) durability of automotive component structures.

The project is closely coordinated with the Automotive Composites Consortium (ACC). The point of contact within ACC for the project is E. M. Hagerman of General Motors. An ad hoc durability group consisting of representatives from Chrysler, Ford, and General Motors provides the overall coordination for ACC. The candidate composite materials currently being addressed were chosen and provided by ACC.

The project strategy has been to initially focus on one representative reference material—a continuous-strand glass mat reinforcement in a liquid-molded urethane matrix—and to develop the initial design criteria on the basis of this one material. This document and the resulting design rules (Part 1) are the result of that strategy.

The follow-on strategy being pursued in FY 1998 is to (1) add a second glass-fiber composite (P4 directed, chopped fiber/urethane material being used in the ACC Focal Project II pickup box) and (2) begin the transition to carbon-fiber composites by initially focusing on a ±45° stitch-bonded carbon fiber/urethane. These materials will be added to the design criteria in the future.

1.2 REFERENCE COMPOSITE

This report and the companion design rules (Part 1) exclusively address the initial reference composite—a structural reaction injection-molded (SRIM) polyisocyanurate reinforced with continuous-strand, swirl-mat E-glass. The polyisocyanurate system is DOW MM 364, and the reinforcing is Certainteed/Vetrotex Unifilo U750. The fiber bundles consist of several hundred 0.0006-in.-diam monofilaments.

The material was supplied by ACC in the form of 25 × 25 × 1/8-in.-thick plaques (Fig. 1.1). Five layers of mat, all oriented the same to maximize anisotropy, were used in each plaque, resulting in a fiber content of about 25% by volume (40 to 50% by weight). The glass transition temperature, T_g, was determined by ACC to be in the 329 to 338°F range.[1]

1.3 OVERVIEW OF PART 1 RULES

Part 1 provides detailed rules and guidelines for (1) the properties to be used in structural analyses, (2) design allowables for static loadings, (3) design rules for cyclic loadings, and (4) damage tolerance design for low-energy impacts. In each case, the range of automotive environments is taken into account. A final chapter condenses the more detailed rules into a simplified set of rules consisting of knockdown factors applied to static properties. Both the detailed and simplified rules are intended to ensure the long-term (15-year) durability of automotive composite structures.

1.4 OVERVIEW OF PART 2

The rules of Part 1 and the background information of Part 2 are the results of over 3 years of effort on the reference material. Two major progress reports[2,3] provide the detailed results through FY 1996 (September 1996). Those reports include a description of the test methods and specimen designs employed. Near the beginning of the project a panel of experts was assembled to provide an authoritative treatment of the current status of the key durability issues. The resulting report[4] helped to establish the scope and focus of the work reported here.

This background document consists of 16 position papers. Each summarizes, condenses, and focuses the information generated in a key area supporting the design rules. The rules of Part 1 result directly from the data, correlations, and models presented here. References to chapters in this document are frequently made as the rules are presented in Part 1.

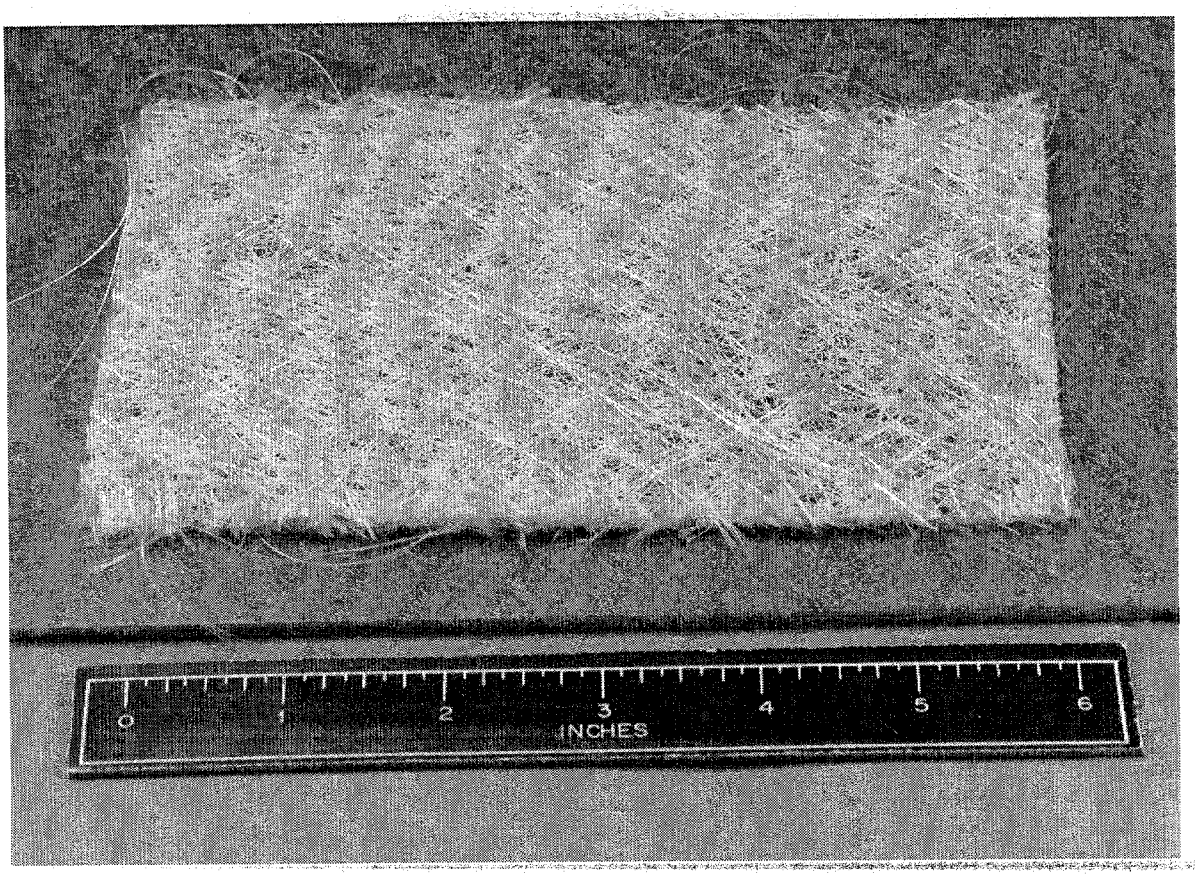

Fig. 1.1. Reference composite plaque with layer of swirl-mat reinforcement.

The following chapter addresses the basis for using just two elastic constants in elastic design analyses. Chapters 3, 4, and 5 then provide the basic tensile, compressive, shear, and flexural properties of the reference composite. Temperature and environmental effects are included.

Chapter 6 provides supporting data for choosing the maximum shear stress theory for the multiaxial failure criterion. This criterion leads to the simple stress intensity quantity used in Part 1 for the equivalent stress representing multiaxial stresses.

Chapters 7, 8, and 9 present creep and creep-rupture results in tension and compression. Again the effects of temperature and various environments are included. A reference creep equation (creep strain vs time) is derived, and factors are developed for accounting for temperature and environments. Likewise, creep-rupture curves are developed, and again factors for accounting for temperature and environments are given. Design curves, used in Part 1, are recommended.

Chapters 10 and 11 address fatigue. Tensile fatigue, compressive fatigue, and fully reversed fatigue curves are given. Block loading results are also given. From these, design curves are developed, a modified Goodman relation is recommended for handling mean stresses, and Miner's rule for damage accumulation is chosen. Temperature effects are included, and environmental degradation factors are given.

Chapter 12 presents the results of studies that quantify the effects of prior loadings—static preloads, cyclic loads, and sustained loads—on subsequent strength and stiffness. These results are factored into the allowable stresses of Part 1.

Chapter 13 presents extensive impact test results as well as residual tensile, compressive, and fatigue strength data. A correlation between impact damage area and impactor mass and velocity is developed that holds for a variety of impactors, including bricks, and for various environments. Plots of strength degradation vs damage area are also given. Chapter 14, on sensitivity to stress concentrations, also relates to areas of damage. Tensile, fatigue, and creep-rupture test results on specimens with holes are presented, and the effective stress concentration factor is shown to be considerably less than the theoretical one. Strength degradation due to impact can be estimated by representing the damage area by a circular hole.

Chapter 15 presents confirmatory test results on subscale component shapes cut from "hat sections." The hat sections have typical geometric discontinuities (bends) representative of real structures. Both monotonic and cyclic bending and torsion tests were done, simulating various stress states. The measured deformations compared well with elastic finite-element predictions, and the failure loads were well above the design limits of Part 1.

Chapter 16 presents a damage-based viscoelastic predictive model for time-dependent deformation. The model, which predicts both creep and recovery, can be used in detailed inelastic design analyses of critical areas.

Finally, Chap. 17 summarizes observations made of damage development and growth for various loadings and environments. Such observations were used to interpret mechanical behavior in terms of damage development.

REFERENCES

1. Personal communication from E. M. Hagerman, ACC/General Motors, to J. M. Corum, Lockheed Martin Energy Research Corp., Oak Ridge National Laboratory, October 16, 1997.

2. J. M. Corum, *Durability of Lightweight Composite Structures for Automotive Applications: Progress Report for Period Ending September 30, 1995*, ORNL/TM-13176, Lockheed Martin Energy Research Corp., Oak Ridge National Laboratory, March 1996.

3. J. M. Corum, *Durability of Lightweight Composite Structures for Automotive Applications: Annual Progress Report for Period Ending September 30, 1996*, ORNL/TM-13345, Lockheed Martin Energy Research Corp., Oak Ridge National Laboratory, December 1996.

4. J. M. Corum, W. A. Simpson, Jr., C. T. Sun, R. Talreja, and Y. J. Weitsman, *Durability of Polymer Matrix Composites for Automotive Structural Applications: A State-of-the-Art Review*, ORNL-6869, Lockheed Martin Energy Research Corp., Oak Ridge National Laboratory, July 1995.

2. ELASTIC ANALYSIS

G. T. Yahr

Typical room-temperature tensile stress-strain curves in the 0° and 90° directions for the reference continuous-strand-mat (CSM) reinforced isocyanurate composite are shown in Fig. 2.1. Although the stress-strain curves are nonlinear, elastic analysis is recommended. The secant modulus up to the basic short-time allowable stress is <10% less than the initial tangent modulus, so elastic analysis, using the elastic tangent modulus, is reasonable for this material. Note also that the initial tangent modulus in the 90° direction is 18% higher than the initial tangent modulus in the 0° direction. Use of the 0°-direction modulus will provide conservative predictions of deformations. Predicted stresses will be unconservative in deformation-controlled situations such as discontinuity stresses and thermal stresses.

Any stress on a volume element can be resolved into nine stress components, as shown in Fig. 2.2. There are three normal stresses perpendicular to the three faces of the cube and six tangential stresses or shear stresses. By considering the equilibrium of the element, the following equalities can be shown to hold: $\tau_{21} = \tau_{12}$, $\tau_{23} = \tau_{32}$, and $\tau_{13} = \tau_{31}$. Thus, the stress can be completely specified by only six independent components, which are three normal stresses, σ_1, σ_2, σ_3, and three tangential stresses, τ_{12}, τ_{23}, τ_{31}.

For each stress component, there is a corresponding strain component. Thus, there are three normal strains, ε_1, ε_2, ε_3, and three shear strains, γ_{12}, γ_{23}, and γ_{31}. The linear relations between stress and strain components are the generalized form of Hooke's law and are given by the following set of equations:

$$
\begin{aligned}
\sigma_1 &= c_{11}\varepsilon_1 + c_{12}\varepsilon_2 + c_{13}\varepsilon_3 + c_{14}\gamma_{23} + c_{15}\gamma_{31} + c_{16}\gamma_{12} \\
\sigma_2 &= c_{21}\varepsilon_1 + c_{22}\varepsilon_2 + c_{23}\varepsilon_3 + c_{24}\gamma_{23} + c_{25}\gamma_{31} + c_{26}\gamma_{12} \\
\sigma_3 &= c_{31}\varepsilon_1 + c_{32}\varepsilon_2 + c_{33}\varepsilon_3 + c_{34}\gamma_{23} + c_{35}\gamma_{31} + c_{36}\gamma_{12} \\
\tau_{23} &= c_{41}\varepsilon_1 + c_{42}\varepsilon_2 + c_{43}\varepsilon_3 + c_{44}\gamma_{23} + c_{45}\gamma_{31} + c_{46}\gamma_{12} \\
\tau_{31} &= c_{51}\varepsilon_1 + c_{52}\varepsilon_2 + c_{53}\varepsilon_3 + c_{54}\gamma_{23} + c_{55}\gamma_{31} + c_{56}\gamma_{12} \\
\tau_{12} &= c_{61}\varepsilon_1 + c_{62}\varepsilon_2 + c_{63}\varepsilon_3 + c_{64}\gamma_{23} + c_{65}\gamma_{31} + c_{66}\gamma_{12}
\end{aligned}
$$

These equations may be written in matrix form as

$$
\begin{bmatrix} \sigma_1 \\ \sigma_2 \\ \sigma_3 \\ \tau_{23} \\ \tau_{31} \\ \tau_{12} \end{bmatrix}
=
\begin{bmatrix}
c_{11} & c_{12} & c_{13} & c_{14} & c_{15} & c_{16} \\
c_{21} & c_{22} & c_{23} & c_{24} & c_{25} & c_{26} \\
c_{31} & c_{32} & c_{33} & c_{34} & c_{35} & c_{36} \\
c_{41} & c_{42} & c_{43} & c_{44} & c_{45} & c_{46} \\
c_{51} & c_{52} & c_{53} & c_{54} & c_{55} & c_{56} \\
c_{61} & c_{62} & c_{63} & c_{64} & c_{65} & c_{66}
\end{bmatrix}
\begin{bmatrix} \varepsilon_1 \\ \varepsilon_2 \\ \varepsilon_3 \\ \gamma_{23} \\ \gamma_{31} \\ \gamma_{12} \end{bmatrix}
$$

The c's are called stiffness constants, and the square matrix is called the stiffness matrix.

Thermodynamic considerations, namely the presumed existence of a strain-energy potential,[1] show that the stiffness matrix is symmetrical about the principal diagonal. Thus, the matrix becomes

$$
\begin{bmatrix}
c_{11} & c_{21} & c_{31} & c_{41} & c_{51} & c_{61} \\
c_{21} & c_{22} & c_{32} & c_{42} & c_{52} & c_{62} \\
c_{31} & c_{32} & c_{33} & c_{43} & c_{53} & c_{63} \\
c_{41} & c_{42} & c_{43} & c_{44} & c_{54} & c_{64} \\
c_{51} & c_{52} & c_{53} & c_{54} & c_{55} & c_{65} \\
c_{61} & c_{62} & c_{63} & c_{64} & c_{65} & c_{66}
\end{bmatrix}
$$

where there are only 21 independent constants.

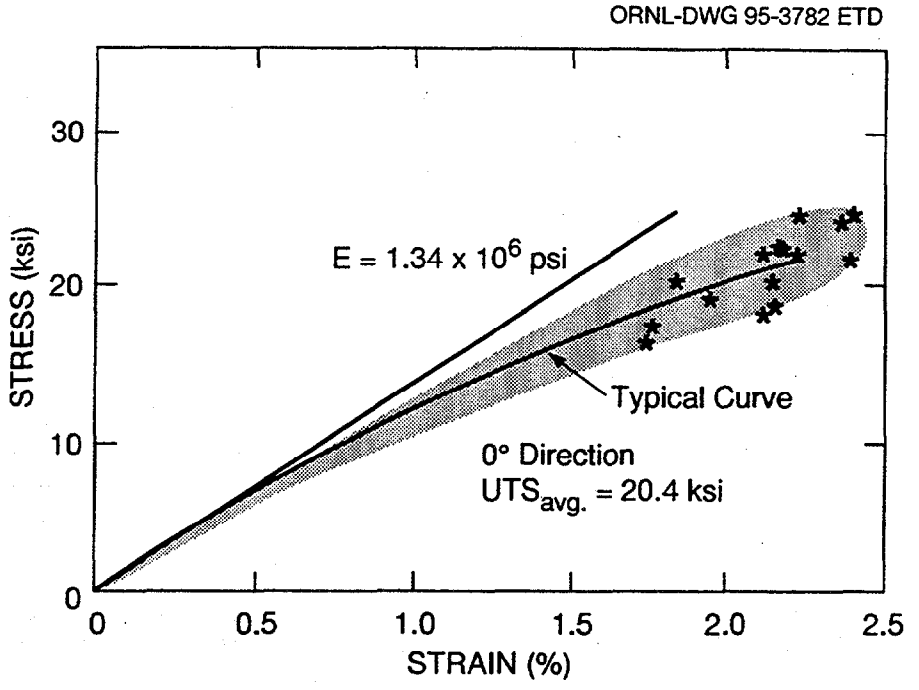

a. 0° direction

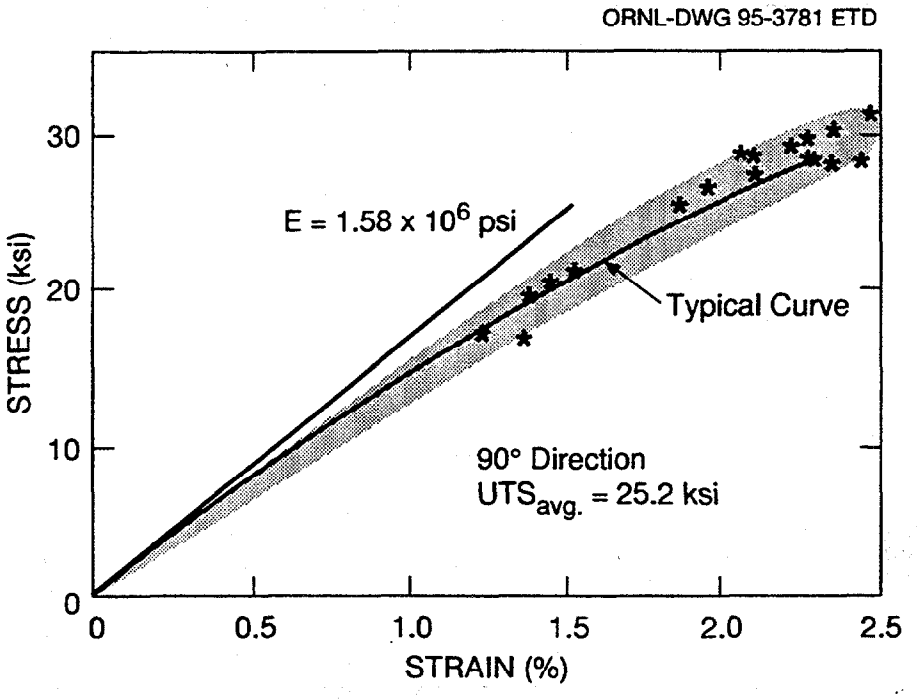

b. 90° direction

Fig. 2.1. Tensile stress-strain behavior for plaques 1–5.

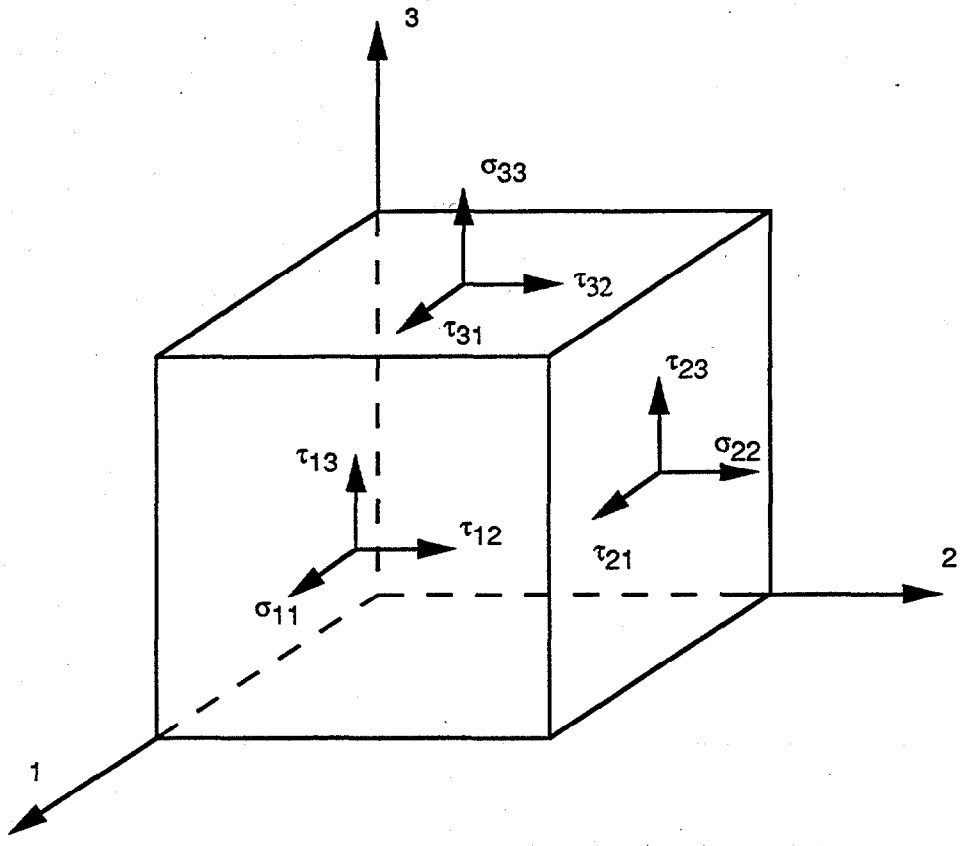

Fig. 2.2. The stresses acting on a volume element.

It is assumed that the reference CSM/isocyanurate is isotropic in the plane of the plaque. Under this assumption, the stiffness matrix has only five independent elements. By choosing the 1 and 2 directions to lie in the plane of the plaque and the 3 direction as the transverse direction, the matrix reduces to

$$\begin{bmatrix} c_{11} & c_{12} & c_{13} & 0 & 0 & 0 \\ c_{12} & c_{11} & c_{13} & 0 & 0 & 0 \\ c_{13} & c_{13} & c_{33} & 0 & 0 & 0 \\ 0 & 0 & 0 & c_{44} & 0 & 0 \\ 0 & 0 & 0 & 0 & c_{44} & 0 \\ 0 & 0 & 0 & 0 & 0 & (c_{11}-c_{12})/2 \end{bmatrix}$$

The five stiffness constants may be related to five independent material constants that can be determined experimentally.

A more direct identification with experimental data is achieved when the stress-strain relations are expressed in the following forms:[2]

$$\varepsilon_1 = \frac{1}{E_1}\left[\sigma_1 - \nu_{12}\sigma_2 - \nu_{13}\sigma_3\right] ,$$

$$\varepsilon_2 = \frac{1}{E_1}\left[\sigma_2 - \nu_{13}\sigma_3 - \nu_{12}\sigma_1\right] ,$$

$$\varepsilon_3 = \frac{1}{E_3}\left[\sigma_3 - \frac{E_3}{E_1}\nu_{13}\left(\sigma_1 + \sigma_2\right)\right] ,$$

$$\gamma_{23} = \frac{1}{G_4}\tau_{23} ,$$

$$\gamma_{31} = \frac{1}{G_4}\tau_{31} ,$$

$$\gamma_{12} = \frac{2(1+\nu_{12})}{E_1}\tau_{12} .$$

By setting $\sigma_1 = \sigma_2 = 0$ in the above expression for $\in_1$, it follows that

$$\varepsilon_1 = \frac{1}{E_1}\left(-\nu_{13}\sigma_3\right) .$$

It also follows from the definition of Poisson's ratio ν_{31}, $\nu_{31} = -\frac{\varepsilon_1}{\varepsilon_3}$, that

$$\varepsilon_1 = \frac{1}{E_3}\left(-\nu_{31}\sigma_3\right) .$$

Thus, the following relationship is implied:

$$\nu_{31} = \frac{E_3}{E_1}\nu_{13} .$$

This expression stems from the symmetry of the stiffness matrix.

The modulus, E_1, and Poisson's ratio, ν_{12}, were measured with in-plane tensile tests. The shear modulus measured with the Iosipescu specimens is not G_4. It is not an independent constant. It is related to E_1 and ν_{12} by the relation

$$G_1 = \frac{E_1}{2(1+\nu_{12})} .$$

Because the CSM/isocyanurate is usually used in thin sections, only the in-plane stresses are important for most practical situations (i.e., $\sigma_3 \approx 0$). For plane stress problems, Hooke's law reduces to

$$\varepsilon_1 = \frac{1}{E_1}\left[\sigma_1 - \nu_{12}\sigma_2\right] ,$$

$$\varepsilon_2 = \frac{1}{E_1}\left[\sigma_2 - \nu_{12}\sigma_1\right] ,$$

$$\varepsilon_3 = \frac{-\nu_{13}}{E_1}\left[\sigma_1 + \sigma_2\right] .$$

Except for ν_{13}, which is required for calculating the strain in the thickness direction of the plates, we have measured the required constants for plane stress problems.

The recommended elastic constants at room temperature are $E_1 = 1.37$ Msi and $\nu_{12} = 0.31$.

REFERENCES

1. A. E. H. Love, *A Treatise on the Mathematical Theory of Elasticity*, 4th ed., Dover Publications, New York, 1944.
2. R. M. Christensen, *Mechanics of Composite Materials*, Wiley, 1979.

3. TENSILE, COMPRESSIVE, AND FLEXURAL ELASTIC CONSTANTS AND STRENGTH PROPERTIES

M. B. Ruggles and G. T. Yahr

3.1 IN-AIR ELASTIC CONSTANTS AND STRENGTH PROPERTIES AS A FUNCTION OF TEMPERATURE

3.1.1 Tensile Elastic Constants and Strength Properties

The following in-air room temperature values of stiffness, E, ultimate tensile strength (UTS) and failure strain, ε_f, are averages based on results of 277 tensile tests, 185 tests in the 0° direction, and 92 tests in the 90° direction. The average value of Poisson's ratio is based on results of 16 tests conducted on 0°-direction specimens from plaque P8. Tensile results are recapitulated in Tables 3.1 and 3.2, where the number of specimens tested from each particular plaque and the plaque averages are presented for the 0° and 90° directions, respectively. The averages are tabulated below.

Values	0° direction	90° direction
E, Msi	1.37	1.68
UTS, ksi	21.32	28.52
ε_f, %	2.12	2.17

The average value of Poisson's ratio for the 0° direction, ν, is 0.31.

Figure 3.1 is a plot of UTS vs stiffness. Included in the figure are results of all 277 tensile tests as well as results obtained in compression tests. Tensile results obtained for the 0° and 90° directions form a consistent set of data. The 90° results fall on the high end of the set, forming a natural continuation of the 0° distribution. The UTS increases with increasing stiffness. Moreover, the dependence of UTS on stiffness can be reasonably well approximated with a linear correlation:

$$\sigma_{UTS} = -4666 + 0.02E \ .$$

Tensile properties as a function of temperature were established based on tensile tests conducted at –40, 70, 135, 190, and 250°F on specimens from selected plaques. Average values of stiffness and UTS are presented in Table 3.3. Values of stiffness and UTS obtained at elevated temperatures are noticeably lower than those obtained at and below room temperature. Likewise, tensile strength and stiffness appear to increase with decreasing temperature, resulting in "stronger" material at –40°F.

Percent reductions in stiffness and strength as a function of temperature are presented in Fig. 3.2. Results in Fig. 3.2 indicate that simple straight-line approximations may be used to represent reductions in

Table 3.1. Tensile properties, 0° direction

Plaque	Number of specimens	E (Msi)	UTS (ksi)	Failure strain (%)
P1	3	1.34	21.5	2.31
P2	3	1.27	18.57	2.03
P3	3	1.47	21.88	2.04
P4	3	1.38	22.07	2.18
P5	3	1.26	17.74	1.93
P6	4	1.36	19.48	1.99
P8	2	1.49	22.53	1.92
P9	2	1.43	21.01	1.96
P11	19	1.37	20.36	2.25
P12	19	1.28	19.89	2.42
P13	19	1.36	19.37	1.98
P14	15	1.37	20.09	2.36
P15	15	1.29	19.72	2.26
P17	3	1.38	19.15	1.99
P18	3	1.34	19.3	2.04
P19	3	1.37	22.71	2.31
P20	5	1.48	22.76	2.13
P21	10	1.42	23.37	2.28
P22	4	1.59	24.92	2.19
P23	4	1.45	21.37	1.96
P26	4	1.44	21.38	1.98
P27	1	1.52	27.86	2.00
P30	7	1.44	24.50	2.32
P33	3	1.44	20.70	1.86
P34	4	1.50	22.60	1.95
P35	4	1.56	23.90	2.03
P36	6	1.48	26.00	2.46
P37	5	1.53	25.02	1.87
P42	5	1.48	23.44	2.17
P43	4	1.39	23.79	2.33
P44	4	1.46	26.25	2.54
Overall average		1.37	21.32	2.12
Standard deviation		0.13	2.67	0.30
Coefficient of variation (%)		9.48	12.52	14.15

Table 3.2. Tensile properties, 90° direction

Plaque	Number of specimens	E (Msi)	UTS (ksi)	Failure strain (%)
P1	4	1.57	29.22	2.38
P2	2	1.54	23.38	1.94
P3	4	1.63	27.57	2.14
P4	4	1.61	26.74	2.09
P5	4	1.52	18.07	1.37
P6	3	1.68	27.51	2.06
P7	3	1.75	30.14	2.24
P8	4	1.70	29.59	2.22
P9	2	1.73	29.87	2.23
P11	3	1.52	25.81	2.21
P12	3	1.65	29.64	2.27
P13	3	1.61	27.19	2.16
P14	3	1.58	28.75	2.29
P15	3	1.69	29.78	2.22
P17	3	1.75	30.06	2.13
P18	3	1.75	30.83	2.19
P19	5	1.74	28.43	2.13
P21	3	1.76	30.12	2.27
P23	4	1.63	26.43	2.09
P30	4	1.57	29.51	2.44
P33	6	1.80	29.08	2.16
P34	6	1.80	30.35	2.10
P35	3	1.77	29.24	2.14
P37	3	1.81	31.79	2.29
P42	3	1.79	31.09	2.32
P43	4	1.60	31.27	2.54
Overall average		1.68	28.52	2.17
Standard deviation		0.13	3.20	0.26
Coefficient of variation (%)		7.74	11.22	11.98

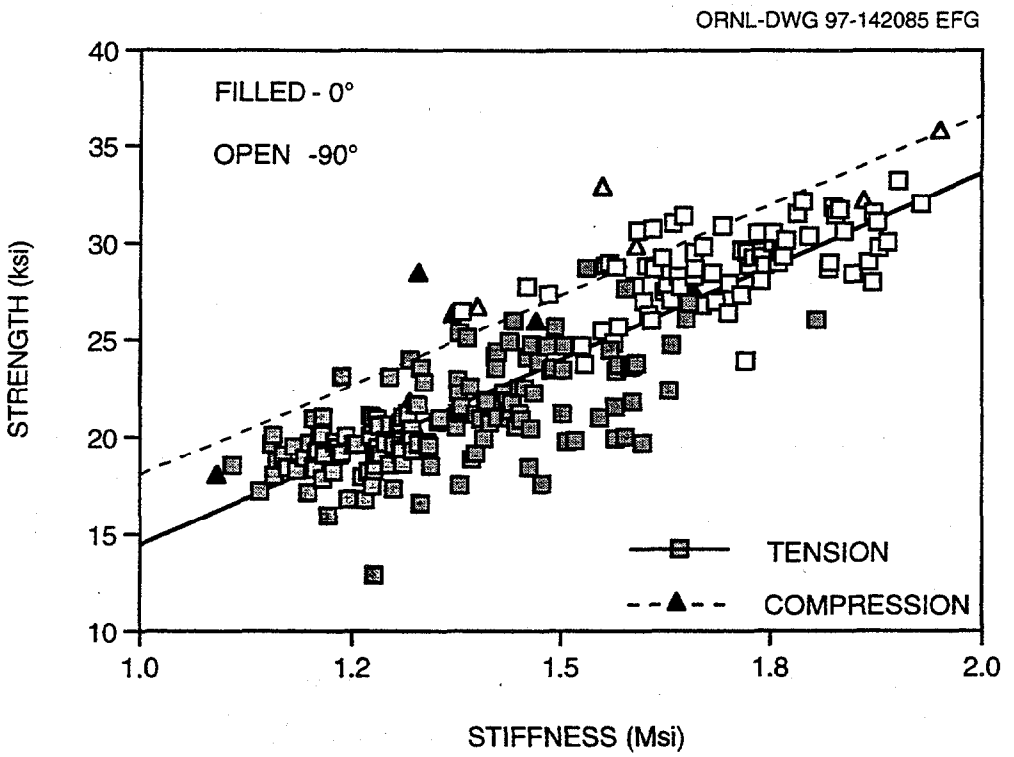

Fig. 3.1. Relation between strength and stiffness.

Table 3.3. Tensile properties as a function of temperature

Temperature (°F)	Stiffness (Msi)	Change in stiffness (%)	UTS (ksi)	Change in UTS (%)
250	0.94	–36.15	19.38	–25.52
190	1.00	–34.3	19.25	–28.91
135	1.14	–24.88	21.08	–22.16
70	1.48	0	26.02	0
–40	1.83	23.65	34.78	33.67

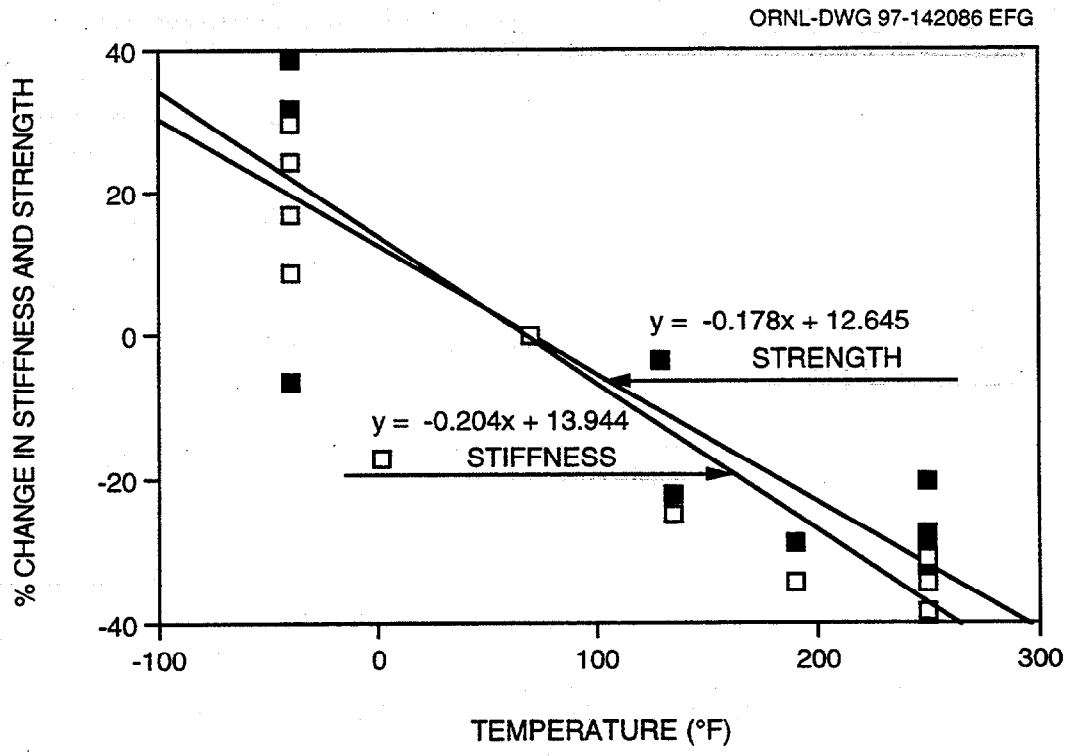

Fig. 3.2. Change in stiffness and strength as a function of ambient temperature.

stiffness and strength with changing ambient temperature.* The following linear correlations are thus proposed:

$$\Delta\sigma_{UTS} \times 100\% = 12.65 - 0.18\,T\ , \tag{3.1}$$

and

$$\Delta E \times 100\% = 13.94 - 0.2\,T\ . \tag{3.2}$$

3.1.2 Compressive Elastic Constants and Strength Properties

The following average in-air room temperature values of compressive stiffness, E_C, ultimate compressive strength (UCS), and compressive failure strain, ε_{fC}, are based on 12 compressive tests, 7 in the 0° direction, and 5 in the 90° direction. Compressive specimens were cut from plaques P10 and P37.

Values	0° direction	90° direction
E_C, Msi	1.37	1.67
UCS, ksi	–24.09	–31.54
ε_{fC}, %	–2.41	–2.60

*The scatter in Fig. 3.2 is largely a result of the changes being related to average values rather than to virgin values for each individual specimen or plaque.

It can be seen that the stress-strain behavior is symmetric; that is, compressive and tensile properties are comparable, with compressive failure strain being slightly higher than the tensile value.

UCS is plotted vs compressive stiffness in Fig. 3.1. To facilitate comparison with tensile behavior, absolute values of UCS are used. The tensile and compressive sets of data can be approximated with straight lines of the same slope; that is, linear laws with the same coefficients can be used to describe dependence of strength on stiffness for both tension and compression.

3.1.3 Flexural Elastic Constants and Strength Properties

Five beams, two in the 0° and three in the 90° direction, were tested under three-point loading to determine the in-plane modulus of rupture (MOR), equal to elastically calculated maximum bending stress at failure. The average MOR values were 30.6 ksi and 33.5 ksi for the 0° and 90° orientations, respectively. The MOR value for the 0°-orientation specimens was 22% higher and the MOR value for the 90° orientation was 5.4% higher than the tensile strength for the corresponding orientation in the same plaque.

The 1-in.-wide by 1/8-in.-high beam specimens were tested to determine the following average out-of-plane flexural properties:

Values	0° direction	90° direction
E_F, Msi	1.60	1.79
MOR, ksi	40.56	53.99
ε_{fF}, %	2.98	3.07

The above stiffness values were calculated from $E = [(1 - \nu^2)/\varepsilon]\sigma$, which partially accounts for wide beam effects. In addition, 3/8-in.-wide by 1/8-in.-high beams were tested in three-point bending, yielding average MOR values of 45.14 ksi and 50.11 ksi for the 0° and 90° directions, respectively. It is seen that the 1-in.-wide and the 3/8-in.-wide beams produce comparable average MOR values. It is recognized that the out-of-plane MOR values are more than a factor of two greater than the UTS. That is, the load-carrying capacity is more than twice that which would be indicated by limiting the elastically calculated maximum stress to the UTS. It is thus appropriate to provide a higher allowable for primary out-of-plane bending than for primary membrane loading in the design guide. A factor of 1.5 is suggested. It must be noted that this observation only applies to out-of-plane bending. In the case of in-plane bending, the MOR values are much closer to the UTS values.

3.2 PROPORTIONAL LIMIT, STRENGTH VALUES, AND DAMAGE DEVELOPMENT IN TENSILE LOADING

Results of 253 tensile tests (171 on 0° specimens and 82 on 90° specimens) were assessed to establish a proportional limit for the reference material.[1] The proportional limit was defined as the point (σ_{PL}, ε_{PL}) in stress-strain space where the tensile stress-strain curve departs from linearity.* Proportional limit stress and strain values were established for each of the 253 specimens.

The following average values were calculated:

*The following procedure was adopted to calculate proportional limit stress and strain values:

(1) Establish the elastic stiffness value based on the stresses and strains in the elastic region (0.8 ksi < stress < 4 ksi).

(2) Calculate the running stiffness for each pair of stress-strain values forming the remaining stress-strain curve.

(3) Divide the running stiffness by the elastic stiffness. The stress-strain point where the stiffness ratio becomes, and remains, less than 1.0 is the proportional limit.

Values	0° direction	90° direction
UTS, ksi	21.27	28. 40
σ_{PL}, ksi	5.08	6.19
ε_f, %	2.12	2.15
ε_{PL}, %	0.38	0.37

The proportional limit stress is 24% and 22% of the UTS for the 0° and 90° directions, respectively. The proportional limit strain constitutes 18% and 17% of the failure strain for the 0° and 90° directions, respectively.

Damage development in tensile loading, as manifested by changes in stiffness with increasing stress and strain, was explored in tensile tests with intermittent stiffness checks. During this test a specimen was loaded to 20% UTS and then unloaded to zero stress, at which point a stiffness check was performed. This sequence, consisting of loading to a specific load/stress level, unloading to zero stress, and a stiffness check, was repeated for the load levels of 40, 60, and 80% UTS. Stiffness check, loading to 80% UTS, and unloading to zero stress were followed by loading to failure. Results are presented graphically in Fig. 3.3, where percent change in stiffness is plotted vs prior maximum load given in terms of percent UTS. No significant changes in stiffness occur below 30% UTS. Above this threshold, stiffness decreases with increasing prior load, and this decrease may be described with the following linear law:

$$\Delta E \times 100\% = 5.5 - 0.186 \frac{\sigma}{UTS} \times 100\% \ . \tag{3.3}$$

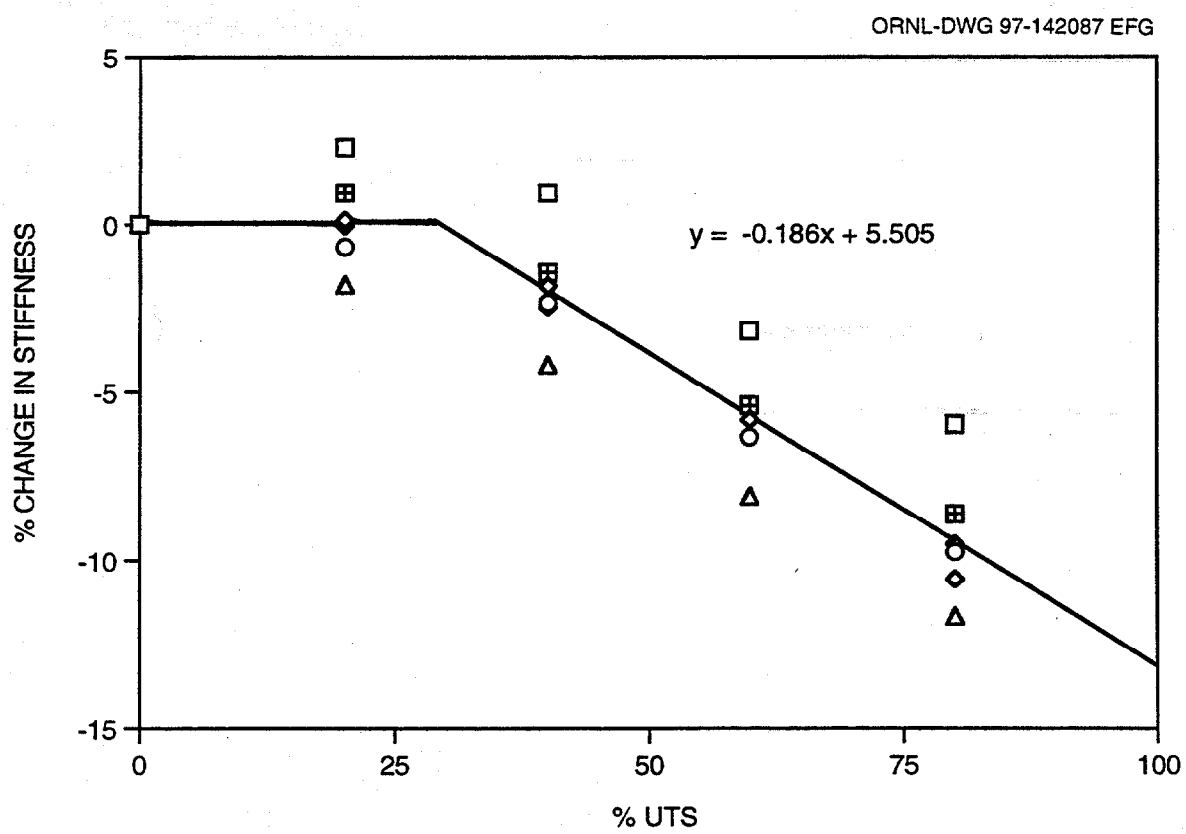

Fig. 3.3. Percent change in stiffness vs maximum prior tensile load given in terms of percent UTS.

3.3 EFFECT OF STRAIN RATE

The effect of strain rate on tensile behavior was assessed through constant strain rate tests performed at strain rates of 10^{-6}, 10^{-4}, 10^{-2}, and 10 s^{-1}. Stress-strain curves produced at different strain rates are presented in Fig. 3.4. Results in Fig. 3.4 indicate that while there is a slight strain-rate sensitivity, it decreases with increasing strain rate.

The effect of rate on compressive behavior was investigated in tests conducted at the following constant load rates (with equivalent strain rates given in parentheses): 7.5 lb/min (10^{-6} s^{-1}), 2330 lb/min (3×10^{-4} s^{-1}), and 13,980 lb/min (2×10^{-3} s^{-1}). Stress-strain curves presented in Fig. 3.5 indicate that, as in the case of tension, a slight rate sensitivity is observed in compression at the slower rates.

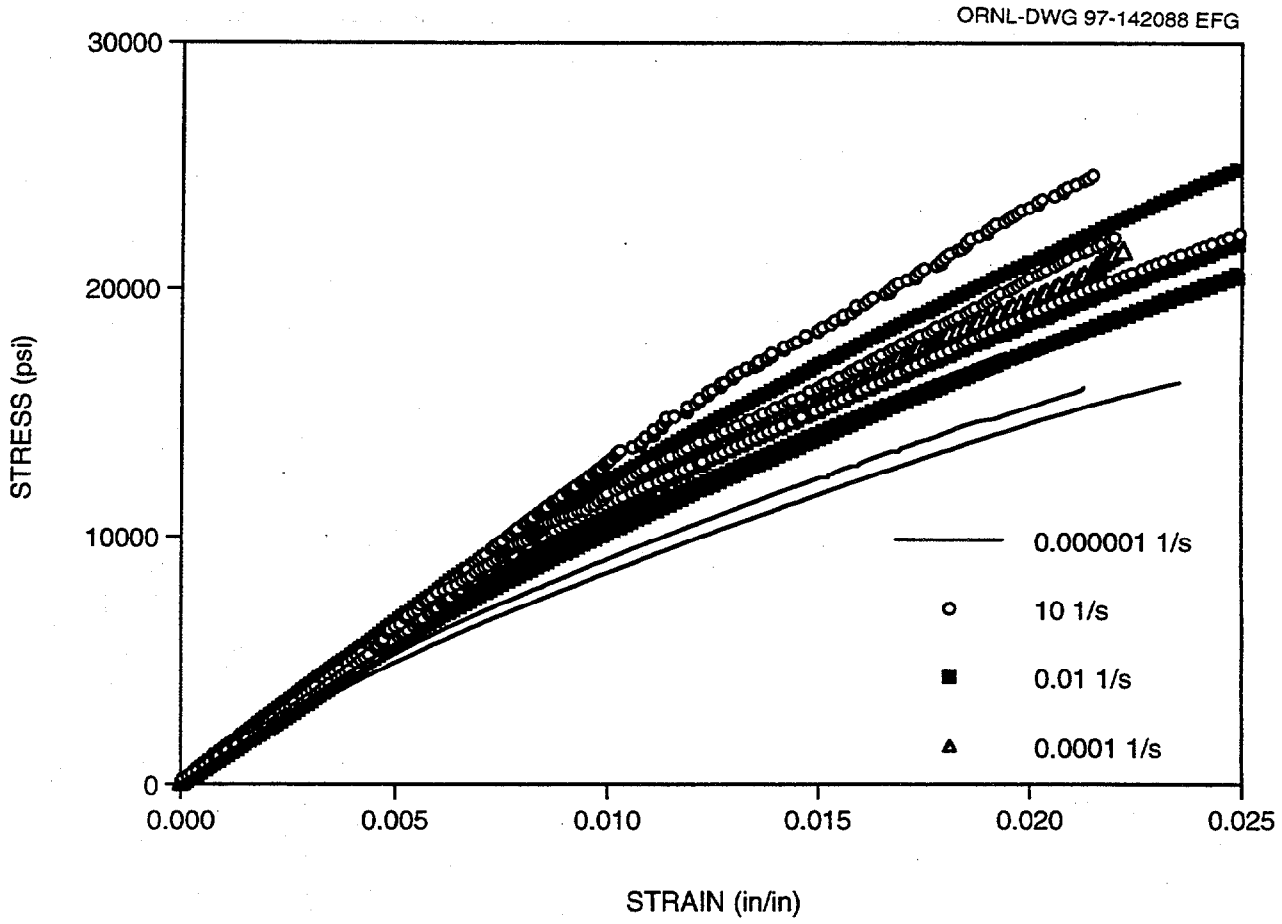

Fig. 3.4. Effect of strain rate on tensile stress-strain behavior.

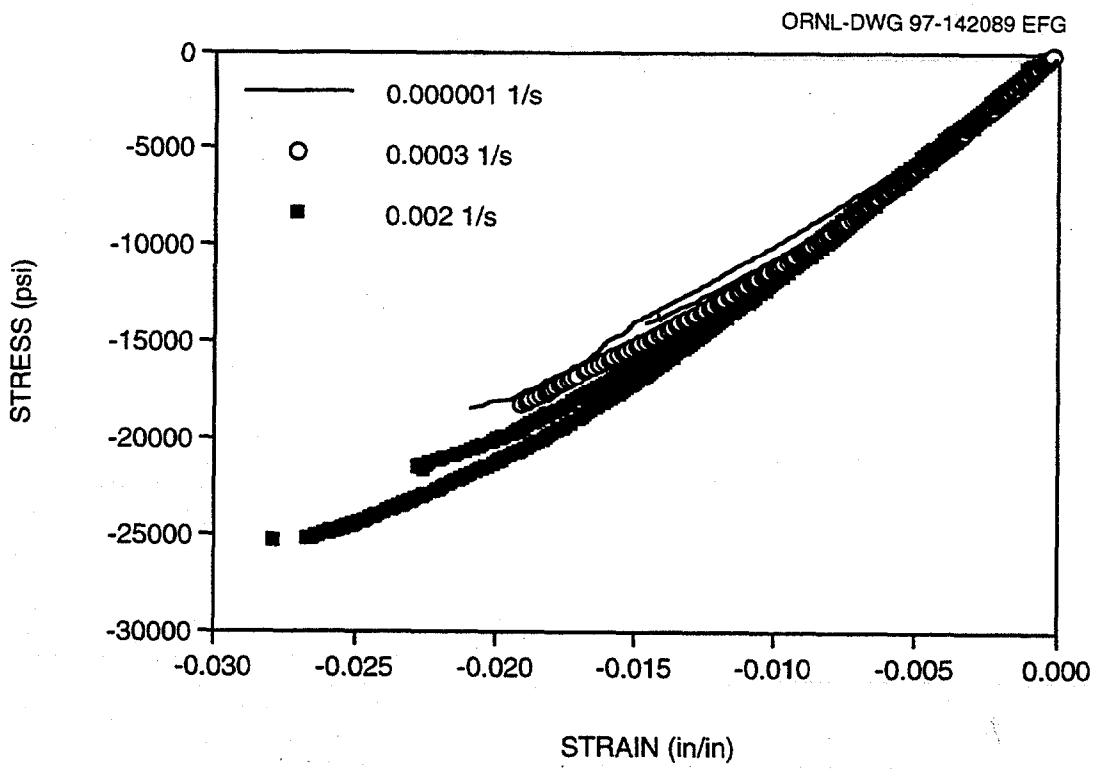

Fig. 3.5. Effect of strain rate on compressive stress-strain behavior.

REFERENCE

1. M. B. Ruggles, *Tensile and Compressive Behavior of a Swirl Mat Composite*, ORNL/TM-13519, Lockheed Martin Energy Research Corp., Oak Ridge National Laboratory (to be published).

4. IN-PLANE AND INTERLAMINAR SHEAR PROPERTIES

G. T. Yahr

4.1 IN-PLANE SHEAR MODULUS AND STRENGTH

The in-air room-temperature values of the elastic shear modulus, ultimate shear strength, and failure shear strain were determined using Iosipescu specimens oriented in the 0° and 90° directions. There were five specimens oriented in the 0° direction and six specimens oriented in the 90° direction. As would be expected, the data from the two directions were in good agreement. All of the specimens came from plaque 37. The average in-plane shear modulus, G_{12}, shear strength, τ_{12}^f, and shear strain at failure, γ_{12}^f were $G_{12} = 0.65$ Msi, $\tau_{12}^f = 16.0$ ksi, and $\gamma_{12}^f = 3.2\%$.

The in-plane shear modulus was also measured on 1-in.-deep beams from plaque 37 tested under three-point loading. Five beams from plaque 37, two in the 0° direction and three in the 90° direction, were tested with a strain-gage rosette across the centerline of the beam. The average in-plane shear modulus from the beams was 0.65 Msi, which is in agreement with the shear modulus determined from shear specimens.

It should be noted that the average tensile moduli of plaque 37 were 11.7 and 7.7% (average = 9.7%) more than the averages for the 0° and 90° directions, respectively, for all the plaques. A corresponding adjustment in the measured in-plane shear modulus provides a value for G_{12} of 0.59 Msi. An adjustment of 12% in the shear strength based on the tensile data gives a value of 14 ksi.

4.2 INTERLAMINAR SHEAR

A series of beams was subjected to out-of-plane loading in an attempt to measure the *interlaminar* shear strength, (τ_{13}, τ_{31}, τ_{23}, τ_{32}, in Fig. 2.2).* This approach for measuring interlaminar shear strength is standardized in Ref. 2. The MOR in a rectangular beam is given by

$$\mathrm{MOR} = \frac{3P\ell}{bh^2} ,$$

where P is the load, ℓ is the distance from the support to the load, b is the width of the beam, and h is the height (thickness) of the beam.

The maximum shear stress, τ, away from the load is given by

$$\tau = \frac{3}{4}\frac{P}{bh} .$$

The ratio of the MOR to the maximum shear strength is given by

$$\frac{\mathrm{MOR}}{\tau} = \frac{4\ell}{h} .$$

By testing a series of beams with shorter and shorter distances between the loads and supports, one can tell when the beam is short enough to fail in shear instead of in tension. The beams were 3/8-in. high and 1/8-in. thick. Beams with a dimension ℓ of 0.08 in., 0.32 in., and 0.59 in. were tested. The first set was tested in four-point bending, and the last two were tested in three-point bending. The results of the tests are shown in Fig. 4.1.

*The term interlaminar is used even though the reference composite does not generally behave as a laminate.

ORNL-DWG 97-142090 EFG

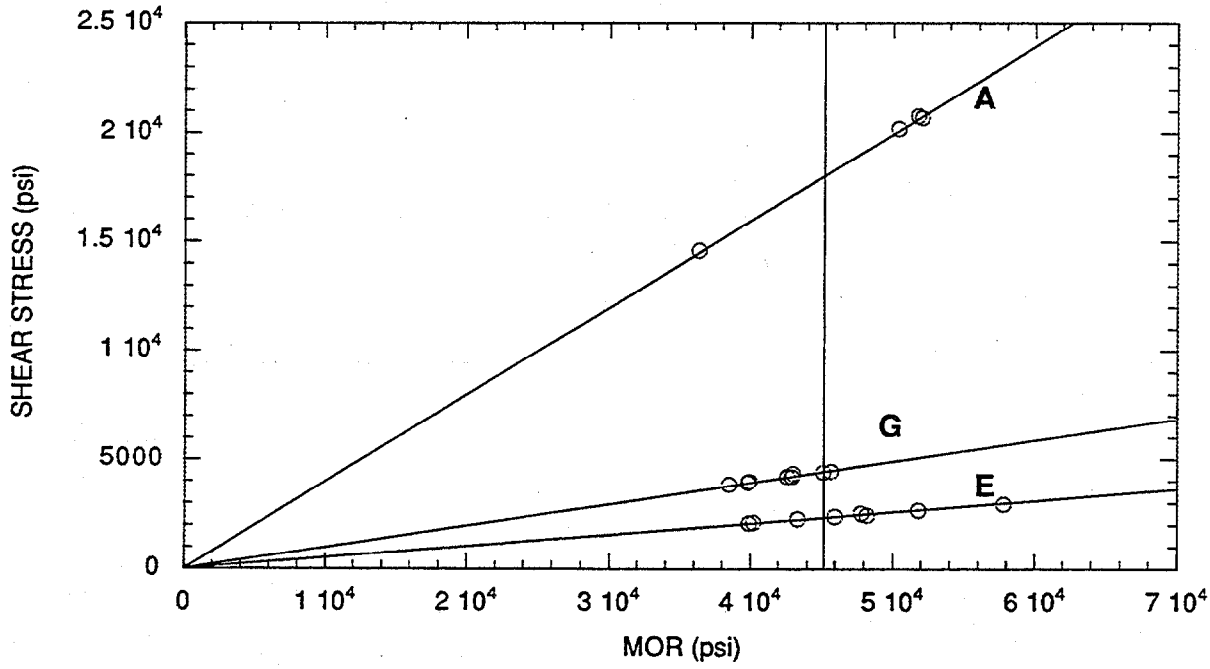

a. 0°-direction

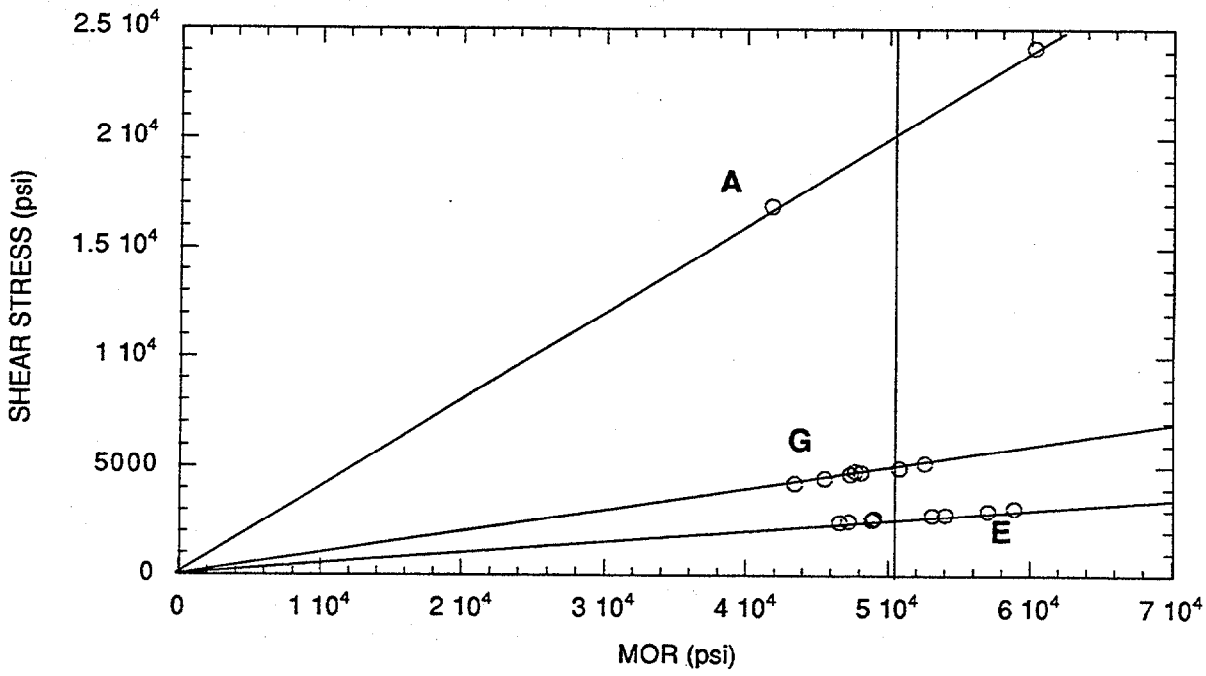

b. 90°-direction

Fig. 4.1. None of the three-point bend tests loaded normal to the plaque failed in interlaminar shear as evidenced by them all failing at the same MOR value.

The beams all failed in tension as evidenced by the fact that the MOR was very nearly the same value for each set of beams. The beams with a distance ℓ between load and support of 0.08 in. were the shortest that could be tested. There, the results exhibited significant scatter because the support and load rollers were so close together. As far as interlaminar shear strength is concerned, we can only conclude that the shear strength is greater than 14.60 ksi for the 0° direction and 16.90 ksi for the 90° direction. Thus, the interlaminar shear strength is at least one-third of the MOR, and interlaminar shear should not be a problem in application of this material.

4.3 ENVIRONMENTAL DEGRADATION

Iosipescu specimens from plaque 37 were soaked in distilled water at room temperature for 2200 h, battery acid at room temperature for 2200 h, or demineralized water at 180°F for 1080 h and then tested. The effect of the environment is shown in Fig. 4.2. The percentage reduction in shear modulus, shear strength, and shear strain at failure for the different environments were as follows:

	Distilled water	Battery acid	Water at 180°
G_{12}	–8	–3	–13
τ_{12}^{f}	–14	0	–35
γ_{12}^{f}	–16	+8	–27

Visual examination of the specimens indicated that the battery acid had attacked the matrix, leaving fibers exposed on the surface. However, the shear strain at failure was actually increased 8% by the soak in battery acid. The soak in demineralized water at 180°F was the most deleterious; it decreased the shear strength by 35%. Note that the reduction in tensile and compressive strength was approximately 50%.

Typical Iosipescu specimens from each of the environments are shown in Fig. 4.3. The cracks started at or near the bottom of the V-notches but ran into the tabs.

4.4 OBSERVATIONS AND RECOMMENDATIONS

The Young's modulus, E, shear modulus, G, and Poisson's ratio, ν, in an isotropic material are related by the expression

$$E = 2G\,(1 + \nu)\ .$$

Plaque 37 had average Young's modulus values of 1.53 and 1.81 Msi in the 0° and 90° directions, respectively. Using the expression above with G = 0.65 and ν = 0.3, a Young's modulus of 1.69 can be calculated, which falls between the measured averages for the two directions. It is recommended that the designer assume that this material is isotropic in the plane of the plates and use the 0° direction Young's modulus.

It is reasonable to expect that the properties transverse to the plane of the plate are considerably different. An attempt was made to measure the interlaminar shear strength. Although the interlaminar shear strength could not be measured, the tests did show that it is at least one-third the in-plane tensile strength.

The measured in-plane shear strength provides evidence that the maximum shear stress failure criterion is reasonable for limiting in-plane biaxial stresses, as discussed in Chap. 6 on the multiaxial failure criterion.

Finally, because (1) the environmental degradation of shear properties was less than for tensile properties and (2) there was a larger data base for examining the environmental degradation of tensile properties, the environmental degradation factors for tension should be applied to shear as well.

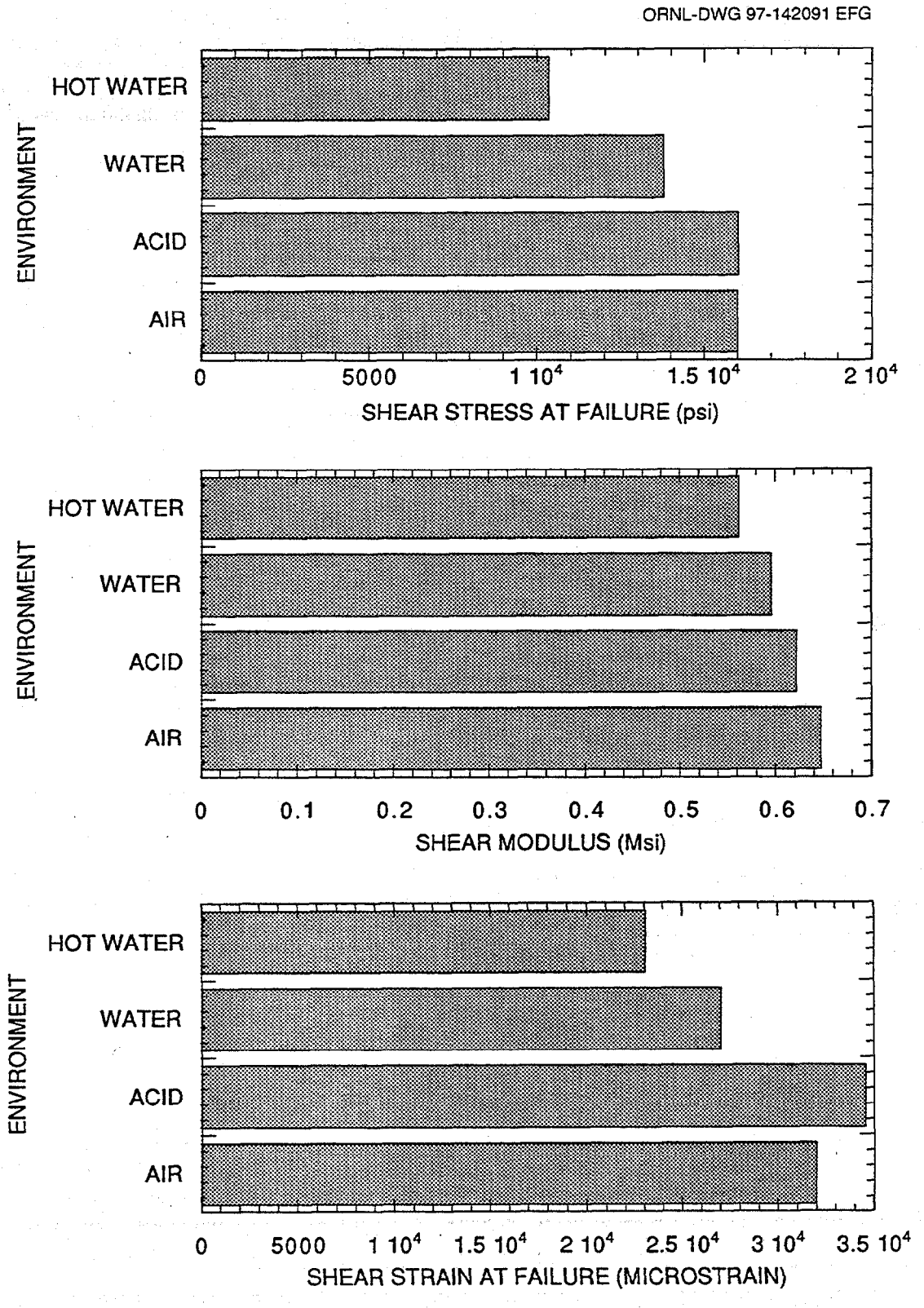

Fig. 4.2. Effect of battery acid, distilled water, and 180°F demineralized water on the in-plane shear behavior.

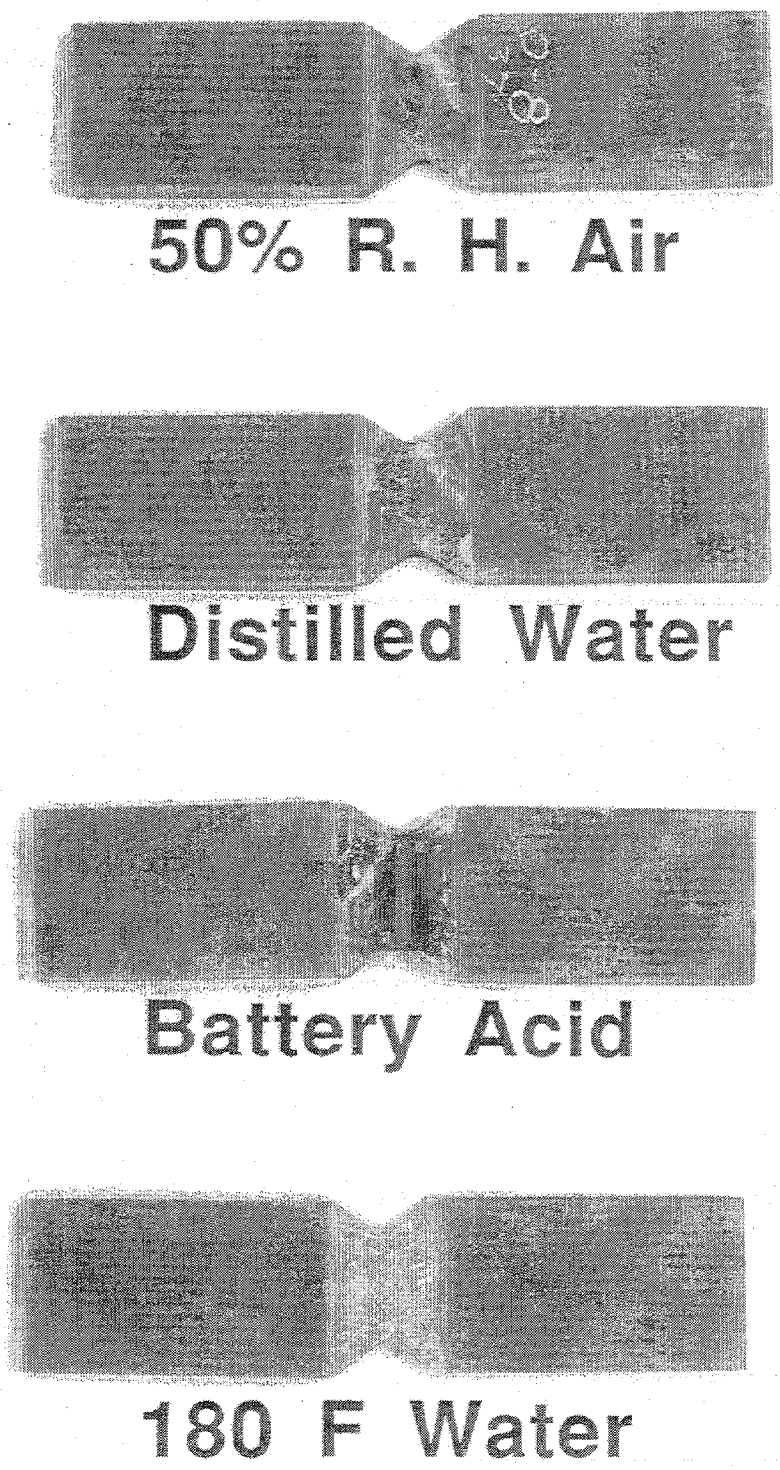

Fig. 4.3. Typical Iosipescu specimens that were tested after being exposed to four different environments.

REFERENCES

1. ASTM Standard D 5379/D 5379M-93, *Standard Test Method for Shear Properties of Composite Materials by the V-Notched Beam Method*, American Society for Testing and Materials.

2. ASTM Standard D 2344-84, *Standard Test Method for Apparent Interlaminar Shear Strength of Parallel Fiber Composites by Short-Beam Method*, American Society for Testing and Materials.

5. ENVIRONMENTAL DEGRADATION OF STRENGTH AND STIFFNESS

M. B. Ruggles

5.1 CORRELATIONS OF EFFECTS OF MOISTURE EXPOSURE ON STRENGTH AND STIFFNESS

The study of environmental effects on strength and stiffness demonstrated that exposure time and weight gain provide measures of degradation for a given set of conditions.

Moisture effects on tensile strength and stiffness vs time are shown in Figs. 5.1 and 5.2, respectively. A single data point, representing an average of all specimens subjected to this particular set of conditions, is

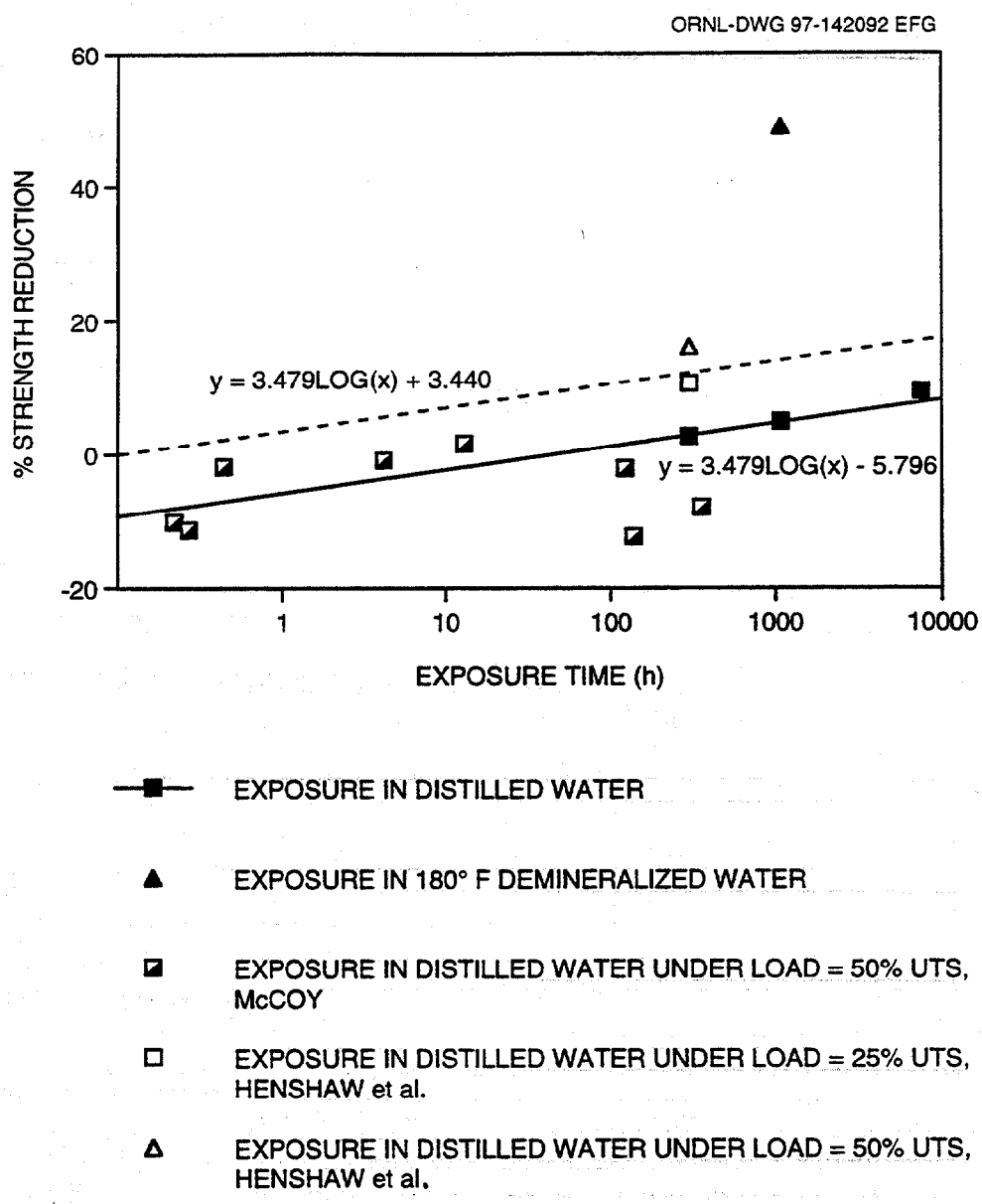

Fig. 5.1. Effect of moisture exposure time on strength.

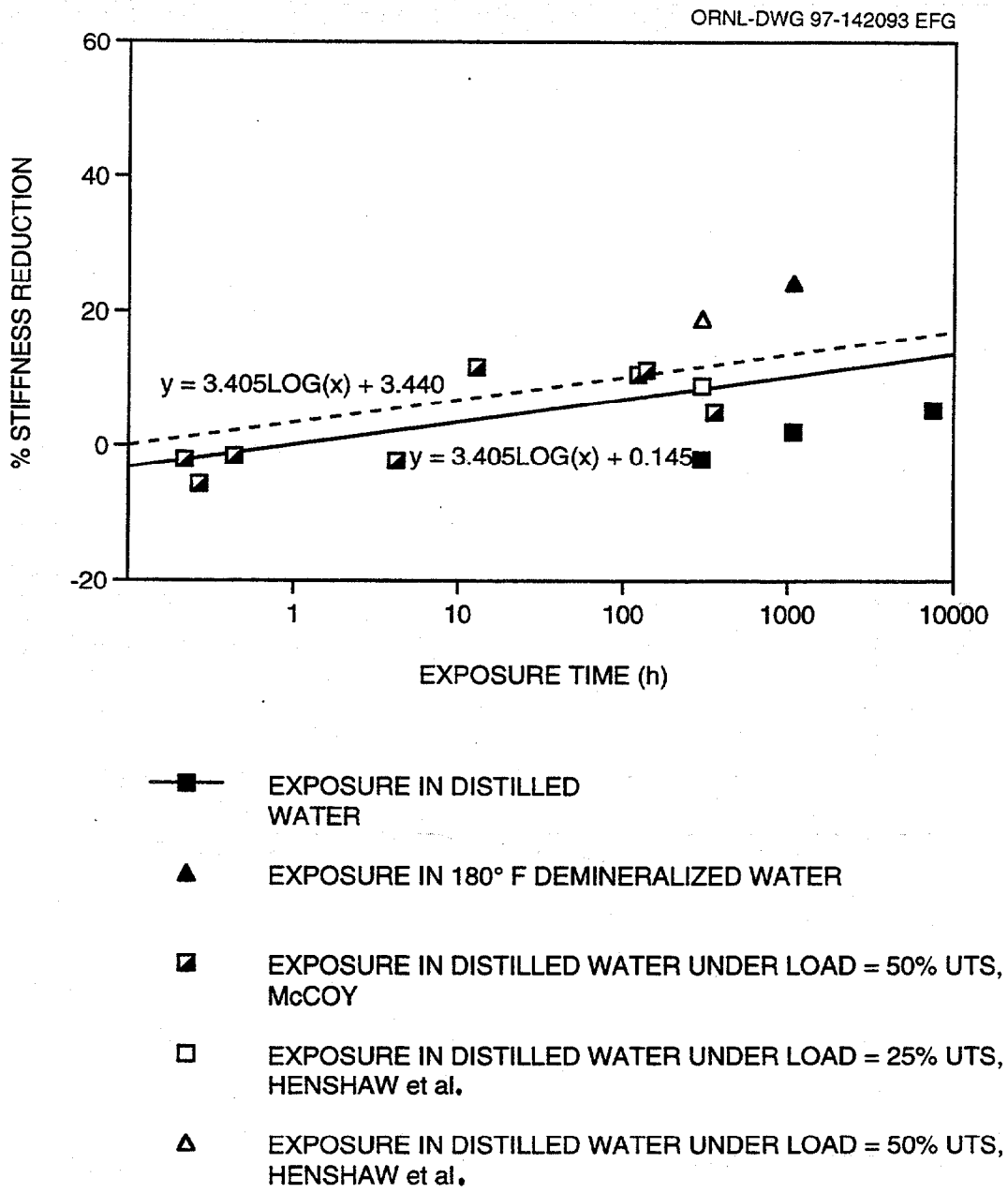

Fig. 5.2. Effect of moisture exposure time on stiffness.

given for each value of time. Included in Figs. 5.1 and 5.2 are results due to (1) exposure in room-temperature distilled water with and without simultaneous loading (superimposed loads were 25 and 50% UTS) and (2) exposure in 180°F demineralized water. Exposure in 180°F demineralized water was introduced into the study of moisture effects for the purpose of accelerating the sorption process. Exposure under load is expected to serve a similar purpose (i.e. to accelerate the sorption process). Plots of weight gain vs exposure time given in Fig. 5.3 confirm these expectations. For a given exposure time, weight gain due to moisture absorption is significantly increased by superimposed load as well as by elevated temperature. However, it should be noted that the number of data points representing exposure under load as well as exposure at elevated temperature is very limited. Thus, the dashed lines in Fig. 5.3 are, in fact, hypothetical approximations that may be modified once more experimental data points become available.

ORNL-DWG 97-142094 EFG

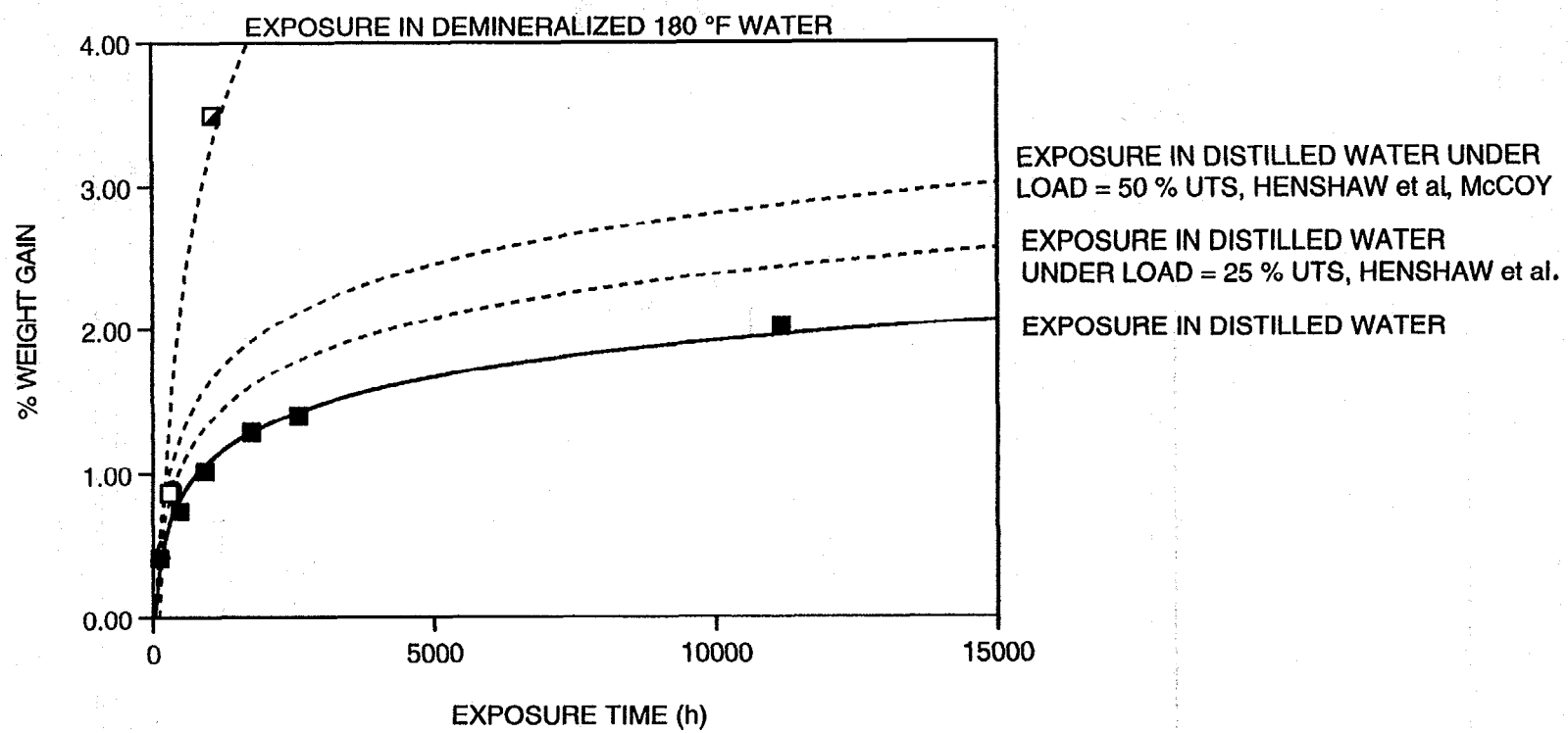

Fig. 5.3. Weight gain due to moisture absorption.

Figures 5.1 and 5.2 show that strength and stiffness decrease with increasing exposure time. Exposure time correlates strength and stiffness reductions fairly well. Because the reductions were referenced to average values from several plaques, the solid curve fits in Figs. 5.1 and 5.2 do not pass through zero, as they should. Therefore, they were adjusted (see dashed lines) to represent zero reduction in strength and/or stiffness at zero exposure time. Using the adjusted curves in Figs. 5.1 and 5.2, the following equations can be proposed to represent strength and stiffness reduction due to room-temperature exposure without load:

$$\Delta\sigma_{UTS} \times 100\% = 3.48 \log_{10} t_E + 3.44 \ , \tag{5.1.a}$$

and

$$\Delta E \times 100\% = 3.41 \log_{10} t_E + 3.44 \ . \tag{5.1.b}$$

In view of the close similarity of Eqs. (5.1.a) and (5.1.b), a single equation can be proposed to represent reduction in strength and/or stiffness, ΔR, with exposure time, t_E:

$$\Delta R \times 100\% = 3.44 \log_{10} t_E + 3.44 \ . \tag{5.2}$$

Equation (5.2) yields a 17% reduction in strength and/or stiffness after exposure for 1 year. This is a conservative estimate of reduction for any of the automotive fluids considered, except battery acid, which produced slightly higher reductions in strength and/or stiffness.

Strength and stiffness reductions are plotted vs weight gain in Figs. 5.4 and 5.5 to demonstrate that weight gain is also a measure of degradation. As in Figs. 5.1 and 5.2, a single data point represents an average of all specimens subjected to a particular set of conditions. A number of conditions not included in Figs. 5.1 and 5.2 appear in Figs. 5.4 and 5.5. For example, shown in Figs. 5.4 and 5.5 are results obtained for specimens where an 11,160-h exposure was followed by a 1,540-h drying period. Clearly, exposure time alone could not be used to correlate this set of data. Experimental observations revealed that (1) during the drying period, specimens rapidly lost most of the weight gained; and (2) the strength and stiffness loss due to exposure was largely recovered. These observations are well represented when strength and stiffness loss are correlated with weight gain. Results in Figs. 5.4 and 5.5 show that strength and stiffness decrease with increasing weight. In addition, greater reductions in strength and stiffness are observed under load and at an elevated temperature, conditions that cause higher weight gain in a given exposure time. Weight gain can be employed to correlate degradation in strength and stiffness due to room-temperature exposure without simultaneous loading via simple power laws:

$$\Delta\sigma_{UTS} \times 100\% = 2.87(\Delta W \times 100\%)^{2.132} \ , \tag{5.3}$$

and

$$\Delta E \times 100\% = 1.69(\Delta W \times 100\%)^{2.676} \ . \tag{5.4}$$

Observations regarding moisture effects on tensile strength and stiffness can be extended to compressive properties. Exposure to room-temperature distilled water and 180°F demineralized water resulted in degradation of compressive strength and stiffness. Reduction of compressive properties is compared to that of tensile properties in Fig. 5.6. Presoaking in 180°F demineralized water has a significantly greater effect on both tensile and compressive properties than presoak in room-temperature distilled water. The effect of the 180°F demineralized water presoak on compressive properties is

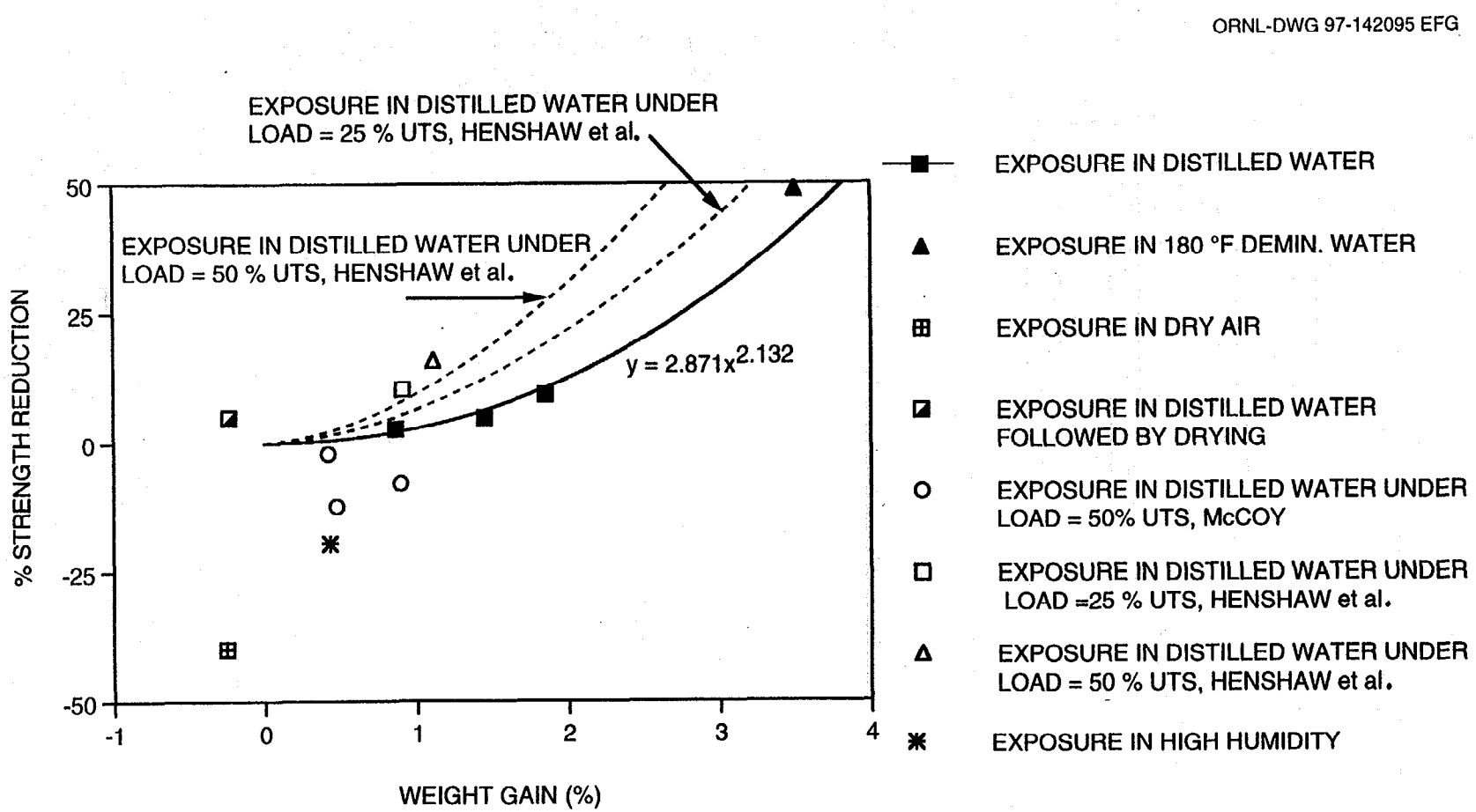

Fig. 5.4. Reduction in strength due to moisture weight gain.

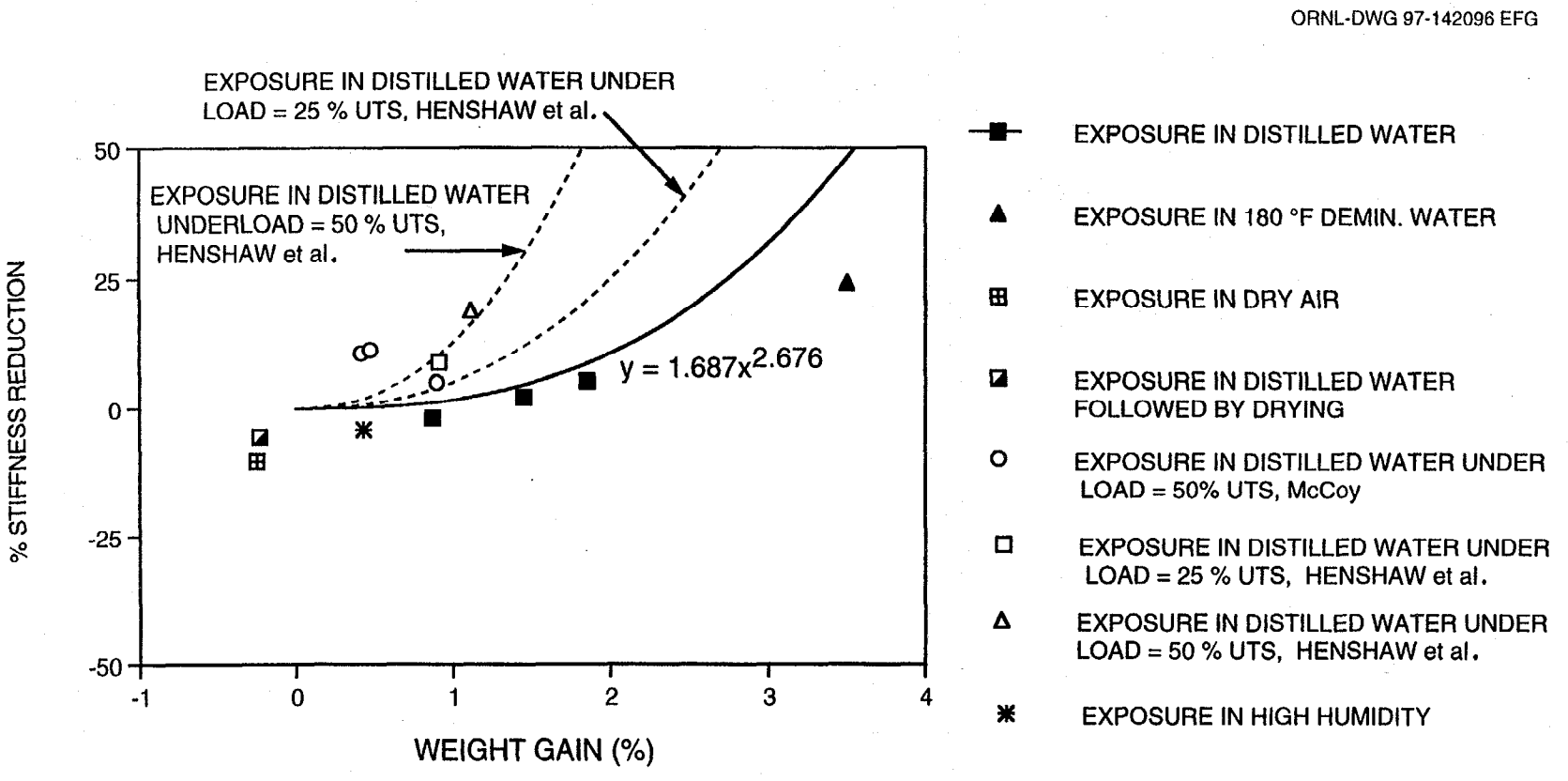

Fig. 5.5. Reduction in stiffness due to moisture weight gain.

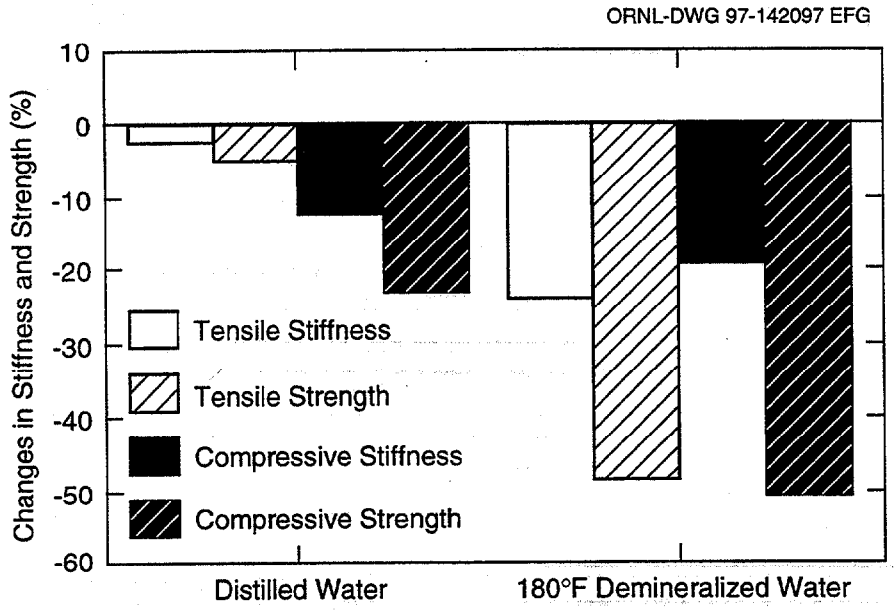

Fig. 5.6. Effects of 1080 h presoak in 180°F demineralized water and room-temperature distilled water on tensile and compressive properties.

comparable to that on tensile properties. Although the effect of distilled water presoak on compressive properties appears to be considerably greater than that on tensile properties, this discrepancy is viewed as an artifact of data scatter. Thus, it is proposed that conclusions reached with respect to moisture effects on tensile strength and stiffness be applied to compressive behavior as well.

5.2 FACTORS FOR OTHER FLUIDS

In addition to distilled and demineralized water, the following seven automotive fluid environments were investigated in this study: saltwater, antifreeze, windshield washer fluid, used motor oil, battery acid, gasoline, and brake fluid. Details of the fluid composition as well as sources of fluids are given in Ref. 1. The average changes in strength and stiffness due to exposure for 1080 h and 7540 h are presented in Fig. 5.7. Strength results in Fig. 5.7 demonstrate that battery acid has the largest degrading effect followed by windshield washer fluid and distilled water, and then saltwater. Motor oil and brake fluid appear to increase the strength. Stiffness results in Fig. 5.7 indicate that battery acid and windshield washer fluid have the largest degrading effect (about a 20% reduction) for 7540-h exposure. The other changes in stiffness are all less than 10%. As in the case of moisture, the longer exposure times cause greater degradation.

Observations made for tensile properties can be extended to compression. Compression tests on specimens presoaked in battery acid for 1080 h produced a 17% reduction in stiffness and a 14% reduction in strength. These values are somewhat higher than the corresponding ones in tension. This may need to be accounted for by introducing a somewhat higher reduction factor for compression in the design guideline.

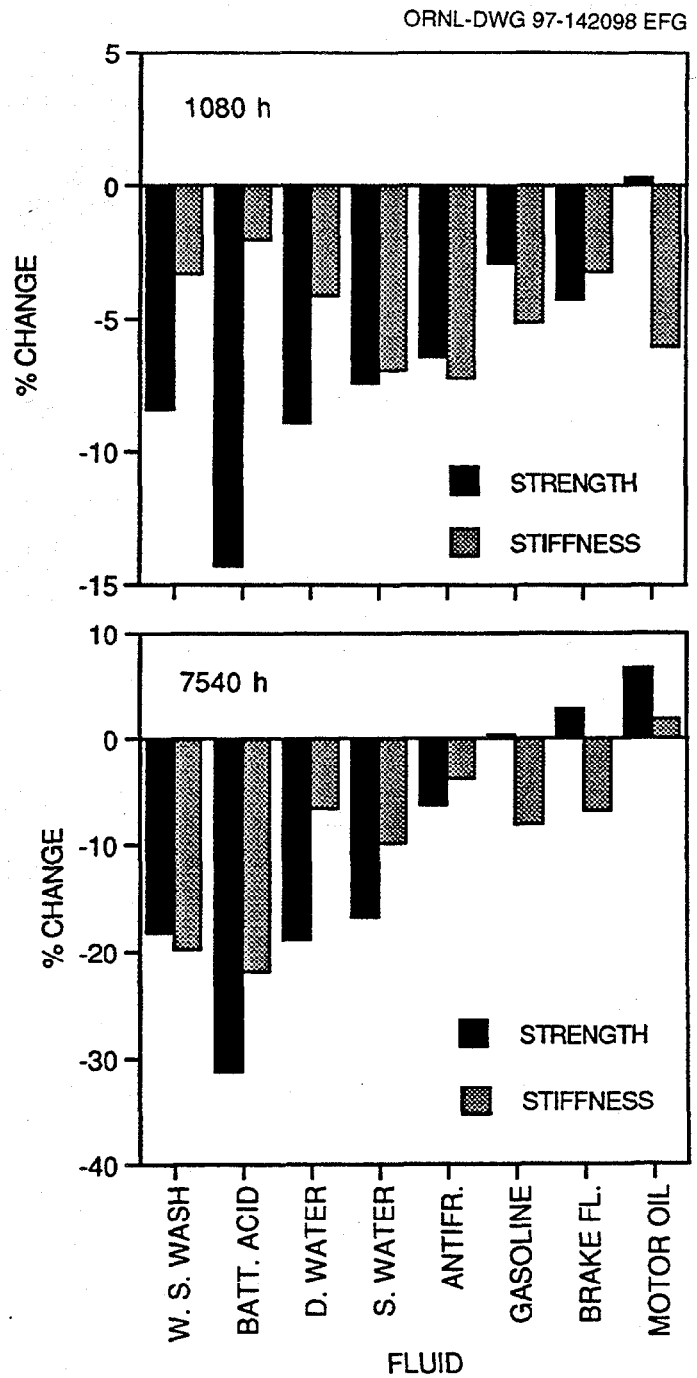

Fig. 5.7. Effects of prior exposure to various automotive fluids on tensile strength and stiffness.

REFERENCE

1. J. M. Corum, *Durability of Lightweight Composite Structures for Automotive Applications: Progress Report for Period Ending September 30, 1995*, ORNL/TM-13176, Lockheed Martin Energy Research Corp, Oak Ridge National Laboratory, March 1996.

6. MULTIAXIAL STRENGTH CRITERION

G. T. Yahr

Because the designer is usually only provided with uniaxial strength values, while the stresses in components are often multiaxial, he or she must have a multiaxial strength criterion. Because the material is generally in a plate or shell form that is loaded so that the stresses are in the plane of the plate, only a biaxial strength criterion is required.

Many different strength criteria have been proposed. Some of them account for different strengths in tension and compression and for different strengths in different directions. However, such criteria become quite complex for the designer to use and require extensive materials testing to determine all the required constants. To keep the criterion simple and easy for the designer to use, the strength is assumed to be the same in tension and compression and in all directions in the plane of the plaque. Thus, the only strength value used is the tensile strength in the 0° direction.

Five candidate strength criteria are shown in Fig. 6.1. The maximum normal stress criterion is the square; failure is predicted when the algebraically largest principal stress reaches the value of the 0° direction tensile strength. The maximum normal strain theory is the rhombus; failure occurs when the algebraically largest principal strain reaches the value of the elastically calculated strain corresponding to the 0° direction tensile strength. The maximum shear stress theory is the diamond; failure occurs when the difference between the maximum and minimum principal stress reaches the value of the 0° direction tensile strength. The ellipse is the maximum work theory; failure occurs when the principal stresses satisfy the relation

$$\sqrt{\sigma_1^2 - \nu\sigma_1\sigma_2 + \sigma_2^2} \geq S_t \ ,$$

where σ_1 and σ_2 are the principal stresses, ν is Poisson's ratio, and S_t is the value of the 0° direction tensile strength. The circle is a modification of the maximum work theory that was suggested by Owen and Found[1] to fit data from tension-tension tests; failure occurs when

$$\sqrt{\sigma_1^2 + \sigma_2^2} \geq S_t \ .$$

Note that all five criteria predict the same uniaxial strengths. They differ most when there is equal tension or compression and when the maximum principal stress is tension and the minimum tensile stress is the same absolute value but in compression. This is the condition in pure shear. Therefore, the shear strength determined using Iosipescu specimens can be used to evaluate the failure criterion in the second and fourth quadrants of Fig. 6.1.

Data are also needed to evaluate the criterion in the first and third quadrant of Fig. 6.1. Tubular specimens are often tested under combinations of internal or external pressure and axial tension or compression to define the failure criterion. Our material could not be made as tubular specimens. Cruciform specimens are used for testing sheet material. However, such tests are extremely expensive and difficult.

The maximum stress in a circular plate that is simply supported at the edge and subjected to a concentric ring load is, on the surface opposite the load, in equibiaxial tension everywhere inside the load ring according to classic elastic plate theory. Therefore, this test was chosen for evaluating the failure criterion in the first quadrant.

Tests were run on 3.7-in.-diam circular disks supported on a plate with a 3.5-in.-diam hole and loaded with a plunger that made contact at a radius of 0.75 in. According to classic elastic plate analysis, a uniform equibiaxial tension stress exists everywhere inside the load ring on the surface away from the plunger. Large deflection elastic finite-element analysis showed that the classic plate analysis only applied for deflections that were less than half the thickness of the disk. A value of 1.37 Msi was used for the modulus

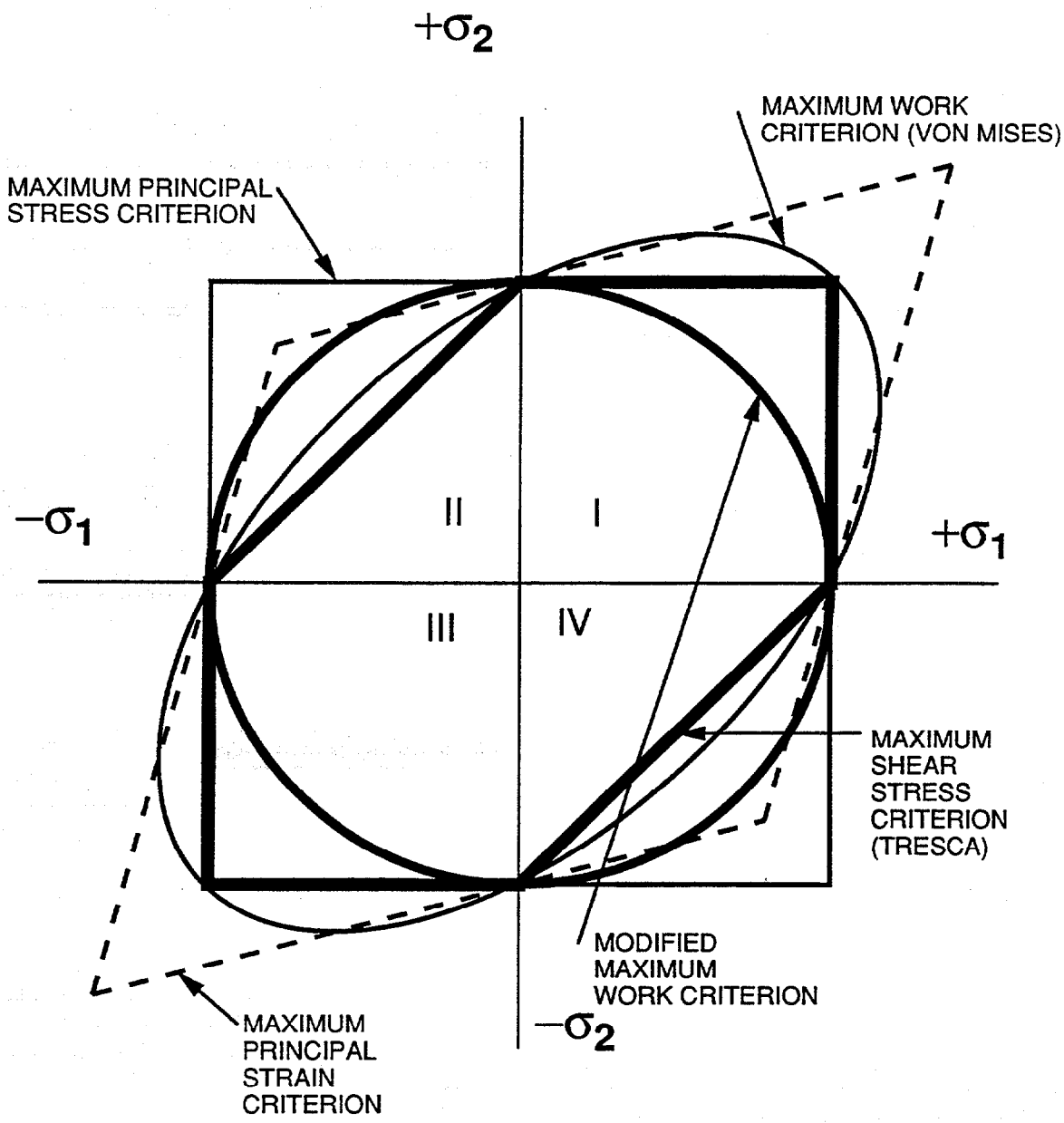

Fig. 6.1. Candidate failure criteria.

of elasticity. The elastic finite-element results are shown in Fig. 6.2. The stresses are divided by the load because this quantity can then be used directly to calculate the stress from the load applied in the test. Fourteen disks were tested. The results are given in Table 6.1.

The average deflection at failure was 2.26 times the disk thickness. Therefore, the radial stress on the bottom of the disk directly under the load was ~70% higher than the stress at the center of the disk on the face away from the load. Note that the specimens all failed where the load was applied, as predicted by the analysis.

A three-gage strain-gage rosette was used to measure the strain at the center of 12 of the specimens on the face away from the load. The three gages were in good agreement. The initial slope of the load vs strain curves was converted to modulus of elasticity by using the finite-element analysis to convert load to stress

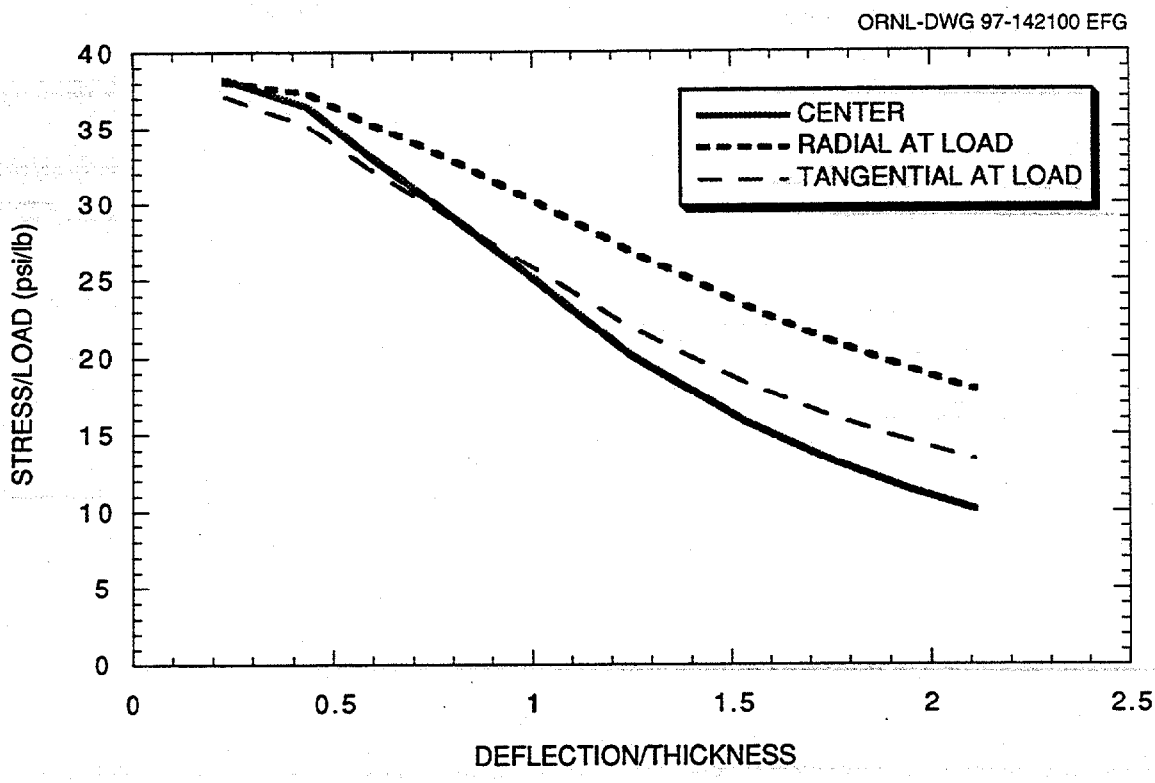

Fig. 6.2. Finite-element results on bottom of plate.

Table 6.1. Data from tests on circular disks subjected to ring load

	Ram deflection at failure (in.)	Peak load (lb)	Modulus of elasticity (Msi)	$S_r = S_t$ at center (psi)	S_r at load (psi)	S_t at load (psi)
Average	0.282	2665	1.62	29,040	49,960	37,553
Standard deviation	0.011	225	0.07	782	2503	1653
COV, %	4	8	4	3	5	4

and multiplying the slope of the stress vs strain curve by one minus the Poisson's ratio because of the equibiaxial stress state. The average elastic modulus of 1.62 Msi is the same as the modulus value measured on beams in the 90° direction from the same plaque.

The peak load values were used to estimate the stresses at failure at the center of the disk and under the load on the face away from the load.

Figure 6.3 shows two of the circular disk specimens after they were tested. The cracking on the simply supported side can be seen in the specimen on the left. The load plunger side of one of the specimens is shown on the right.

Tensile strength and MOR values were measured on the same plaque. The MOR in the 0° direction was 47.25 ksi, which was twice the tensile strength. Because the disks are loaded in bending, comparisons were made with MOR values when evaluating failure criteria. The average maximum stress in the disk is

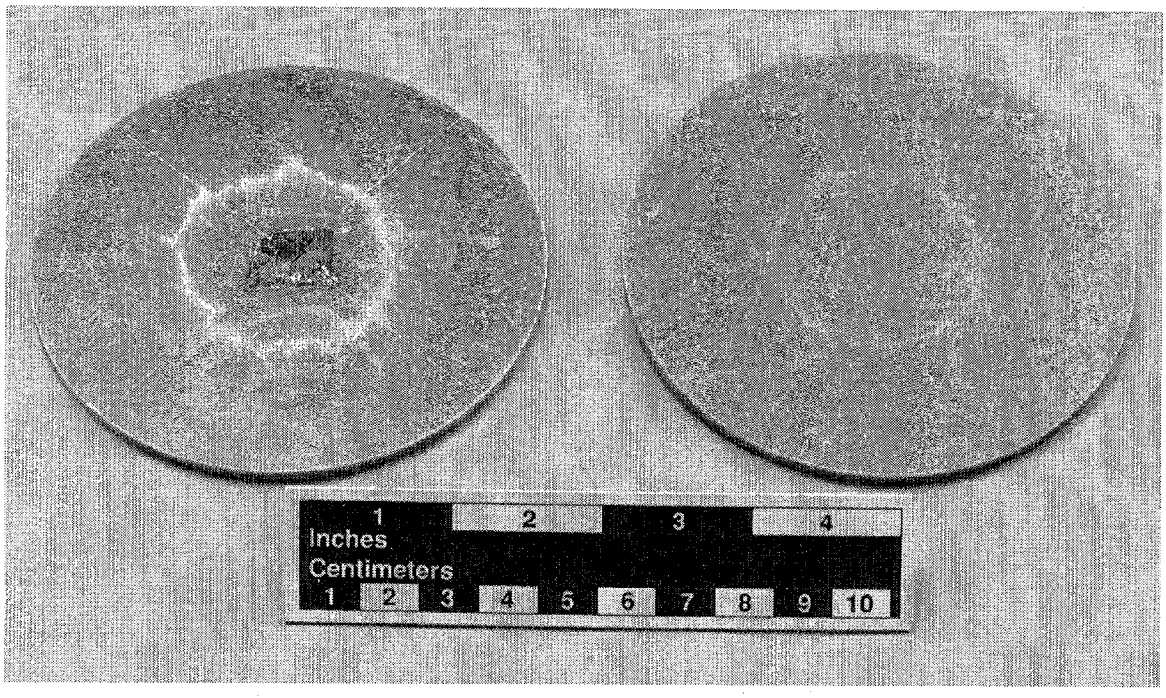

Fig. 6.3. Circular disk specimens after being tested.

compared to the failure criteria in Fig. 6.4. The average failure point was plotted at two points that are symmetrical about a 45° line. The average maximum stress in the disk agrees well with the maximum shear and maximum stress theories of failure. The maximum work theory agrees almost as well, but is unconservative. The modified maximum work theory is extremely conservative, and the maximum strain theory is extremely unconservative. Therefore, either the maximum stress or maximum shear theory would be a good failure criterion for quadrant one, where they are identical. Those two criteria are very different in the second and fourth quadrants (see Fig. 6.1).

The principal stresses in the case of pure shear are tension in one direction and equal compression perpendicular to the tensile stress. Therefore, shear strength provides the data needed for evaluating the criteria in the second and fourth quadrants. The average tensile strength in the 0° direction of the strongest of the 30 plaques tested was 57% higher than for the weakest plaque. The strongest plaque in the 90° direction was 76% stronger than the weakest plaque. To evaluate the different failure criteria with the multiaxial test results, one must account for the variation in strength of the different plaques since all the shear specimens were from plaque P37 and the circular disks were from plaque P43. The 0° direction tensile strength of plaque P37 was 18% higher than the average of all the plaques, and the 0° direction tensile strength of plaque P43 was 12% higher than the average for all the plaques. The average shear strength corrected to account for the higher tensile strength of plaque P37 was 14 ksi. The principal stresses were, therefore, +14 ksi and −14 ksi. The data point from the shear test is plotted in both the second and fourth quadrants in Fig. 6.5. The data point from the disk test was reduced by the ratio of the average tensile strength in the 0° direction to the average MOR of the 0° direction beams from plaque 43 and is plotted in Fig. 6.5.

The average 90° direction tensile strength and compressive strengths are also plotted. Clearly, the maximum stress theory is unconservative in the second and fourth quadrant. Only the maximum shear and modified work criteria are both conservative relative to all the average data points. The maximum shear criterion is more conservative than the modified work criterion in the second and fourth quadrant. However, the modified work criterion is extremely conservative in the first quadrant. Unfortunately, data in the third quadrant are not available for evaluating the failure criteria. The maximum shear criterion is recommended because it is widely used by designers and is very simple.

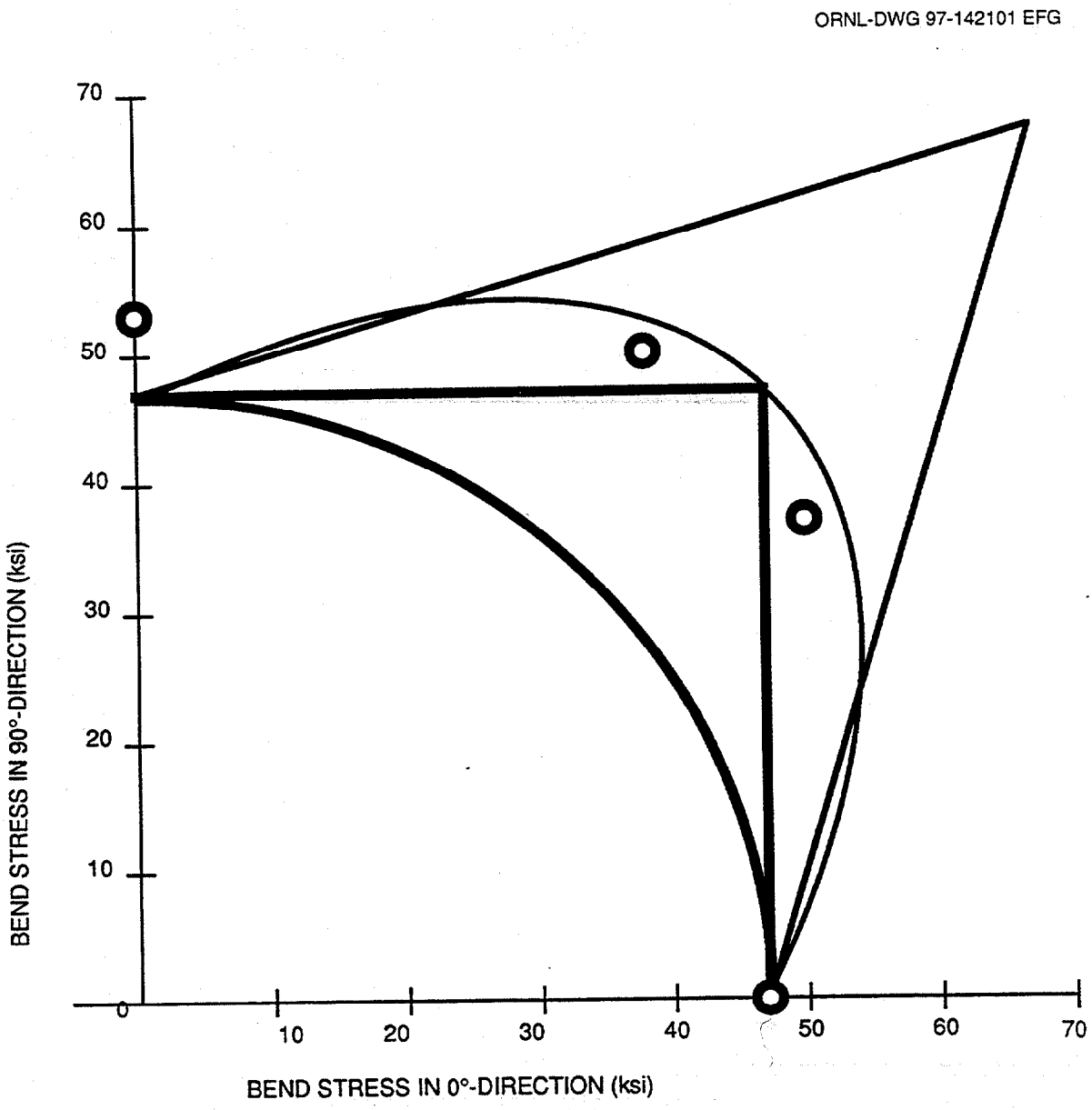

Fig. 6.4. Average maximum stresses at failure in the disks compared with five failure criteria.

ORNL-DWG 97-142102 EFG

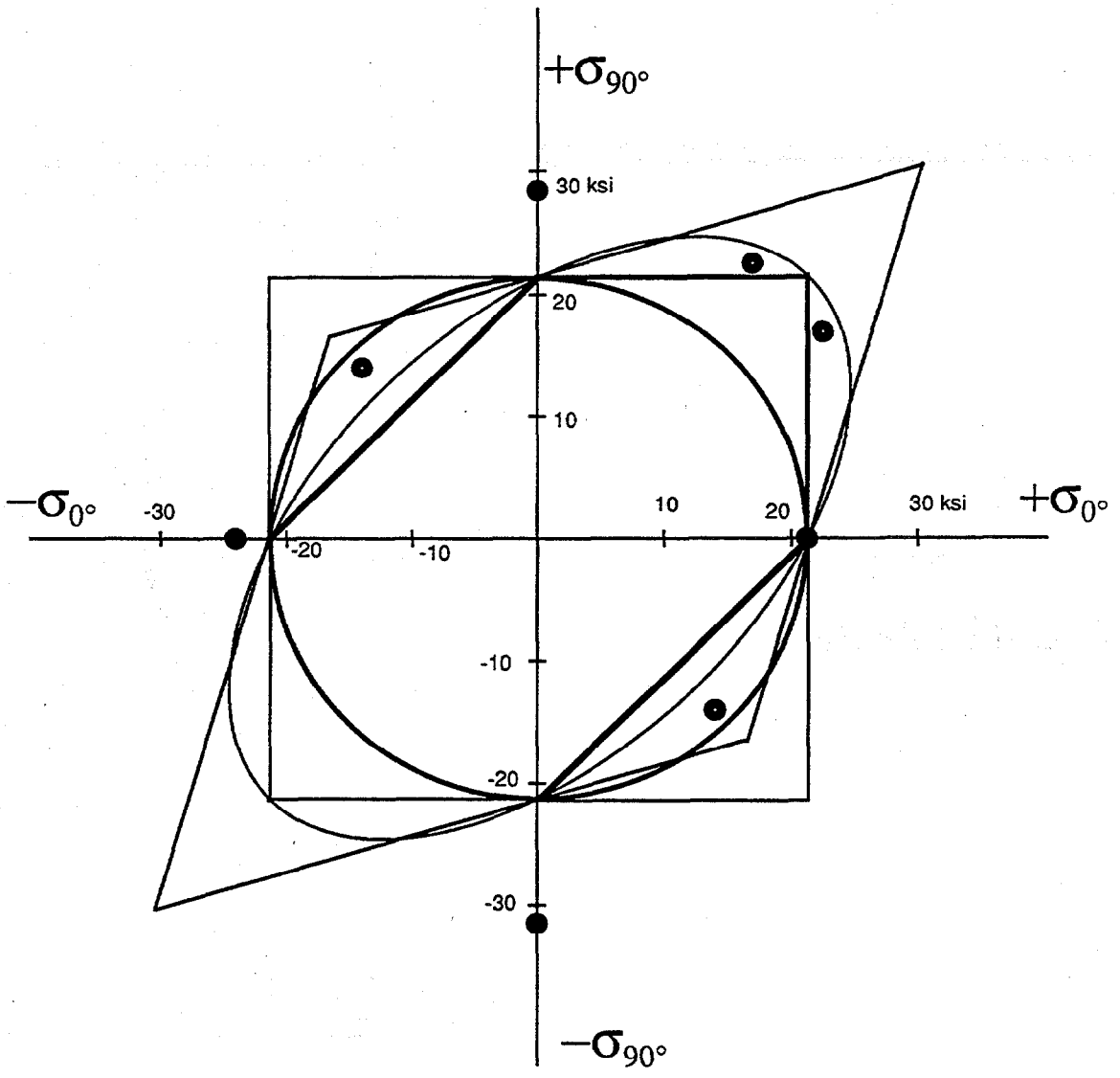

Fig. 6.5. Available data indicate maximum shear criterion applies.

REFERENCE

1. M. J. Owen and M. S. Found, "Static and Fatigue Failure of Glass Fibre Reinforced Polyester Resins under Complex Stress Conditions," *Faraday Special Discussions of the Chemical Society*, No. 2, Solid/Solid Interfaces, pp. 77–89, 1972.

7. REPRESENTATION OF CREEP UNDER VARIOUS STRESS, TEMPERATURE, AND ENVIRONMENTAL CONDITIONS

D. N. Robinson, University of Akron*

7.1 INTRODUCTION

Creep data are analyzed for the swirl-mat reference material at several stress levels, temperatures, and environmental conditions. Reference conditions are taken as 75°F (room temperature), a stress range of ≈0–17 ksi, and an air environment with ≈50% relative humidity. Reference data are represented in terms of an empirical *creep equation*; creep response under other conditions is assessed relative to this equation.†

Service conditions dictate that creep response be characterized up to 3000 h and beyond (possibly up to ≈130,000 h). As the longest test time in the data set is ≈3000 h, we recognize the importance of quantifying the creep rate at 3000 h as accurately as possible, allowing some confidence in extrapolation beyond 3000 h.

The temperature range 75 to 250°F is considered in detail. Because service conditions extend to –40°F, an extrapolation of the creep characterization, unsupported by experimental data, is given in an appendix.

7.2 REFERENCE CREEP EQUATION

We first consider an equation for creep-strain rate. It is taken in a simple, *separable* form; that is,

$$\dot{\varepsilon}(\sigma,t,T) = Kf(\sigma)g(t)F(T) \ . \tag{7.1}$$

The creep strain is similarly separable as

$$\varepsilon(\sigma,t,T) = Kf(\sigma)\int g(t)dtF(T) = Kf(\sigma)G(t)F(T) \ . \tag{7.2}$$

Equations (7.1) and (7.2) must satisfy

$$f(0) = 0 \ , \quad G(0) = 0 \ , \quad \text{and} \quad F(T_0) = 1 \ . \tag{7.3}$$

T_0 is a reference temperature [i.e., T_0 = 535°R (75°F)], and K is an *environmental factor*. The latter may be a constant or, more generally, a function of stress and temperature. We specify K = 1 under the reference conditions.

The reference creep data suggest that for relatively low stresses ($\sigma \leq 14$ ksi) the creep response is nearly linear. This is corroborated by examining the creep curves for 2.5, 5, 10, and 12 ksi in Fig. 7.1. For example, the 5 ksi creep curve (as well as its corresponding creep rates) is essentially double that for 2.5 ksi; likewise, the 10 ksi curve is double that for 5 ksi. As most of the creep data presented here, these curves represent smoothed averages of several tests.

At the higher stress levels (e.g., 16 and 17 ksi in Fig. 7.1), nonlinearity is apparent. The creep curves begin to *fan out* above $\sigma \approx 14$ ksi. This feature is also evident in Fig. 7.2, a log-log plot of creep-strain rate at 3000 h vs stress. The slope of the curve in Fig. 7.2 for $\sigma \leq 14$ ksi is ≈1 (linear); that for $\sigma > 14$ ksi, including 16 and 17 ksi, approaches ≈5–7.

---

*Oak Ridge Institute for Science and Education faculty research participant at ORNL.

†The creep equation is a fit of the data obtained under constant stress. It is not a constitutive equation and is incapable of alone predicting the creep response to variable stress (e.g., step-stress, recovery, relaxation, etc.).

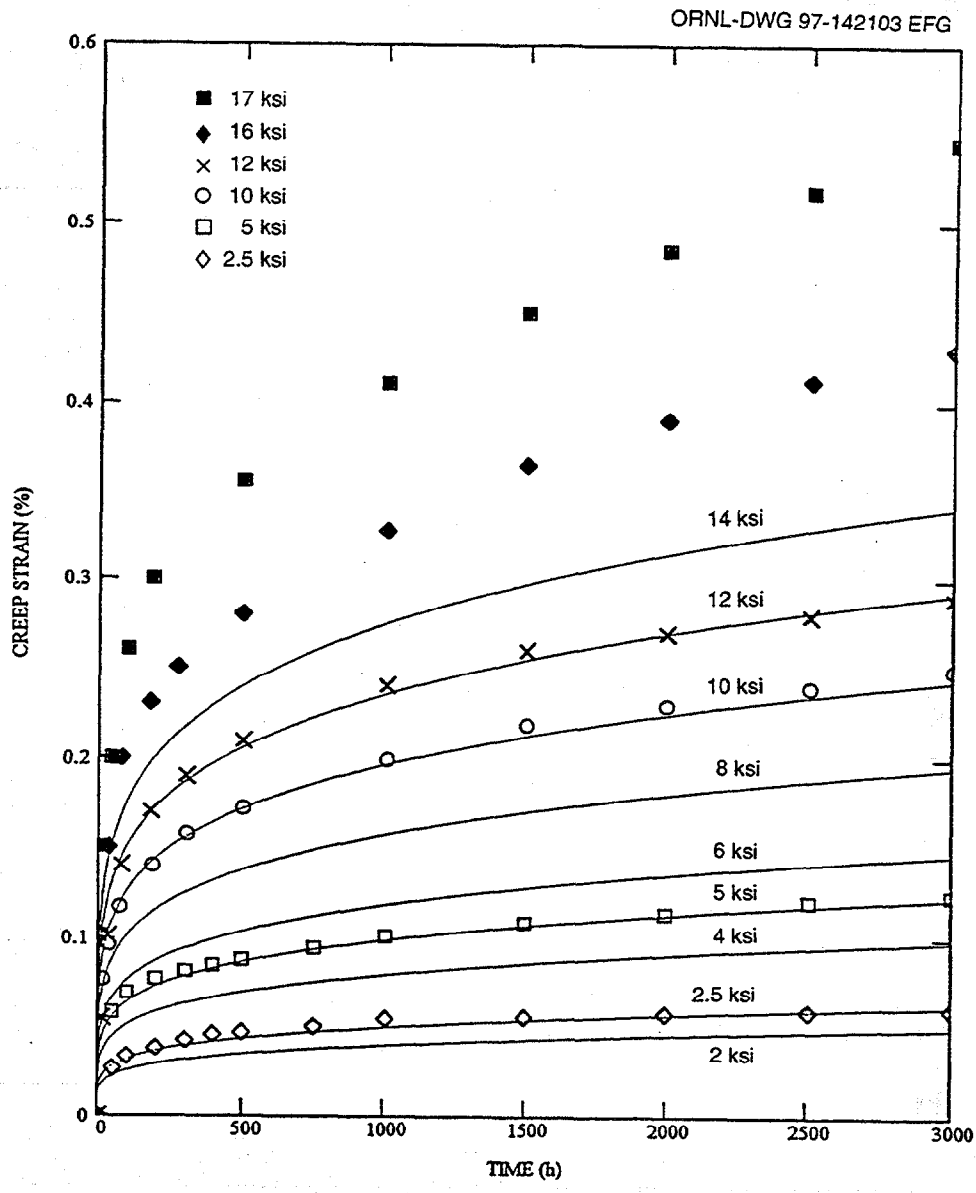

Fig. 7.1 Creep at reference conditions. Solid lines are calculated results at 75°F based on Eq. (7.10).

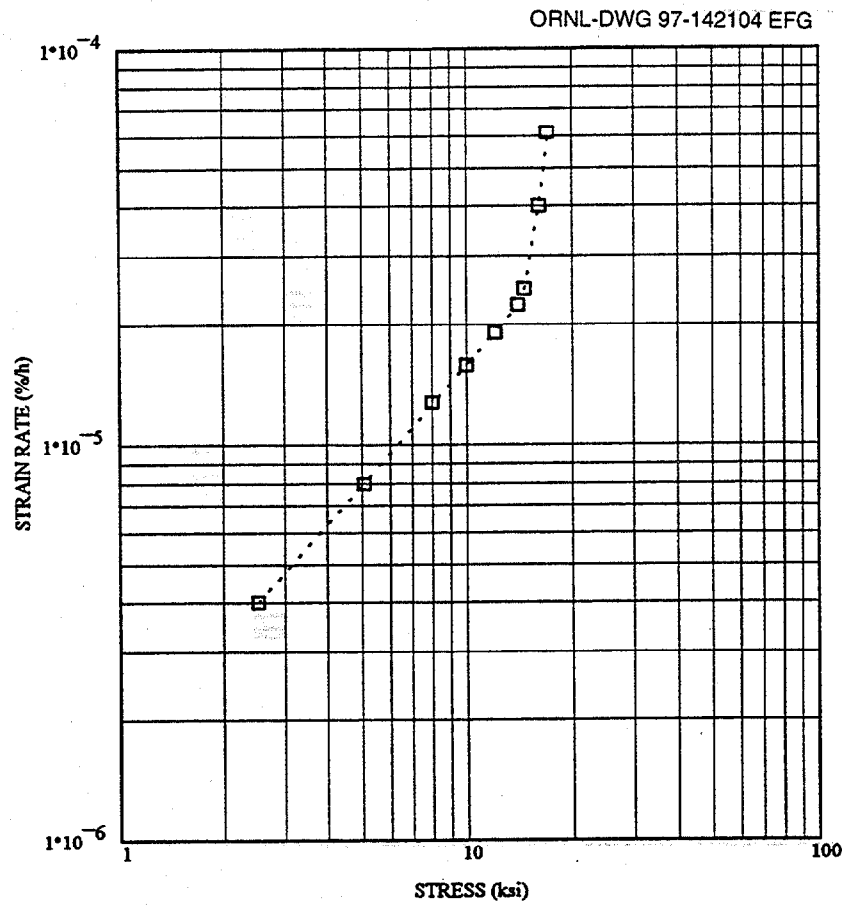

Fig. 7.2. Creep-strain rate at 3000 h vs stress at reference conditions.

Focusing on the stress range $\sigma \leq 14$ ksi, we take

$$f(\sigma) = C\sigma \tag{7.4}$$

to satisfy Eq. (7.3).

We adopt the well-established WLF equation for representing the temperature dependence; that is,

$$F(T) = \exp\left[\frac{C_1(T-T_0)}{C_2+T-T_0}\right], \tag{7.5}$$

where C_1 and C_2 are constants, and $T_0 = 535°R = 75°F$ is the reference temperature.* Note that $F(T_0) = F(535°R) = 1$ in accordance with Eq. (7.3).

*The WLF equation was originally introduced for time-temperature shifting related to the glass transition region [i.e., the transition region surrounding T_g (≈330°F for our material)]. Although not intended for our temperature range, it represented the data satisfactorily.

Finally, we adopt a power law for the time dependence, viz.,

$$G(t) = t^{\beta} \ , \tag{7.6}$$

where $\beta \leq 1$ is a constant. Again, $G(0) = 0$ in keeping with Eq. (7.3).

In these terms the creep Eq. (7.2) specialized for the reference conditions is

$$\varepsilon(\sigma,t,T) = C\sigma \cdot t^{\beta} \ , \tag{7.7}$$

and the rate Eq. (7.1) is

$$\dot{\varepsilon}\,(\sigma,t,T) = \beta \cdot C\sigma \cdot t^{\beta-1} \ . \tag{7.8}$$

A least-squares fit of the smoothed reference data yields

$$C = 5.07 \times 10^{-3} \quad \text{and} \quad \beta = 0.196 \ , \tag{7.9}$$

resulting in a *reference creep equation* valid for 75°F, $\sigma \leq 14$ ksi, and $t \leq 3000$ h; that is,

$$\varepsilon(\sigma,t) = 5.07 \times 10^{-3} \cdot \sigma \cdot t^{0.196} \ , \tag{7.10}$$

and a *reference creep-rate equation*

$$\dot{\varepsilon}\,(\sigma,t) = 9.94 \times 10^{-4} \cdot \sigma \cdot t^{-0.804} \ . \tag{7.11}$$

Equations (7.10) and (7.11) are consistent with the units; kips per square inch for stress (σ), percent for creep strain (ε), and hour (h) for time (t).

The curves in Fig. 7.1 corresponding to 2, 2.5, 4, 5, 6, 8, 10, 12, and 14 ksi are calculated from Eq. (7.10). Correlation with existing data is seen to be satisfactory.

The data and information included in Figs. 7.1 and 7.2 along with Eqs. (7.10) and (7.11) characterize the creep behavior of the swirl-mat model material at the reference conditions. This is used subsequently to assess the effects of other environmental conditions on creep.

7.3 TEMPERATURE DEPENDENCE

We now extend the correlation to include temperature dependence. As $F(T) \neq 1$ for $T > T_0$, we return to the more general forms of Eqs. (7.1) and (7.2) that include F(T) given by Eq. (7.5). Creep data for temperatures above the reference temperature [i.e., 595°R (135°F), 650°R (190°F), and 710°R (250°F)] are used to specify the constants C_1 and C_2 in Eq. (7.5).

The most abundant and reliable data available are at the uppermost temperature of interest, 710°R (250°F). Creep data at 2.5, 5, 7.5, 9, and 10 ksi for this temperature are shown in Fig. 7.3. The creep curves are seen to begin *fanning out* above ≈7.5 ksi (i.e., for 9 and 10 ksi). Estimates of the creep rates corresponding to the 2.5, 5, 7.5, and 9 ksi data at 3000 h are made and plotted vs stress in Fig. 7.4. For comparison, the room-temperature data from Fig. 7.2 are also plotted in Fig. 7.4.

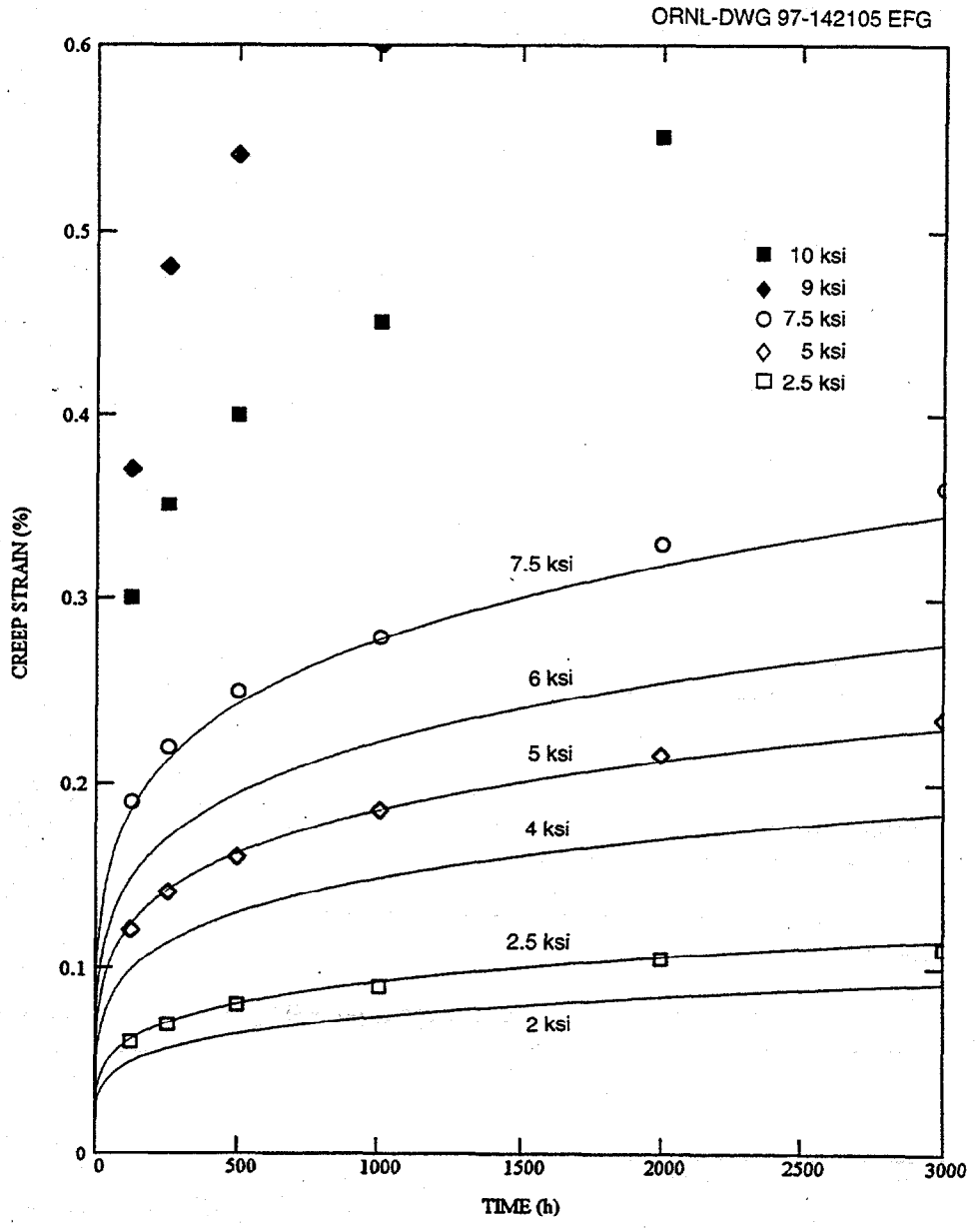

Fig. 7.3. Creep at 710°R (250°F). Solid lines are calculated results based on Eq. (7.13).

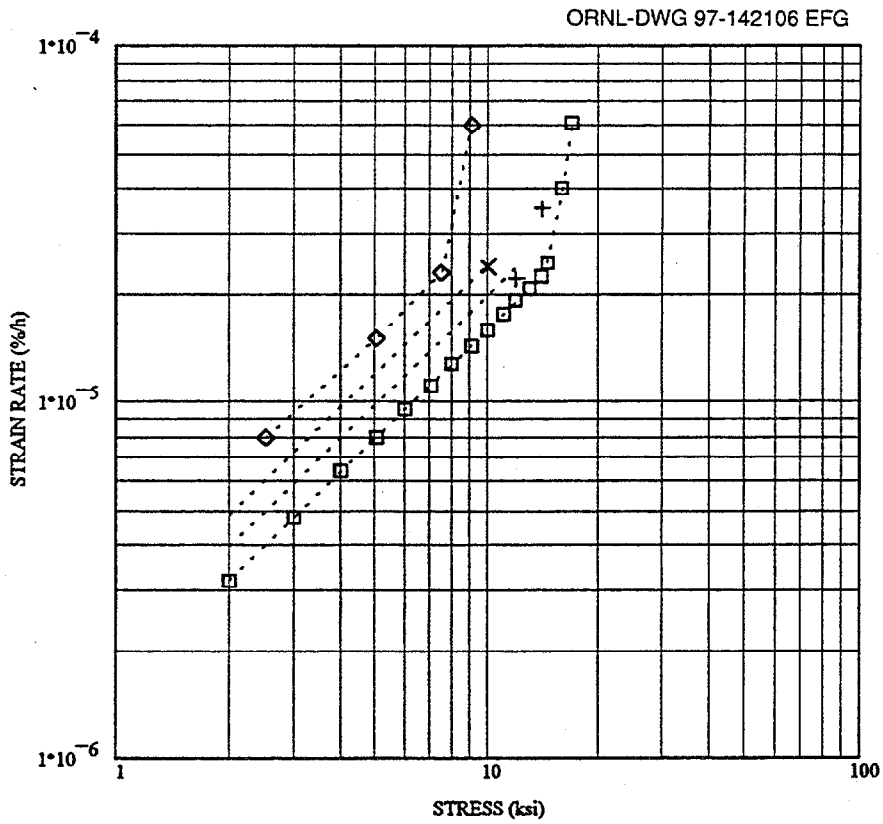

Fig. 7.4. Creep-strain rate at 3000 h vs stress. Experiments: (box symbols) 535°R (75°F), (diamond symbols) 710°R (250°F), (x symbols) 650°R (190°F), (cross symbols) 595°R (135°F).

By comparison, the data sets for 535°R (75°F) and 710°R (250°F) in Fig. 7.4 are very similar. Each has a linear portion at low stress; each has a distinct break point defining the onset of nonlinearity. A reasonable interpretation of the data is that the departure from linearity shifts from ≈ 14 ksi at 535°R (75°F) to ≈7.5 ksi at 710°R (250°F), whereas the respective linear regions are shifted vertically. For example, at 5 ksi the vertical shift amounts to a ratio in strain rates of ≈1.88. This provides one condition for determining the constants C_1 and C_2 in Eq. (7.5). A second comes from data at an intermediate temperature.

Reliable data at intermediate temperatures are sparse. At present, they are limited to two tests at 595°R (135°F) and one at 650°R (190°F). The two at 135°F are for 12 and 14 ksi; that at 190°F is for 10 ksi. The estimated creep rates at 3000 h associated with these data are shown in Fig. 7.4. The former are plotted as cross symbols (+), the latter by (x) symbols.

Judging by the nature of the data, the data point at 190°F and 10 ksi likely lies in or near the linear range, and we use it as a second condition for determination of the constants in the WLF Eq. (7.5). This yields a corresponding ratio of strain rates (with respect to that at 75°F) of ≈1.52. Together with the condition established earlier from the 250°F data, we get

$$C_1 = 64 \quad \text{and} \quad C_2 = 17.5 \times 10^3 \ . \tag{7.12}$$

The details of this calculation are shown in Appendix 7.A.

The constants Eq. (7.12) with the reference temperature T_0 = 535°R (75°F) complete the specification of the WLF Eq. (7.5). It is plotted vs temperature in Fig. 7.5. The two intermediate dotted lines in Fig. 7.4 are the calculated linear ranges for 595°R (135°F) and 650°R (190°F) consistent with Eq. (7.12).

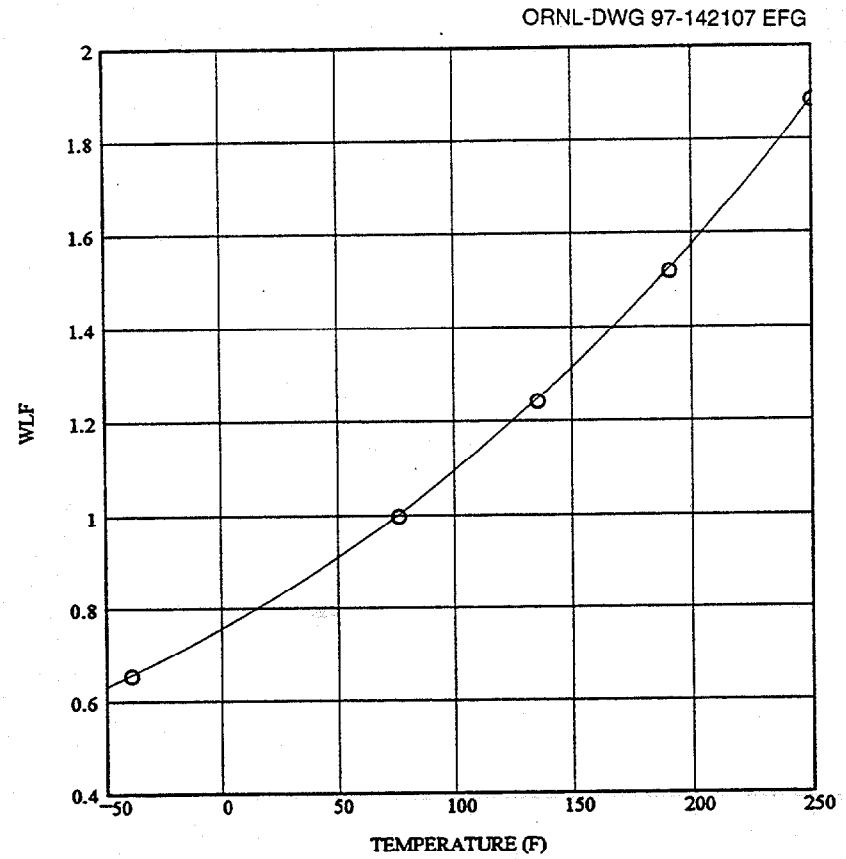

Fig. 7.5. WLF Eq. (7.5) vs temperature. Points represent –40, 75, 135, 190, and 250°F.

We now state the *creep* and *rate equations* complete with temperature dependence. Thus,

$$\varepsilon(\sigma,t,T) = K \cdot C\sigma \cdot \exp\left[\frac{C_1(T-T_0)}{C_2+T-T_0}\right] \cdot t^{\beta} \ , \tag{7.13}$$

and

$$\dot{\varepsilon}(\sigma,t,T) = \beta \cdot K \cdot C\sigma \cdot \exp\left[\frac{C_1(T-T_0)}{C_2+T-T_0}\right] \cdot t^{\beta-1} \ , \tag{7.14}$$

where

$$\begin{aligned} K &= (\textit{environmental factor}) \\ C &= 5.07 \times 10^{-3} \\ \beta &= 0.196 \\ C_1 &= 64 \\ C_2 &= 17.5 \times 10^{3} \\ T_0 &= 535°R\ (75°F) \end{aligned} \tag{7.15}$$

The units are kips per square inch for stress, percent for strain, degrees R (Rankine) for temperature, and hours for time. Equations (7.13), (7.14), and (7.15) are valid for

$$710°R\ (250°F) \geq T \geq T_0 \quad \text{and} \quad t \leq 3000\ h \tag{7.16}$$

and in the *linear ranges* defined approximately by:

$$\begin{aligned} \sigma &\leq 14\ ksi \quad \text{for} \quad 535°R\ (75°F) \\ \sigma &\leq 12\ ksi \quad \text{for} \quad 595°R\ (135°F) \\ \sigma &\leq 10\ ksi \quad \text{for} \quad 650°R\ (190°F) \\ \sigma &\leq 7.5\ ksi \quad \text{for} \quad 710°R\ (250°F)\ . \end{aligned} \tag{7.17}$$

For reference, we include Figs. 7.6–7.9, which are creep curves calculated from Eq. (7.13) at constant stress at the indicated temperatures.

Based on service conditions, temperatures of interest extend below room temperature to –40°F. Although no data at this temperature currently exist in this data set, an extrapolation of the creep representation is given in Appendix 7.B.

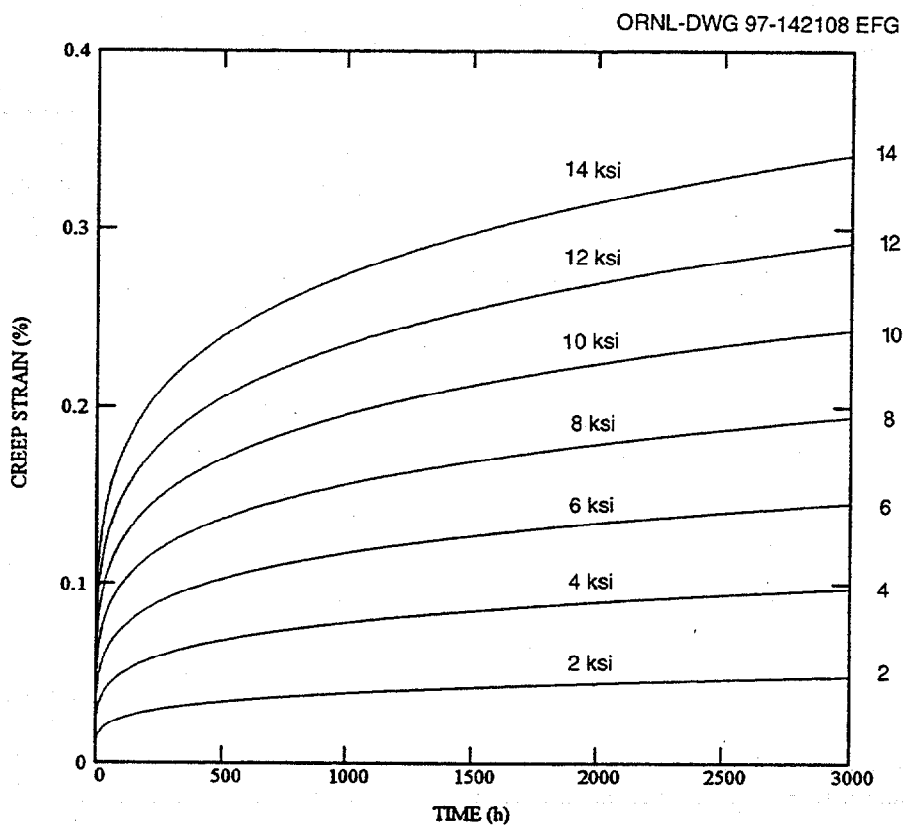

Fig. 7.6. Creep curves for 2–14 ksi at 535°R (75°F). Calculated using Eq. (7.13).

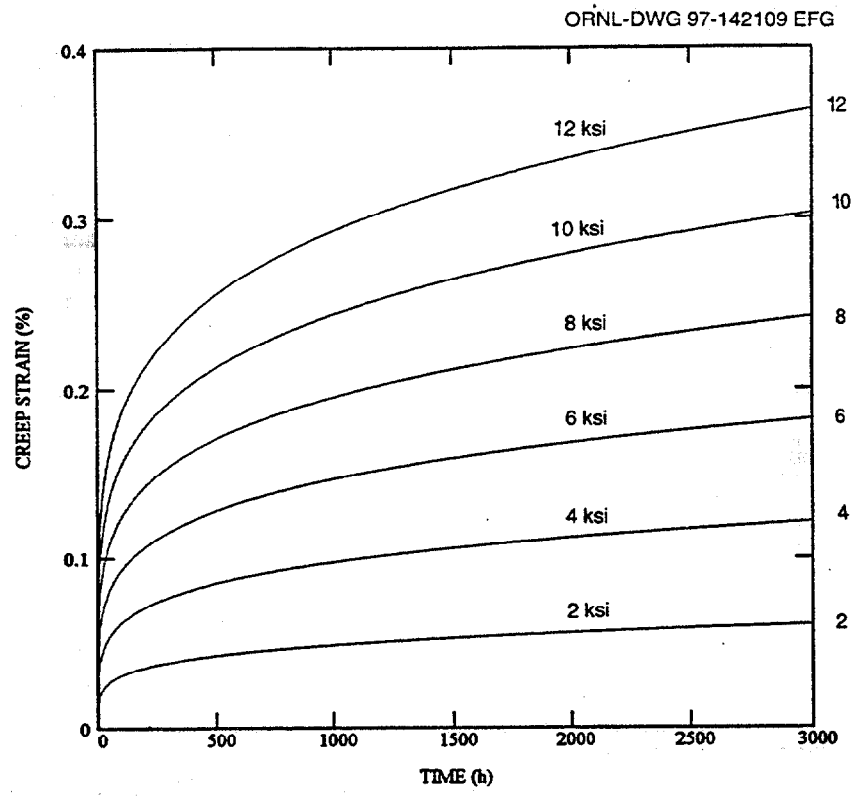

Fig. 7.7. Creep curves for 2–12 ksi at 595°R (135°F). Calculated using Eq. (7.13).

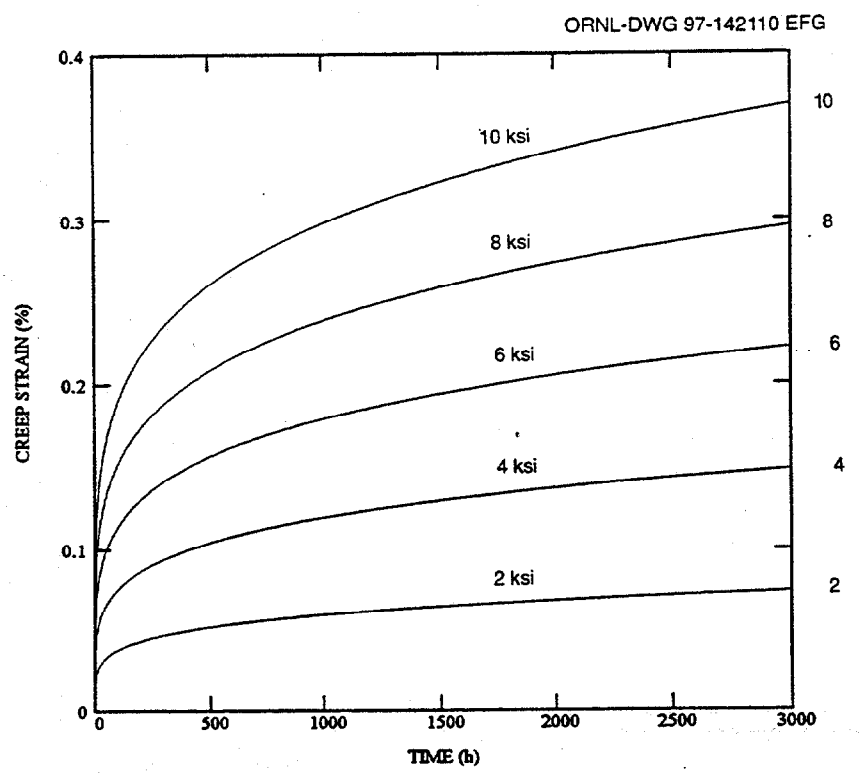

Fig. 7.8. Creep curves for 2–10 ksi at 650°R (190°F). Calculated using Eq. (7.13).

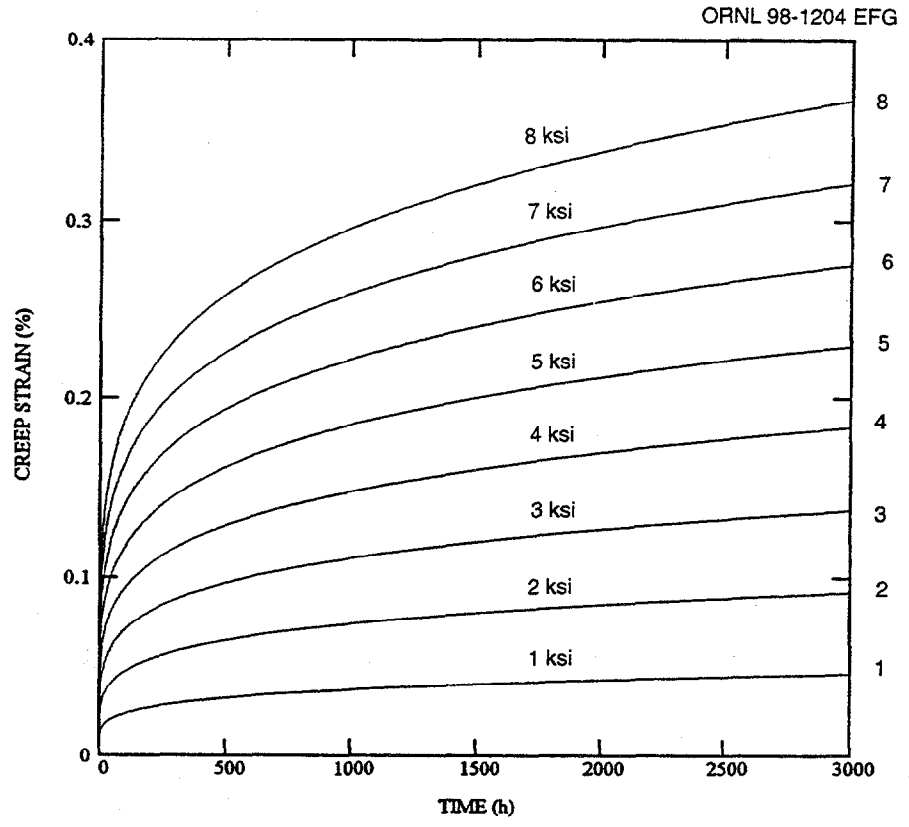

Fig. 7.9. Creep curves for 1–8 ksi at 710°R (250°F). Calculated using Eq. (7.13).

7.4 EFFECT OF DISTILLED WATER ON CREEP (ROOM TEMPERATURE)

We now examine the effect of a distilled water environment on creep response at 535°R (75°F). Data from four specimens tested at 8, 9, 11, and 12 ksi are considered. These specimens received a presoak in distilled water for 100 h prior to testing. Creep testing was then conducted in distilled water. Fig. 7.10 shows the data for each of the specified creep tests.

Guided by the approach followed in characterizing temperature dependence, we estimate the creep rates for each test at 3000 h (that for the 12 ksi test is very approximate). The results are shown in Fig. 7.11 as diamond symbols. Again, we include the results from the reference tests at 535°R (75°F), shown in box symbols.

Considering the qualitative nature of the data observed so far in the strain rate-stress space, we might reasonably expect a linear portion of the distilled water data curve to be at low stresses. Conclusively, of course, we need data at the lower stresses. In their absence we assume a linear region exists and represent it by the dotted line drawn parallel to the reference data in Fig. 7.11. The ratio of strain rates corresponding to a vertical shift of the reference curve to the assumed dotted line is ≈1.6. This serves as an environmental factor K in Eqs. (7.13) and (7.14) for the effect of distilled water on creep at 535°R (75°F). Thus,

$$K_{DW} = 1.6 \tag{7.18}$$

for the *assumed* linear region.

In principle, we can extend this approach into the nonlinear region. That is, we can consider the vertical *shift*, or correspondingly the environmental factor, to be a function of stress. Applying this notion

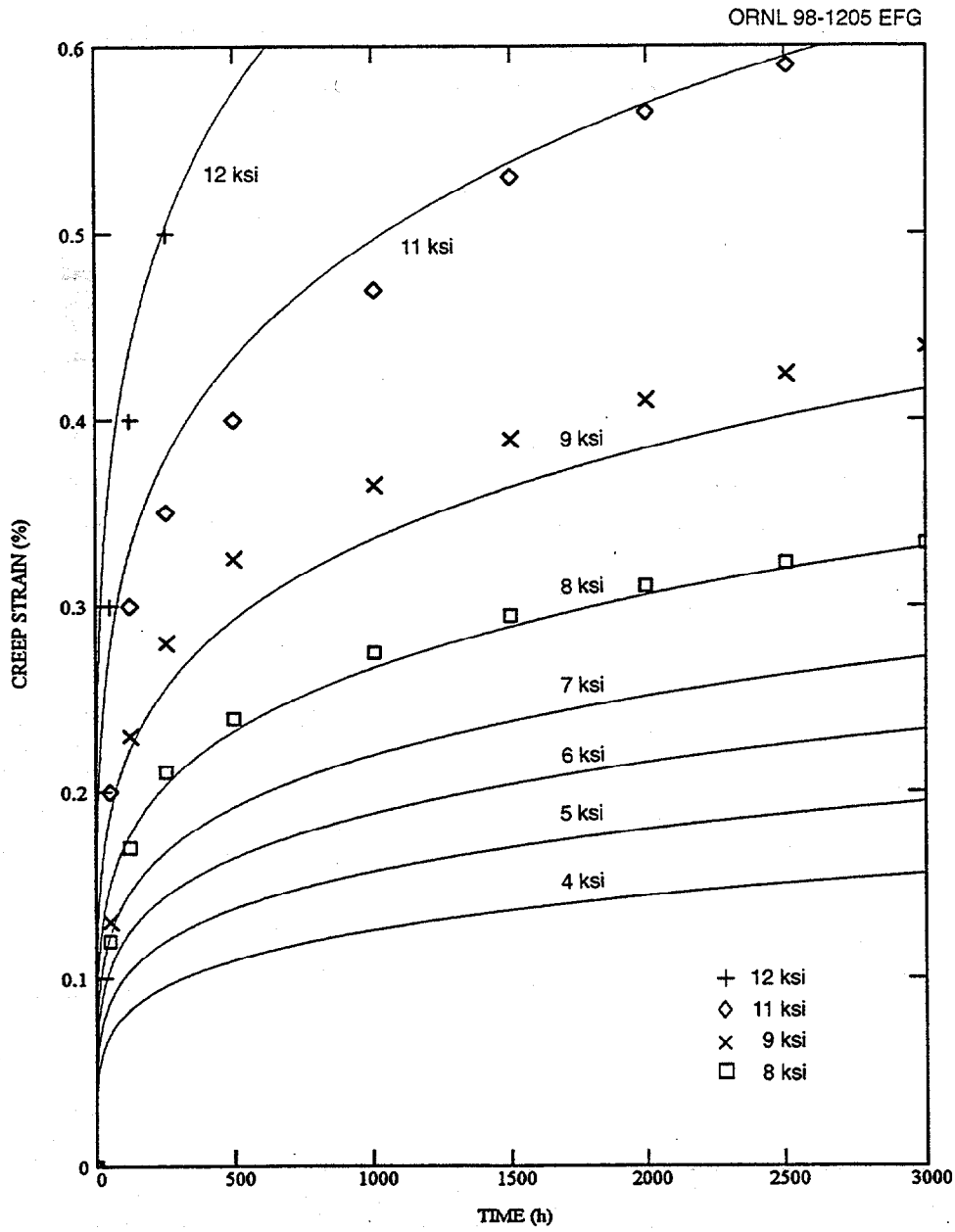

Fig. 7. 10. Creep in distilled water at 535°R (75°F). Solid lines are calculated results based on Eq. (7.13).

to the 8, 9, 11, and 12 ksi data points in Fig. 7.11, we get the result shown in Fig. 7.12, which is a plot of K_{DW} vs stress. Up to ≈7 ksi we take $K_{DW} = 1.6$. For higher stress (viz., for 8, 9, 11, and 12 ksi) K_{DW} increases as shown.

Using the hypothesized variation of K_{DW} given in Fig. 7.12 in the creep Eq. (7.13) with T = 535°R (75°F), we calculate the creep curves for 4, 5, 6, 7, 8, 9, 11, and 12 ksi shown as solid lines in Fig. 7.10. Although no data are available for comparison in the low stress, *linear* region, the correlation with creep curves at the higher stresses, 8, 9, 11, and 12 ksi is quite good.

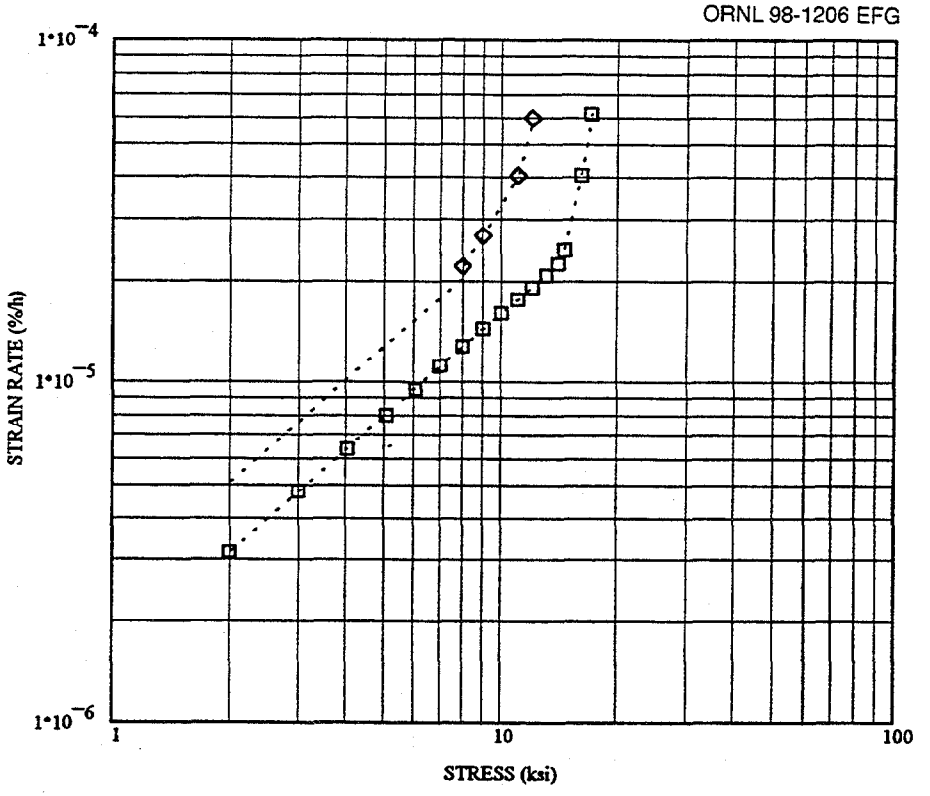

Fig. 7.11. Creep-strain rate at 3000 h vs stress in distilled water at 75°F. Distilled water data (diamond symbols), reference data (box symbols).

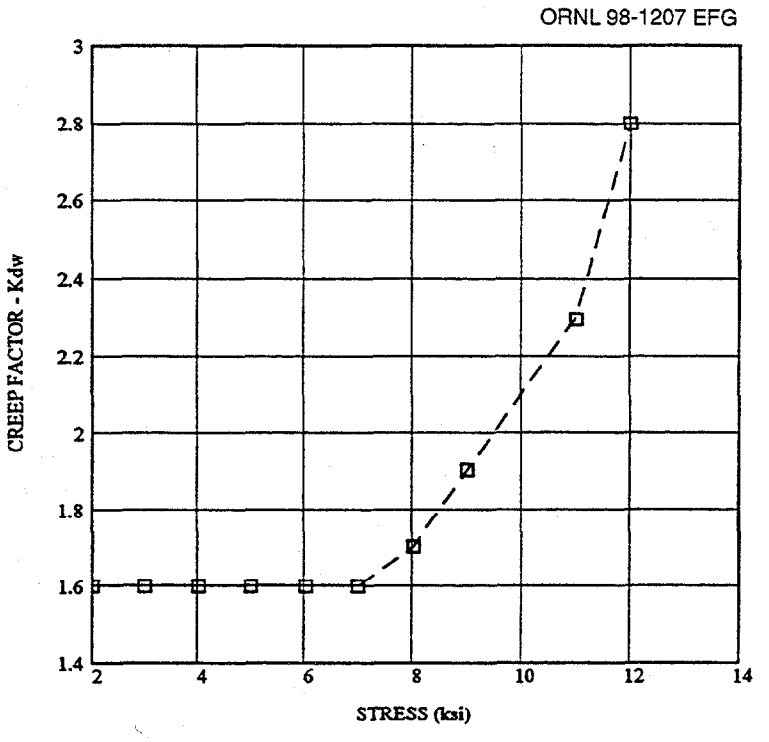

Fig. 7.12. Distilled water environmental factor K_{DW} vs stress.

7.5 EFFECTS OF OTHER ENVIRONMENTS ON CREEP

Creep under reference (ambient) conditions, the effect of elevated temperature, and the effect of a distilled water environment have been characterized in considerable detail. This was possible because ample and reliable data are available for these conditions. Comparable data are not available for other environmental conditions of interest. The effects of these environments are estimated by comparing their relevant creep data with that analyzed for the conditions previously specified. The earlier detailed characterizations are viewed as establishing a scale against which other environmental effects can be ranked.

The ranking of the effects of specified environments in Table 7.1 is based on the creep Eqs. (7.13)–(7.15), written as

$$\varepsilon(\sigma,t,T) = K_C \cdot 5.07\times10^{-3} \cdot \sigma \cdot t^{0.196} \tag{7.19}$$

in which the *creep factor* K_C is defined as

$$K_C = K\cdot\exp\left[\frac{64(T-T_0)}{17.5\times10^3+(T-T_0)}\right] . \tag{7.20}$$

T_0 = 535°R (75°F) is the reference temperature, and K is the *environmental factor* defined earlier. Note that the *creep factor* K_C = 1 for the *reference condition* 75°F air 50% RH.

Table 7.1. Estimated creep factor for various conditions

Environment	K_C
–40°F air 50% RH	0.65*
75°F air 50% RH	1.00
Motor oil	1.05
135°F air 50% RH	1.24
Brake fluid	1.30
Windshield wash	1.50
Saltwater	1.50
190°F air 50% RH	1.52
75°F air > 90% RH	1.55
Distilled water	1.60
Battery acid	1.65
250°F air 50% RH	1.88

*This is an extrapolation, cf., Appendix 7.A. It is not based directly on experimental data.

APPENDIX 7.A

Figure 7.A.1 is a schematic illustration of a log-log plot of creep-strain rate at a given time vs stress. Shown are three linear curves (suggested as becoming nonlinear at higher stresses) for three temperatures $T_2 > T_1 > T_0$, where T_0 is taken as the reference temperature. At a particular stress σ in Fig. 7.A.1, we define three values of strain rate ε_2, ε_1, and ε_0 as indicated.

The constants C_1 and C_2 in the WLF Eq. (7.5) are then given by:

$$\begin{bmatrix} C_1 \\ C_2 \end{bmatrix} = \begin{bmatrix} (T_2 - T_0) & -\ln\left(\dfrac{\dot{\varepsilon}_2}{\dot{\varepsilon}_0}\right) \\ (T_1 - T_0) & -\ln\left(\dfrac{\dot{\varepsilon}_1}{\dot{\varepsilon}_0}\right) \end{bmatrix}^{-1} \begin{bmatrix} (T_2 - T_0)\cdot\ln\left(\dfrac{\dot{\varepsilon}_2}{\dot{\varepsilon}_0}\right) \\ (T_1 - T_0)\cdot\ln\left(\dfrac{\dot{\varepsilon}_1}{\dot{\varepsilon}_0}\right) \end{bmatrix}.$$

In the present case, $T_2 = 710°R$, $T_1 = 650°R$, $T_0 = 535°R$, $\varepsilon_2/\varepsilon_0 = 1.88$, and $\varepsilon_1/\varepsilon_0 = 1.52$ giving $C_1 = 64$ and $C_2 = 17.5 \times 10^3$.

ORNL 98-1209 EFG

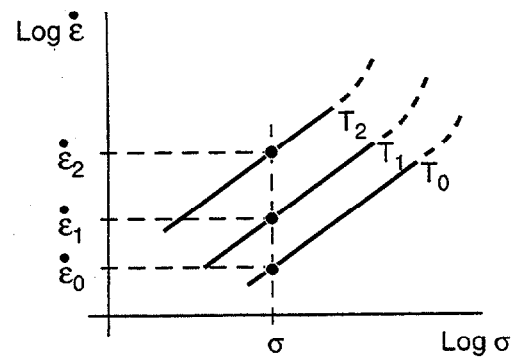

Fig. 7.A.1. Schematic of a log-log plot of creep-strain rate at a given time vs stress.

APPENDIX 7.B

The WLF Eq. (7.5) was specialized using data in the range 75–250°F, resulting in Eq. (7.12). As service conditions extend to –40°F, we consider extrapolation of our representation, Eqs. (7.13)–(7.17). Figure 7.5 shows a plot of the WLF equation, with the constants Eq. (7.12), over the extended temperature range –50–250°F. Included in the figure are points corresponding to the temperatures in 75–250°F, considered earlier, as well as a point at –40°F. Visually, the extrapolation to –40°F does not seem excessive.

Theoretically, the WLF equation is usually assumed to be valid in the region around T_g (recall, here $T_g \approx 330$°F). We conjecture that an extrapolation to –40°F is not unreasonable. Figure 7.5 illustrates the value of WLF at –40°F is ≈0.65, which is the same for the *creep factor* K_C in Eq. (7.20) (i.e., with K = 1 for air 50% RH). This value is entered in Table 7.1.

Figure 7.B.1 is a plot of estimated creep curves for 2–14 ksi at –40°F. These were calculated using Eq. (7.13) with K_C, defined by Eq. (7.20), equal to 0.65. Figure 7.B.1 is drawn to the same scale as Figs. 7.6–7.9 for comparison.

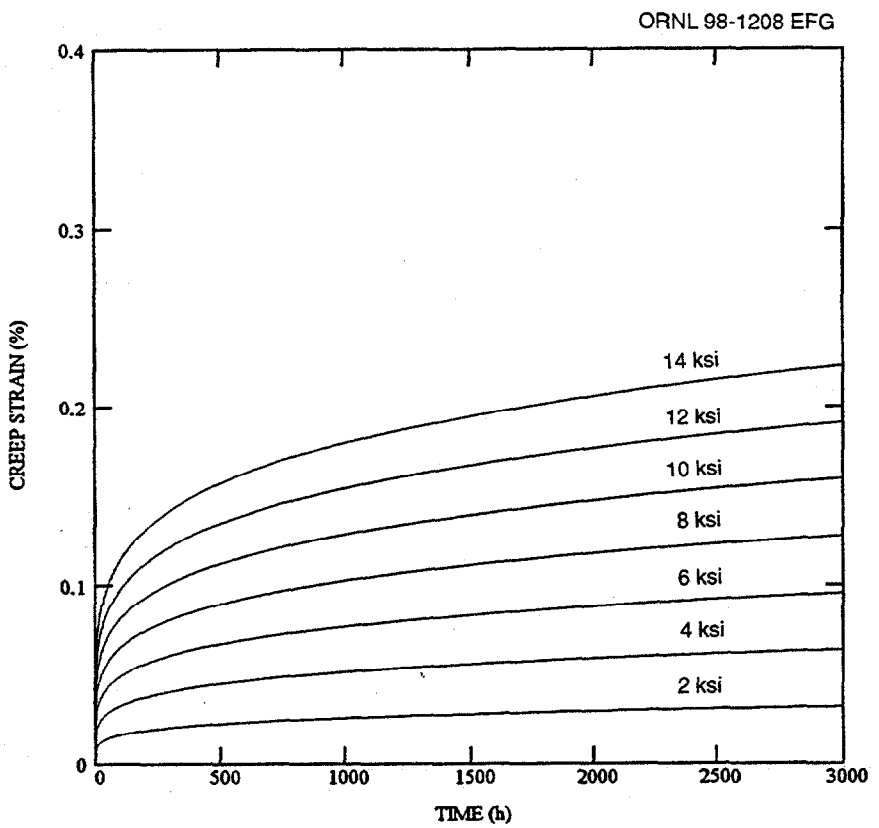

Fig. 7.B.1. Extrapolated creep curves for 2–14 ksi at 420°R (–40°F). Calculated using Eq. (7.13).

APPENDIX 7.C

We now reconsider a uniaxial constitutive model based on a single state variable α. The forms Eqs. (7.C.1) and (7.C.2) are borrowed from those ordinarily considered for *dislocation* creep and rate sensitivity of metals at high temperature. In that application the *Bailey-Orowan form* of the evolutionary Eq. (7.C.2) reflects competing hardening and softening micro-mechanisms on the atomic or (defect) scale, their *balance* allows *steady-state* creep.

In the case of polymers, we focus instead on the molecular scale. One important feature relating to creep of polymers is that of *free volume*. As the free volume f increases, due to increased thermal agitation, or whatever mechanism, molecules can slip by each other more easily and creep is enhanced. Conversely, a decrease in free volume impedes creep.

A possible identification of a phenomenological internal variable for a creeping polymer might be, say, $\alpha = 1 - f$ or, perhaps the reciprocal of f. Then α increases with decreasing f, resulting in hardening; and α decreases with increasing f relating to softening. Balance of the mechanisms affecting free volume would then lead to steady-state creep. Obviously, this is affected by the degree of cross linking of molecules.

In any case, we hypothesize that these forms may be appropriate and write

$$\frac{\dot{\varepsilon}}{\dot{\varepsilon}_0} = \left|\frac{\sigma-\alpha}{\sigma_0}\right|^n \frac{\sigma-\alpha}{|\sigma-\alpha|} \quad \textit{(flow law)} \ , \tag{7.C.1}$$

$$\frac{\dot{\alpha}}{\sigma_0\dot{\varepsilon}_0} = \frac{H}{|\alpha/\sigma_0|^\beta}\frac{\dot{\varepsilon}}{\dot{\varepsilon}_0} - R\left|\frac{\alpha}{\sigma_0}\right|^{m-\beta}\frac{\alpha}{|\alpha|} \quad \textit{(evolutionary law)} \ , \tag{7.C.2}$$

$$\dot{\varepsilon}_0 = \dot{\varepsilon}_{00}\left[\frac{C_1(T-T_0)}{C_2+T-T_0}\right] , \quad \text{and} \quad R = R_0\left[\frac{C_1(T-T_0)}{C_2+T-T_0}\right] . \tag{7.C.3}$$

The material parameters in Eqs. (7.C.1) and (7.C.2) are

$$\sigma_0,\ \dot{\varepsilon}_{00},\ T_0,\ n,\ \beta,\ m,\ R_0,\ H,\ C_1,\ C_2 \ . \tag{7.C.4}$$

σ_0 is a reference stress, chosen for convenience in the stress range of interest, having the units of stress (ksi). T_0 is a reference temperature with the units R. The material constant $\dot{\varepsilon}_{00}$ has the units (%/h); the remaining constants are nondimensional.

We have determined a set of material parameters Eq. (7.C.4) that correlate with the creep data for the swirl-mat reference material (cf., Fig. 7.C.1). These are:

$$\begin{aligned} \sigma_0 &= 4 \text{ ksi} \\ \dot{\varepsilon}_{00} &= 0.00165 \ \%/\text{h} \\ n &= 1.9 \\ \beta &= 0.25 \\ m &= 1.0 \\ R_0 &= 0.049 \\ H &= 10 \\ C_1 &= 64 \\ C_2 &= 17500 \\ T_0 &= 535°\text{R} \ . \end{aligned} \tag{7.C.5}$$

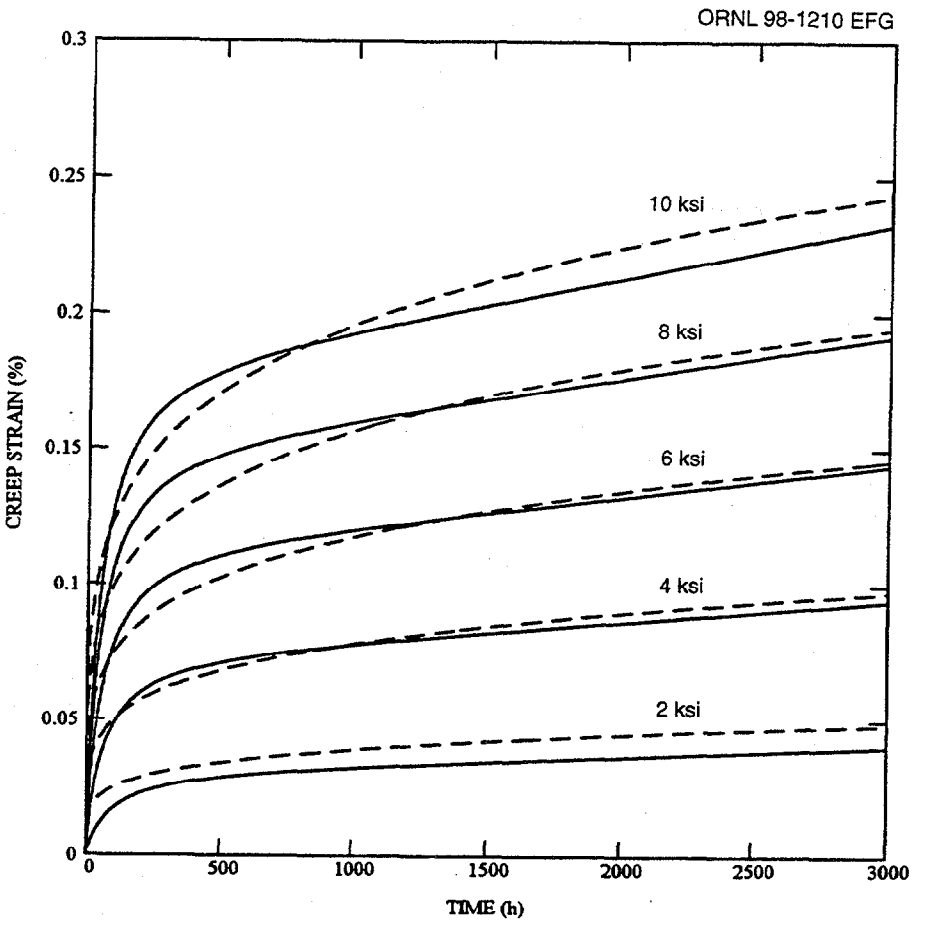

Fig. 7.C.1. Correlation of Appendix 7.C model (solid lines) with "data" (dashed lines). Data are taken as calculations from creep Eq. (7.10). Curves are for 2, 4, 6, 8, and 10 ksi at 75°F.

Figure 7.C.1 compares the predicted creep responses (solid lines) under the constant stresses 2, 4, 6, 8, and 10 ksi at 535°R (75°F) using Eqs. (7.C.1)–(7.C.5). The dotted lines in Fig. 7.C.1 are the responses under the same conditions calculated from the creep Eq. (7.13).

Figure 7.C.2 compares the predicted and measured creep at 4 ksi (75°F) followed by a recovery period at zero stress. The experimental results are from Smith and Weitsman.

Figure 7.C.3 compares the predicted and measured response of a three-step creep test in which the stress is increased from 4 to 6 to 8 ksi at 75°F. The experimental results are from Ren.

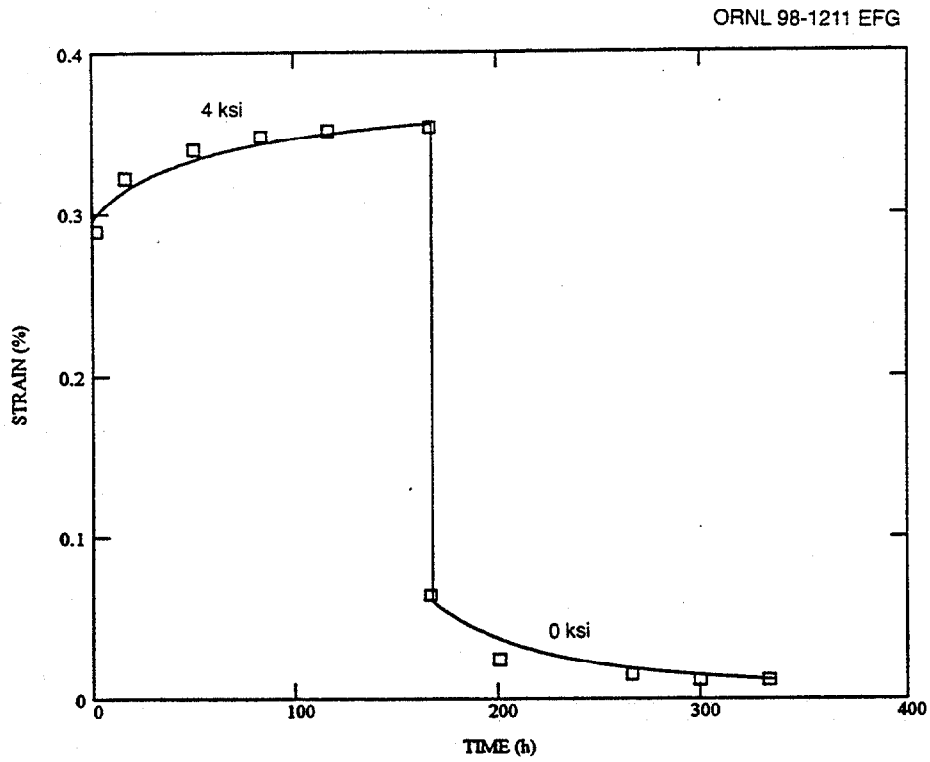

Fig. 7.C.2. Predicted (lines) and measured (symbols) creep and recovery for 4 to 0 ksi step at 75°F. Experiments from Smith and Weitsman, specimen P10-0-21.

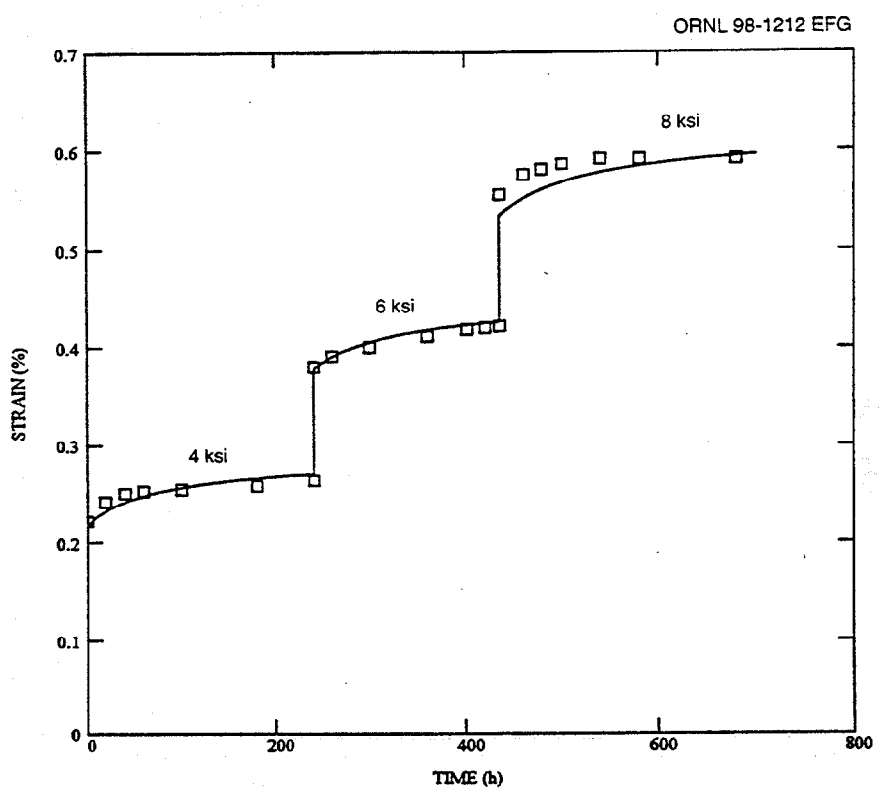

Fig. 7.C.3. Predicted (lines) and measured (symbols) creep of a step test at 4, 6, and 8 ksi and 75°F. Experiment from W. Ren specimen 29102.

8. DEVELOPMENT OF CREEP-RUPTURE CORRELATIONS AND DESIGN CURVES IN VARIOUS ENVIRONMENTS

W. Ren and C. R. Brinkman

8.1 INTRODUCTION

In this chapter, proposed stress allowables for time-dependent creep rupture under static and superimposed cyclic and static loading conditions are calculated for the isocyanurate continuous-strand, swirl-mat E-glass material. Data are analyzed from tests conducted in several environments, including air/50% relative humidity (air/50% RH), air with relative humidity less than 10% (air < 10% RH), air with relative humidity greater than 90% (air > 90% RH), distilled water, several water- and oil-based fluids, and sulfuric acid. Test temperatures range from 20 to 250°F, but not in all environments. Average and minimum creep-rupture behaviors are defined, where possible; suggested maximum time-dependent stress allowables are calculated by multiplying minimum values by 0.8.

8.2 CREEP-RUPTURE CURVES AND EQUATIONS FOR VARIOUS TEMPERATURES IN AIR/50% RH

A total of 154 specimens have been tested in air/50% RH at temperatures of 20, 75, 135, 190, and 250°F. The specimens were from plaques 1, 2, 3, 4, 5, 6, 7, 17, 18, 20, 21, 33, 34, 35, and 42. Of these 154 tests, 67 reached the rupture point to generate creep-rupture curves and equations.

Figure 8.1(*a*) gives the test results for air/50% RH at 75°F.[1] The data were generated from 30 tests on specimens from plaques 5, 6, 7, 17, 18, 20, 21, and 34, which should represent the average behavior of the material. The curve designated as average for 75°F/50% RH in Fig. 8.1(*a*) was derived from the test data by power law curve fitting. The curve labeled as minimum for 75°F/50% RH is obtained by a parallel graphical shift of the average curve downward to a lower bound for all the data points. The average and minimum curves for air/50% RH at 75°F will be used as the basis for comparison with test results under the other testing temperatures and environments. Another curve given in Fig. 8.1(*a*), defined as the maximum design-allowable stress, is simply 80% of the minimum rupture value. The equations for minimum creep-rupture and maximum design-allowable stress curves are also presented in Fig. 8.1(*a*). They have the form

$$\sigma = Bt^m \ . \tag{8.1}$$

The procedures employed in developing these curves and their equations will be discussed in detail in Sect. 8.6. These equations can be used for the derivation of alternate design guidelines if desired.

The test data and maximum design-allowable stress curves and equations for air/50% RH at 20, 135, 190, and 250°F are given in Figs. 8.2(*a*)–8.5(*a*). In Fig. 8.2 as well as other figures throughout this paper, data points with an arrow represent tests discontinued at the indicated time in the figure.

These figures illustrate that significant data scatter exists. In an effort to decrease data scatter, the original data were normalized by dividing the creep stress by the room-temperature UTS of the respective plaque from which the data were obtained, except plaque 7 whose UTS was not available; therefore, the average UTS of all the plaques was used. Figures 8.1(*b*)–8.5(*b*) present the same data as given in Figs. 8.1(*a*)–8.5(*a*) with the stress normalized and expressed as a percentage of UTS. To compare scattering between the original and normalized data when curve fitting, the linear correlation coefficient, R, was employed. With a value ranging from 0 to 1, the R represents how well the curve fits the data. For a perfect fit, which usually indicates no data scatter for the fit, R approaches or is equal to 1. The comparison of R values for air/50% RH at various temperatures is given in Table 8.1. Data for 20 and 190°F are sparse and are, therefore, not included in the table. At 75 and 250°F the R values are greater for the normalized data, indicating less data scatter for the power law curve fitting.

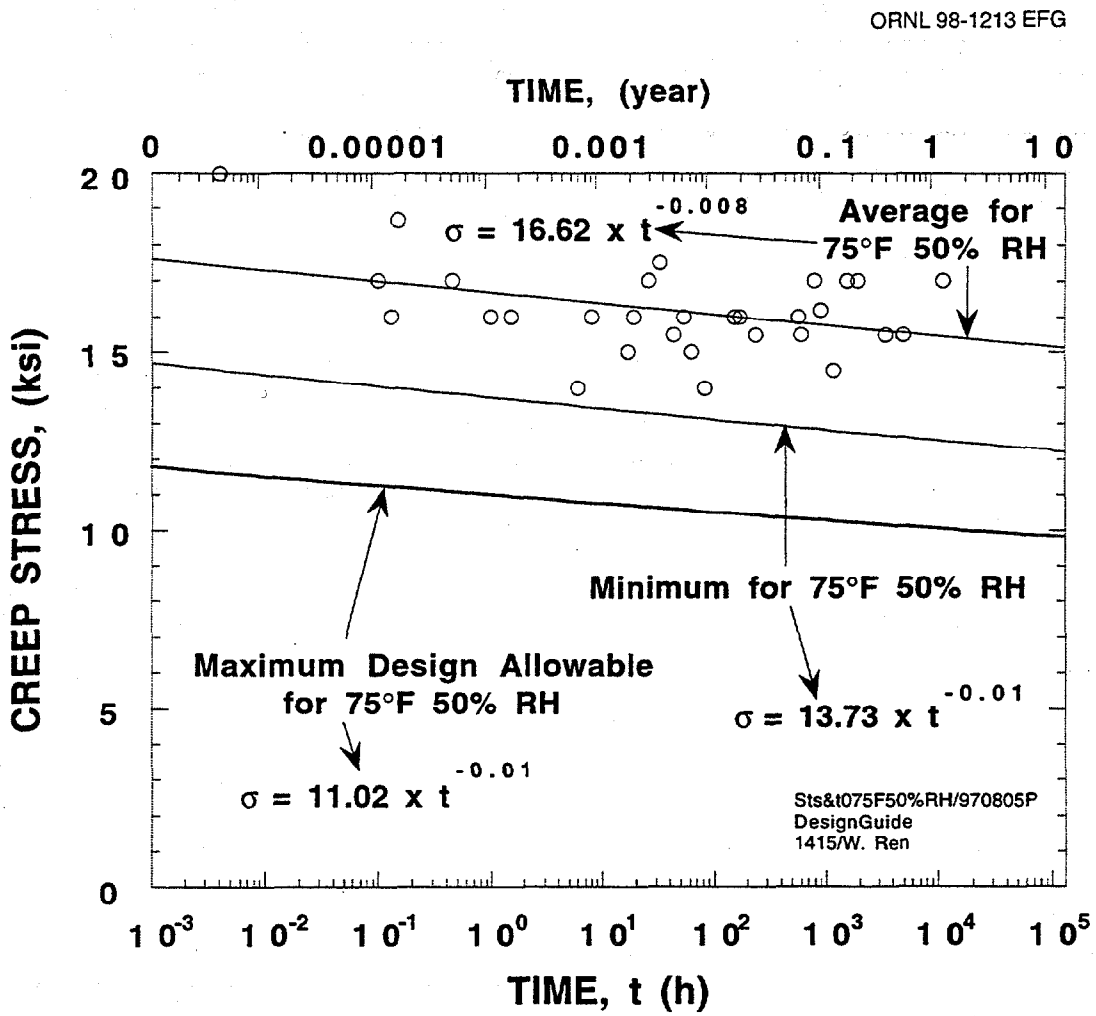

Fig. 8.1(*a*). Average, minimum creep-rupture, and maximum design-allowable curves and equations for air/50% RH at 75°F.

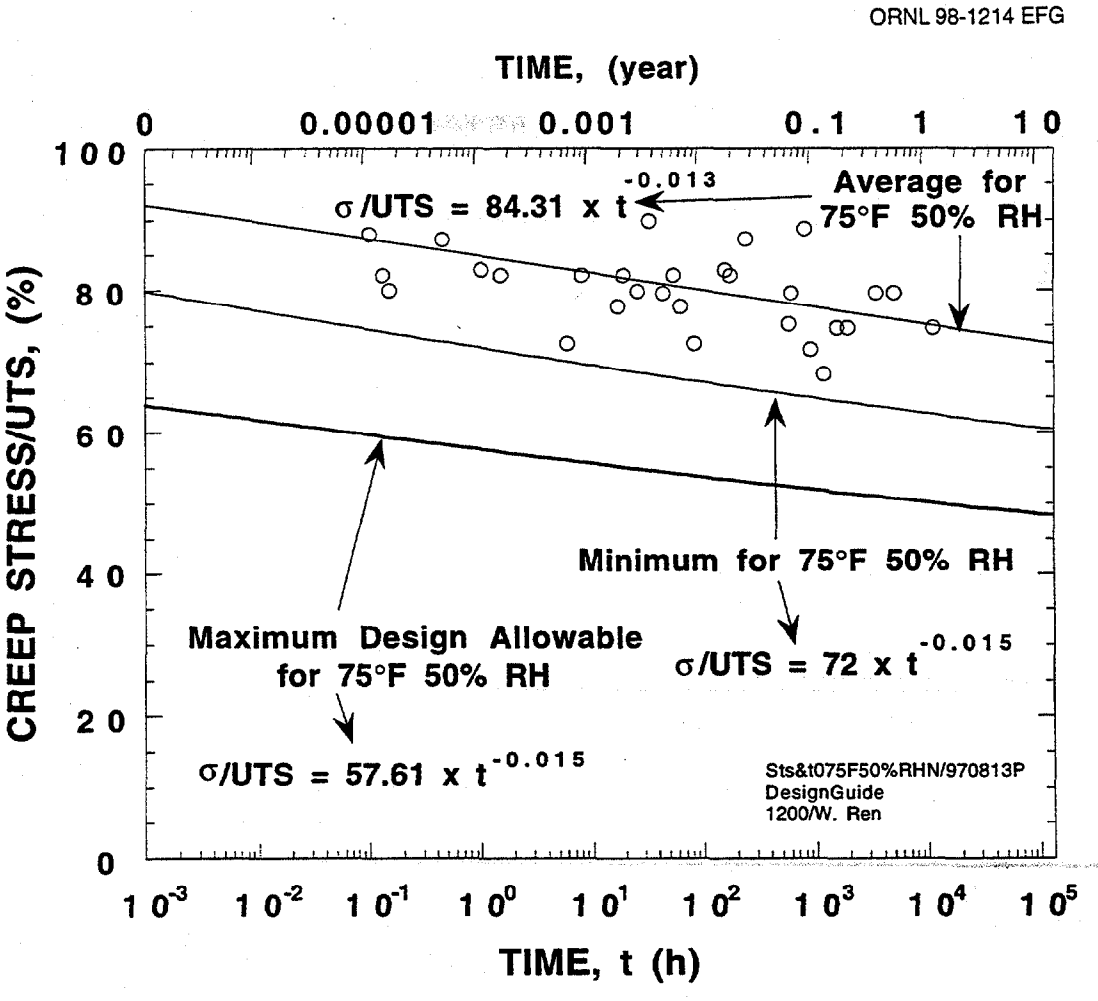

Fig. 8.1(*b*). Average, minimum creep-rupture, and maximum design-allowable curves and equations for air/50% RH at 75°F on the normalized data base.

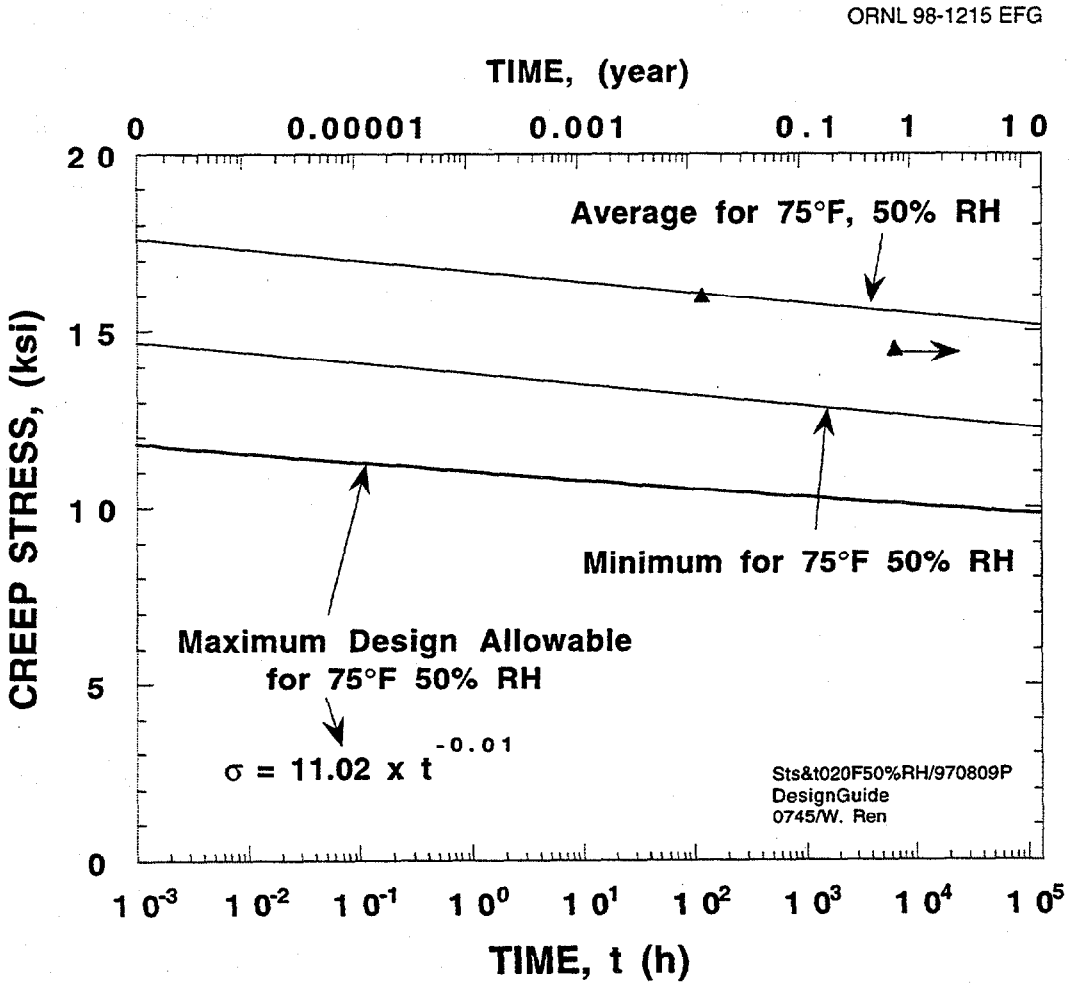

Fig. 8.2(*a*). Maximum design-allowable curve and equation for air/50% RH at 75°F are suggested for 20°F.

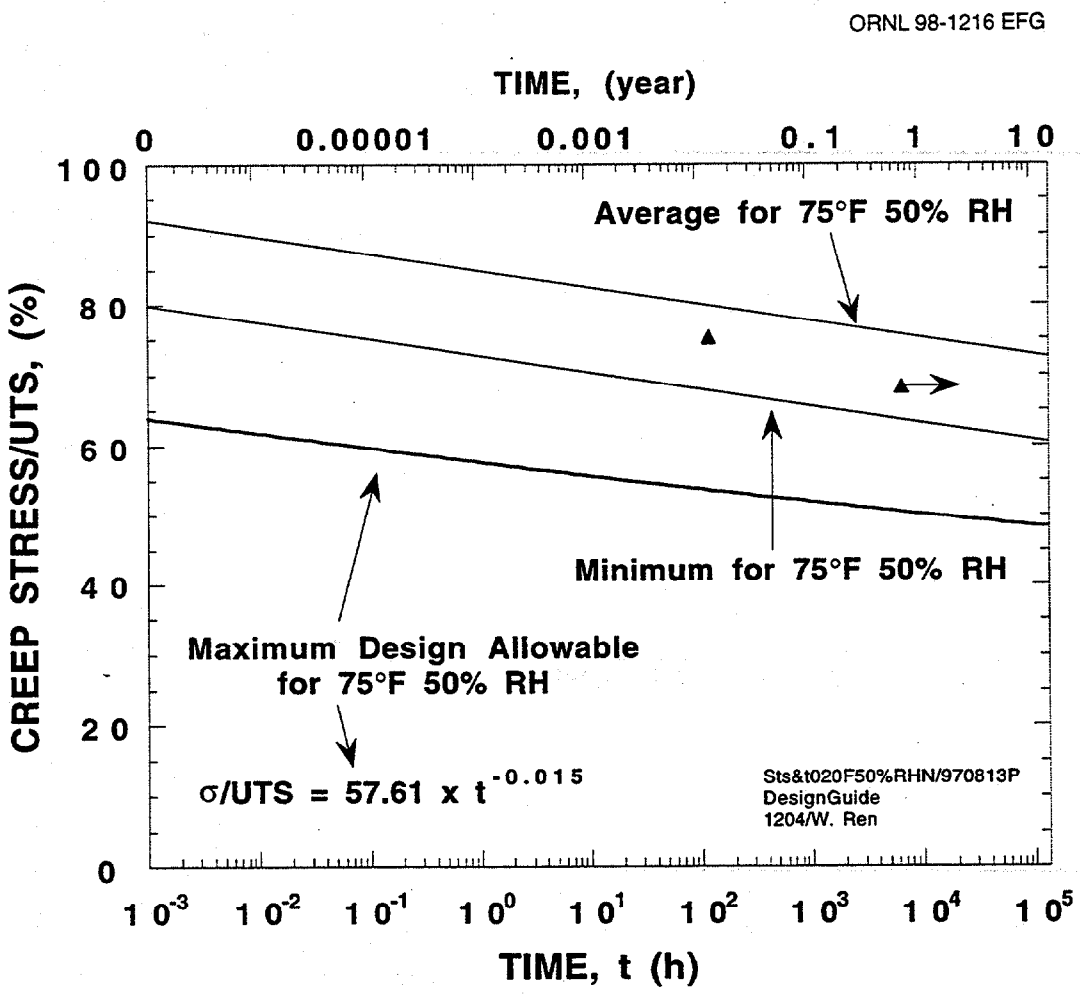

Fig. 8.2(*b*). Maximum design-allowable curve and equation for air/50% RH at 75°F are suggested for 20°F on the normalized data base.

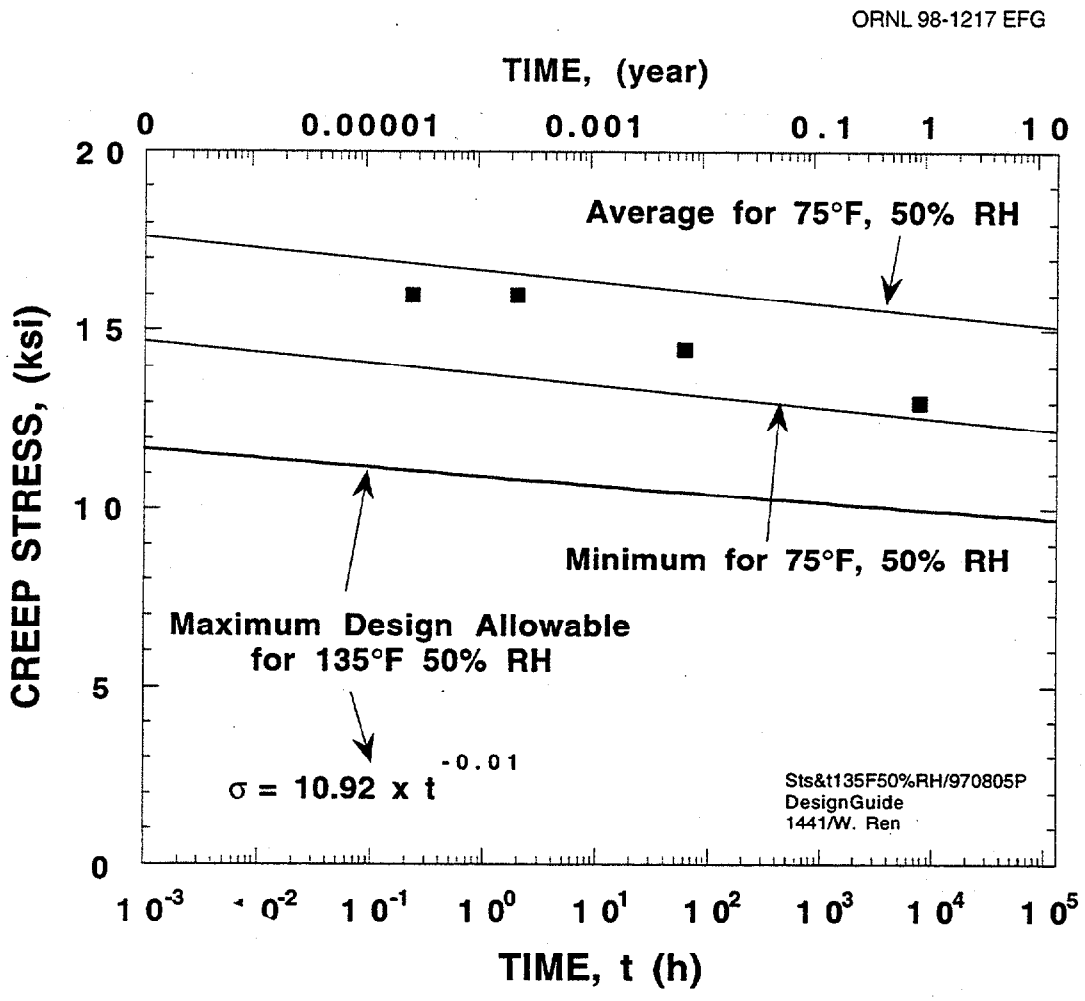

Fig. 8.3(*a*). Maximum design-allowable curve and equation for air/50% RH at 135°F.

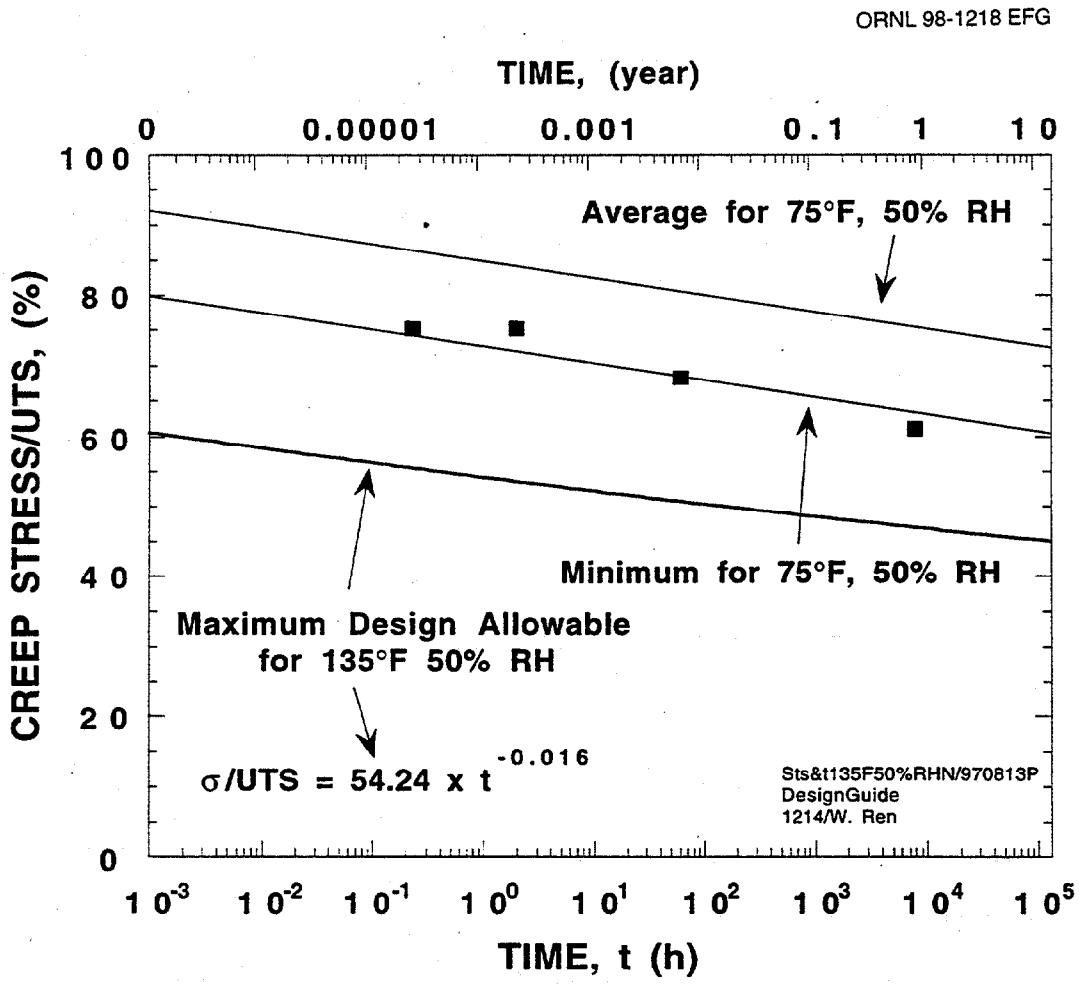

Fig. 8.3(*b*). Maximum design-allowable curve and equation for air/50% RH at 135°F on the normalized data base.

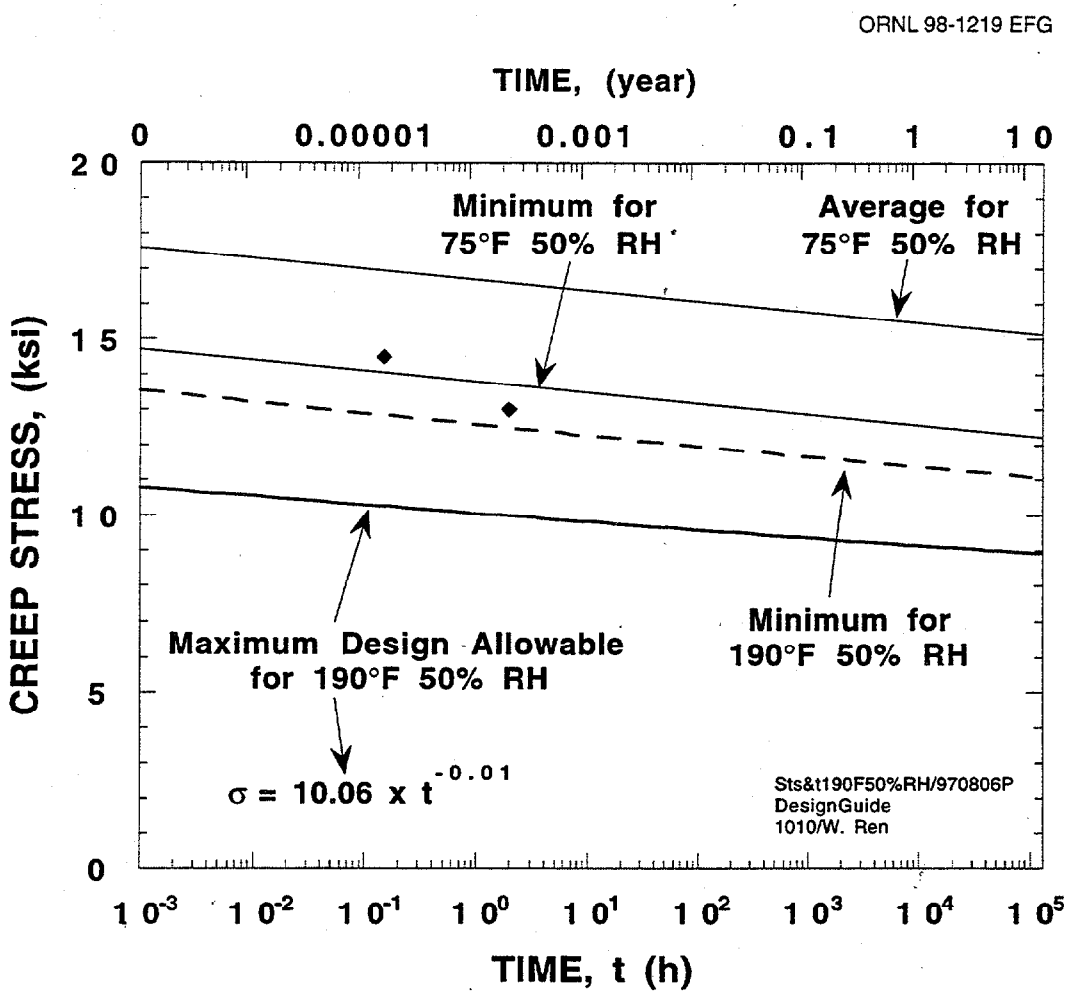

Fig. 8.4(*a*). Minimum creep-rupture and maximum design-allowable curves and equation for air/50% RH at 190°F.

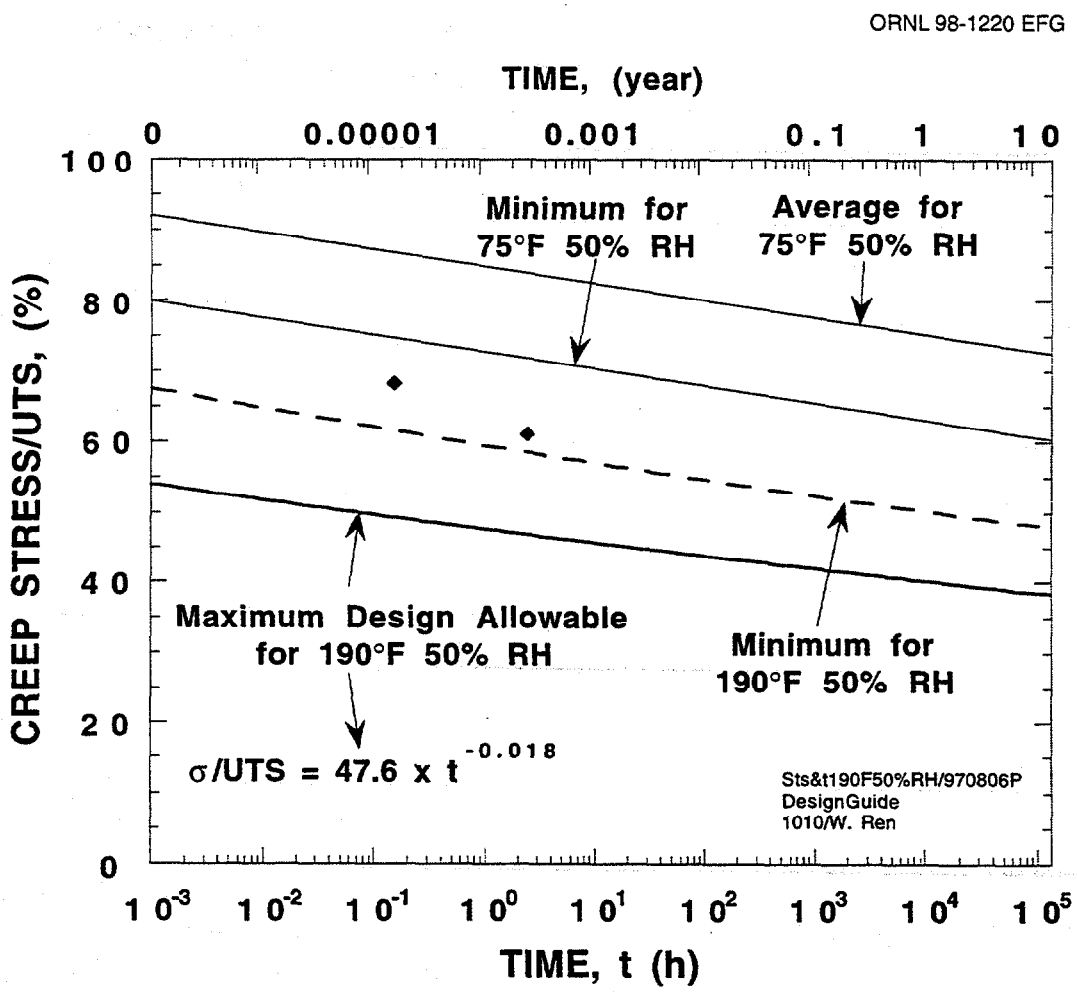

Fig. 8.4(*b*). Minimum creep-rupture and maximum design-allowable curves and equation for air/50% RH at 190°F on the normalized data base.

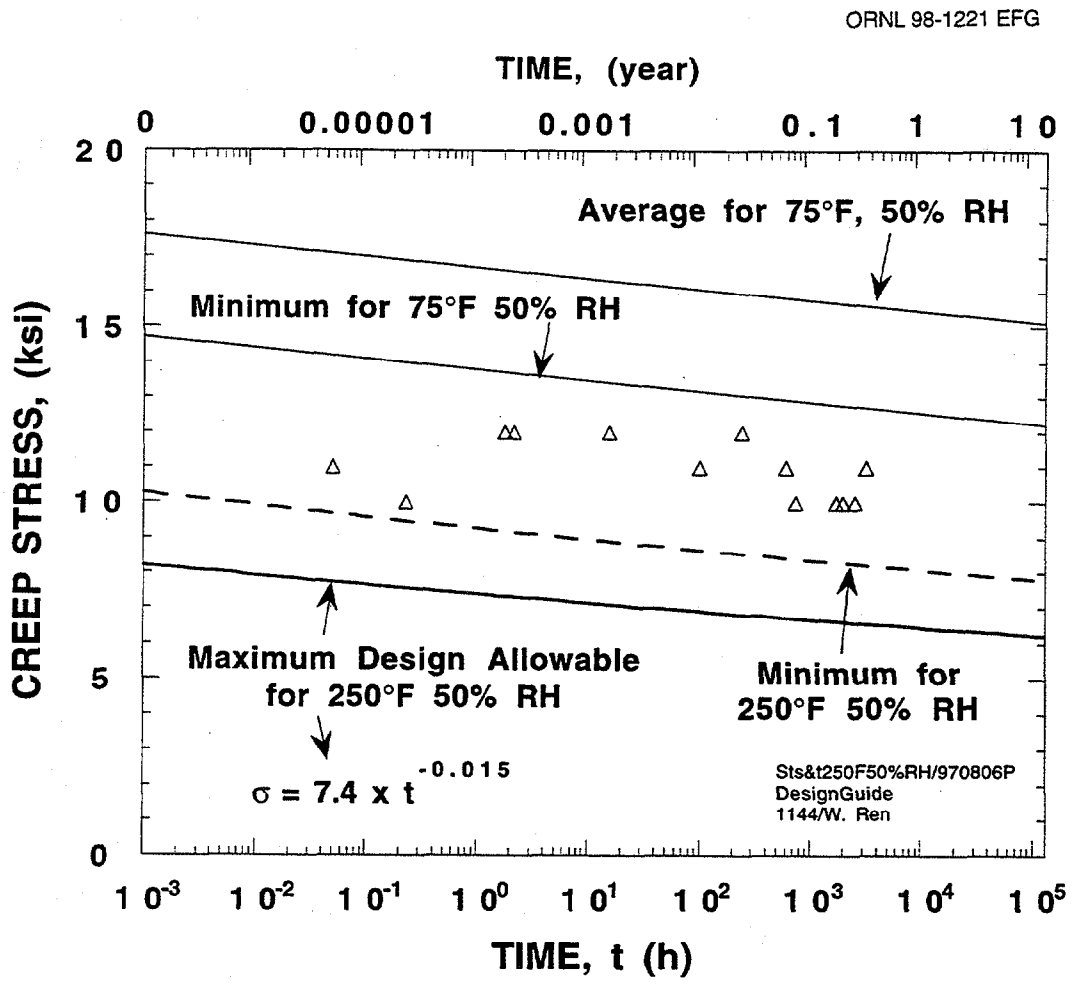

Fig. 8.5(*a*). Minimum creep-rupture and maximum design-allowable curves and equation for air/50% RH at 250°F.

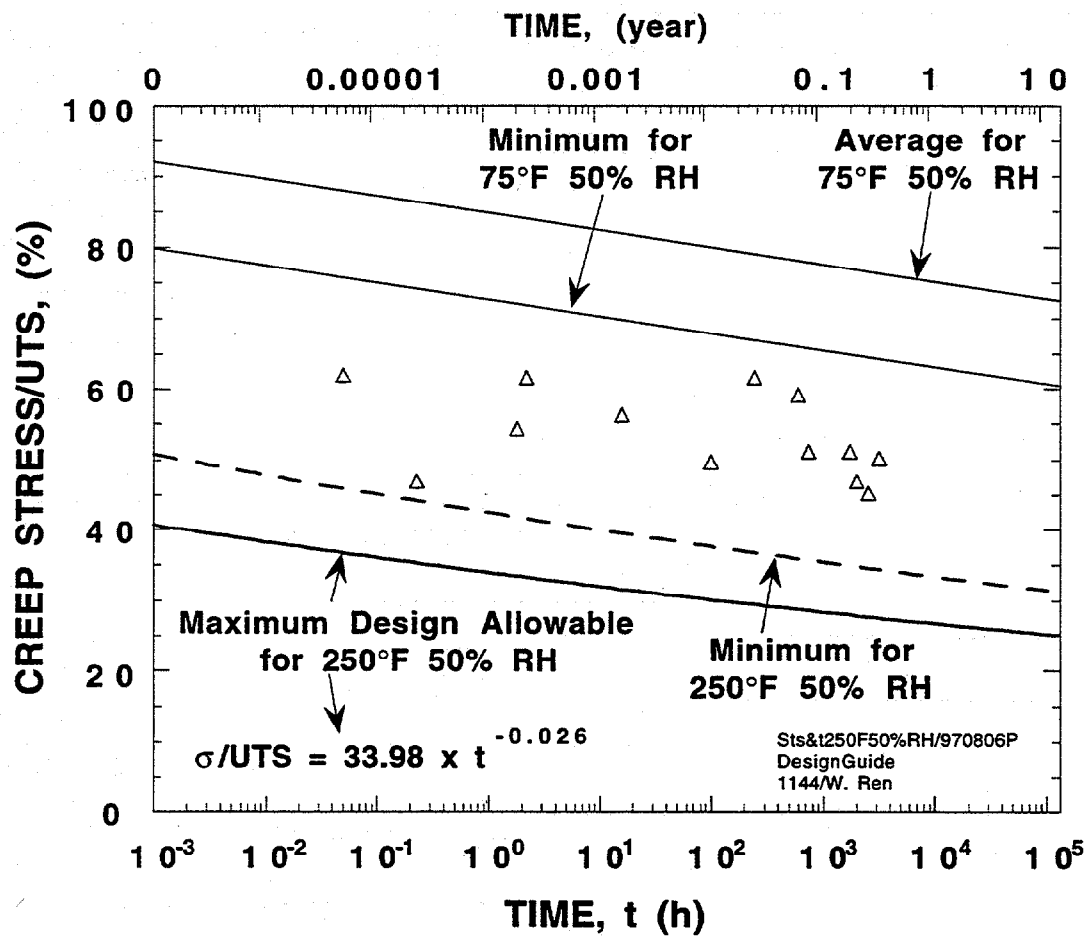

Fig. 8.5(*b*). Minimum creep-rupture and maximum design-allowable curves and equation for air/50% RH at 250°F on the normalized data base.

Table 8.1. Comparison of the R values for power law curve fitting between original and normalized data for air/50% RH

	75°F		135°F		250°F	
	Original	Normalized	Original	Normalized	Original	Normalized
R	0.42648	0.59236	0.97726	0.97726	0.35585	0.41446
B	16.622	84.312	15.826	74.442	11.235	56.049
m	–0.008081	–0.012824	–0.021329	–0.021329	–0.007497	–0.012043

8.3 TABLE OF TIME/TEMPERATURE VALUES

The maximum design-allowable stress values for different time limits at various temperatures in air/50% RH and the same results from the normalized data are given in Table 8.2. These maximum design-allowable stress values were calculated from the respective equations given in Figs. 8.1–8.5 for various times and temperatures. It can be observed from Fig. 8.2 that the material may have higher creep resistance at 20°F than 75°F. However, because of the lack of data at this temperature, the maximum design-allowable stress equation for 75°F is used for calculating the values for 20°F in Table 8.2. The values of parameters B and m used in Eq. (8.1) for the calculation are also listed.

8.4 DESIGN CURVES AND TABLE

8.4.1 In Air

The maximum design-allowable curves for air/50% RH at various temperatures have been given in Figs. 8.1–8.5. For dry and humid conditions, maximum design-allowable stress curves and equation parameters are given in air < 10% RH and air > 90% RH, respectively, in Figs. 8.6 and 8.7(*a*). In air < 10% RH condition, the material shows greater creep resistance than in the air/50% RH environment, and the minimum creep-rupture curve is above that for air/50% RH. In Fig. 8.7(*a*), the maximum design-allowable stress curve for 75°F air > 90% RH intersects at t_0 with the minimum creep-rupture curve for 75°F/50% RH. It should be pointed out that the maximum design-allowable stress curve and equation for such a case can only be used for time beyond the intersection time t_0. For times shorter than t_0, the minimum for 75°F/50% RH may be used if desired. It can be considered as if there were not enough time for the environmental effects to take place. The calculated maximum design-allowable stresses for various time limits in air < 10% RH and air > 90% RH are given in Table 8.3. The normalized results for air > 90% RH are given in Fig. 8.7(*b*). The comparison of the original and normalized data for air > 90% is given in Table 8.4. In this case, the greater R value for the original data indicates that the normalization increased the scatter slightly. Normalizing data through dividing the stress by the respective UTS does not necessarily decrease data scatter significantly for this material.

Table 8.2. Maximum design-allowable stress in air/50% RH for specific no-rupture time limits

Temperature (°F)	Maximum design-allowable stress (ksi)								Parameter	
	10 h	1000 h	3000 h	5000 h	1 year	5 years	10 years	15 years	B	m
20	10.77	10.28	10.17	10.12	10.06	9.90	9.83	9.79	11.02	–0.010
75	10.77	10.28	10.17	10.12	10.06	9.90	9.83	9.79	11.02	–0.010
135	10.67	10.19	10.08	10.03	9.97	9.81	9.75	9.71	10.92	–0.010
190	9.83	9.39	9.29	9.24					10.06	–0.010
250	7.15	6.67	6.56	6.51					7.4	–0.015
Temperature (°F)	**Normalized maximum design-allowable stress (%)**								**Parameter**	
	10 h	1000 h	3000 h	5000 h	1 year	5 years	10 years	15 years	B	m
20	55.65	51.94	51.09	50.70	50.28	49.08	48.57	48.27	57.61	–0.015
75	55.65	51.94	51.09	50.70	50.28	49.08	48.57	48.27	57.61	–0.015
135	52.28	48.56	47.72	47.33	46.91	45.71	45.21	44.92	54.24	–0.016
190	45.67	42.03	41.21	40.83					47.60	–0.018
250	32.01	28.39	27.59	27.23					33.98	–0.026

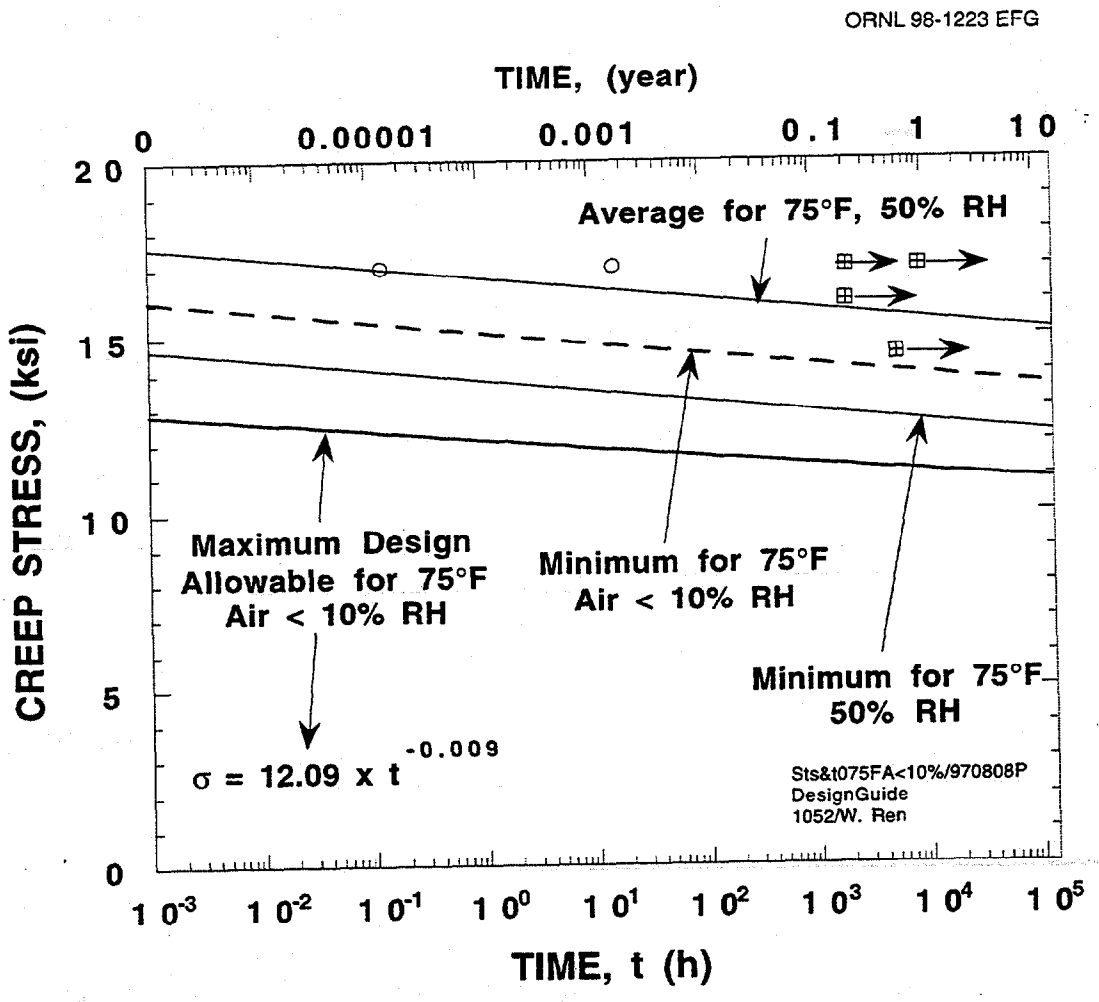

Fig. 8.6. Minimum creep-rupture and maximum design-allowable curves and equation for air < 10% RH at 75°F.

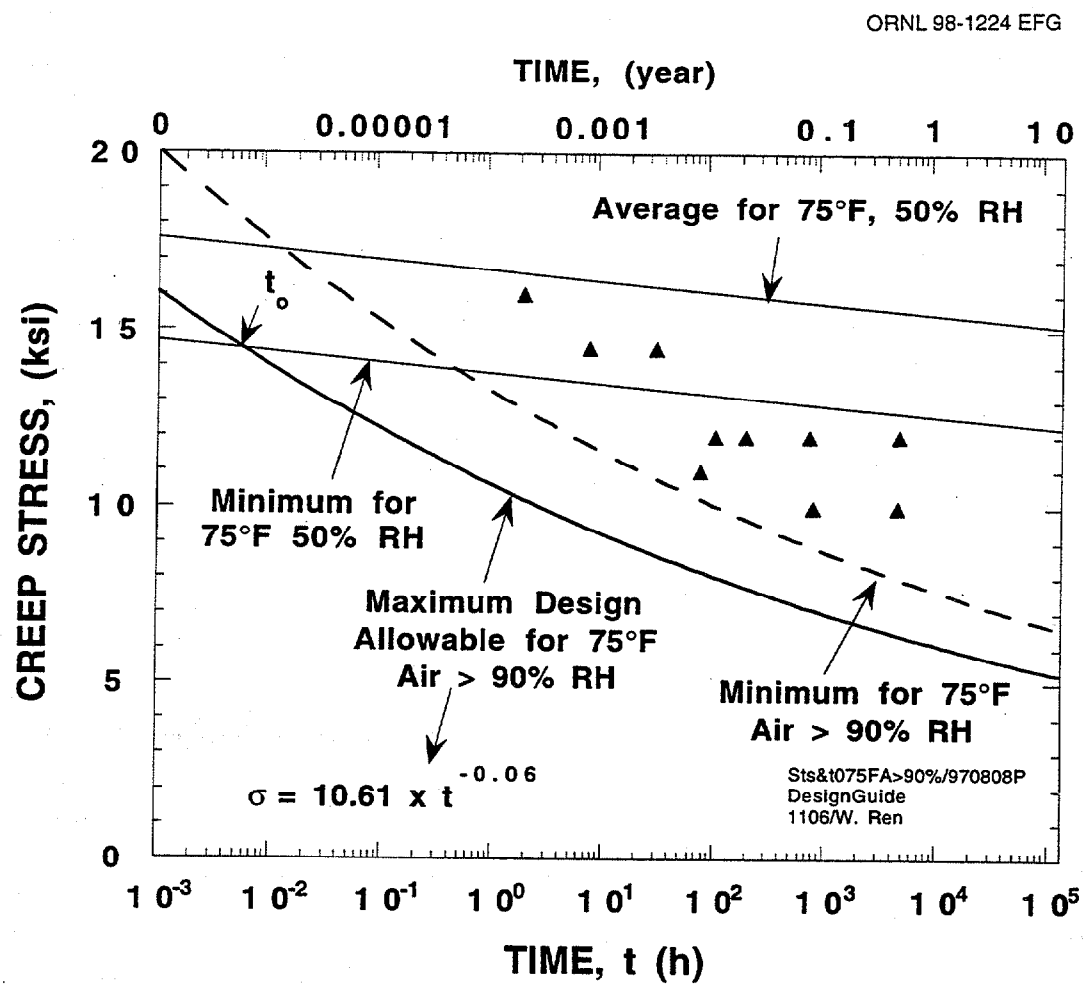

Fig. 8.7(*a*). Minimum creep-rupture and maximum design-allowable curves and equation for air > 90% RH at 75°F.

Table 8.3. Maximum design-allowable stress (ksi) in air < 10% RH and air > 90% RH for specific no-rupture time limits

Air RH	Maximum design-allowable stress (ksi)								Parameter	
%	10 h	1000 h	3000 h	5000 h	1 year	5 years	10 years	15 years	B	m
<10	11.84	11.36	11.25	11.20	11.14	10.98	10.91	10.87	12.09	–0.009
>90	9.24	7.01	6.56	6.36	6.15	5.59	5.36	5.23	10.61	–0.060

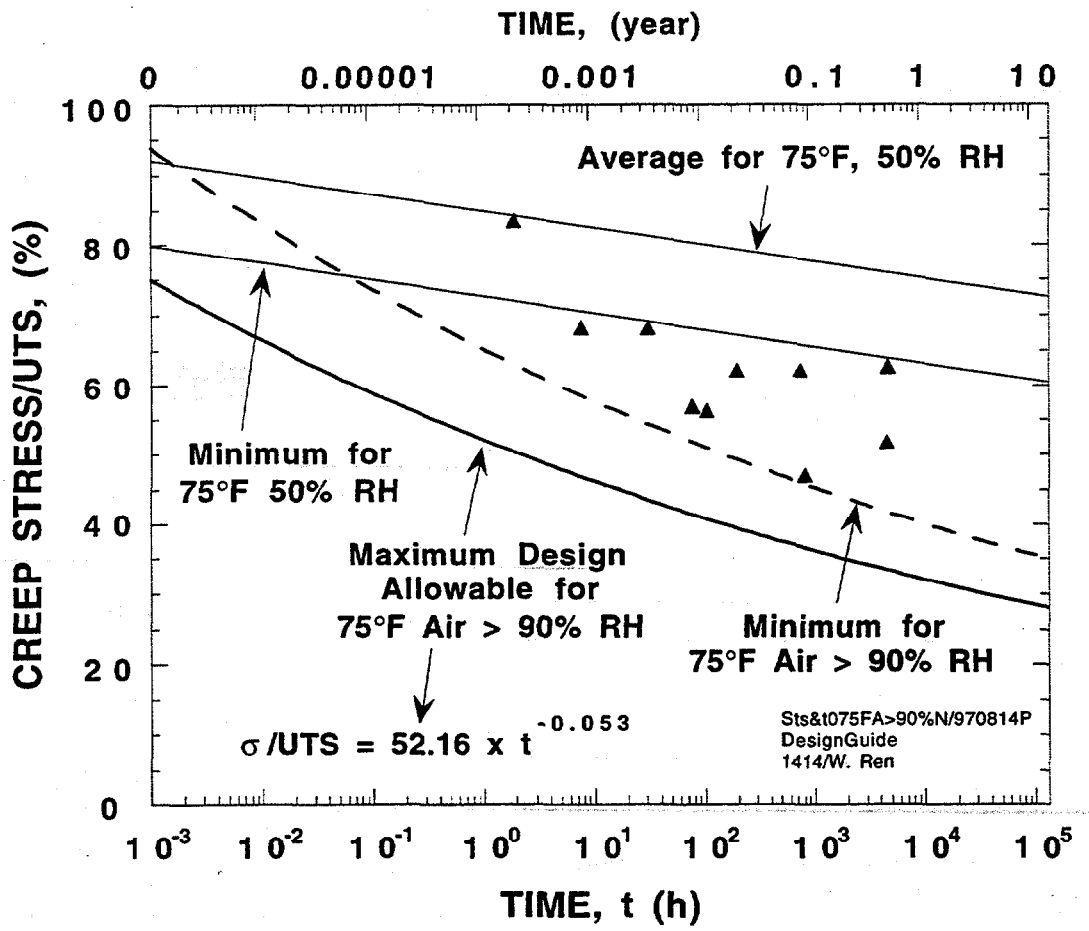

Fig. 8.7(*b*). Minimum creep-rupture and maximum design-allowable curves and equation for air > 90% RH at 75°F on the normalized data base.

Table 8.4. Comparison of the R values for power law curve fitting between original and normalized data for air > 90% RH at 75°F

Parameter	Original	Normalized
R	0.84756	0.76193
B	15.776	76.641
m	–0.04992	–0.04452

8.4.2 In Distilled Water

The maximum design-allowable stress curves and equations for distilled water at temperatures of 75, 135, and 190°F are presented in Figs. 8.8–8.10. The respective parameters for the maximum design-allowable stress equation and the calculated results are presented in Table 8.5. Note that the maximum design-allowable stresses for 75 and 135°F are very close to each other. This does not suggest that increasing temperature from 75 to 135°F has little effect on the creep behavior in water. As a matter of fact,

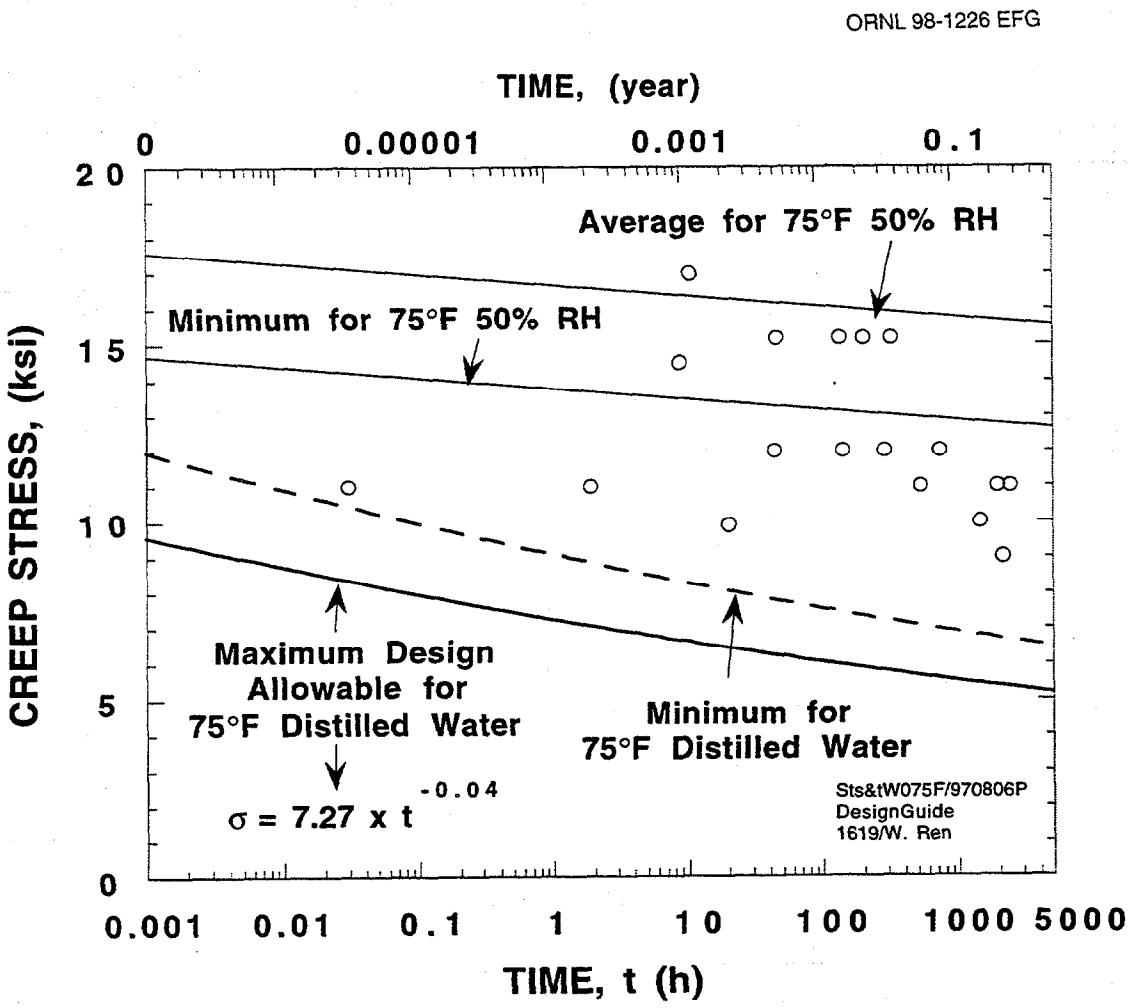

Fig. 8.8. Minimum creep-rupture and maximum design-allowable curves and equation for distilled water at 75°F.

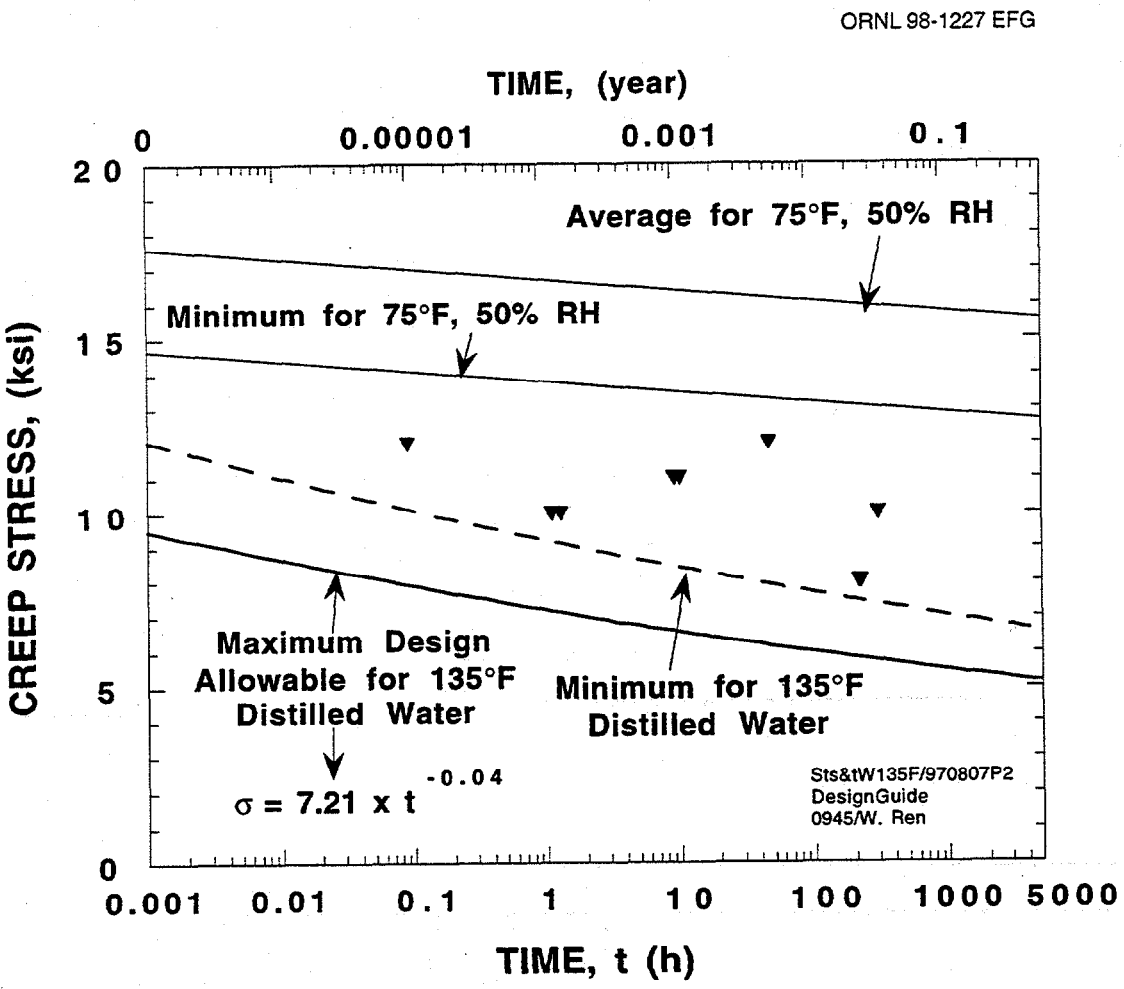

Fig. 8.9. Minimum creep-rupture and maximum design-allowable curves and equation for distilled water at 135°F.

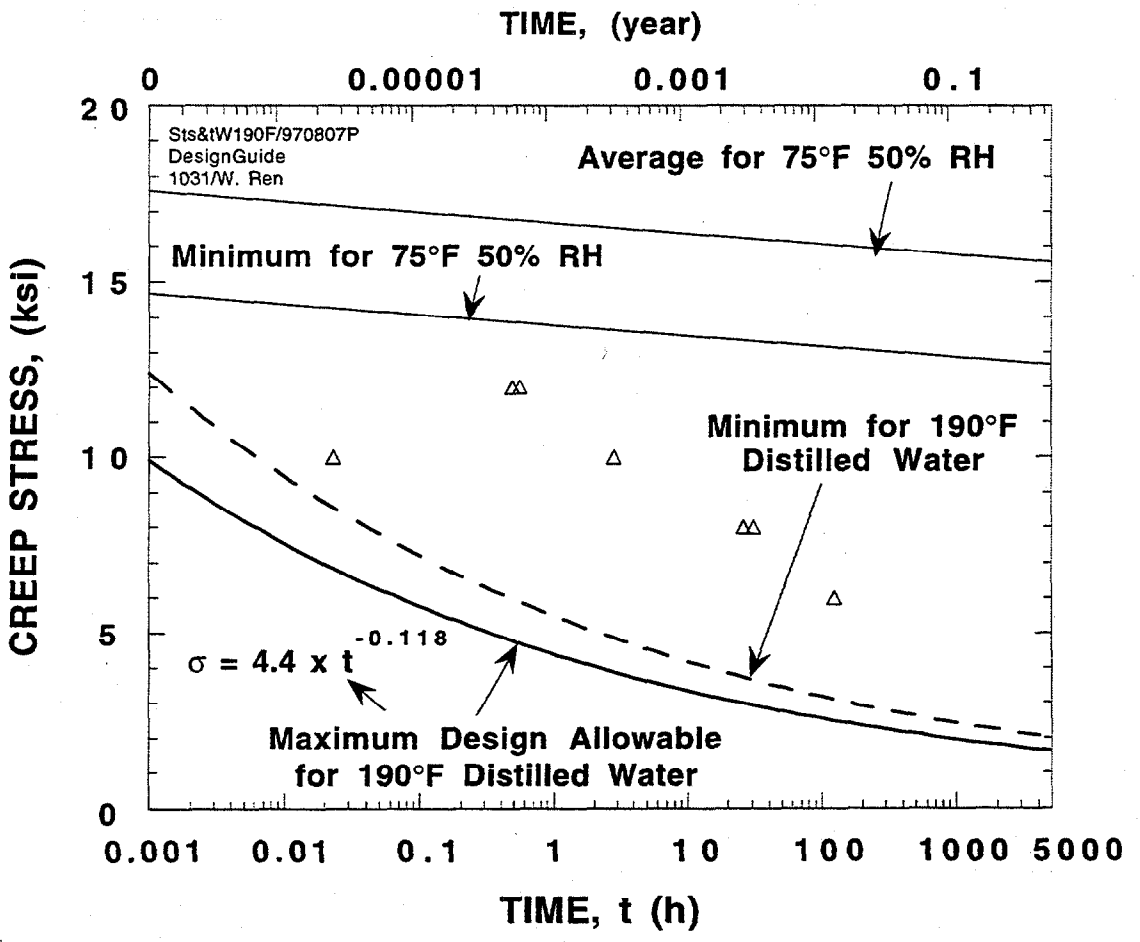

Fig. 8.10. Minimum creep-rupture and maximum design-allowable curves and equation for distilled water at 190°F.

Table 8.5. Maximum design-allowable stress in distilled water for specific no-rupture time limits

Temperature (°F)	Maximum design-allowable stress (ksi)				Parameter	
	10 h	1000 h	3000 h	5000 h	B	m
75	6.63	5.51	5.28	5.17	7.27	–0.040
135	6.58	5.47	5.23	5.13	7.21	–0.040
190	3.35	1.95	1.71	1.61	4.4	–0.118

the data employed for the derivation of the maximum design-allowable stress curve for 75°F included results from the specimens weakened by a 1080-h presoak at 180°F. Including these weakened material data may cause a somewhat conservative estimation for 75°F.

8.4.3 Superimposed Motor Vibration and Low-Frequency Impulse Load Cycling on Creep-Rupture Strength

Figures 8.11–8.13 present the maximum design-allowable stress curves and equations for motor vibration in air/50% RH and for low-frequency load cycling (a simulation of possible roadway conditions) in air/50% RH and distilled water. The motor vibration tests were conducted using a motor with an eccentric load to supply the vibratory component.[2] The vibratory component had a frequency of about 2000 cycles/min and a strain range of about 200 μin. The low-frequency load cycling tests were performed with a constant load and an air-driven piston applying an additional pulsating load.[2] The force of the piston could be varied by the applied air pressure, and the frequency was 30 cycles/min. The stress given for low-frequency load cycling is the total stress (i.e., static plus the additional pulsating stress). The minimum-to-maximum stress ratio ($\sigma_{min}/\sigma_{max}$) was 0.4–0.5 in air/50% RH and 0.3–0.5 in water. The respective parameters for the maximum design-allowable stress equation and the calculated results are presented in Table 8.6. Note that for an air environment, load cycling produced the lower stress allowables. For load cycling conditions, the curve and equation parameters only apply to time beyond t_0, the intersection with air/50% RH minimum.

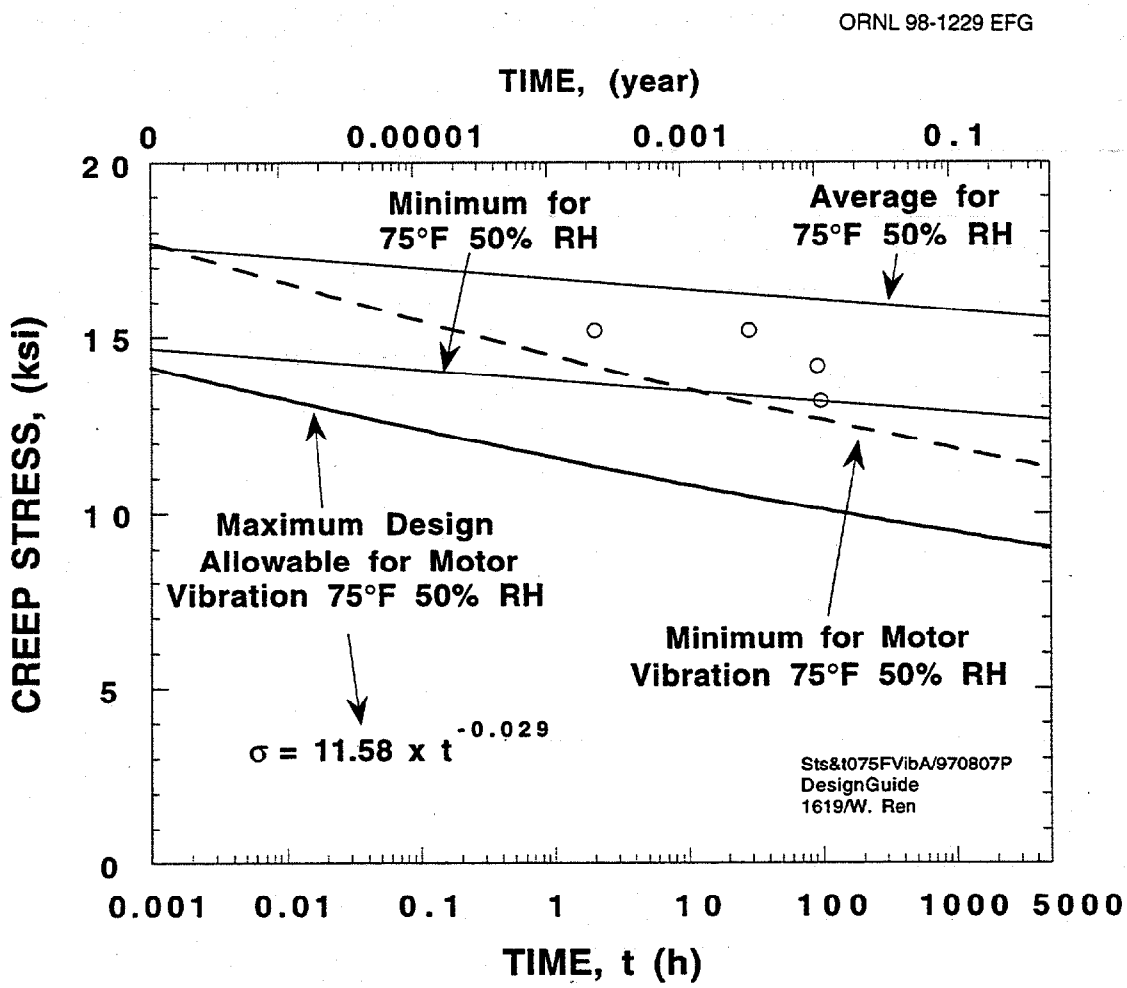

Fig. 8.11. Minimum creep-rupture and maximum design-allowable curves and equation for motor vibration in air/50% RH at 75°F.

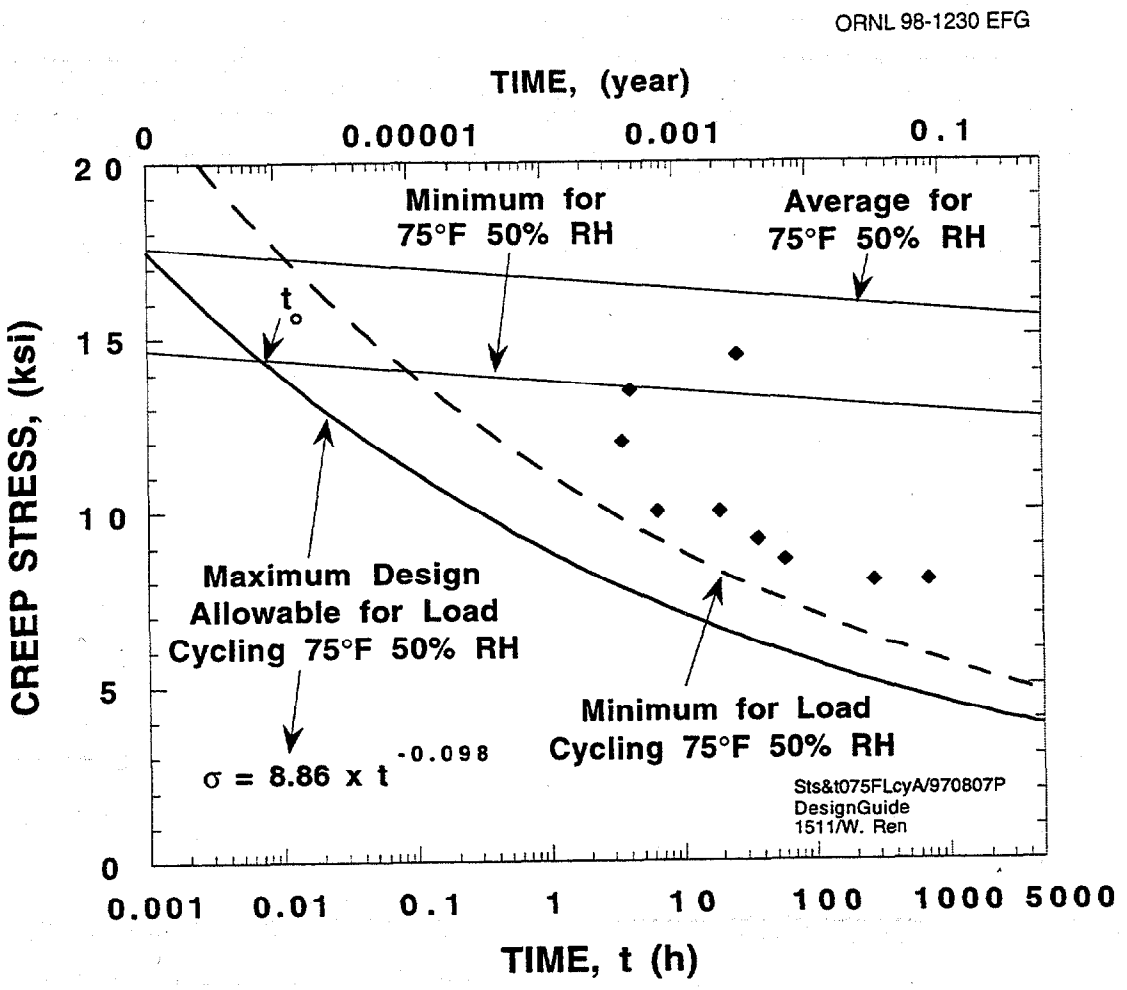

Fig. 8.12. Minimum creep-rupture and maximum design-allowable curves and equation for low-frequency load cycling in air/50% RH at 75°F. The minimum to maximum stress ratio ($\sigma_{min}/\sigma_{max}$) was 0.4–0.5, and the frequency was 30 cycles per minute.

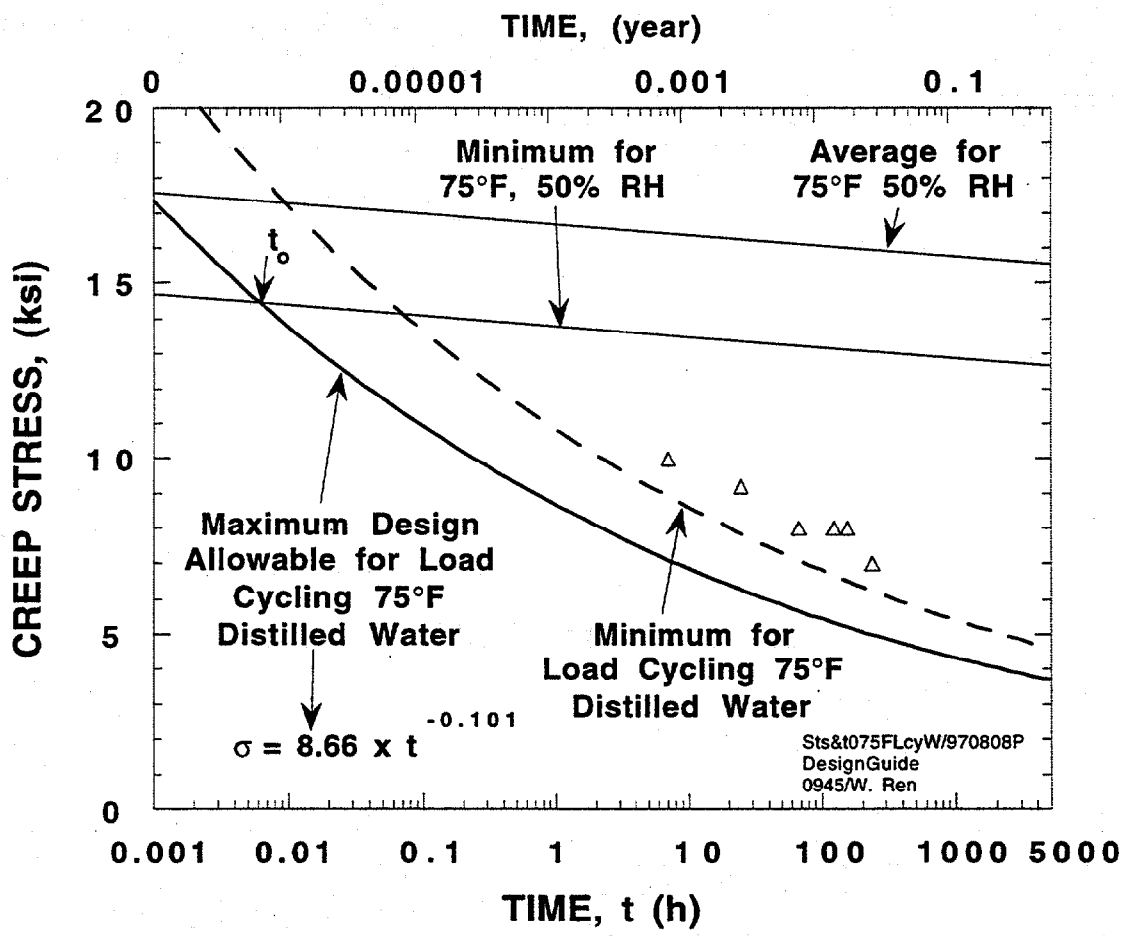

Fig. 8.13. Minimum creep-rupture and maximum design-allowable curves and equation for low-frequency load cycling in distilled water at 75°F. The minimum to maximum stress ratio ($\sigma_{min}/\sigma_{max}$) was 0.3–0.5, and the frequency was 30 cycles per minute.

Table 8.6. Maximum design-allowable stress under motor vibration and low-frequency load cycling for specific no-rupture time limits

Condition	Maximum design-allowable stress (ksi)				Parameter	
	10 h	1000 h	3000 h	5000 h	B	m
Motor vibration	10.83	9.48	9.18	9.05	11.58	–0.029
Load cycling in air	7.07	4.50	4.04	3.85	8.86	–0.098
Load cycling in water	6.86	4.31	3.86	3.66	8.66	–0.101

8.4.4 In Water-Based Fluids

Data for the three water-based fluids—saltwater (saturated solution at room temperature), windshield washing fluid (Krystal Kleer Windshield Washer Solvent, South Win, Ltd., P.O. Box 20461, Greenesboro, NC 27420), and coolant (50% by volume water and 50% Ethylene Glycol Base Anti Freeze-Texaco, Anti-Freeze Coolant, Texaco Lubricants Co., Houston, TX 77052)—are presented in Figs. 8.14 and 8.15. It is obvious from the limited exposure data for these three fluids that saltwater, windshield washing fluid, and coolant have effects on the creep-rupture strength similar to distilled water. Because these three fluids are water based and the data are limited, it is reasonable and practical to assume that the maximum design-allowable stress curve and equation for distilled water at 75°F can be used for these three fluids.

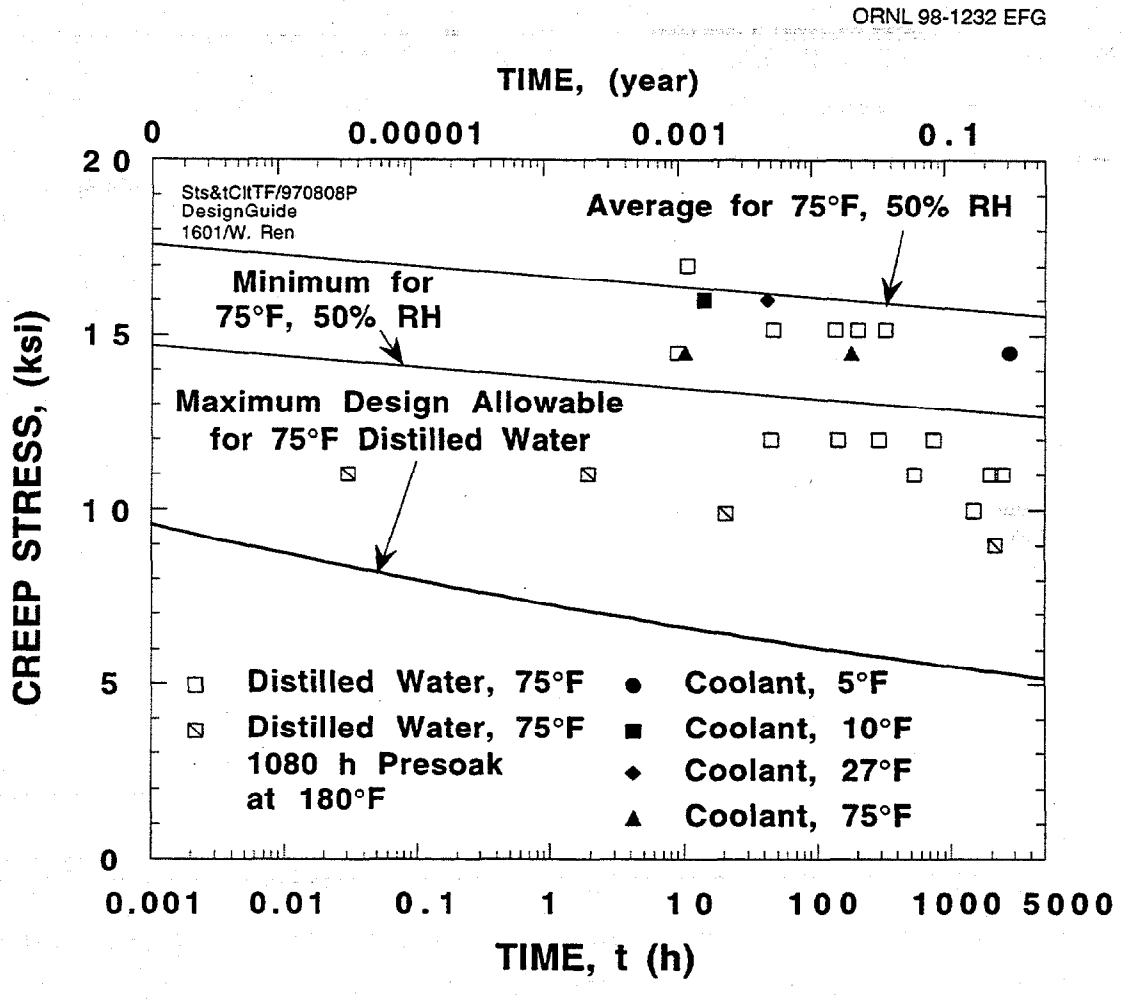

Fig. 8.14. Maximum design-allowable creep-rupture curve and equation for coolant at various temperatures indicated are assumed to be equivalent to that for distilled water at 75°F.

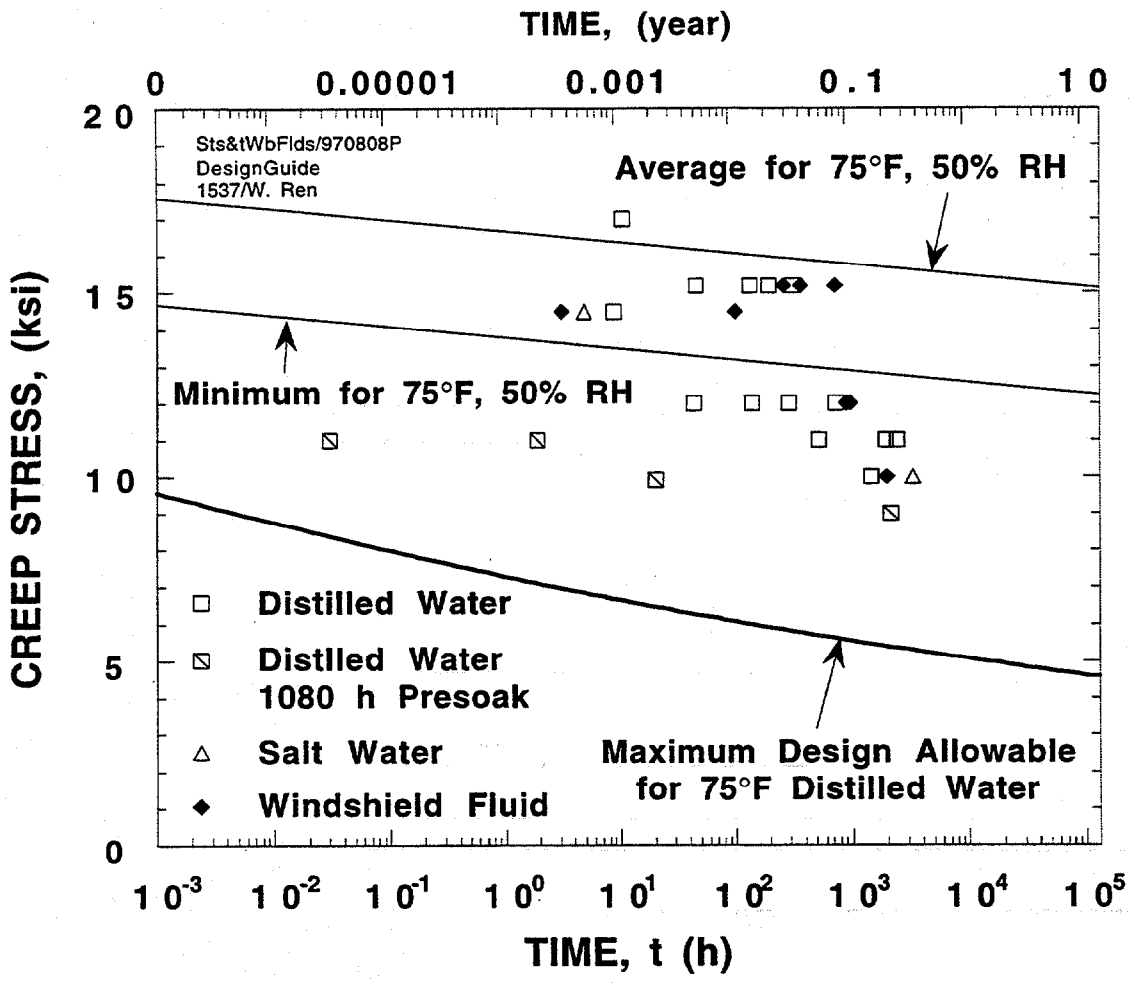

Fig. 8.15. Maximum design-allowable creep-rupture curve and equation for two water-based fluids (i.e., saltwater and windshield washing fluid) are assumed to be equivalent to that for distilled water at 75°F.

8.4.5 In Oil-Based Fluids

Results for the two oil-based fluids, used motor oil and brake fluid (Brake Fluid, Western Auto Super Heavy Duty Stop Rite, Brake Fluid for Drum or Disc Brakes, Western Auto Supply Company, Kansas City, Missouri 64108), are given in Figs. 8.16 and 8.17. Because the data are limited and the brake fluid seems to have greater effects on the creep-rupture behavior of the material than used motor oil, the maximum design-allowable stress curve and equation for brake fluid are suggested to be used for both oil-based fluids at 75°F. The respective parameters for the maximum design-allowable stress equation and the calculated results are presented in Table 8.7.

8.4.6 In Sulfuric Acid Environment

Figure 8.18 presents the maximum design-allowable stress curve and equation parameters for sulfuric acid (35 wt %) and sulfuric acid spot conditions. The spot tests were done to simulate acid splatters. About 3 cm^3 of acid solution was placed on the surface of a virgin specimen. The specimen was then heated for

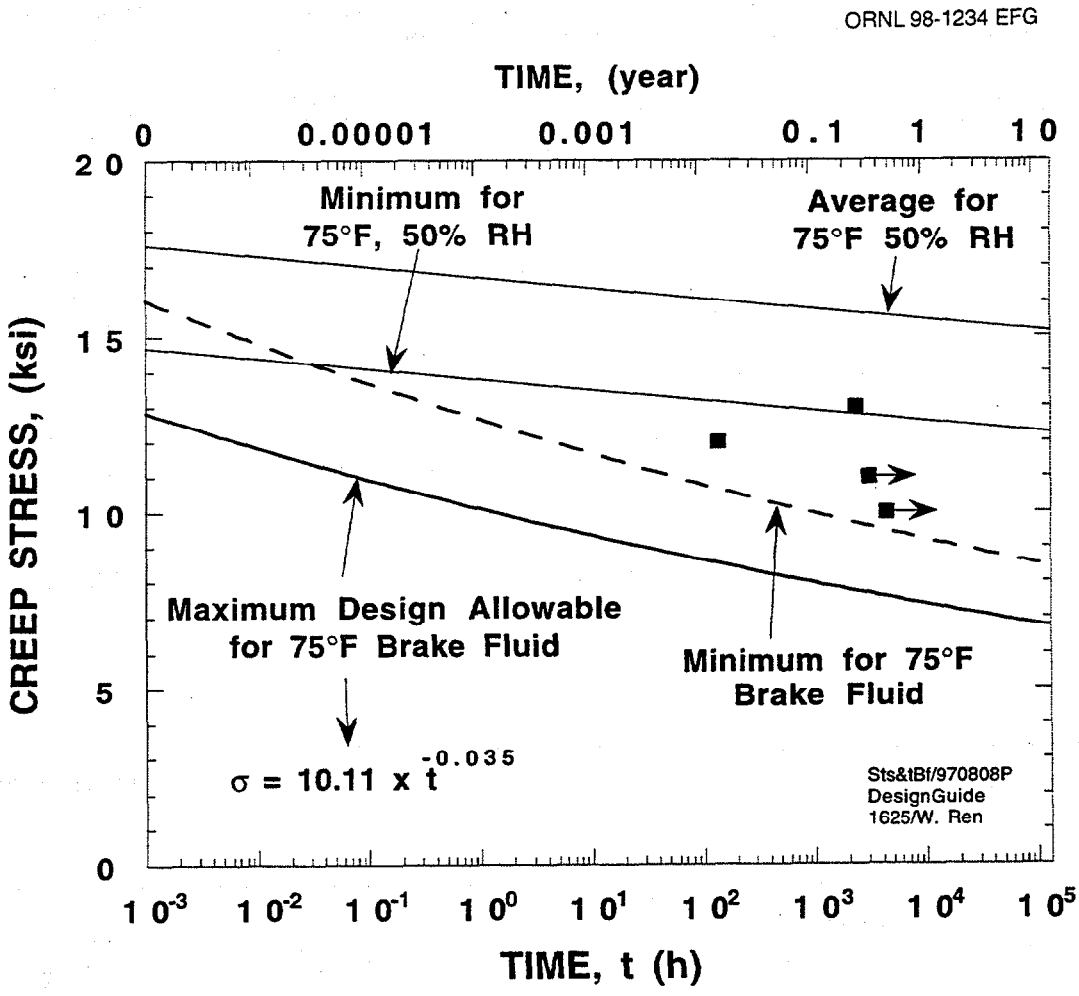

Fig. 8.16. Creep-rupture minimum and maximum design-allowable curves and equation for brake fluid at 75°F.

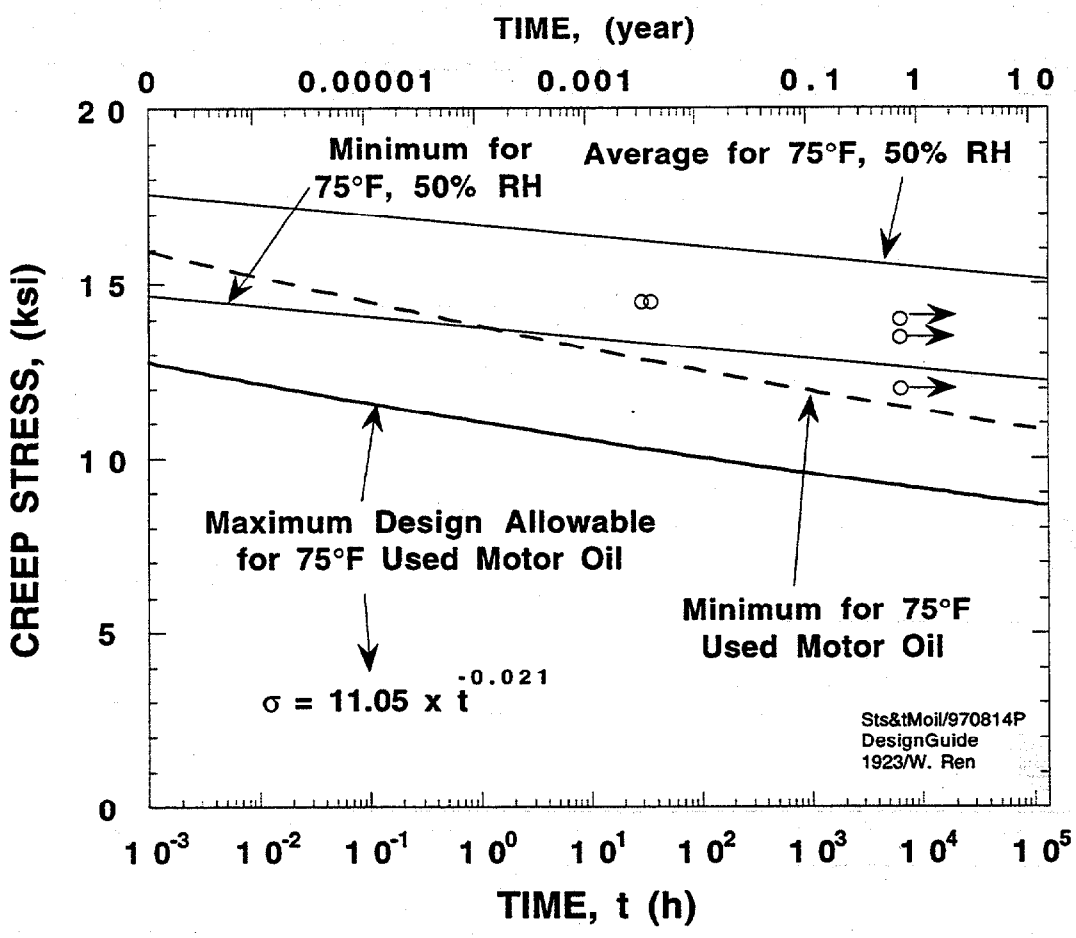

Fig. 8.17. Creep-rupture minimum and maximum design-allowable curves and equation for used motor oil at 75°F.

Table 8.7. Maximum design-allowable stress in oil-based fluids for specific no-rupture time limits

Oil type	Maximum design-allowable stress (ksi)								Parameter	
	10 h	1000 h	3000 h	5000 h	1 year	5 years	10 years	15 years	B	m
Brake	9.33	7.94	7.64	7.50	7.36	6.96	6.79	6.69	10.11	–0.035
Motor	10.53	9.56	9.34	9.24	9.13	8.83	8.70	8.63	11.05	–0.021

24 h at 150°F so that absorption occurred.[2] The sample was then creep tested in air/50% RH. The limited data suggest that the sulfuric acid exposure is more deleterious than acid splatters. Therefore, the maximum design-allowable stress curve and equation parameters for sulfuric acid are proposed for both conditions. The respective parameters for the maximum design-allowable stress equation and the calculated results are presented in Table 8.8.

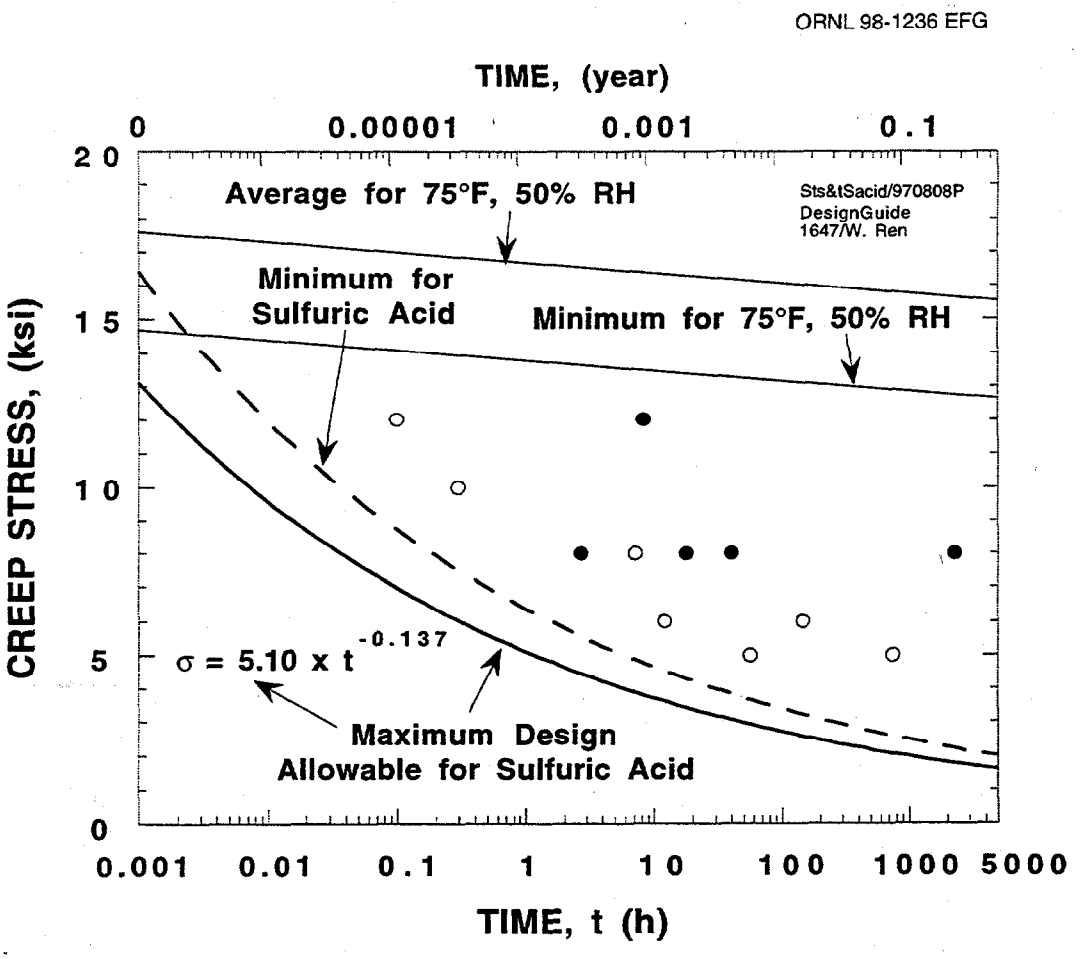

Fig. 8.18. Minimum creep-rupture and maximum design-allowable curves and equation for sulfuric acid environments at 75°F.

Table 8.8. Maximum design-allowable stress in sulfuric acid and sulfuric acid spot conditions for specific no-rupture time limits

	Maximum design-allowable stress (ksi)				Parameter	
Condition	10 h	1000 h	3000 h	5000 h	B	m
Immerse	3.72	1.98	1.70	1.59	5.10	–0.137
Splatter	3.72	1.98	1.70	1.59	5.10	–0.137

8.5 ENVIRONMENTAL KNOCK-DOWN FACTORS

Two methods were employed to derive the environmental knock-down factors to facilitate a direct comparison with the maximum design-allowable stress for air/50% RH at 75°F. The first method was to divide the maximum design-allowable stresses for a specific environment at various time limits as found in Tables 8.1–8.5 by the maximum design-allowable stress for air/50% RH at 131,400 h (15 years). These factors are given in Tables 8.9–8.14. The second method was to divide the maximum design-allowable stresses for a specific environment at various time limits by those for air/50% RH at the respective time limits. These factors are presented in Table 8.15. This table was used to develop the rules of Part 1.

Table 8.9. Stress reduction factor in air/50% RH for specific no-rupture time limits

Temperature (°F)	Stress reduction factor							
	10 h	1000 h	3000 h	5000 h	1 year	5 years	10 years	15 years
20	1.10	1.05	1.04	1.03	1.03	1.01	1.00	1.00
75	1.10	1.05	1.04	1.03	1.03	1.01	1.00	1.00
135	1.09	1.04	1.03	1.02	1.02	1.00	1.00	0.99
190	1.00	0.96	0.95	0.94				
250	0.73	0.68	0.67	0.67				

Table 8.10. Stress reduction factor in air < 10% RH and air > 90% RH for specific no-rupture time limits

Air RH (%)	Stress reduction factor							
	10 h	1000 h	3000 h	5000 h	1 year	5 years	10 years	15 years
<10	1.21	1.16	1.15	1.14	1.14	1.12	1.11	1.11
>90	0.94	0.72	0.67	0.65	0.63	0.57	0.55	0.53

Table 8.11. Stress reduction factor in distilled water for specific no-rupture time limits

Temperature (°F)	Stress reduction factor			
	10 h	1000 h	3000 h	5000 h
75	0.68	0.56	0.54	0.53
135	0.67	0.56	0.53	0.52
190	0.34	0.20	0.17	0.16

Table 8.12. Stress reduction factor under motor vibration in air/50% RH and low-frequency load cycling in air/50% RH and distilled water for specific no-rupture time limits

	Stress reduction factor			
Condition	10 h	1000 h	3000 h	5000 h
Motor vibration	1.11	0.97	0.94	0.92
Load cycling in air	0.72	0.46	0.41	0.39
Load cycling in water	0.70	0.44	0.39	0.37

Table 8.13. Stress reduction factor in oil-based fluids for specific no-rupture time limits

	Stress reduction factor							
Oil type	10 h	1000 h	3000 h	5000 h	1 year	5 years	10 years	15 years
Brake	0.95	0.81	0.78	0.77	0.75	0.71	0.69	0.68
Motor	1.08	0.98	0.95	0.94	0.93	0.90	0.89	0.88

Table 8.14. Stress reduction factor under sulfuric acid conditions for specific no-rupture time limits

	Stress reduction factor			
Condition	10 h	1000 h	3000 h	5000 h
Immerse	0.38	0.20	0.17	0.16
Splatter	0.38	0.20	0.17	0.16

Table 8.15. Stress reduction factor under various conditions for specific no-rupture time limits. The factors are based on the maximum stress allowable curve for 75°F air/50% RH

	Stress reduction factor								Range	
Conditions[a]	10 h	1000 h	3000 h	5000 h	1 year	5 years	10 years	15 years	Minimum	Maximum
75°F air/50% RH	1.00	1.00	1.00	1.00	1.00	1.00	1.00	1.00	1.00	1.00
20°F air/50% RH	1.00	1.00	1.00	1.00	1.00	1.00	1.00	1.00	1.00	1.00
135°F air/50% RH	0.99	0.99	0.99	0.99	0.99	0.99	0.99	0.99	0.99	0.99
190°F air/50% RH	0.91	0.91	0.91	0.91					0.91	0.91
250°F air/50% RH	0.66	0.65	0.65	0.64					0.64	0.66
75°F/air < 10%	1.11	1.11	1.11	1.11	1.11	1.11	1.11	1.11	1.11	1.11
75°F/air > 90%	0.86	0.68	0.65	0.63	0.61	0.56	0.55	0.53	0.53	0.86
75°F/distilled water (T&C)	0.62	0.54	0.52	0.51					0.51	0.62
135°F/distilled water (T)	0.61	0.53	0.51	0.51					0.51	0.61
135°F/distilled water (C)	0.53	0.41	0.38	0.37					0.37	0.53
190°F/distilled water (T)	0.31	0.19	0.17	0.16					0.16	0.31
190°F/distilled water (C)	0.12	0.05	0.05	0.04					0.12	0.04
Motor vibration	1.01	0.92	0.90	0.89					0.89	1.01
Load cycling in air	0.66	0.44	0.40	0.38					0.38	0.66
Load cycling in water	0.64	0.42	0.38	0.36					0.36	0.64
Brake fluid	0.87	0.77	0.75	0.74	0.73	0.70	0.69	0.68	0.68	0.87
Used motor oil	0.98	0.93	0.92	0.91	0.91	0.89	0.88	0.88	0.88	0.98
Sulfuric acid	0.35	0.19	0.17	0.16					0.16	0.35

[a]T = tension, C = compression.

8.6 PROCEDURES FOR DEVELOPING CREEP-RUPTURE CURVES AND ALLOWABLE STRESSES

8.6.1 General Procedures and Precaution for Applications

The ***creep-rupture curve*** was obtained by power law curve fitting of the creep-rupture data. The curve represents the average creep-rupture behavior of the material in the environment under study within the testing duration.

The ***minimum curve*** was developed in principle by shifting the creep-rupture curve graphically downward to embrace the lowest rupture stress data point and then shifting 0.5 ksi further downward. The derivation procedures included first calculating the difference between the creep-rupture curve and the lowest rupture stress data point, then subtracting this difference together with the additional 0.5 ksi from the creep-rupture curves at 0.001 and 131,400 h to obtain the minimum stress values at these two points. The minimum curve was developed by conducting power law curve fitting with the values of these two points.

The ***maximum design-allowable stress curve*** was derived from the minimum equation by multiplying by 0.8. It has the simple power law form given in Eq. (8.1) and is easily used for engineering design.

It should be pointed out that the power law curve fitting employed in developing the maximum design-allowable stress curves makes the curves and equations only empirical ones. It should also be borne in mind that extrapolation was employed in calculating the maximum design-allowable stresses and stress reduction factors for certain times, and the extrapolation was based on the assumption that the material behaves as it did within the testing duration. The mechanical property changes that may happen during long-term exposure to certain environments beyond the test duration have not been theoretically taken into consideration but are believed to be taken into account by the 0.8 factor for the time limits listed in the tables of this chapter.

8.6.2 Some Details in Developing the Maximum Design-Allowable Stress Curves

Because extrapolation is employed in developing the maximum design-allowable stress curve from the creep-rupture curve, the slope of the creep-rupture curve (i.e., the value of m) is considered a critical parameter. The determination of the m values for several environments is described in this section.

Figure 8.19 gives all the creep-rupture data and curves in air/50% RH from 20 to 250°F. The slopes of 75 and 250°F curves are similar and lower than those of 20, 135, and 190°F curves. However, because the two former curves are based on more data points, they are considered more reliable. Furthermore, the three latter curves are based on some data points from discontinued tests. It is not difficult to see from the figure

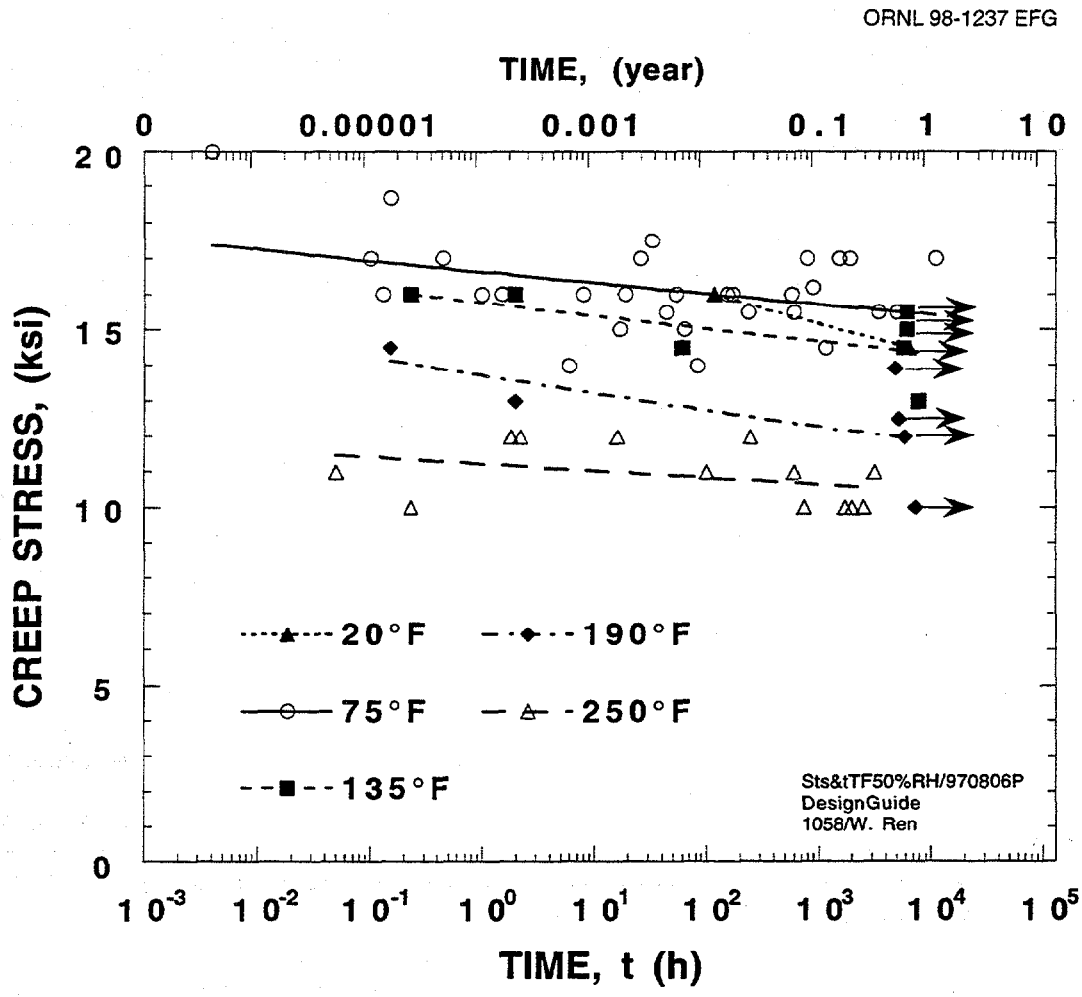

Fig. 8.19. Creep-rupture data and curves at various temperatures in air/50% RH.

that had the tests continued, the slopes of these curves would have decreased. Based on the quantity of data points and the trend for curve slope development, the slope of the creep-rupture curve for 75°F was chosen to derive minimum and maximum design-allowable stress curves for the other four temperatures in air/50% RH.

All the creep-rupture data and curves in air < 10% RH and air > 90% RH are presented in Fig. 8.20 together with the average and minimum for air/50% RH at 75°F. The material shows improved rupture behavior in air < 10% RH in comparison to air/50% RH. For purposes of this effort, although it tends to be conservative, the slope for air/50% RH was used to derive the maximum design-allowable stress curve and equation parameters for air < 10% RH. For air > 90% RH, the actual creep-rupture curve was employed to derive the maximum design-allowable stress curve and equation.

Figure 8.21 gives all the creep-rupture data and curves in distilled water at various temperatures. The slope of the curves increases obviously at 190°F. The slope for 135°F was modified to derive maximum design-allowable stress curves for 75 and 135°F, while that for 190°F was used for the maximum design-allowable stress curve at 190°F.

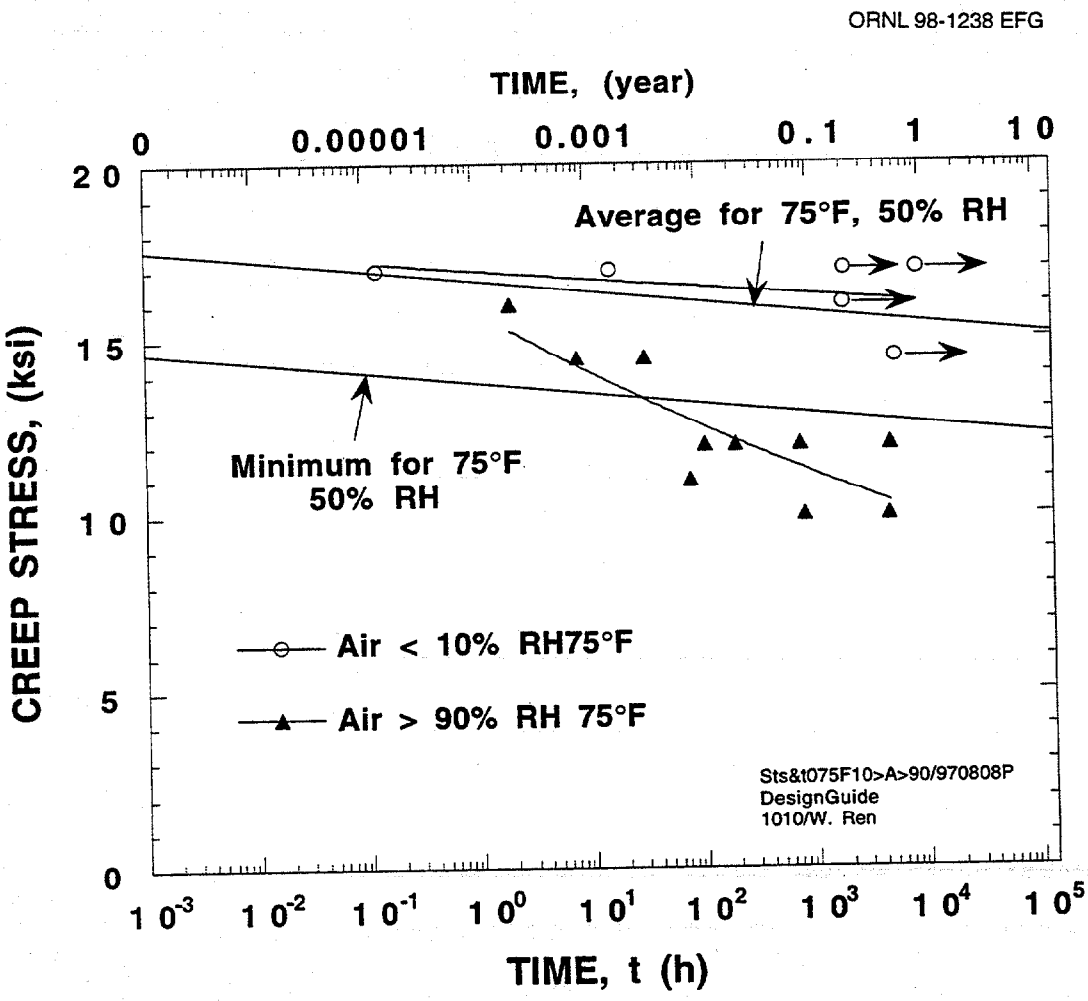

Fig. 8.20. Creep-rupture data and curves in air < 10% RH and air > 90% with the average and minimum for air/50% RH at 75°F.

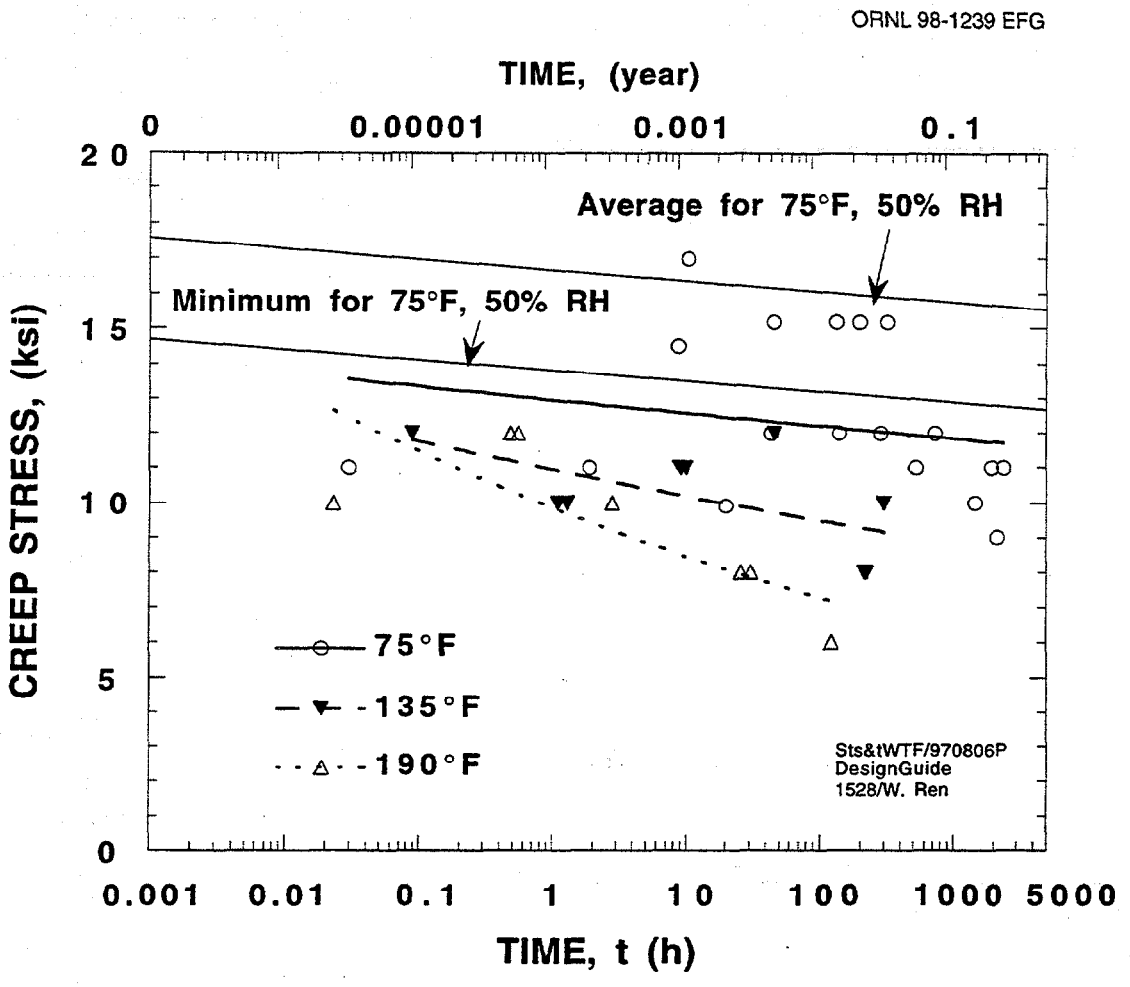

Fig. 8.21. Creep-rupture data and curves in distilled water at various temperatures.

8.7 APPLICABILITY OF TIME FRACTIONS FOR CREEP RUPTURE

Efforts have been made to investigate the applicability of the life-fraction rule proposed by Robinson[3] for steels:

$$\sum_{i=1}^{n} \frac{t_i}{t_r} = 1 \ . \tag{8.2}$$

Unfortunately, because of the significant data scatter of this material, attempts to prove such an applicability have been unsuccessful. The effect of data scatter can be observed in Fig. 8.1(*a*). At a given stress level (for example, 17 ksi), the rupture time varied from 0.1 to 11,061.3 h (6 min to 1.26 years), making any evalution of the Robinson rule very unreliable.

REFERENCES

1. W. Ren and C. R. Brinkman, "Creep-Rupture Behavior of the CSM Isocyanurate Composite," Report at Automotive Composites Consortium/Oak Ridge National Laboratory Coordination Meeting on Durability of Lightweight Composite Structures Project, May 1997.

2. J. M. Corum, *Durability of Lightweight Composite Structures for Automotive Applications: Annual Progress Report for Period Ending September 30, 1996,* ORNL/TM-13345, Lockheed Martin Energy Research Corp., Oak Ridge National Laboratory, December 1996.

3. E. L. Robinson, "Effect of Temperature Variation on the Long-Term Rupture Strength of Steels," *Trans. ASME* **74**: 777 (July 1952).

9. ENVIRONMENTAL EFFECTS ON CREEP DEFORMATION AND RUPTURE DESIGN CURVES OF THE CSM ISOCYANURATE COMPOSITE FOR COMPRESSIVE LOADINGS

W. R. Ren and C. R. Brinkman

9.1 INTRODUCTION

In this chapter, compressive creep deformation and creep-rupture properties of the reference material are evaluated by comparing them to those in Chap. 8 obtained under tensile loading conditions. Proposed stress allowables for time-dependent creep rupture under compressive loading conditions are calculated. Data are analyzed from tests conducted in air at 50% relative humidity (air/50% RH) at 75°F and distilled water at 75, 135, and 190°F by comparing to those obtained under tensile loading conditions. Average and minimum creep-rupture behaviors are defined, where possible; suggested maximum time-dependent stress allowables are calculated by multiplying minimum values by 0.8.

9.2 CREEP DEFORMATION CURVES FOR AIR/50% RH AND DISTILLED WATER

Twenty-one specimens were tested under compressive loading conditions. The specimens were from plaques P7 and P18. Testing conditions include air/50% RH at 75°F and distilled water at 75, 135, and 190°F. Of these 21 tests, 19 reached the rupture point and were used for data analysis.

9.2.1 Creep Deformation in Air/50% RH

Test results show that compressive creep deformation in air/50% RH at 75°F is comparable to that under tensile loading conditions. Figures 9.1 and 9.2 give the comparison of creep deformation curves in air/50% RH at 75°F at 11 and 12 ksi, respectively. Obviously, they are reasonably comparable.

The two compressive curves in Fig. 9.1 were generated from one specimen by unloading at 505.4 h and reloading at 2736.2 h. Figure 9.3 illustrates that the material recovered ~80% of its creep strain after the unloading.

9.2.2 Creep Deformation in Distilled Water

Test results indicate that at 75°F, compressive creep deformation in distilled water is comparable to that under tensile loading conditions. However, at 135°F, it may be greater than that under tensile loading conditions, especially at higher stresses.

Figure 9.4 shows the comparability at 75°F between compressive and tensile creep deformation for distilled water and 12-ksi testing conditions. At 135°F, however, Figs. 9.5–9.7 show that at higher stresses the compressive creep strain at a given stress level is increased compared to that for tensile loading.

9.2.3 Loading Deformation

Loading deformation (i.e., the short-term time-independent deformation recorded in setting up the creep tests) is comparable for compressive and tensile loading conditions in air/50% RH at 75°F, and in distilled water at 75 and 135°F, as shown in Figs. 9.8–9.10.

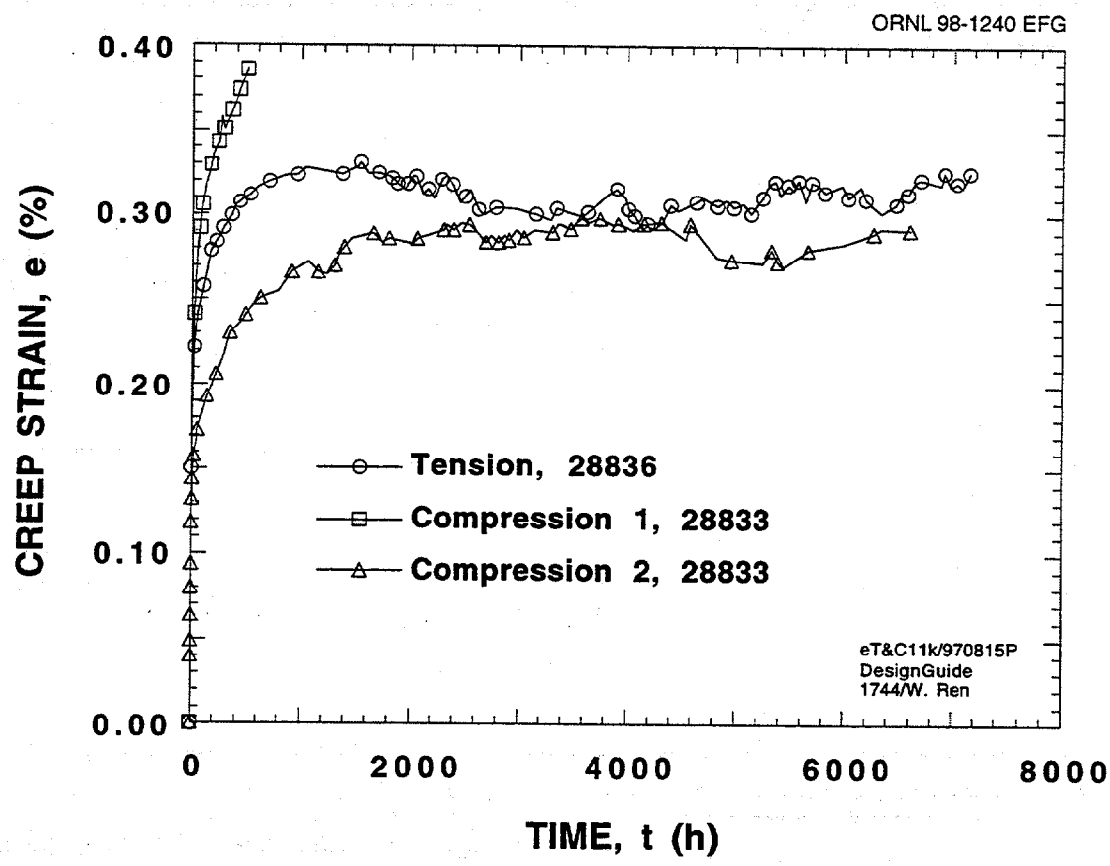

Fig. 9.1. Comparison of tensile and compressive creep deformation curves in air/50% RH at 75°F at 11 ksi shows similar deformation behavior.

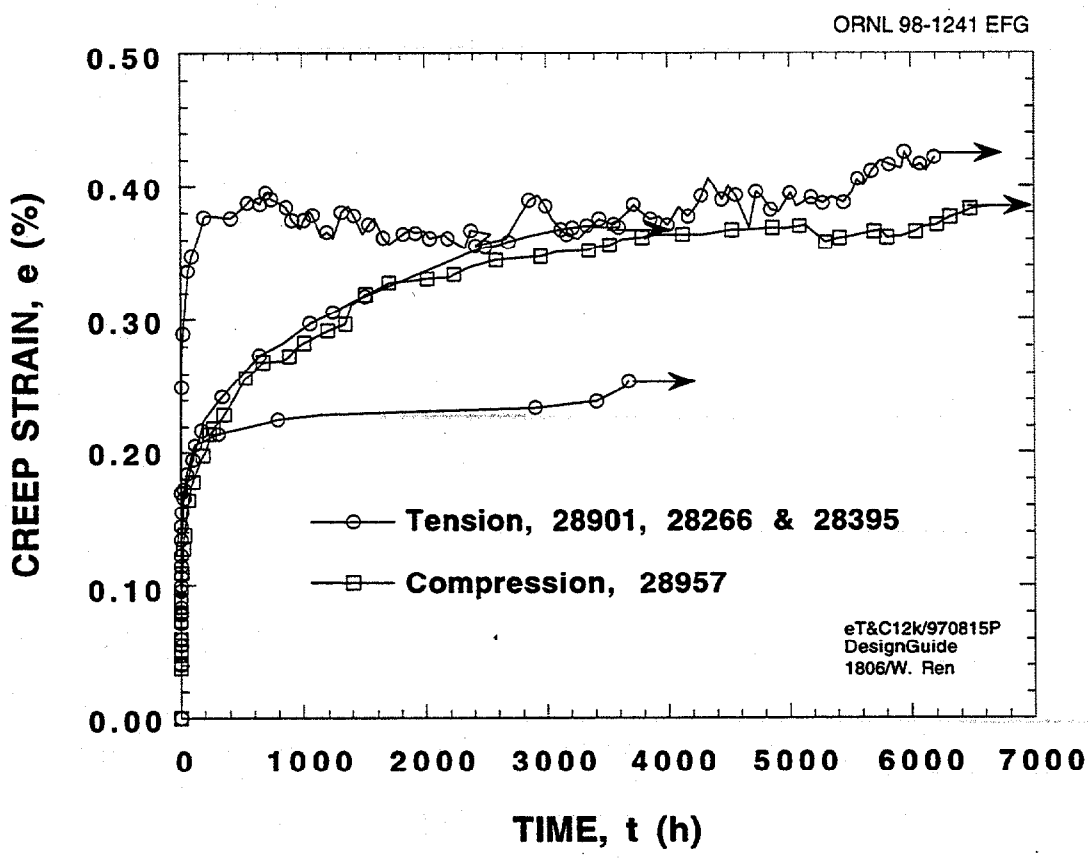

Fig. 9.2. Comparison of tensile and compressive creep deformation curves in air/50% RH at 75°F at 12 ksi shows similar deformation behavior.

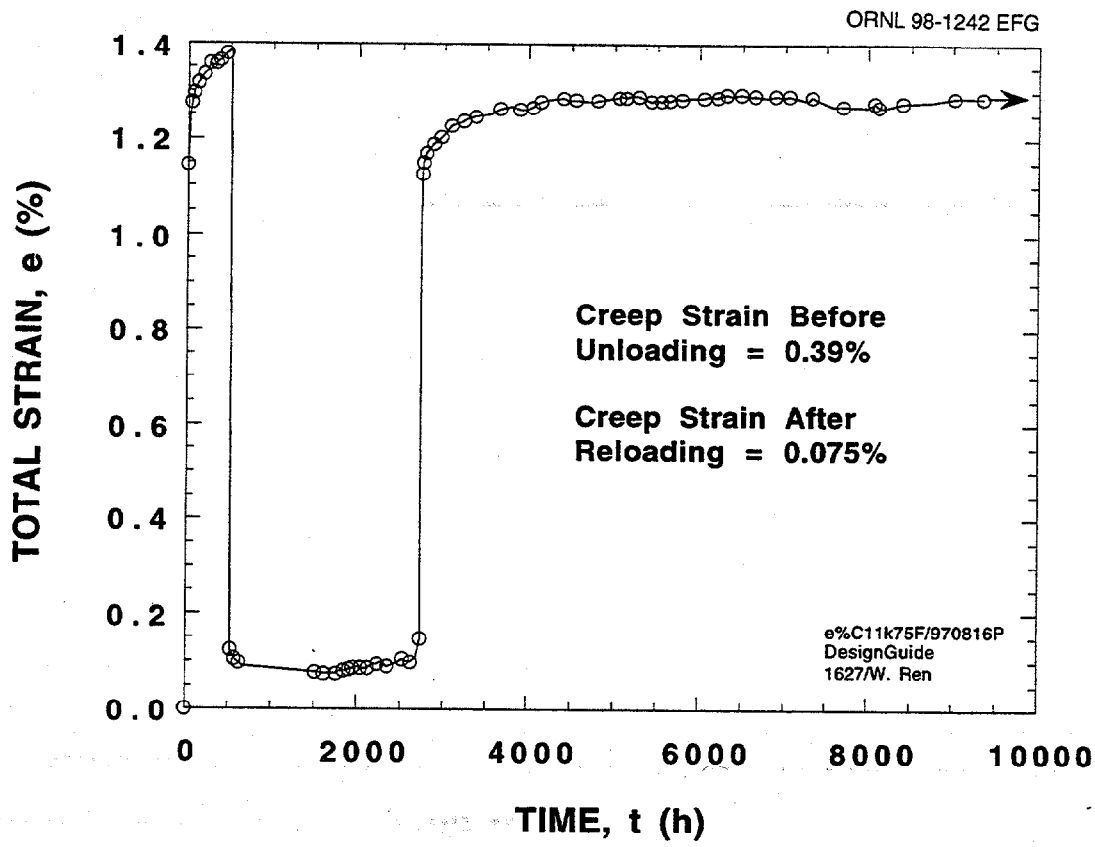

Fig. 9.3. Recovery behavior under compressive loading in air/50% RH at 75°F. Approximately 80% of the creep strain was recovered after the unloading.

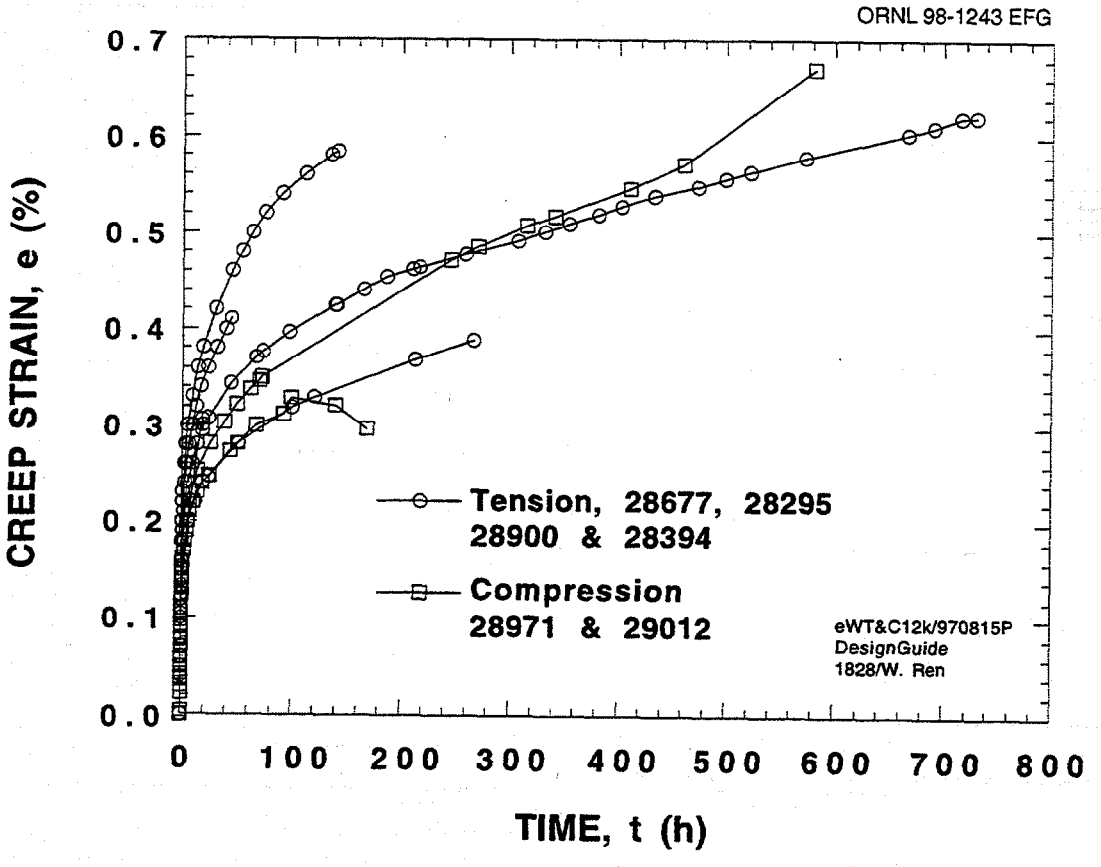

Fig. 9.4. At 75°F in distilled water, compressive and tensile creep deformation at 12 ksi is comparable.

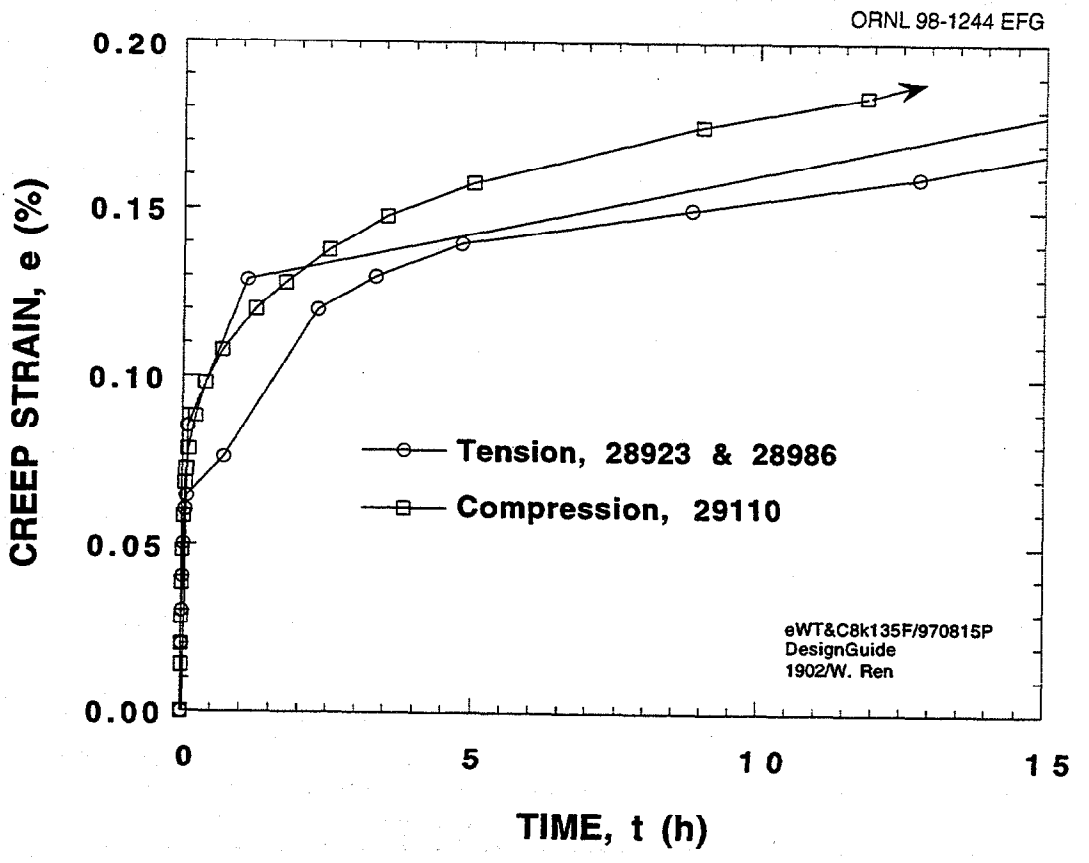

Fig. 9.5. Compressive creep deformation is comparable to tensile creep deformation at 135°F and 8 ksi in distilled water.

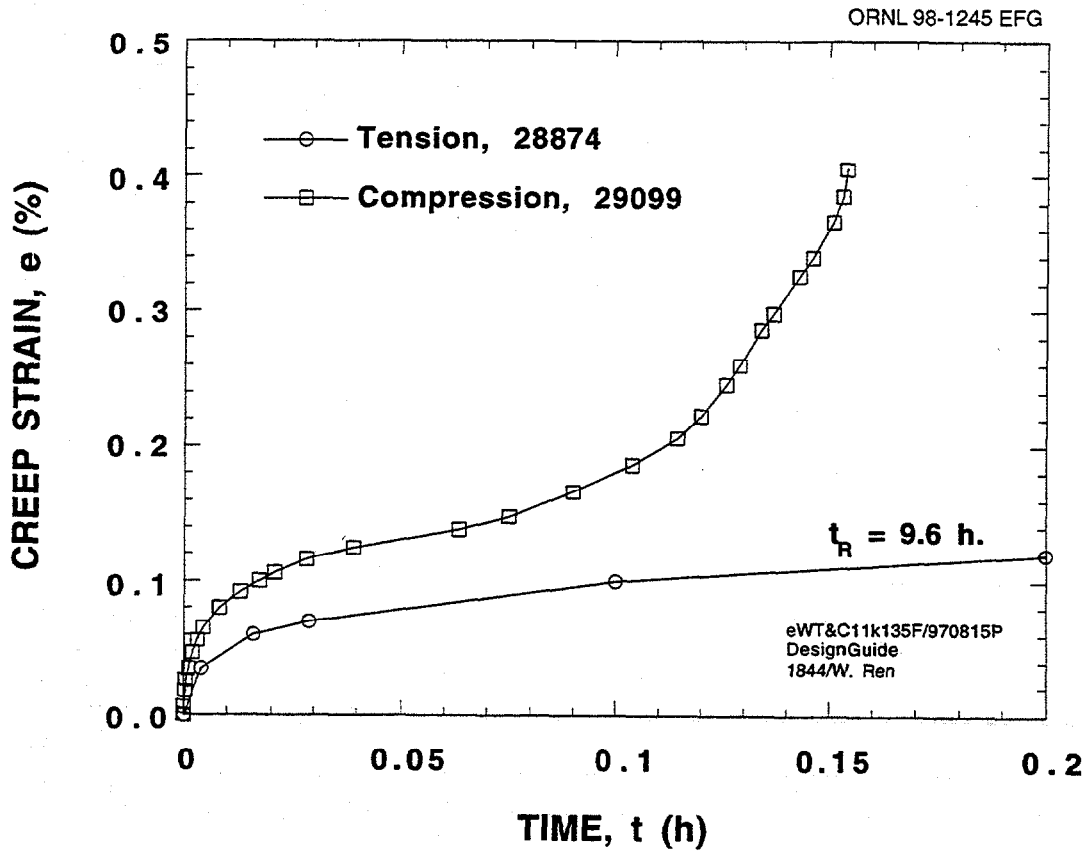

Fig. 9.6. Data suggest that compressive creep deformation is increased compared to tensile creep deformation at 135°F and 11 ksi in distilled water.

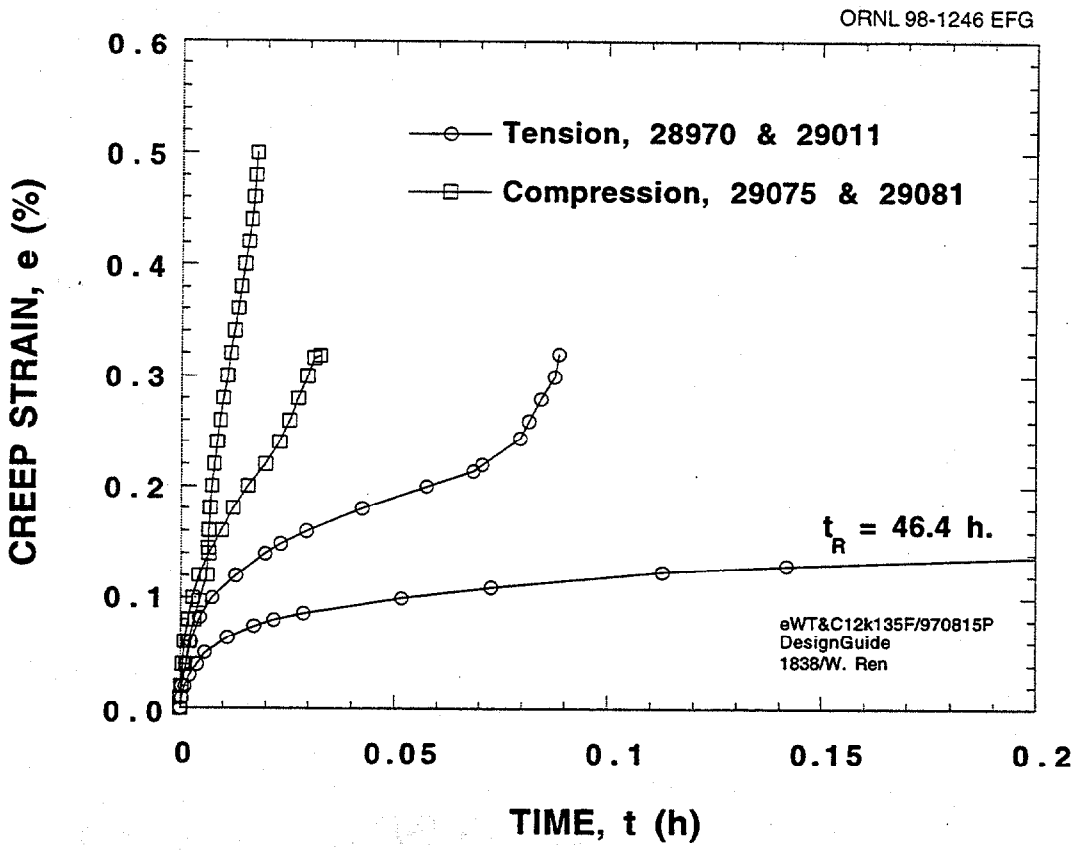

Fig. 9.7. Data suggest that compressive creep deformation is increased compared to tensile creep deformation at 135°F and 12 ksi in distilled water.

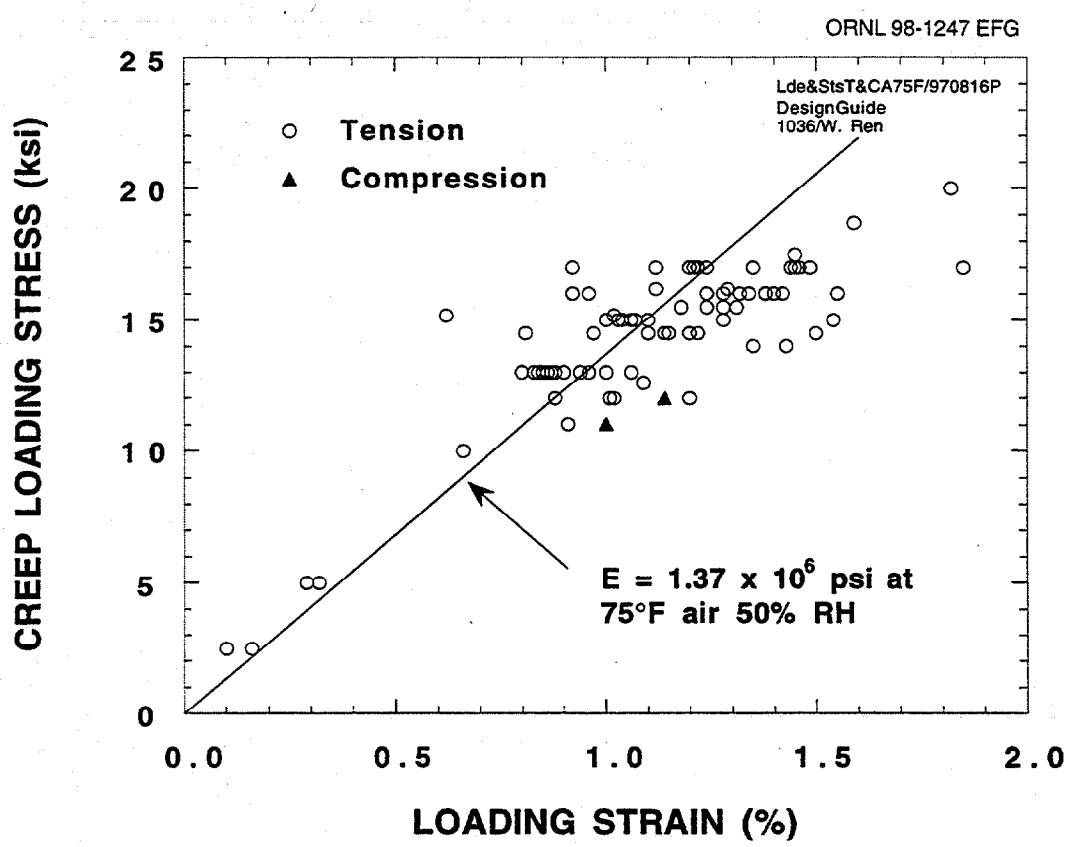

Fig. 9.8. Compressive loading deformation is comparable to tensile loading deformation at 75°F in air/50% RH.

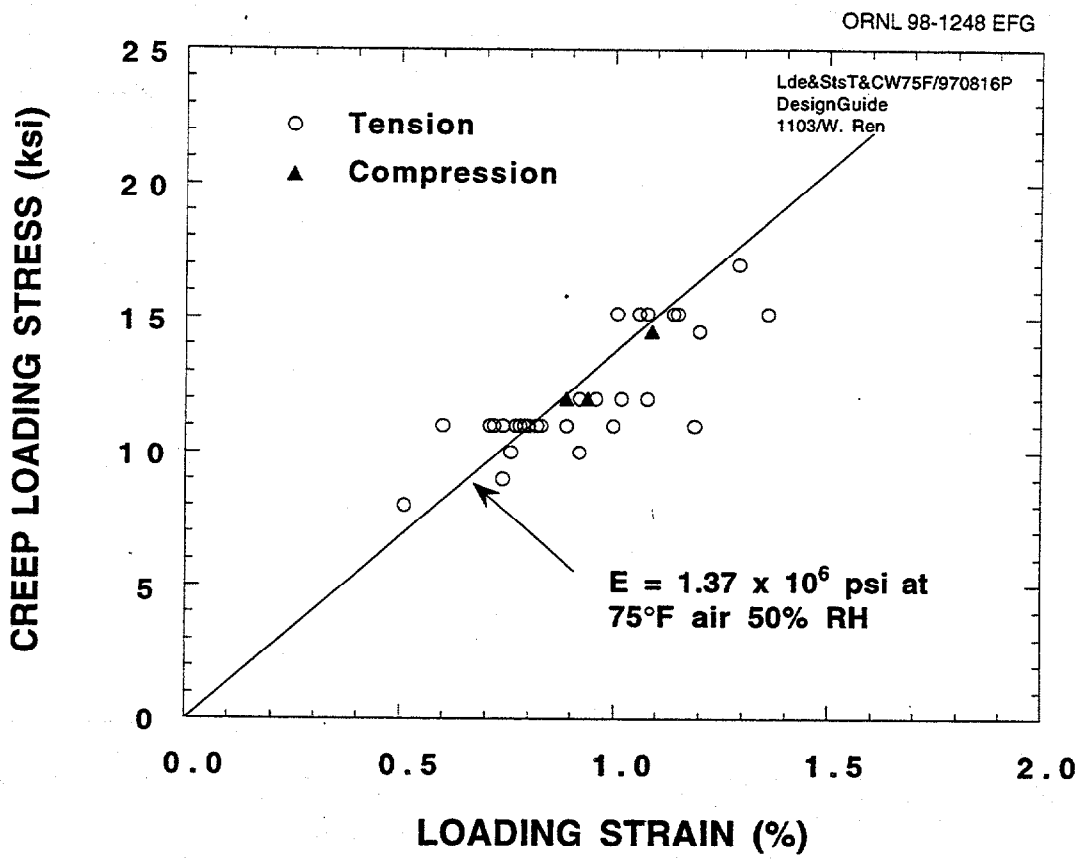

Fig. 9.9. Compressive loading deformation is comparable to tensile loading deformation at 75°F in distilled water.

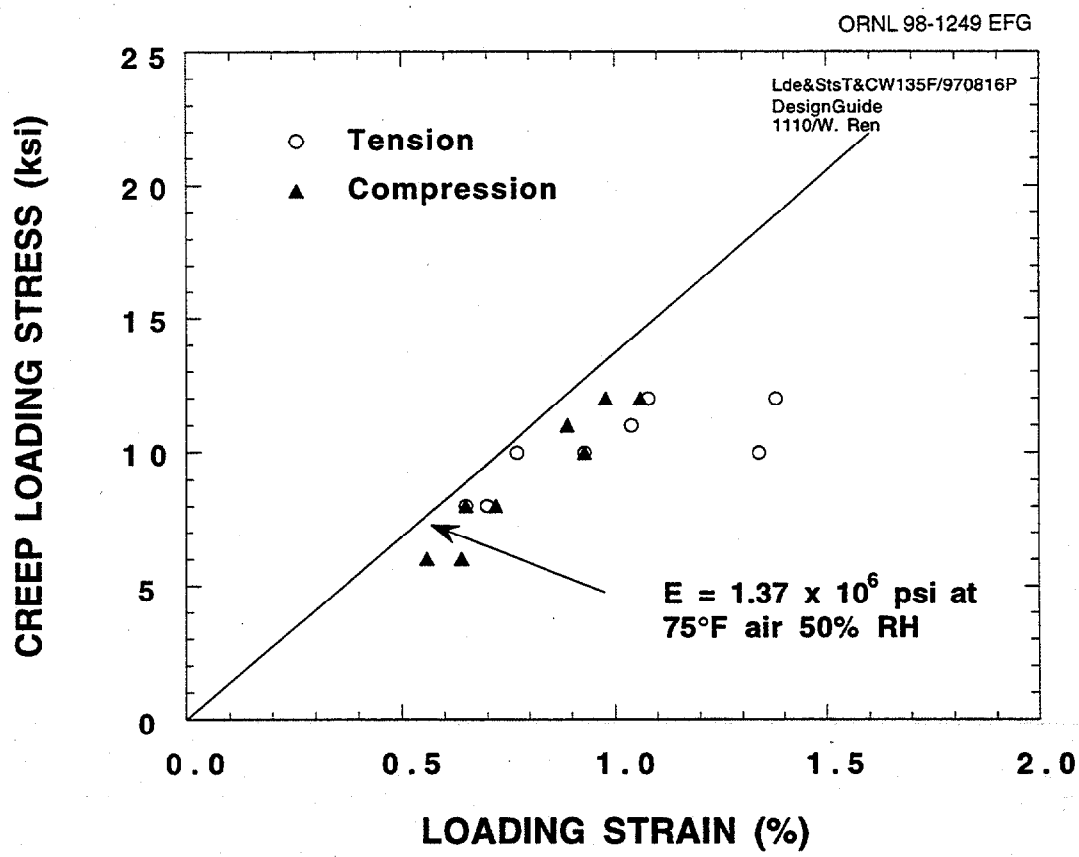

Fig. 9.10. Compressive loading deformation is comparable to tensile loading deformation at 135°F in distilled water.

9.3 COMPRESSIVE CREEP-RUPTURE AND DESIGN CURVES IN AIR/50% RH AND WATER

9.3.1 Creep-Rupture Life and Creep-Rupture Strain

Test results indicate that, compared on a creep-rupture strain basis, compressive creep-rupture life in distilled water is comparable to that under tensile loading conditions at 75°F but tends to be less in time than that under tensile loading conditions at 135°F, as shown in Figs. 9.11 and 9.12.

9.3.2 Creep-Rupture and Design Curves and Equations

Figure 9.13 gives the tensile average, minimum creep-rupture curves and equation, and the maximum design-allowable curve and equation for air/50% RH at 75°F (see Chap. 8). Three compressive data points, one from a ruptured test and the other two from tests still in progress, are also presented in the figure. The very limited data show that compressive creep-rupture behavior is comparable to tensile behavior in air/50% RH at 75°F. Therefore, the minimum creep-rupture and maximum design-allowable curves and equation for tensile loading are suggested for compressive loading in air/50% RH at 75°F.

Figure 9.14 shows the tensile minimum creep-rupture and the maximum design-allowable curves and equation for distilled water at 75°F (see Chap. 8). Three compressive data points are also presented in the figure. The limited data show that compressive creep-rupture behavior is comparable to tensile behavior in distilled water at 75°F. Therefore, the minimum creep-rupture and maximum design-allowable curves and equations for tensile loading are suggested for compressive loading in distilled water at 75°F.

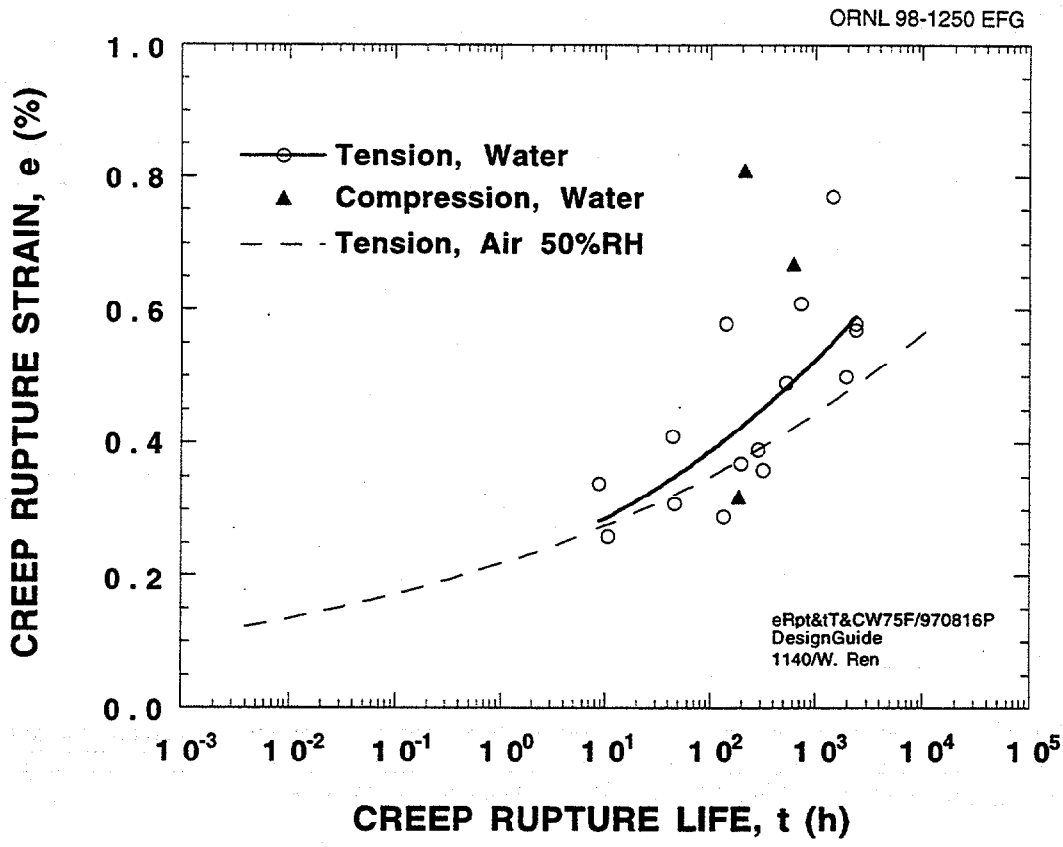

Fig. 9.11. On a creep-rupture strain basis, compressive creep-rupture life in distilled water is comparable to that under tensile loading conditions at 75°F.

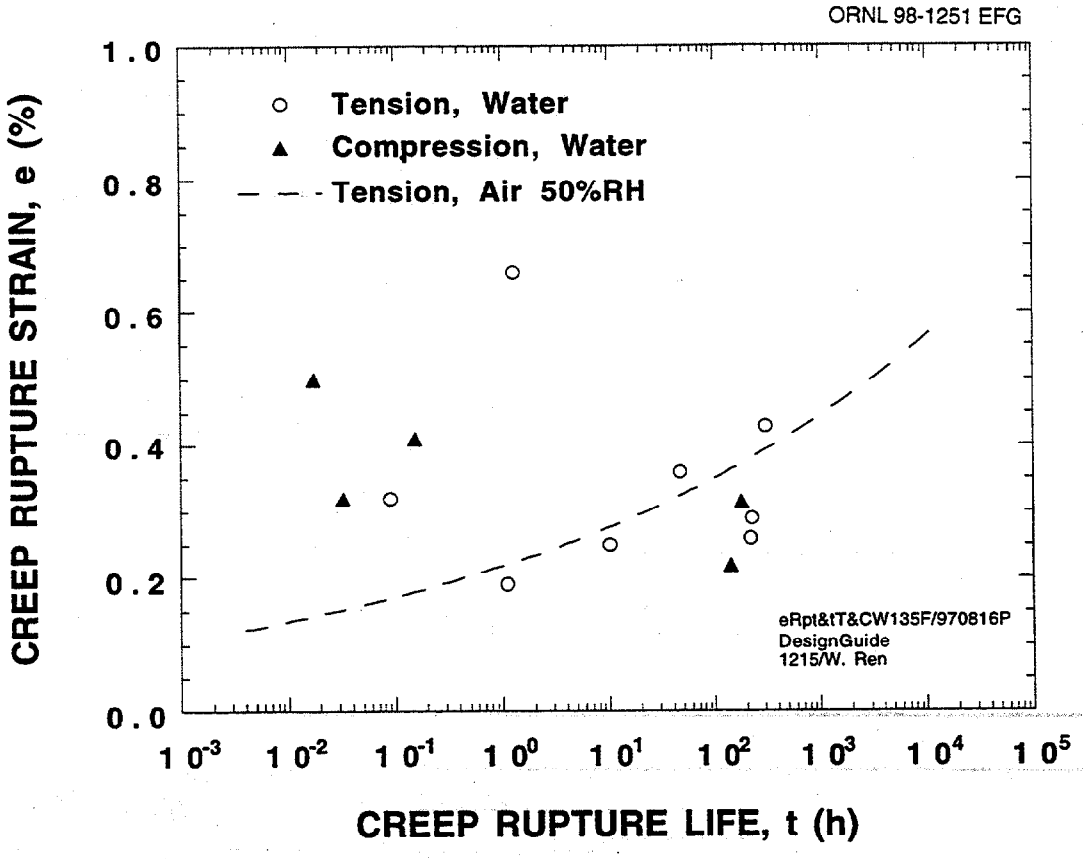

Fig. 9.12. On a creep-rupture strain basis, compressive creep-rupture life in distilled water is slightly shortened relative to that under tensile loading conditions at 135°F.

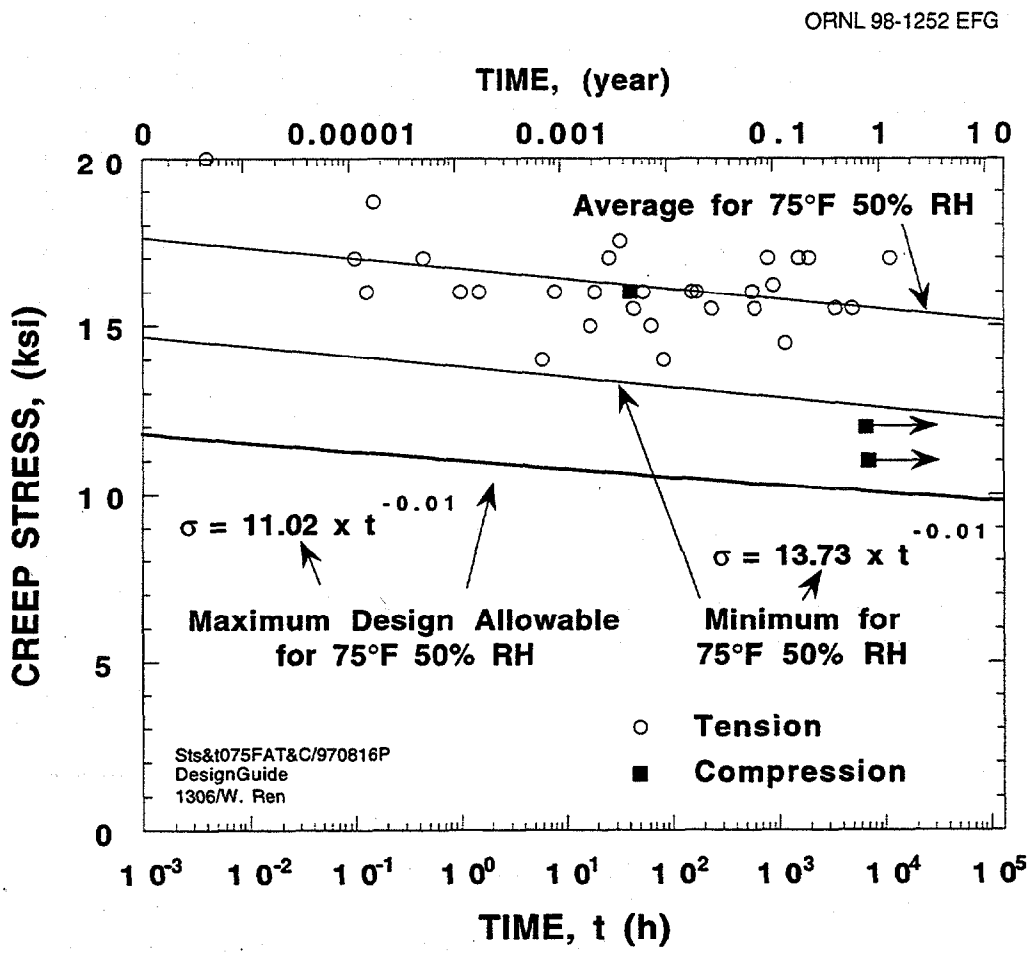

Fig. 9.13. Average and minimum creep-rupture curves and equation, and maximum design-allowable curve and equation for air/50% RH at 75°F for tensile loading are assumed to be equivalent to those for compressive loading.

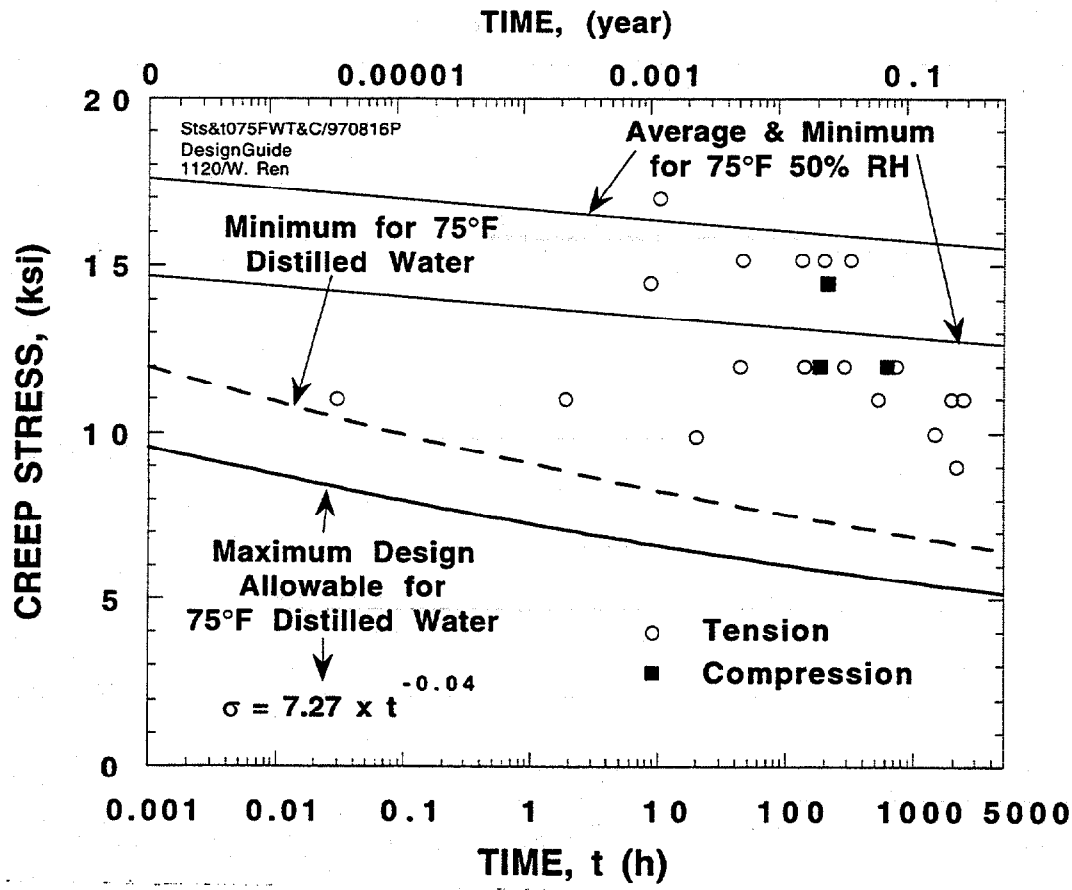

Fig. 9.14. Minimum creep-rupture and maximum design-allowable curves and equation for distilled water at 75°F for tensile loading are assumed to be equivalent to those for compressive loading.

Figures 9.15 and 9.16 present the compressive minimum creep-rupture and the maximum design-allowable curves and equation for distilled water at 135 and 190°F. Tensile data points for the same environment are also presented in the figures. Limited data show that compressive loading tends to decrease creep-rupture life or creep-rupture stress compared to tensile loading in distilled water at 135 and 190°F. The average creep-rupture curves for both tensile and compressive loadings given in Figs. 9.17 and 9.18 more clearly indicate this trend and the important role that temperature plays. It is possible that compression causes additional failure mechanisms related to buckling and matrix shear that reduce creep-rupture stress when the matrix is softened at elevated temperatures.

The parameters for the maximum design-allowable stress equation and the calculated results for compressive loading in air/50% RH at 75°F and distilled water at 75 and 135°F are given in Tables 9.1 and 9.2. The stress reduction factors relative to air/50% RH 75°F are presented in Tables 9.3 and 9.4, which were obtained by dividing the maximum design-allowable stesses for a specific environment at various times by the maximum design-allowable stress for air/50% RH at 131,400 h (15 years).

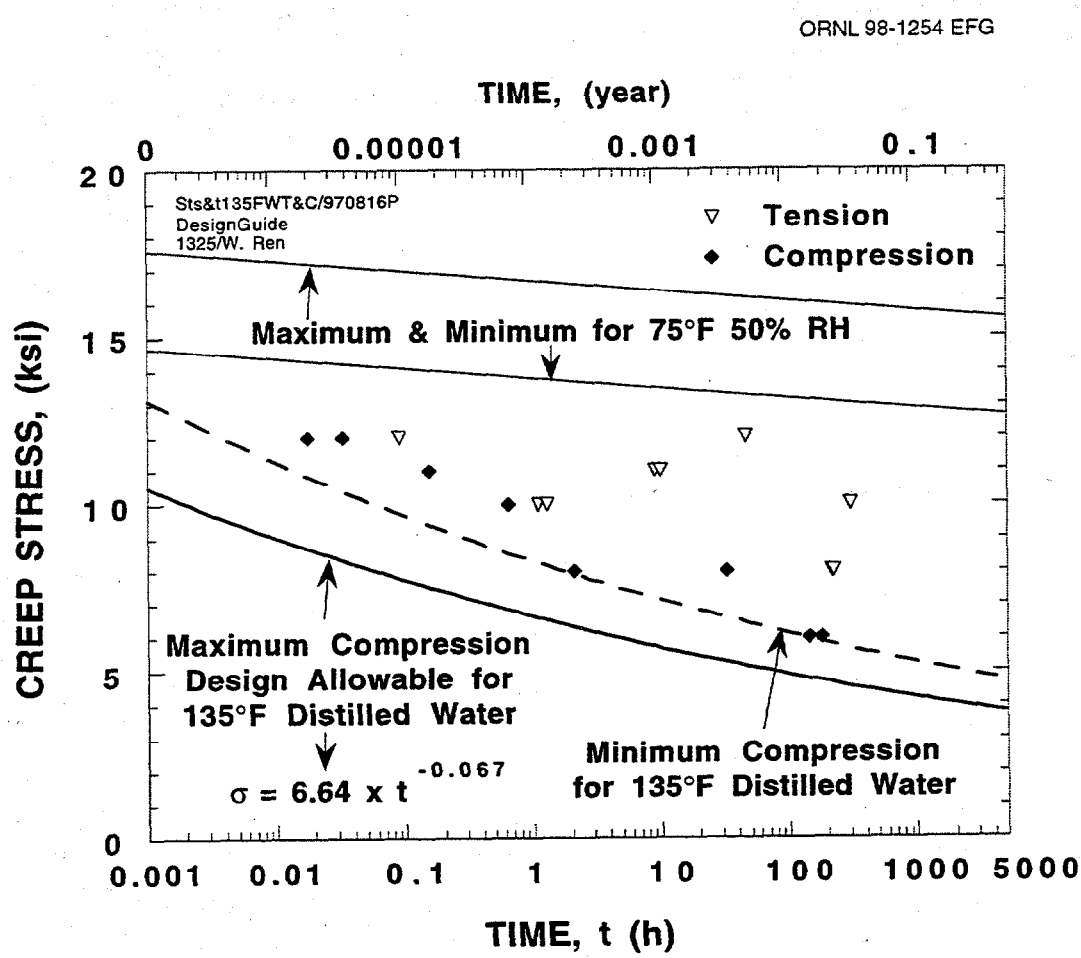

Fig. 9.15. Minimum creep-rupture and the maximum design-allowable curves and equation for distilled water at 135°F. Tensile data points for the same environment are also presented for comparison.

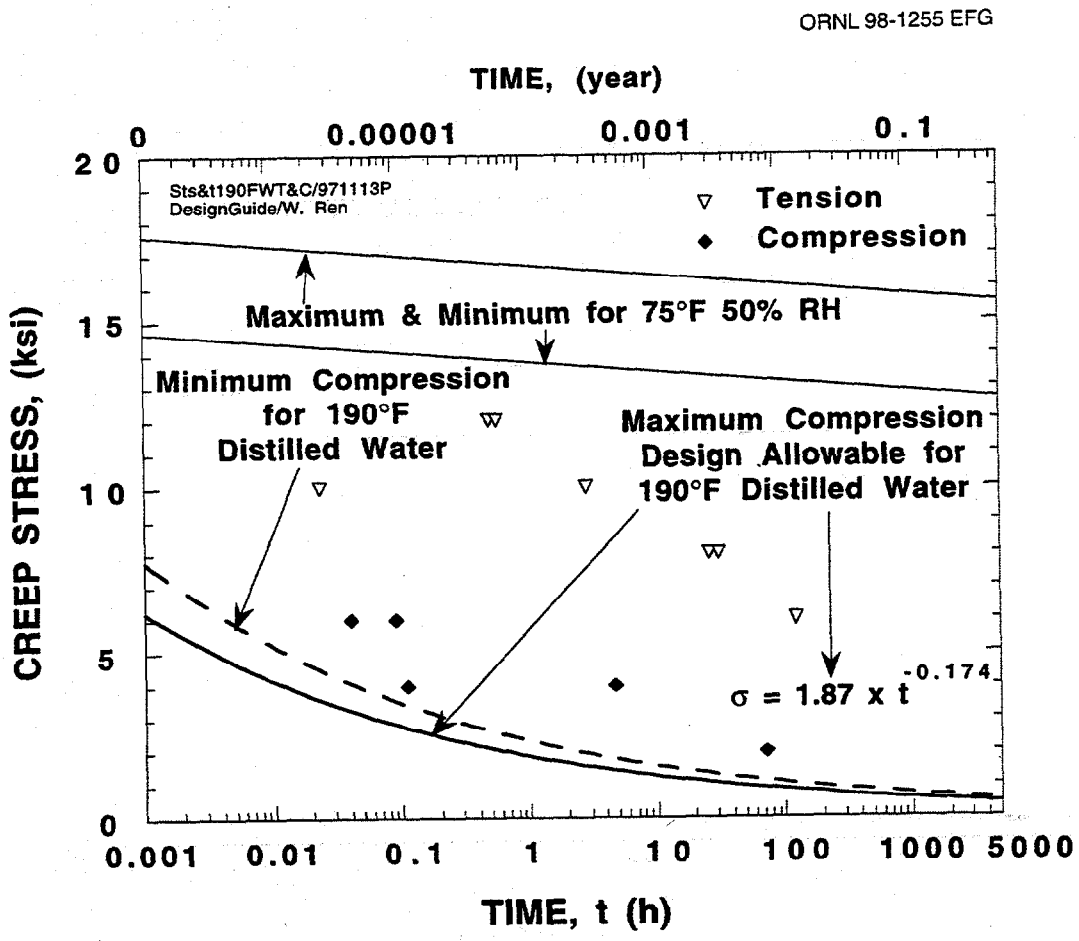

Fig. 9.16. Minimum creep-rupture and the maximum design-allowable curves and equation for water at 190°F. Tensile data points for the same environment are also presented for comparison.

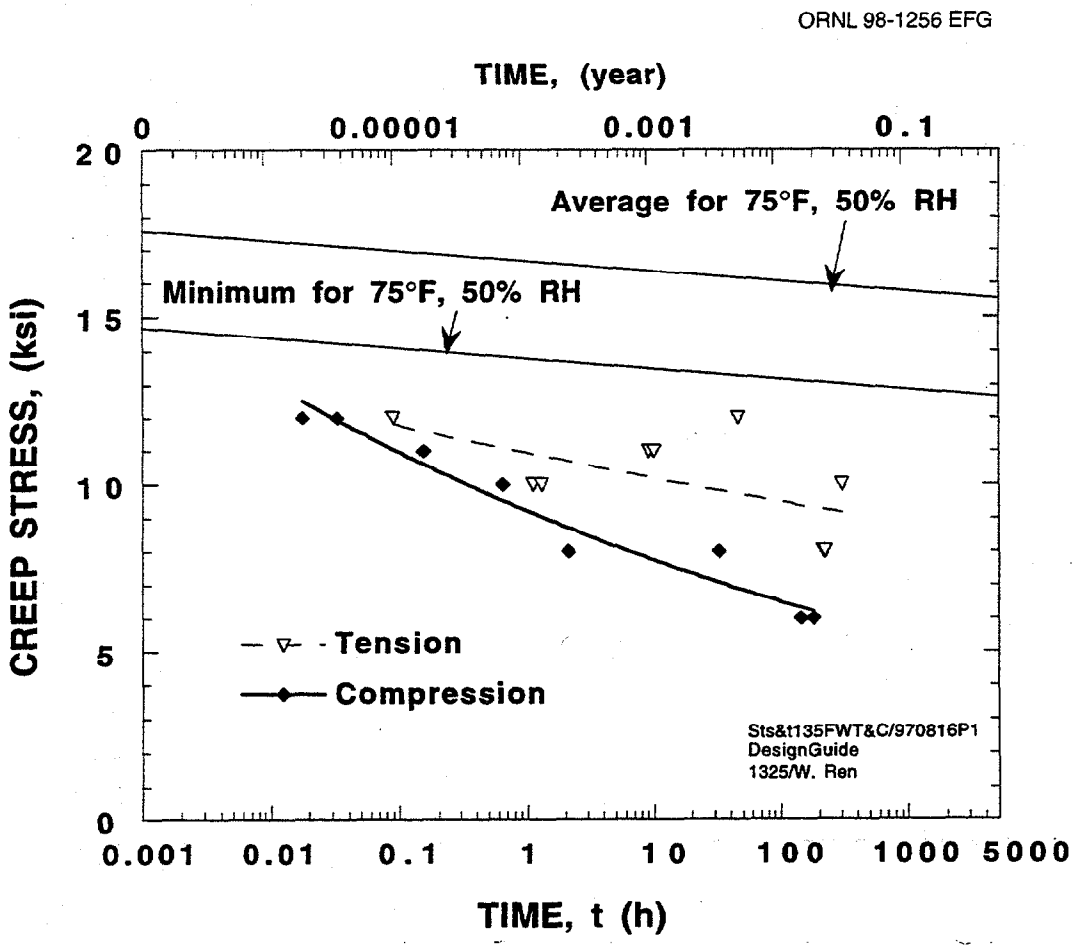

Fig. 9.17. Average creep-rupture curves show that compressive loading tends to decrease creep-rupture life or creep-rupture stress compared to tensile loading in distilled water at 135°F.

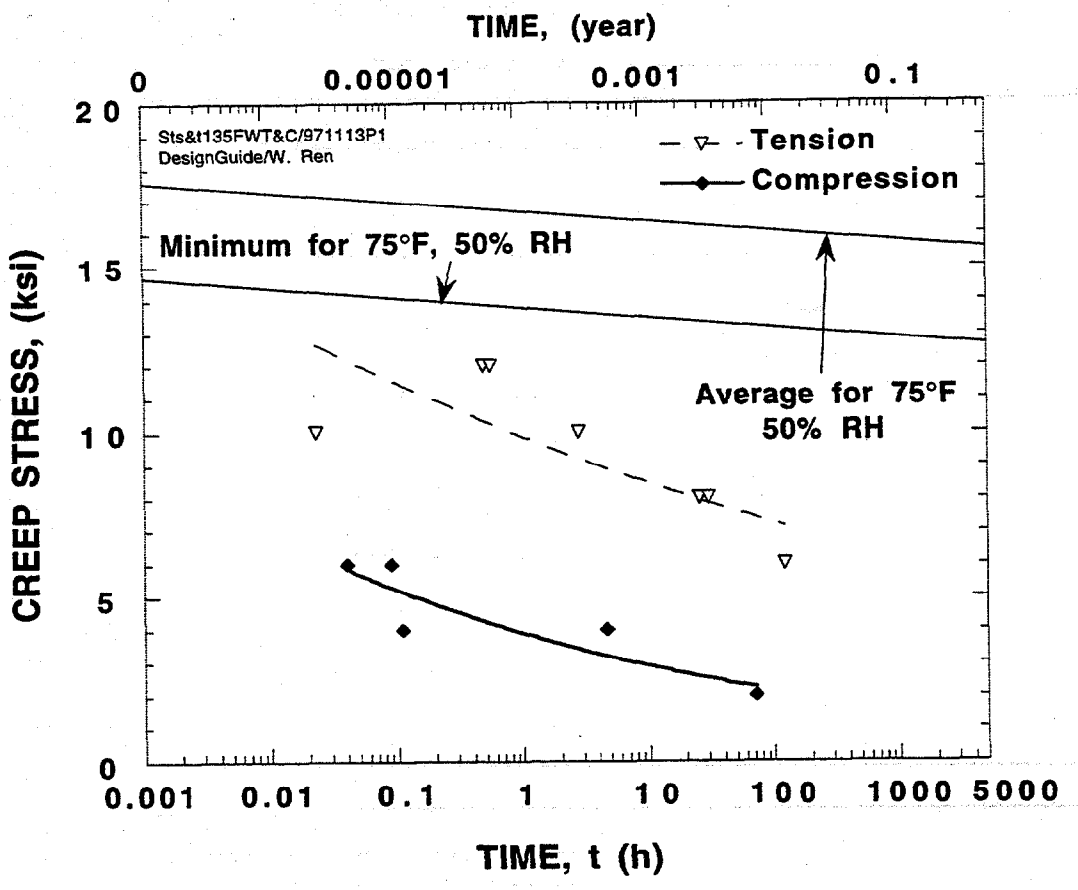

Fig. 9.18. Average creep-rupture curves show that compressive loading tends to decrease creep-rupture life or creep-rupture stress even more at 190°F compared to tensile loading in distilled water at the same temperature.

Table 9.1. Maximum compressive design-allowable stress in air/50% RH for specific no-rupture time limits

Temperature (°F)	Maximum compressive design-allowable stress (ksi)								Parameter	
	10 h	1000 h	3000 h	5000 h	1 year	5 years	10 years	15 years	B	m
75	10.77	10.28	10.17	10.12	10.06	9.90	9.83	9.79	11.02	–0.010

Table 9.2. Maximum compressive design-allowable stress in distilled water for specific no-rupture time limits

Temperature (°F)	Maximum compressive design-allowable stress (ksi)				Parameter	
	10 h	1000 h	3000 h	5000 h	B	m
75	6.63	5.51	5.28	5.17	7.27	–0.040
135	5.69	4.18	3.88	3.75	6.64	–0.067
190	1.25	0.56	0.46	0.42	1.87	–0.174

Table 9.3. Stress reduction factors in air/50% RH for specific no-rupture time limits under compressive loading

Temperature (°F)	Stress reduction factor							
	10 h	1000 h	3000 h	5000 h	1 year	5 years	10 years	15 years
75	1.10	1.05	1.04	1.03	1.03	1.01	1.00	1.00

Table 9.4. Stress reduction factors in distilled water for specific no-rupture time limits under compressive loading

Temperature (°F)	Stress reduction factor			
	10 h	1000 h	3000 h	5000 h
75	0.68	0.56	0.54	0.53
135	0.58	0.43	0.40	0.38
190	0.13	0.06	0.05	0.04

10. BASIC FATIGUE BEHAVIOR AND CORRELATIONS

J. M. Corum and R. L. Battiste

10.1 INTRODUCTION

Dogbone specimens from the 0° direction of a single plaque, P36, of the CSM/isocyanurate reference material were fatigue tested at –40°F, room temperature, and 250°F. All tests were tensile fatigue, with a ratio, R, of minimum to maximum stress of 0.1. With three exceptions, strains and stiffness were monitored throughout each test.

Tensile tests on specimens from the same plaque were also performed at –40°F, room temperature, and 250°F. The results are tabulated in Table 10.1.

10.2 FATIGUE S-N CURVES

The fatigue test results are tabulated in Table 10.2. All specimens were subjected to a pretest stiffness check at room temperature. Those results are provided in the first column, and they indicate the inherent scatter within a single plaque. The initial cyclic modulus values in the –40°F and 250°F tests are also tabulated. In the column labeled Maximum Stress, the stress is given as a percentage of the at-temperature UTS. The average UTS at room temperature from Table 10.1 was used for the room-temperature tests.

Table 10.1. Plaque P36 tensile properties

Specimen No.	E (Msi)	UTS (ksi)	Failure strain (%)	Departure stress (ksi)	Departure strain (%)
		T = –40°F			
P-36-0-33	1.84	36.05	3.45	10	
P-36-0-34	1.73	34.30	2.9	10.5	
P-36-0-35	1.92	33.99	1.72		
Average	**1.83**	**34.78**	**2.69**	**10.25**	
		Room temperature			
P-36-0-29	1.44	26.00	2.50	5.91	0.41
P-36-0-30	1.65	26.93	2.21	5.61	0.34
P-36-0-31	1.53	28.72	2.66	6.57	0.44
P-36-0-51	1.65	26.12	2.45	4.51	0.28
P-36-0-52	1.39	25.15	2.46	4.76	0.34
P-36-0-56	1.24	23.18	2.46	4.93	0.39
Average	**1.48**	**26.02**	**2.46**	**5.38**	**0.37**
		T = 250°F			
P-36-0-36	0.904	18.85	2.54	6.25	
P-36-0-37	0.911	18.55	2.46	8	
P-36-0-38	1.02	20.73	2.45	7.6	
Average	**0.945**	**19.38**	**2.48**	**7.28**	

Table 10.2. Plaque P36 fatigue properties

Specimen No.	Pretest R.T. E_0 (Msi)	Maximum stress (ksi)	Initial cyclic modulus (Msi)	Maximum stress (% UTS)	Cycles to failure	Cycles to 10% stiffness reduction	Calculated N_f (P36 fat. curve)	Stiffness monitored
				T = –40°F				
P36-0-19	1.497	21.776	1.612	69.88	330	4	260	Y
P36-0-20	1.424	16.332	1.513	52.41	2,882	169	3,729	Y
P36-0-21	1.29	10.888	1.423	34.94	47,955	8,761	159,236	Y
P36-0-23	1.582	21.776	1.714	69.88	393	4	260	Y
P36-0-24	1.636	16.332	1.736	52.41	3,852	447	3,729	Y
P36-0-25	1.573	10.888	1.757	34.94	434,495	42,769	159,236	Y
				Room temperature				
P36-0-42	1.435	20.672		79.45	136	1	73	Y
P36-0-55	1.521	20.672		79.45	105	1	73	Y
P36-0-11	1.443	15.348		58.99	1,344	102	1,399	Y
P36-0-14	1.482	15.098		58.02	1,434	65	1,645	Y
P36-0-15	1.382	15.079		57.95	1,178	54	1,666	Y
P36-0-13	1.469	11.44		43.97	22,264	1,522	25,662	Y
P36-0-12	1.424	11.392		43.78	12,770	1,360	26,753	Y
P36-0-16	1.366	7.6		29.21	1,543,627	165,291	1,471,725	Y
P36-0-17	1.448	7.6		29.21	2,744,367	349,577	1,471,725	Y
P36-0-18	1.347	5.826		22.39	>16,651,181		20,456,382	Y
P36-0-10		5.739		22.06	>52,653,065		23,742,393	
P36-0-54	1.573	5.44		20.91	>1,246,568		40,327,124	Y
P36-0-53	1.607	4.08		15.68	>1,723,033		696,010,323	Y
				T = 250°F				
P36-0-26	1.548	16.332	1.043	92.12	59	>59	33	Y
P36-0-27	1.604	10.888	1.077	61.41	1,254	1,247	3,001	Y
P36-0-28	1.484	8.166		46.06	87,617		73,357	
P36-0-40	1.677	16.332	1.061	92.12	61	>61	33	Y
P36-0-41	1.589	10.888	1.021	61.41	951	>951	3,001	Y
P36-0-32	1.571	8.166		46.06	120,340		73,357	

However, at –40°F and 250°F, values calculated from the following correlation developed by Ruggles (Chap. 3) were used:*

$$\Delta UTS\ (\%) = 0.18T\ (°F) - 12.65\ .$$

As shown below, the resulting values are slightly different from those in Table 10.1, which were based on limited tests of adjacent specimens in plaque P36.

Temperature (°F)	UTS from Table 10.1 (ksi)	Calculated UTS (ksi)
–40	34.8	31.2
250	19.4	17.7

The calculated values might be slightly more representative because the correlation came from a larger data base, which included the P36 tests.

Figure 10.1(*a*) shows the fatigue failure data, with power law curve fits, on an S-N plot. Figure 10.1(*b*) shows the same test results, but with maximum stress given as a percentage of the at-temperature UTS. The latter figure shows that normalizing by the UTS brings the –40°F and room-temperature results together, but the 250°F curve is slightly high. Interestingly, if the UTS values in Table 10.1 are used, the 250°F curve nearly coincides with the room-temperature curve, and the –40°F curve is slightly low. Our conclusion is that all the curves in Fig. 10.1(*b*) would likely coincide if a sufficiently large statistical sampling were available. Figure 10.1(*b*) indicates that the 10^8 cycle "endurance limit" is about 20% of the short-time static strength. This is consistent with observations made for CSM/polyester laminates for both tensile and flexural fatigue.[1]

10.3 CYCLIC DAMAGE

Figure 10.2 shows the first and near-last stress-strain loops for representative tests at -40°F, room temperature, and 250°F. These loops reflect the accumulation of cyclic damage in two ways: (1) a permanent strain increment in each cycle and (2) a cyclic softening (stiffness reduction). The incremental permanent strain drops off rapidly in the first few cycles of a test. Likewise, the stiffness drops most rapidly in the early cycles. Overall, it appears that the decrease in stiffness accounts for about half of the increase in the maximum strain observed in the near-last loops of Fig. 10.2.

As will be seen, plots of maximum strain vs cycles give the best overall view of damage accumulation. However, plots of stiffness vs life fraction, n/N_f, are also informative. These are shown in Figs. 10.3–10.5 for –40°F, room temperature, and 250°F tests, respectively.

Focusing on the room-temperature results in Fig. 10.4 first, it can be seen that with the exception of the two tests at 79.5% UTS, the curves are grouped together fairly well. It is believed that the 79.5% UTS specimens were so damaged on the first load-up that the cyclic mechanisms are somewhat masked. The curves in Fig. 10.4 are fit very well by power laws up to a life fraction of at least 0.5. Fitting a power law to the values to 0.5 and then extrapolating to a life fraction of 1.0 gives an average predicted end-of-life stiffness reduction of 16.5% (ignoring the two higher results at 79.5% UTS). Rapid damage development near the end of life increases the reduction above that of the power law prediction in most cases.

For –40°F, the average end-of-life stiffness reduction predicted by the power laws is 17.2%. For 250°F, the value is just 8.1%.

The maximum peak strains in each cycle are plotted as a function of cycles in Figs. 10.6–10.8 for –40°F, room temperature, and 250°F tests, respectively. The points in these figures represent arbitrary cycle numbers chosen for plotting from the large amount of data. Consider the room-temperature test data in

*This correlation references the change in the UTS from the room-temperature value.

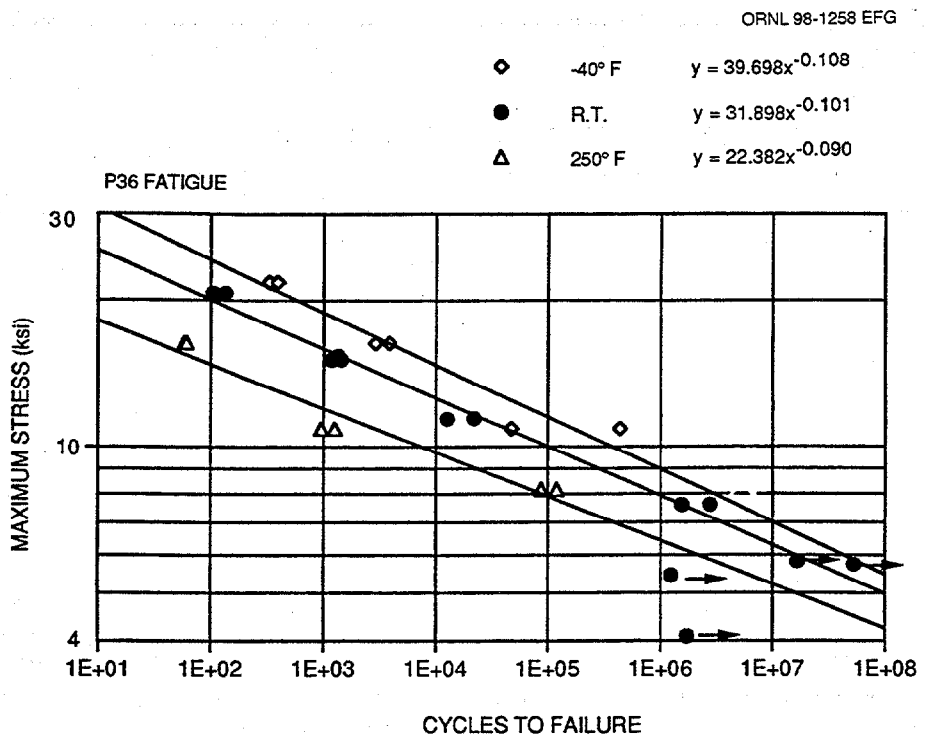

***(a)* Maximum stress in ksi.**

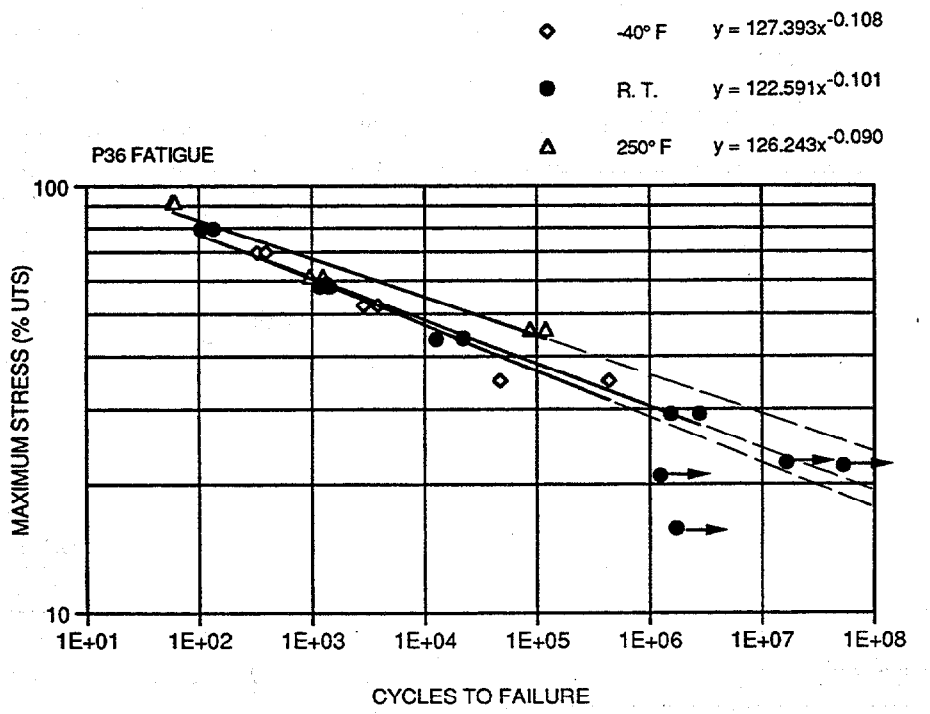

***(b)* Maximum stress as percentage of at-temperature UTS.**

Fig. 10.1. Fatigue S-N curves.

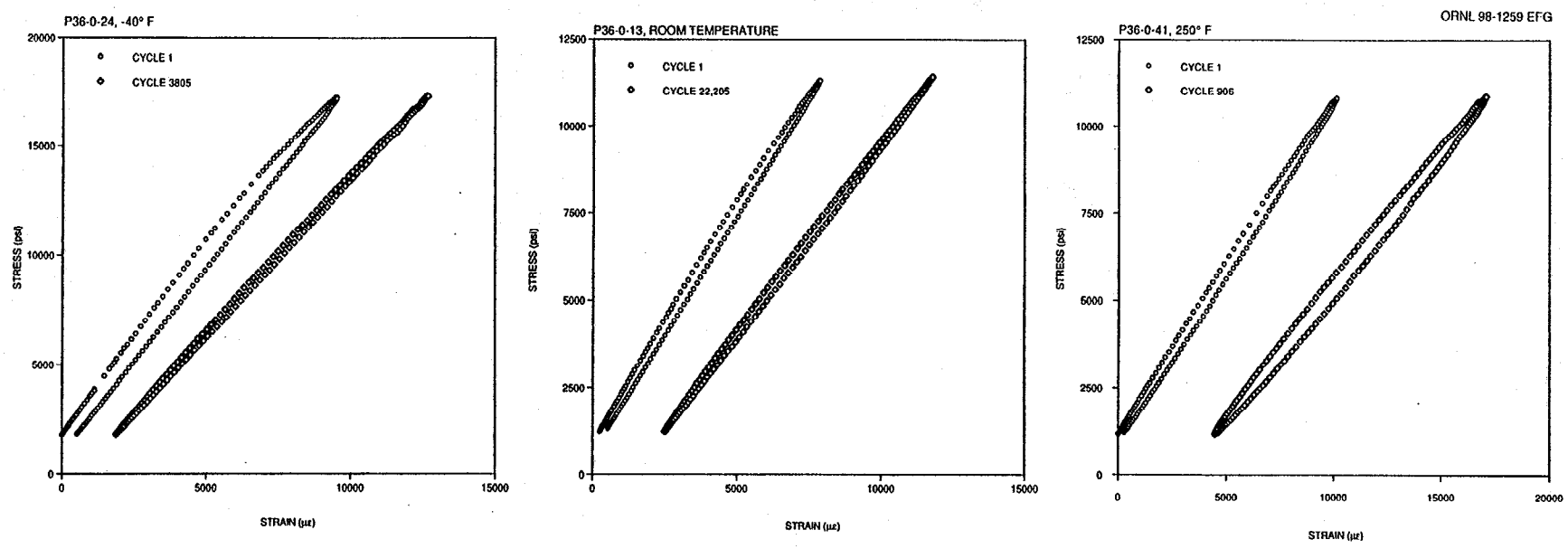

(*a*) –40°F, σ_{max} = 52.4% UTS.

(*b*) Room temperature, σ_{max} = 44.0% UTS.

(c) 250°F, σ_{max} = 61.4% UTS.

Fig. 10.2. Stress-strain loops for selected tests.

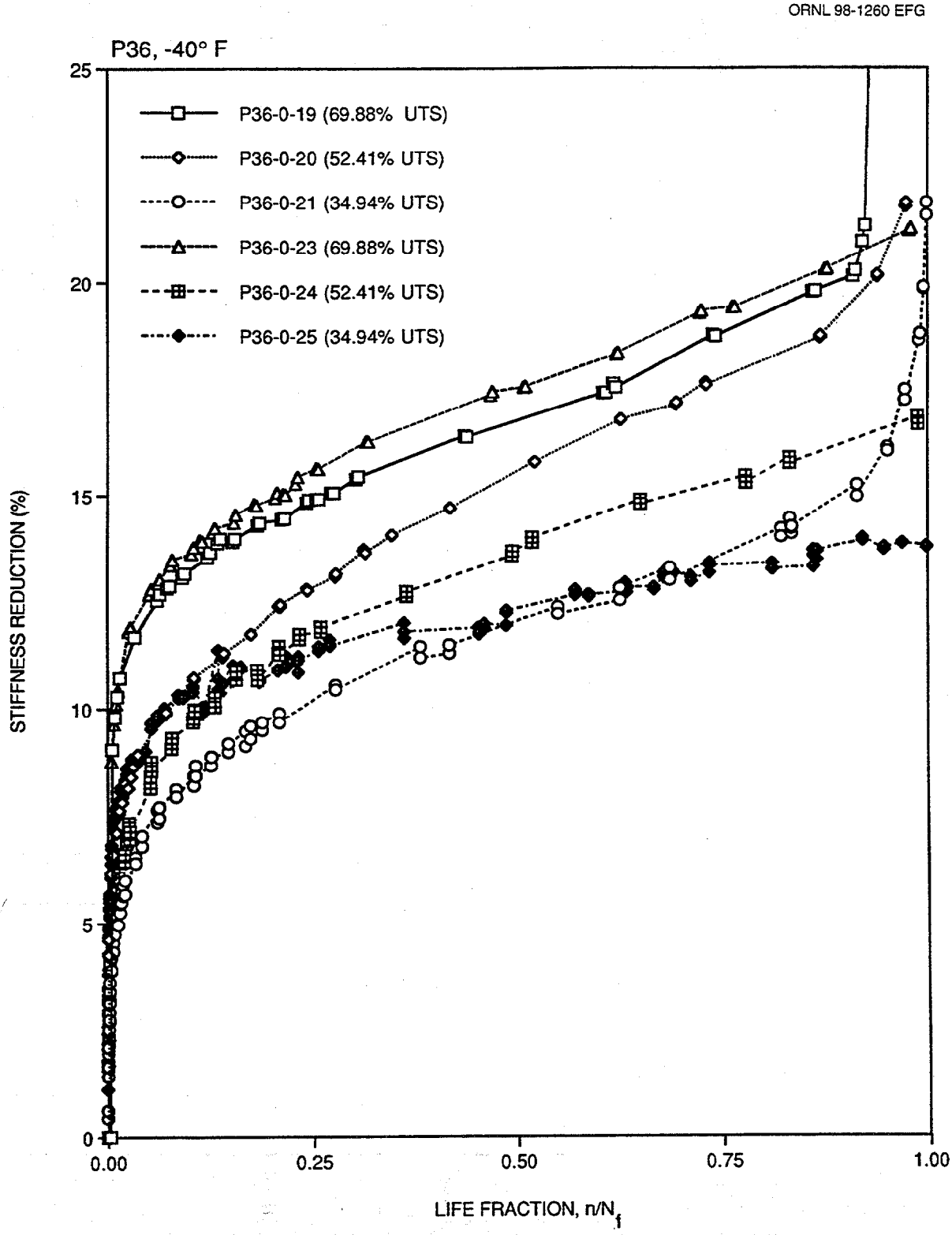

Fig. 10.3. Stiffness reduction vs life fraction at –40°F.

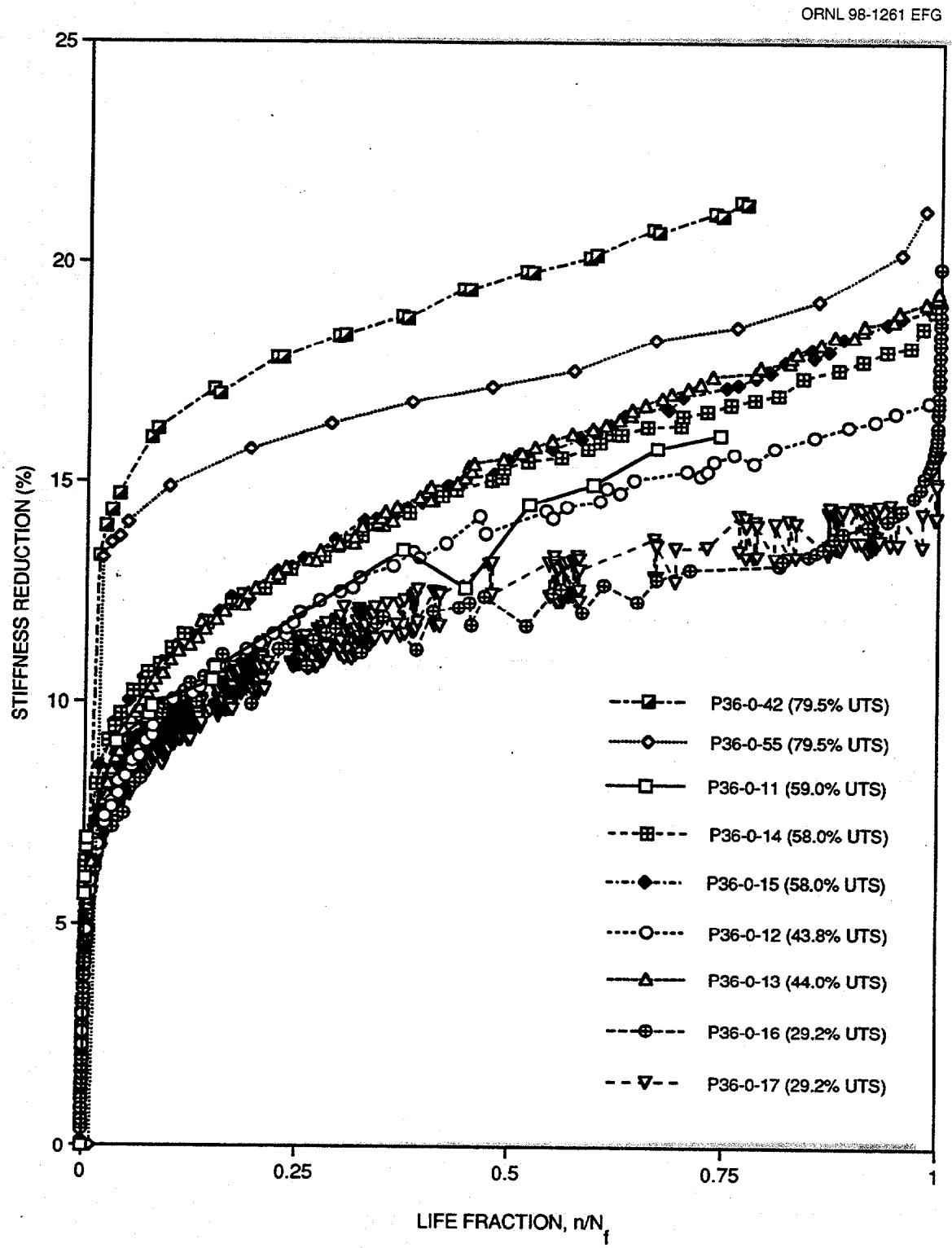

Fig. 10.4. Stiffness reduction vs life fraction at room temperature.

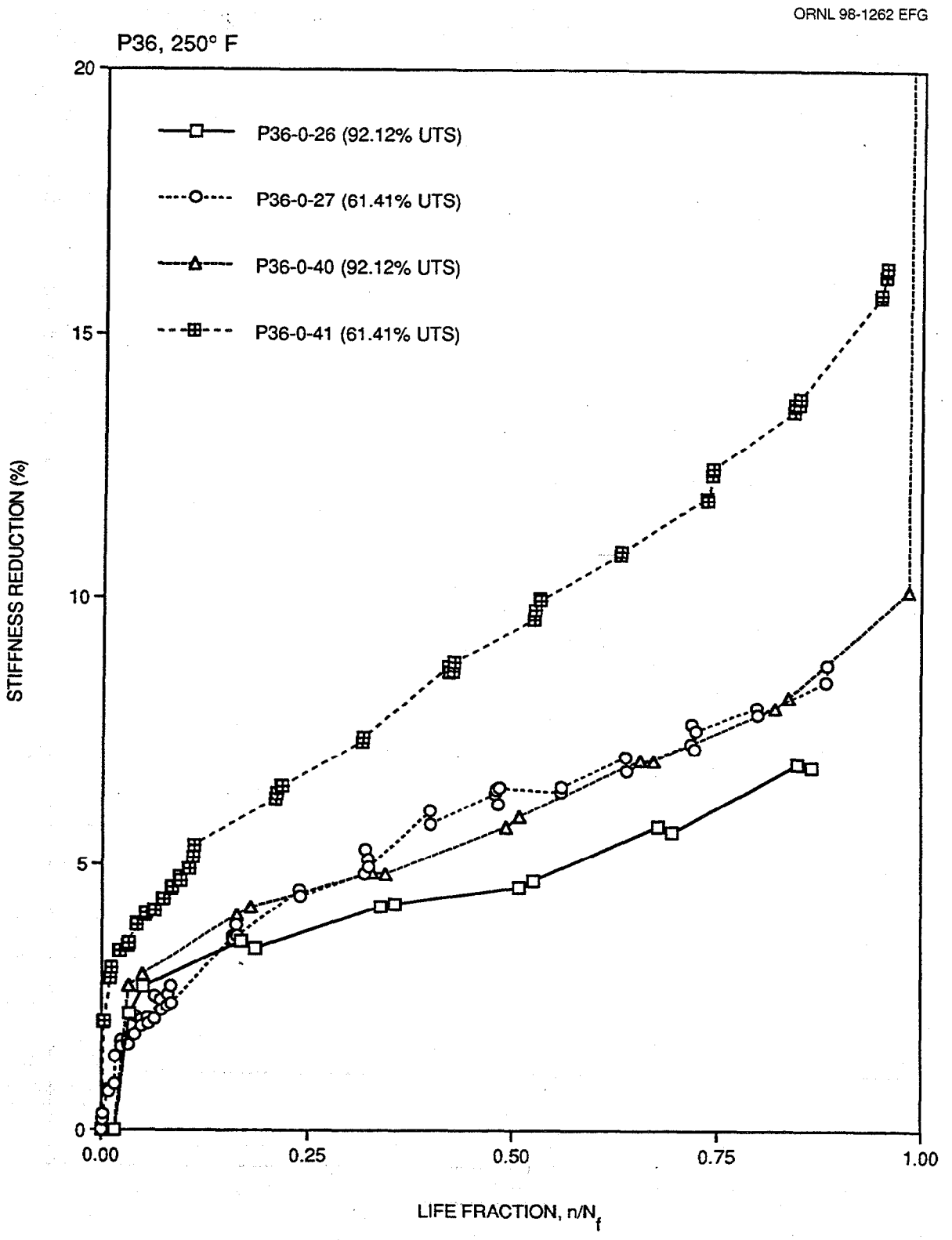

Fig. 10.5. Stiffness reduction vs life fraction at 250°F.

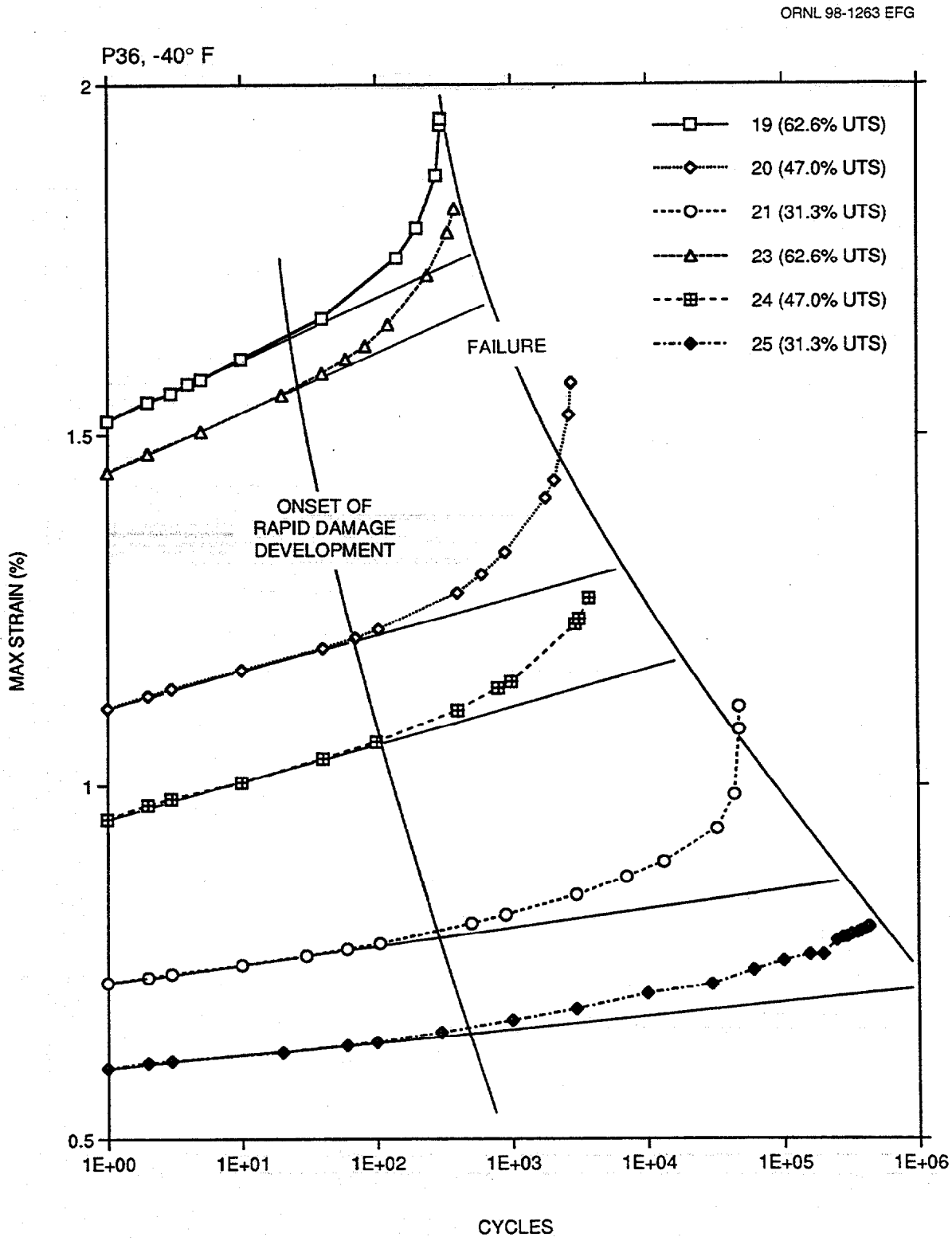

Fig. 10.6. Maximum strain vs cycles at –40°F.

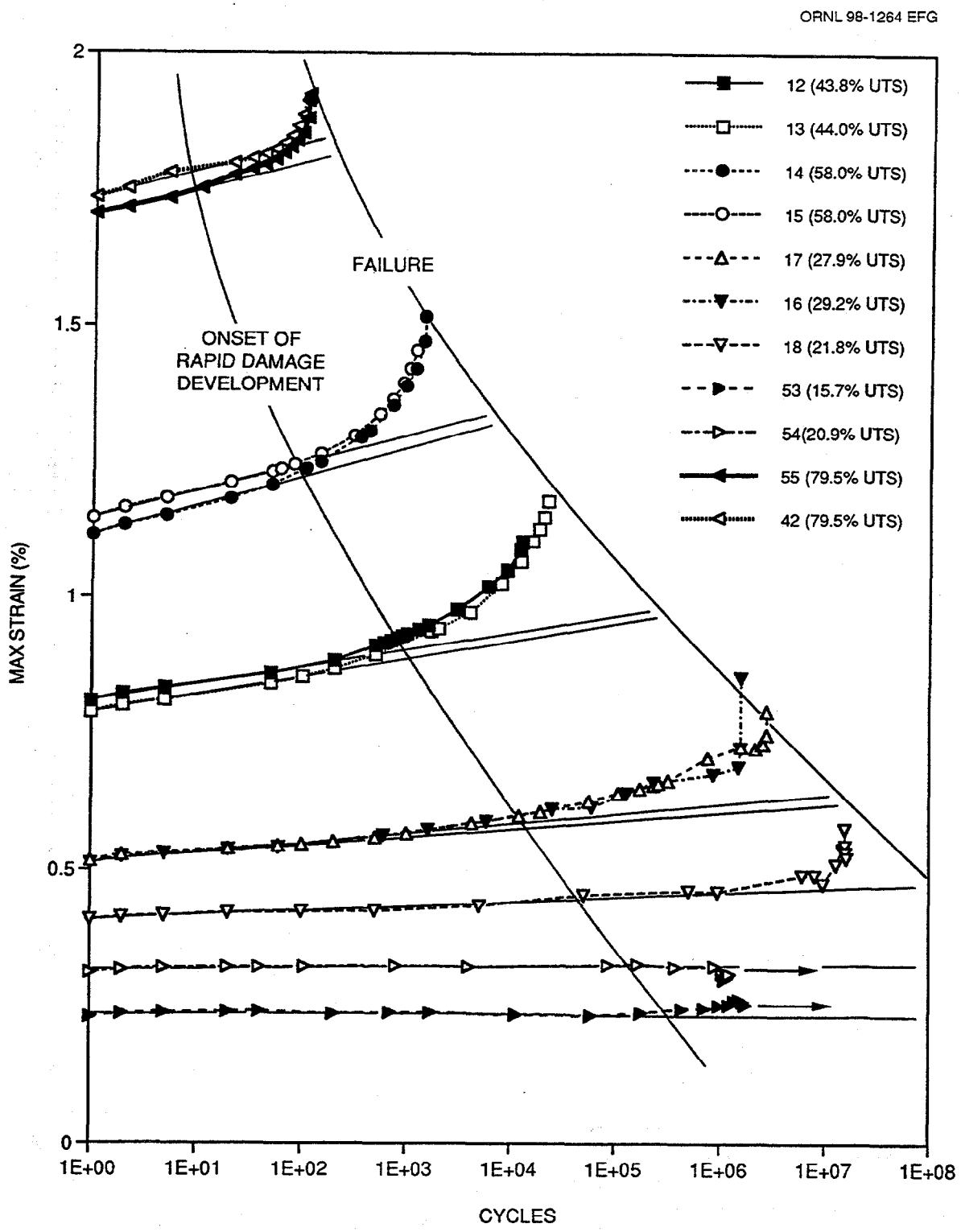

Fig. 10.7. Maximum strain vs cycles at room temperature.

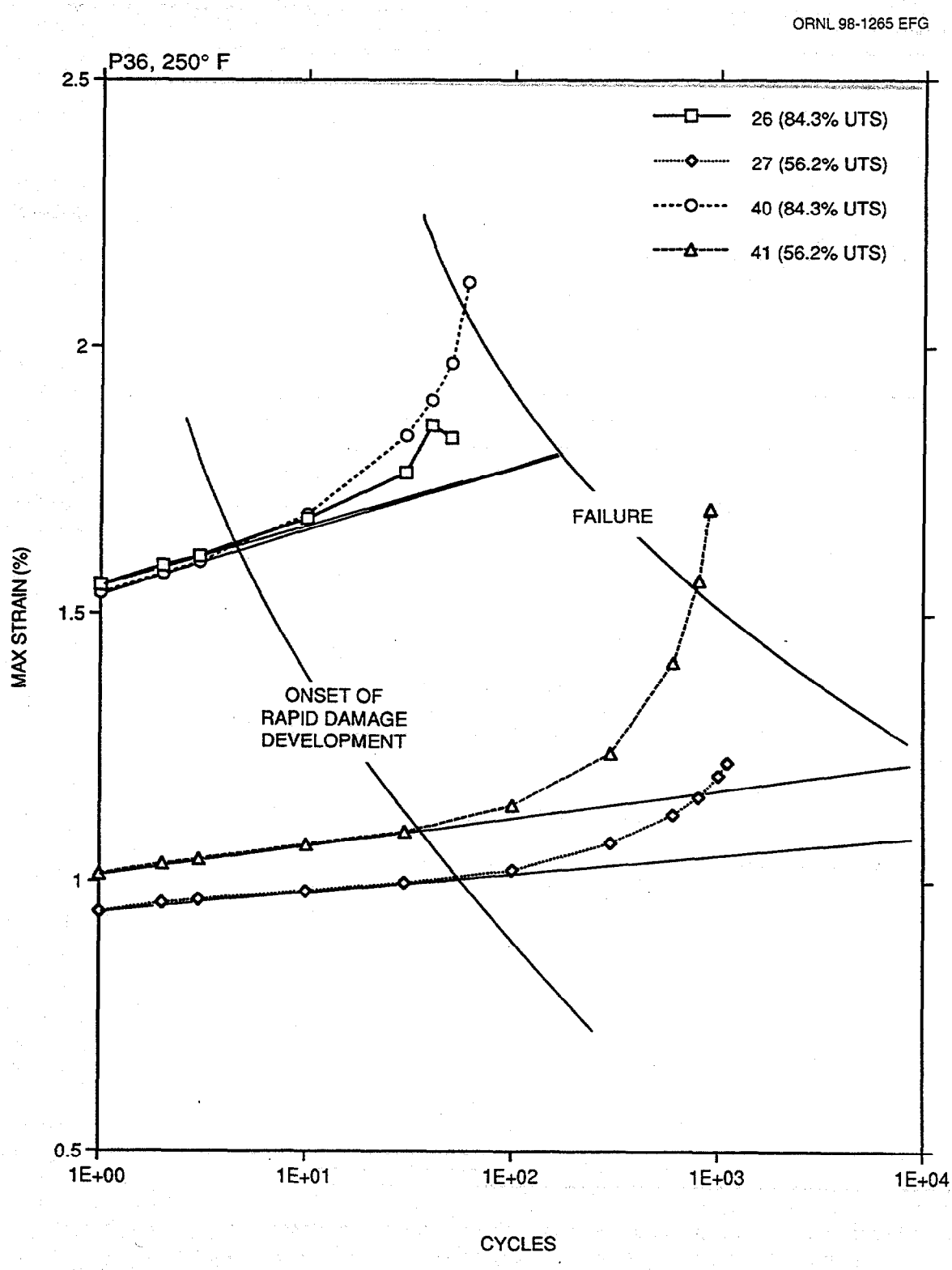

Fig. 10.8. Maximum strain vs cycles at 250°F.

Fig. 10.7. The initial portions of the curves are linear. From microscopic observations of fatigue specimens at various numbers of cycles, D. C. Worley III, of the University of Tennessee has suggested that this linear portion involves mostly matrix cracking (see Chap. 17). Later, where the curves turn up, fiber debonding becomes prevalent.

The initial straight portion of each curve was fit with a straight line (logarithmic curve) as shown. The slopes of these lines are linear with maximum stress, and they extrapolate to a slope of zero at a maximum cyclic stress level of 16.3% UTS, as shown in Fig. 10.9 (again, the two high stress tests at 79.5% UTS are out of line and were not used). Figure 10.9 suggests that the true endurance limit is 16.3% UTS.

Similar curve fits and slope plots at the other temperatures yield apparent endurance limits (zero slope) at 22.8% UTS for –40°F and 42.1% UTS for 250°F. In terms of absolute stress, the indicated endurances range from 4.2 ksi at room temperature to 7.1 and 7.5 ksi at –40°F and 250°F, respectively. Unfortunately, the conclusion for 250°F is suspect because of the paucity of P36 data and because tests on another plaque (P19) at 5.5 and 5.7 ksi failed at 2.6 and 1.4 million cycles, respectively.

10.4 DESIGN MARGINS

Design margins for fatigue ought to reflect some consideration of damage mechanisms. Stiffness reduction, for example, mirrors damage development to some extent. A limit of 10% stiffness reduction is sometimes used for design. Another possibility is to limit allowable cycles to prevent the onset of the rapid damage that was shown in Figs. 10.6–10.8. These two possibilities are plotted on S-N diagrams in Figs. 10.10–10.12 for –40°F, room temperature, and 250°F, respectively. The 10% reduction points were calculated for each test by the power laws previously described. The increased damage development points are from Figs. 10.6–10.8.

Also shown in Figs. 10.10–10.12 are various design margins on failure that are commonly used in metal fatigue—reduction factors of 10 or 20 on cycles and a reduction factor of 2 on stress. A factor of 20 on cycles would limit the stiffness reduction to 10%. However, even a factor of 2 on stress would not limit the onset of rapid damage at the higher cycles. Higher margins would be prohibitive; thus, some of the latter damage will likely have to be tolerated at the higher numbers of cycles.

10.5 CONCLUSIONS

1. The effect of temperature on fatigue strength is the same as on static strength; when maximum cyclic stress is divided by the static, at-temperature, UTS, a single fatigue curve can represent all temperatures.
2. The fatigue life at 10^8 cycles (the maximum cycle number considered in automotive structural design) is approximately 20% of the UTS.
3. Not counting tests at very high stress levels, the degradation in stiffness as a function of cyclic life fraction is relatively independent of stress and, in the first half of life, can be represented by power laws. The average end-of-life stiffness reduction from the power law fits is 16.5% at room temperature, 17.2% at –40°F, and 8.1% at 250°F.
4. The peak cyclic strain, when plotted as a function of cycles, is believed to reflect the accumulation of damage. Damage initially accumulates linearly with log cycles but then begins to accumulate more rapidly part way through the cyclic life. The lower the stress, the earlier in life (on a cycle fraction basis) the onset of rapid damage development occurs.
5. Assuming that zero initial slope of the maximum strain curves would mean that damage never develops, a room-temperature endurance limit of 16.3% UTS is indicated. The apparent endurance limit at –40°F is 22.8% UTS, and at 250°F, it is 42.1% UTS. The latter value is suspect because of insufficient data points.
6. A design margin of 20 on cycles would limit stiffness reduction to 10% during cycling. A larger factor of 2 on stress would limit rapid damage development at high stress, but not at low stress levels. Eliminating rapid damage development is probably too stringent in most cases, and some damage can likely be tolerated.[1]

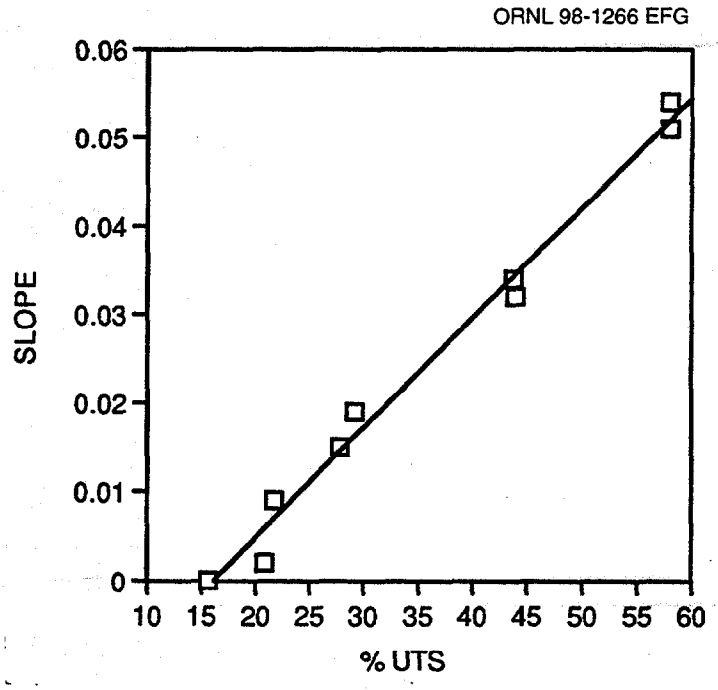

Fig. 10.9. Slope of initial straight lines in Fig. 10.7 vs maximum stress.

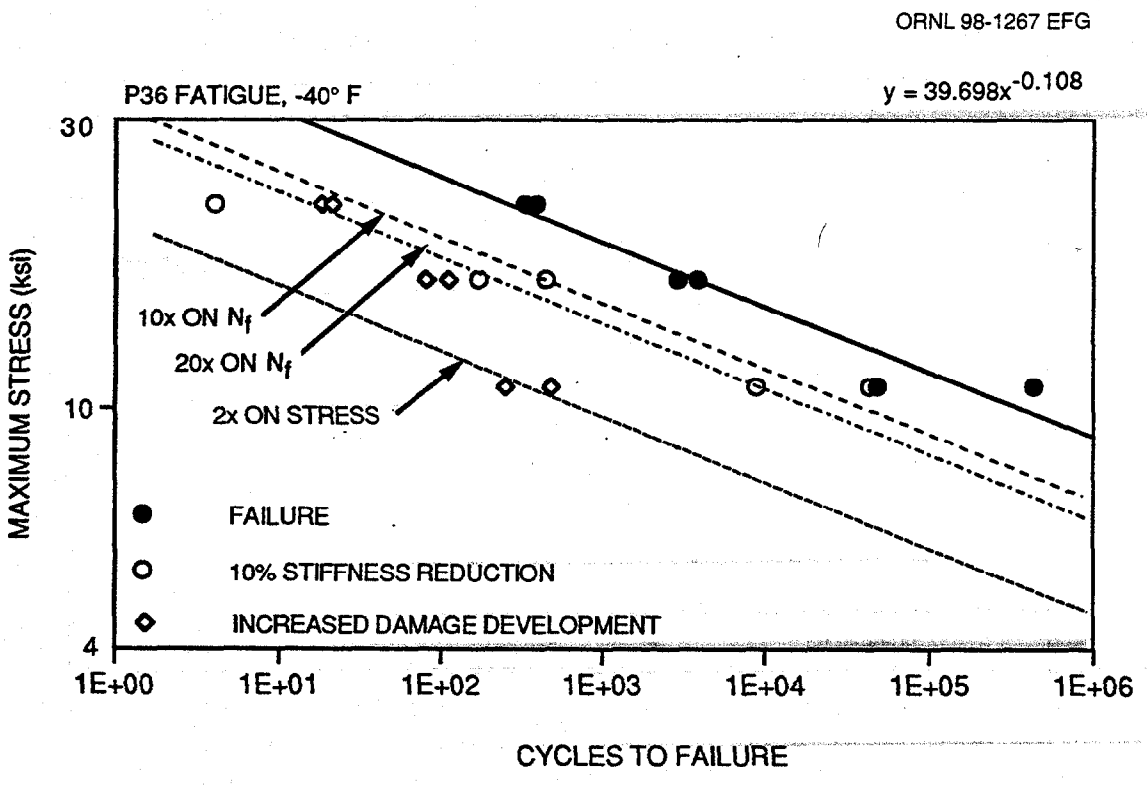

Fig. 10.10. Possible design margins relative to –40°F data.

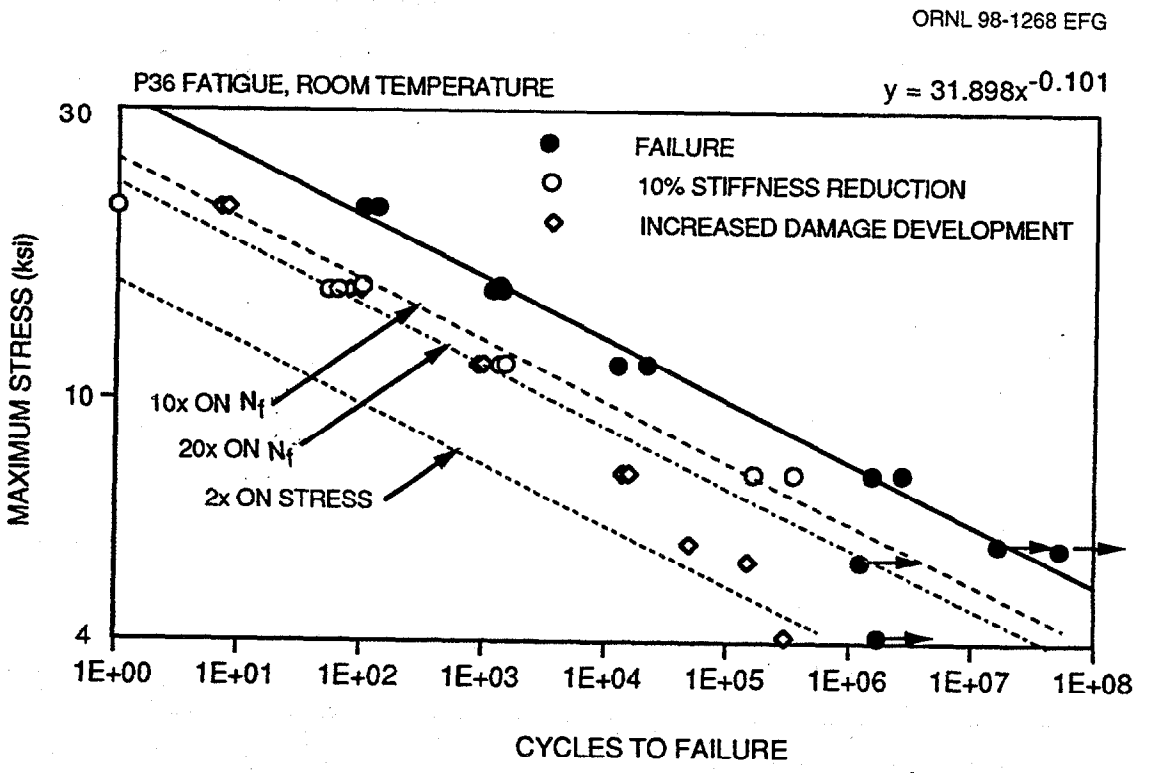

Fig. 10.11. Possible design margins relative to room-temperature data.

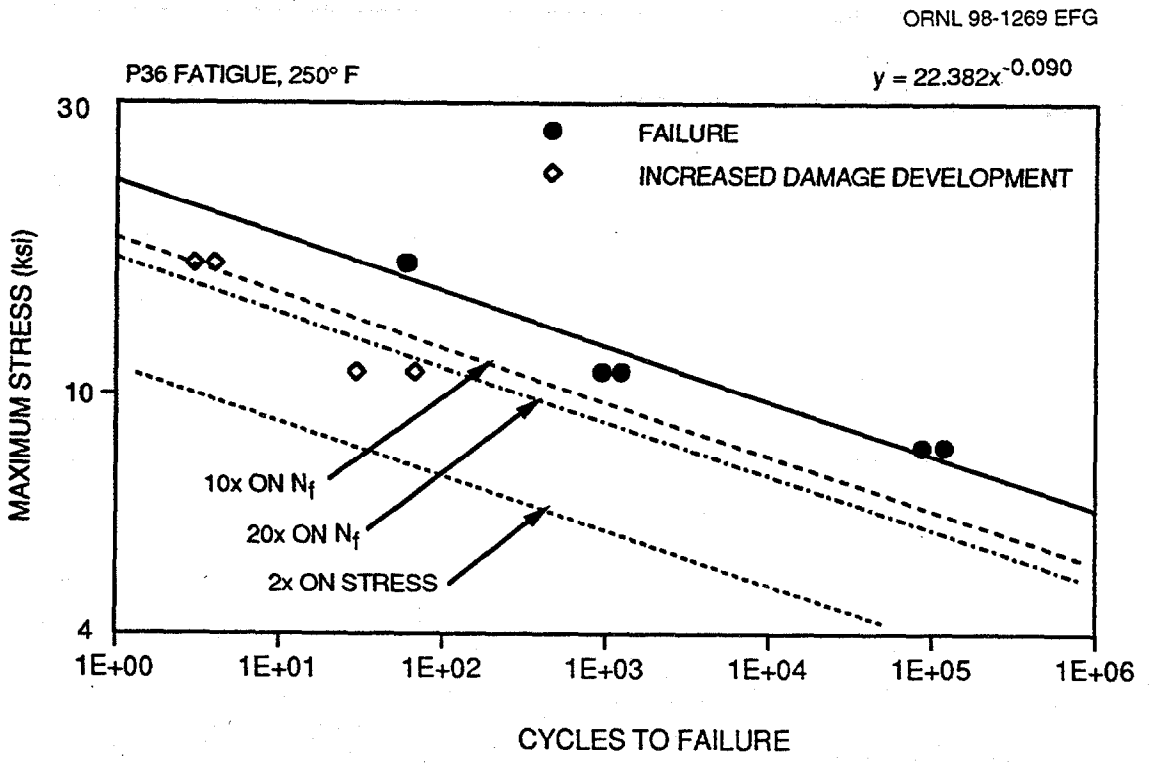

Fig. 10.12. Possible design margins relative to 250°F data.

REFERENCE

1. A. F. Johnson, *Engineering Design Properties of GRP*, The British Plastics Federation, London.

11. RECOMMENDED FATIGUE DESIGN

J. M. Corum, R. L. Battiste, and M. B. Ruggles

11.1 INTRODUCTION

The previous chapter analyzed fatigue data from a single plaque and developed conclusions relative to temperature effects, damage, and possible design margins. Here, fatigue data from other plaques are considered as well, and design curves are developed. Reduction factors for environmental effects are presented. Mean stress effects are assessed, and a method for handling them is proposed. Finally, the appropriateness of cycle fractions as a method of addressing multiple load cycles is addressed.

11.2 FATIGUE DESIGN CURVES

A total of 58 tensile fatigue tests on 0° specimens from 12 plaques has been performed at room temperature in ambient air. The specimens were either uniform, hourglass, or dogbone in shape, and the tests were performed in various test machines. Likewise, 20 fatigue tests on 90° uniform specimens from 5 plaques have been performed. All of these tests had a minimum to maximum stress ratio, R, of 0.1.

All of the data are plotted in Fig. 11.1, where maximum cyclic stress is expressed as a percentage of UTS. The UTS values used were the averages reported in Chap. 3 for all plaques tested (30 for the 0° direction and 25 for the 90° direction): $UTS_{0°} = 21.26$ ksi, and $UTS_{90°} = 28.40$ ksi. It is concluded from Fig. 11.1 that a single fatigue curve can adequately represent both 0° and 90° results when stress is normalized to the appropriate UTS value. The recommended design curves will be based on 0° data.

Figure 11.2 shows just the 0° specimen data with a power law representation of the failure data. The parallel dashed line is a visually drawn minimum of the data points. This line indicates that a reduction factor of approximately 7 on cyclic life is required to cover the data scatter.

Figure 11.3 depicts the same data with lines representing possible design margins of 20× on cycles or 2× on stress. As explained in Chap. 10, a factor of 20× on cycles would, on average, limit stiffness reduction to 10% during cycling. A larger factor of 2× on stress would limit rapid damage development (involving fibers) at lower cycles but not at higher cycles. It is recommended that the 20× on cycles be adopted. This factor will cover data scatter with more than 10× left over for other uncertainties.

The resulting design curve is shown in Fig. 11.4 labeled R = 0.* Note that this is a semilog plot to facilitate reading of stress values. Again, it is intended that this in-air curve apply for any strength or temperature, provided the proper UTS is used to obtain the stress. The second curve labeled R = –1 will be discussed in Sect. 11.4 relative to mean stress effects.

11.3. ENVIRONMENTAL EFFECTS

Room-temperature fatigue curves have been generated for seven different automotive fluids: brake fluid, motor oil, engine coolant, saltwater, distilled water, windshield washer fluid, and battery acid. In all cases, specimens were immersed for 100 h in the respective fluid and then tested in the fluid.

Because moisture is so important, fatigue curves were developed for three additional moisture conditions:

- specimens presoaked for 1080 h in 180°F demineralized water and then tested at room temperature in distilled water (condition designed to provide an extreme case of moisture degradation),
- pre-exposed 100 h and tested in > 90% RH, and
- pre-exposed 100 h and tested in < 10% RH.

*Note that the R = 0 design curve is based on the R = 0.1 data. It is believed that any difference between an R = 0.1 and an R = 0 curve would be small and easily absorbed by the 20× margin.

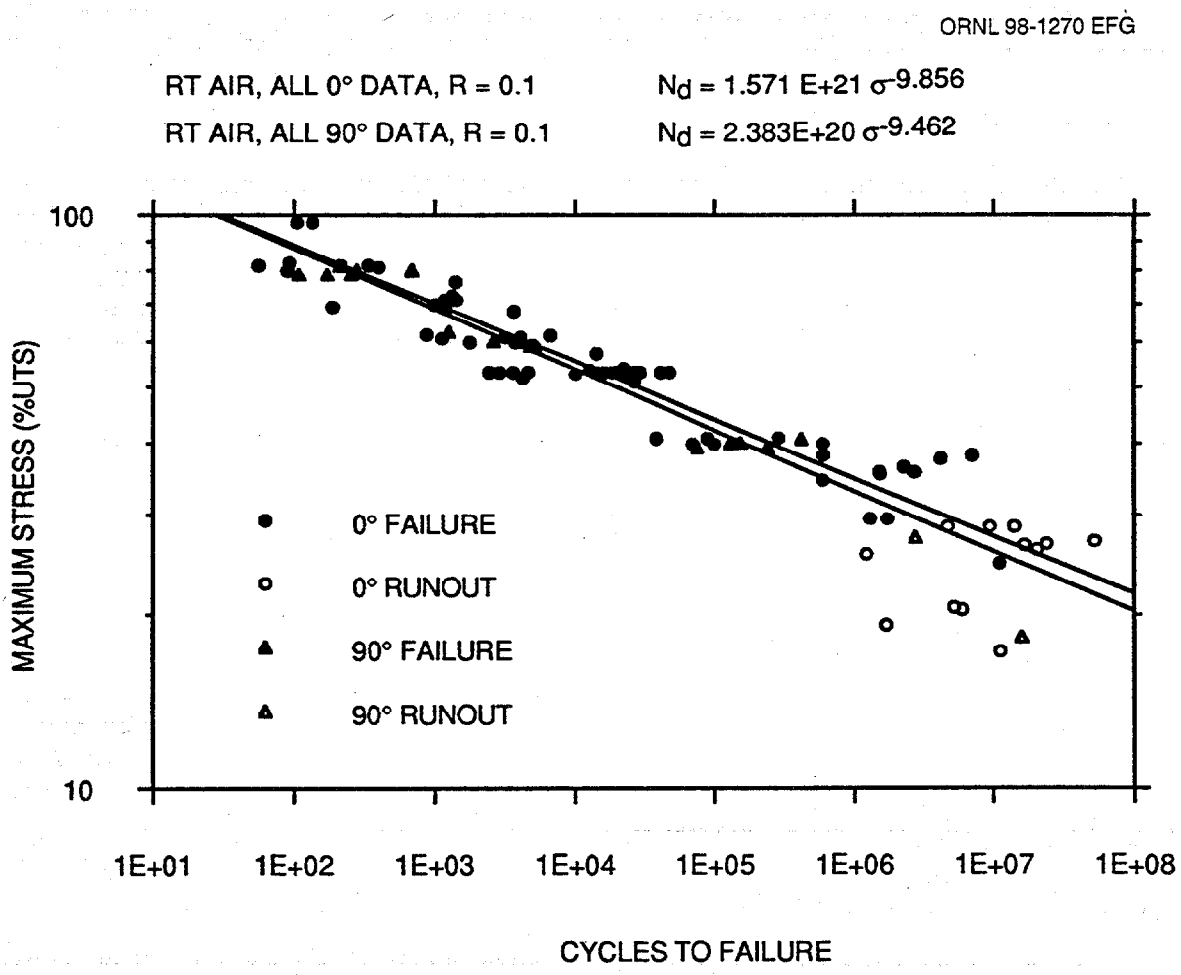

Fig. 11.1. Normalized S-N curve showing near-colinearity of 0° and 90° fatigue data. The lower curve fit represents the 90° data.

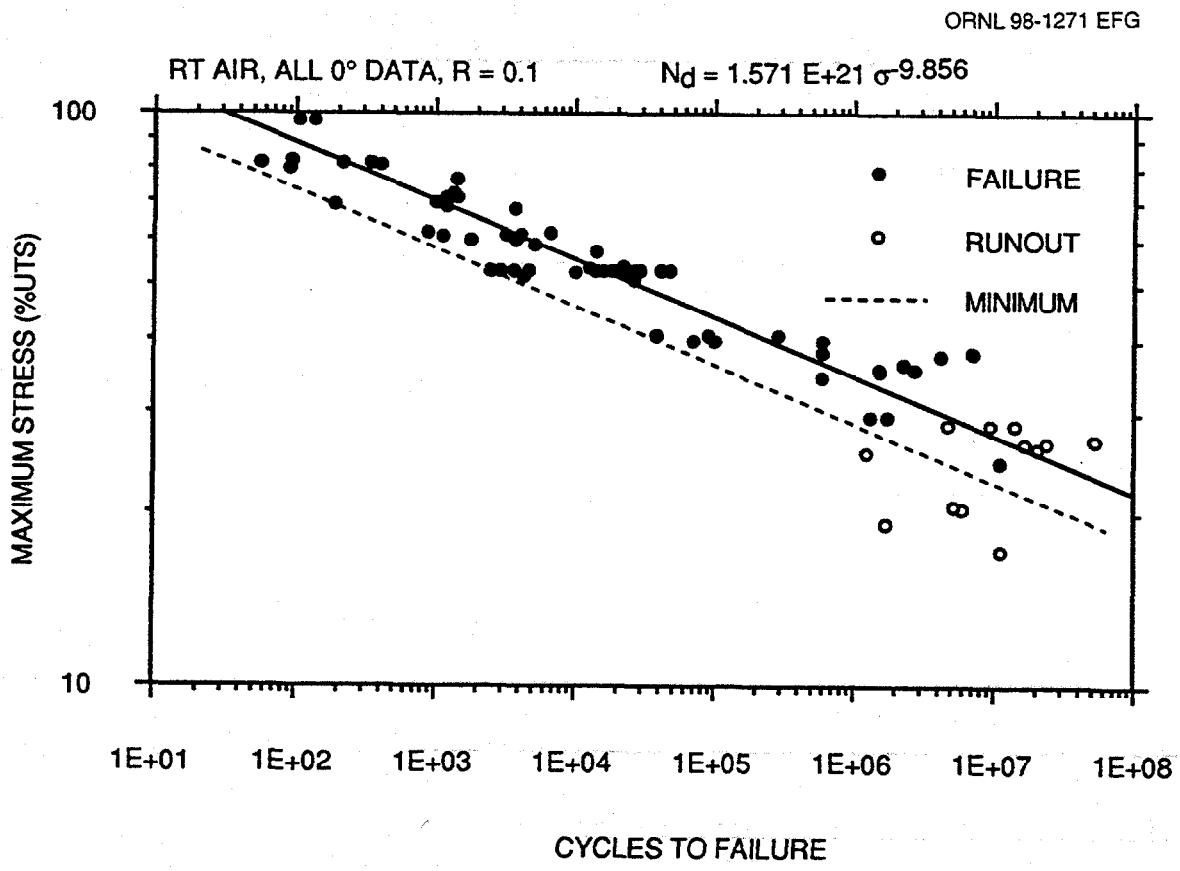

Fig. 11.2. Normalized 0° direction fatigue data with average and minimum representations.

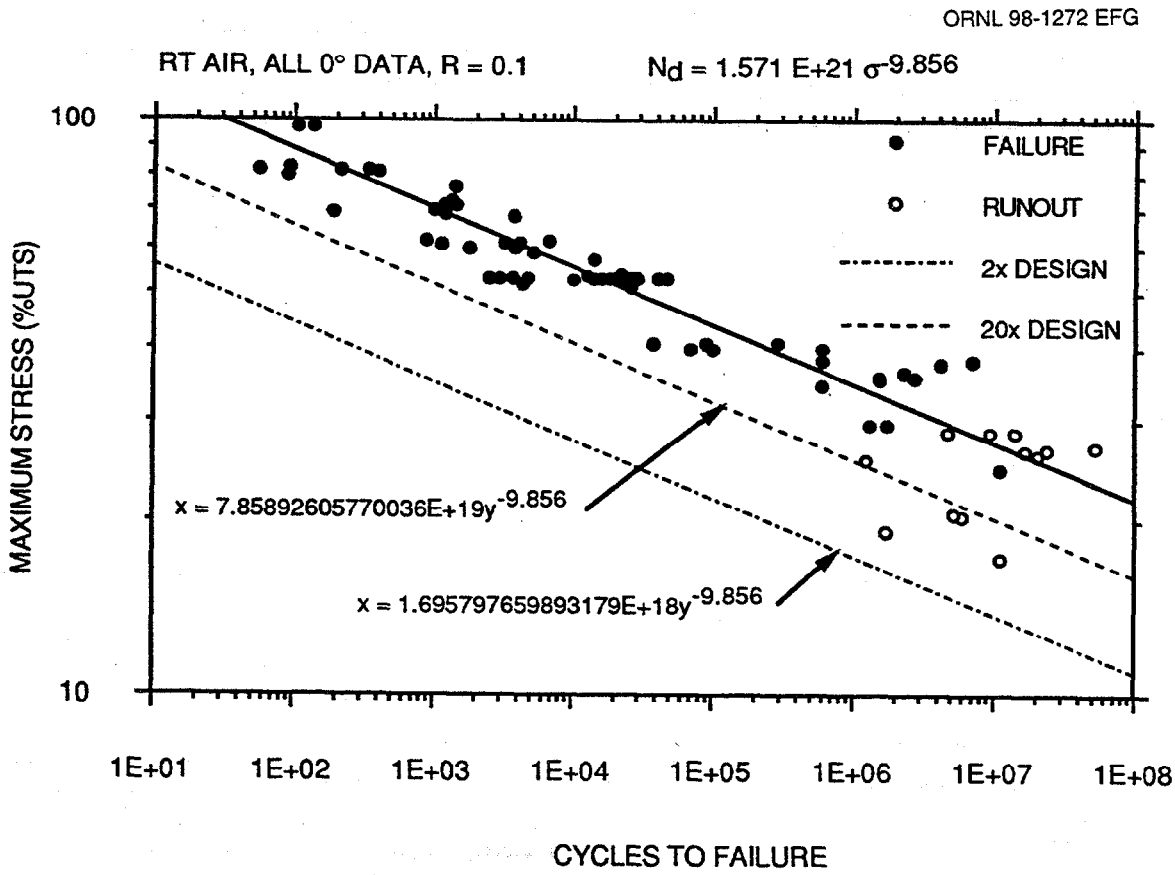

Fig. 11.3. Normalized 0° direction fatigue data with possible design margins. The 20× reduction on cycles is used in Fig. 11.4.

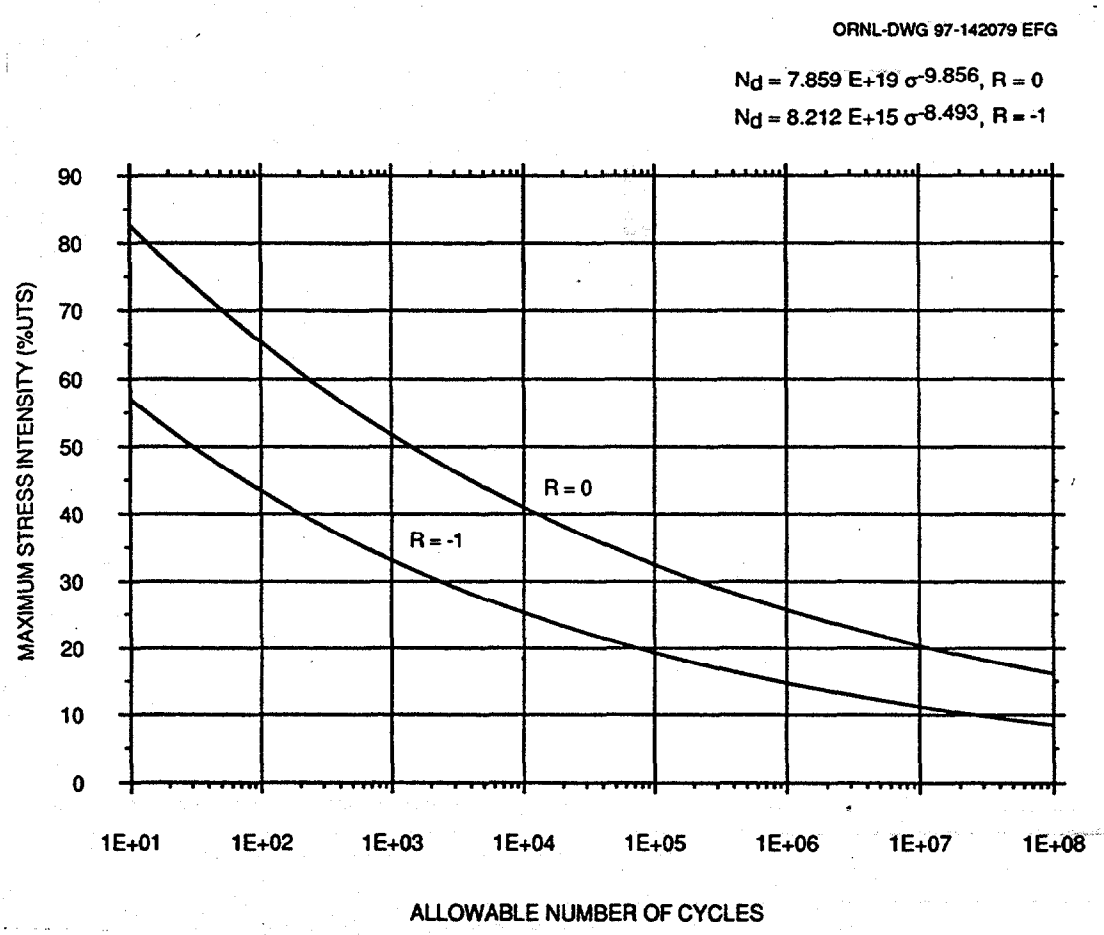

Fig. 11.4. Recommended fatigue design curves. These curves are applicable to both the 0° and 90° directions and to temperatures over the range from –40 to 250°F when the normalized stress is multiplied by the appropriate UTS.

The 180°F exposure had a very significant degrading effect on fatigue. Wet and dry air had little, if any, effect.

In each case, the environmental curve was compared with the corresponding ambient air curve (for the same specimen configuration), as illustrated in Fig. 11.5 for distilled water. The hourglass curve for distilled water was compared with the hourglass curve for air (using power law curve fits) to develop reduction factors at various numbers of design cycles. The resulting factors for distilled water, as well as factors similarly obtained for the other conditions, are shown in Table 11.1. These factors should be used to reduce the cyclic design stress obtained from Fig. 11.4.

In considering the factors in Table 11.1, it should be realized that there is an infinite variety of exposure conditions to which automotive structures could be subjected. The factors in the table were, with the exception of the 180°F water exposure, obtained on specimens submerged for 100 h prior to testing and then tested in the fluid (receiving more than 60 h additional exposure at 10^6 cycles). These are believed to represent reasonably extreme bounding conditions for design. Note that the projected factors for distilled water and for 180°F, 1080 h water at 10^6 cycles are essentially the same, indicating that the specimens are nearly saturated and responding equally at that point. This adds some confidence to the factors.

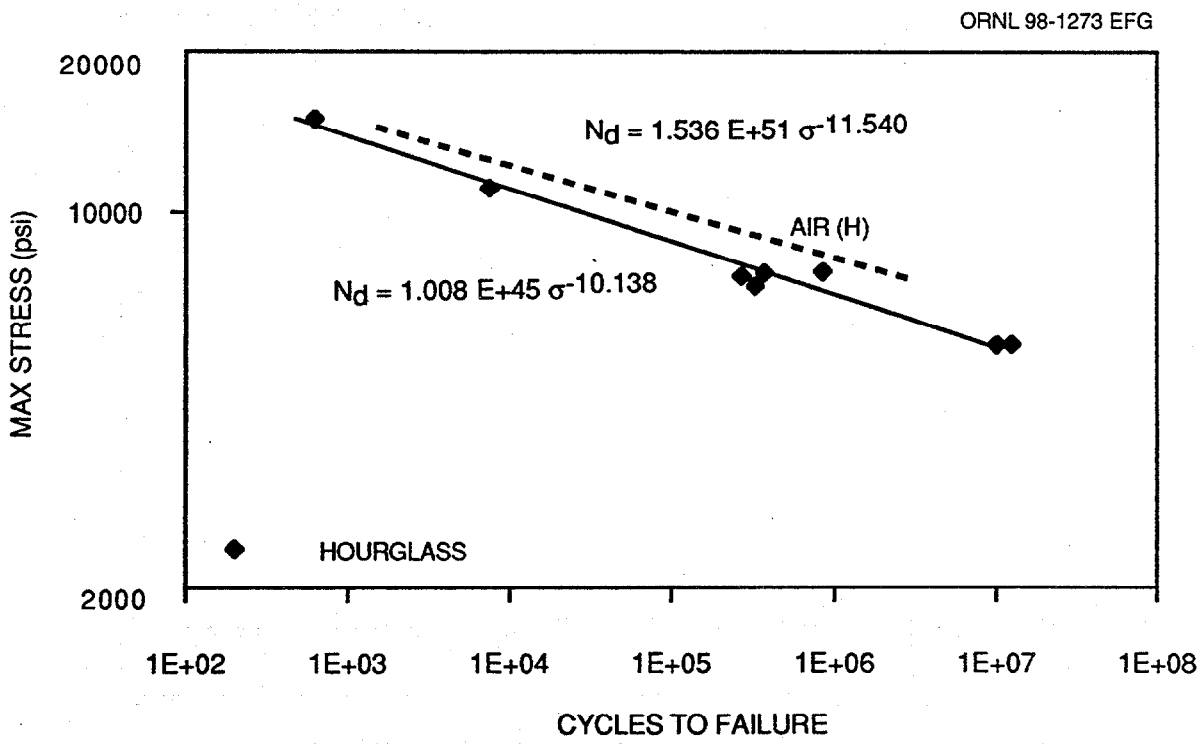

Fig. 11.5. Distilled water fatigue data and power law fits to data and to corresponding ambient air data.

Table 11.1. Fatigue stress reduction factors for various automotive fluid environments

Fluid	Cycles			
	1×10^2	1×10^4	1×10^6	1×10^8
Air	1.00	1.00	1.00	1.00
Brake fluid	1.00	1.00	0.99	0.94
Motor oil	1.00	0.98	0.91	0.84
Engine coolant	1.00	1.00	0.87	0.71
Saltwater	1.00	0.95	0.86	0.78
Distilled water	0.95	0.90	0.85	0.81
Windshield wash	1.00	0.97	0.84	0.73
180°F water, 1080 h	0.64	0.69	0.74	0.80
Battery acid	1.00	0.73	0.50	0.34

11.4 TREATMENT OF MEAN STRESSES

The fatigue data and curves discussed to this point were all tensile fatigue with R = 0.1 (assumed to be applicable to R = 0 as well). These tests probably represent the most common automotive loading condition, so the results are often directly applicable. More generally, however, a cyclic stress of amplitude σ_a is imposed on a mean stress, σ_m. A procedure is needed to handle these situations, because mean stress can have a significant effect.

Owen and Smith[1] have investigated mean stress effects in a composite with similar behavioral characteristics to our CSM/isocyanurate composite. Normally, a master diagram showing the relationship between stress amplitude (cyclic stress range divided by two) and mean stress for various cyclic lives is considered to be the most desirable form of fatigue data. When insufficient test results are available for a master diagram to be produced, as is our case, something akin to the Goodman relation must be used. Three possibilities have been assessed by Owen and Smith:[1]

1. Goodman relation:

$$\sigma_a = \sigma_o \left(1 - \frac{\sigma_m}{\sigma_{ult.}}\right),$$

2. Goodman with creep-rupture strength:

$$\sigma_a = \sigma_o \left(1 - \frac{\sigma_m}{\sigma_r}\right), \quad \text{and}$$

3. modified Goodman with creep-rupture strength:

$$\sigma_a = \sigma_o \left(\frac{1 - \frac{\sigma_m}{\sigma_r}}{1 + \frac{\sigma_m}{\sigma_r}}\right).$$

All of these relations give the stress amplitude, σ_a, in a test with a mean stress, σ_m, in terms of the stress amplitude, σ_o, in a completely reversed, zero mean stress (R = –1) test having the same cyclic life. The second relation is attributed to Boller; Owen and Smith proposed the third relation to add conservatism. These latter two use the creep-rupture strength, σ_r, corresponding to the test time rather than the short-time ultimate.

To assess these relations, a limited amount of mean stress fatigue data has been generated on the CSM/isocyanurate. Figure 11.6 shows data and an experimental curve for zero mean stress compared to the R = 0 (0.1) data and curve. The R = 0 tests had a mean stress equal to one-half the maximum; the amplitude was also one-half the maximum. In the R = –1 case, the maximum stress and the amplitude, σ_o, are the same.

With the R = –1 curve giving σ_o, σ_a for the R = 0 case can be predicted using the relations given previously. The dashed lines depict the resulting predictions. The top dashed curve is from the usual Goodman relation, using the UTS. The middle curve is from the Goodman relation with σ_r corresponding not to the test time, but to 3000 h, the assumed operating life of an automobile and, hence, the maximum time a structure would be subjected to fatigue cycles.* The bottommost conservative curve is from the modified Goodman relation, with σ_r again corresponding to 3000 h.

The second relation, Goodman with σ_r used in place of the UTS, is recommended for design use. It is conservative relative to the R = 0 failure curve but not excessively so at the higher cycles. The R = –1 design curve in Fig. 11.4 corresponds to the curve in Fig. 11.6 with a design margin of 20× on cycles to failure. In cases involving a fixed nonzero mean stress, the R = –1 curve, which gives the allowable σ_o, should be used to determine the allowable stress amplitude, σ_a, corresponding to the mean stress σ_m. The σ_r value should be the 3000-h creep-rupture strength.

*5000 h is a more conservative operating time and is thus used in Part 1.

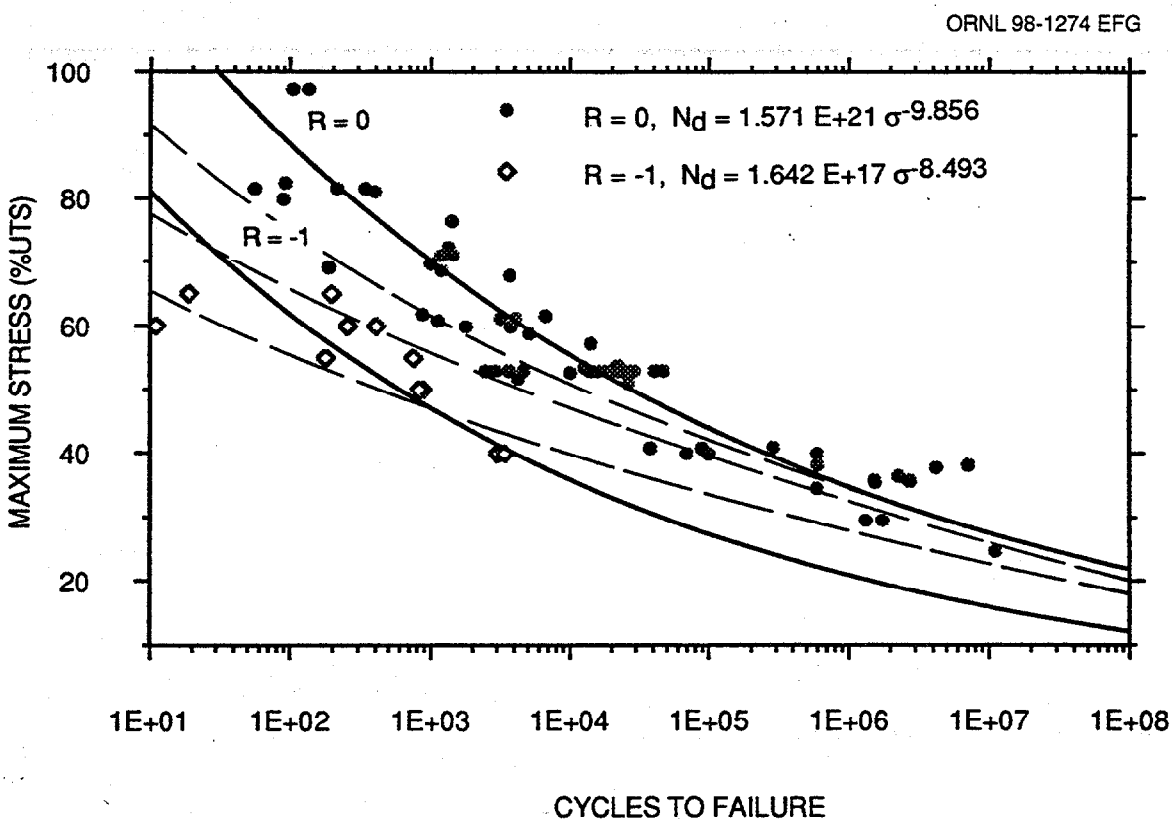

Fig. 11.6. Comparison of R = 0 and R = –1 (zero mean stress) fatigue data. The dashed lines are predictions for R = 0 based on the R = –1 curve using the following Goodman relations.

- Top curve: Goodman with UTS
- Middle curve: Goodman with σ_r corresponding to 3000 h
- Lower curve: modified Goodman with σ_r corresponding to 3000 h

The preceding discussion is for tensile mean stresses. Data have been generated for compression-compression fatigue (R = 0.1). The results are shown in Fig. 11.7 compared with the R = 0.1 tension-tension and the R = –1 fully reversed curves presented earlier. Clearly, compressive cycling is less damaging than tensile cycling for the reference composite. Thus, the design curves in Fig. 11.4 can be used for compression cycling by using the absolute values of the stresses.

11.5 TREATMENT OF CYCLES OF VARYING AMPLITUDES

A small matrix of block loading tests was carried out on 0° specimens from plaque P42. All tests involved just two stress levels—30% and 60% of the P42 UTS of 23.44 ksi. Three duplicate tests were planned at each of the following maximum stress conditions:

- 30% UTS } Baseline to determine N_f at each stress
- 60% UTS }
- 30/60% UTS
- 60/30% UTS

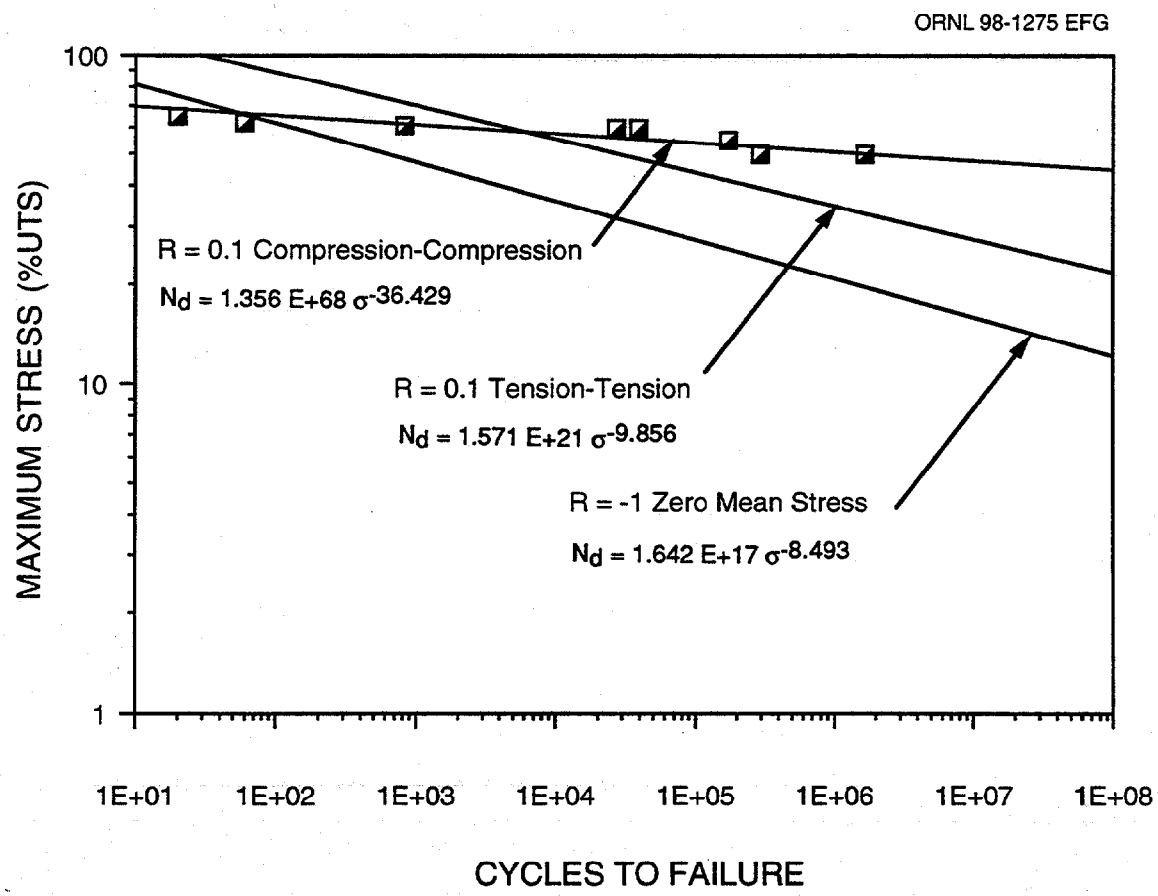

Fig. 11.7. Compression-compression (R = 0.1) fatigue data compared to tension-tension and fully reversed fatigue data.

result in a predicted stiffness reduction of 10%.* The logic for this choice was that even though the cycle fraction at a reduction of 10% is very low, a major amount of damage may have occurred by this point.

Results of the tests are tabulated in Table 11.2.

For metals, Miner's rule, $\Sigma(n/N_f) = 1$, is commonly used. Here, as in past experimental studies,[2] it is difficult to draw firm conclusions regarding the applicability of Miner's rule because of the small size of the data set and the inherent scatter. Based on the numbers in Table 11.2, the average cycle fraction summations for the two block loading series are 30/60: 0.019 + 0.803 = 0.822 and 60/30: 0.015 + 0.578 = 0.593. These numbers are not far out of line with the findings for metals, where cycle fraction summations are quoted as varying from 0.5 for high-low loadings to 5.0 for low-high loadings. The design margin of 20 on cycles can absorb these variations from a value of 1.

11.6 SUMMARY

The following key observations and recommendations have been made:

- Tensile fatigue (R = 0.1) at temperatures ranging from –40 to 250°F and for both the 0° and 90° plaque directions can be represented by a single S-N curve, provided the stress is expressed as a percent of the appropriate UTS.
- A margin of 20 on average cycles to failure is recommended.

*Based on a curve fit to the 10% modulus reduction points for P36 shown in Fig. 10.11 of Chap. 10.

Table 11.2. Results of block loading tests

Test condition (% UTS)	n_1	n_2^a	Average n_2^a
30	0	13,951,961	9,190,026
		4,264,592	
		9,353,524	
60	0	2,712	2,528
		2,086	
		2,787	
30/60	172,540	3,752	2,029
	172,540	849	
	172,540	1,487	
60/30	37	4,782,169	5,307,658
	37	5,320,480	
	37	5,820,324	

[a] n_2 = cycles to failure at second stress.

- Two design fatigue curves are given: one for tensile (or compressive) fatigue (R = 0) and one for completely reversed fatigue (R = –1).
- For cycles with a fixed mean stress, a Goodman relation that employs a 5000-h creep-rupture strength is recommended.
- A table of fatigue stress reduction factors is given to cover the degrading effects of various automotive fluid environments.
- Miner's rule is recommended for assessing cycles of varying amplitudes.

REFERENCES

1. A. F. Johnson, *Engineering Design Properties of GRP*, The British Plastics Federation, London.
2. M. J. Owen and R. J. Howe, "The Accumulation of Damage in a Glass-Reinforced Plastic Under Tensile and Fatigue Loading," in *J. Phys. D: Appl. Phys.* **5**, 1637–1649 (1972).

12. EFFECTS OF PRIOR STATIC, CYCLIC, AND SUSTAINED LOADINGS

J. M. Corum, W. Ren, R. L. Battiste, and M. B. Ruggles

12.1 INTRODUCTION

Four systematic, room-temperature ambient air test series have been undertaken to quantify the effects of prior loading on subsequent strength and stiffness:

- effect of prior static tensile loading on residual stiffness,
- effect of prior fatigue cycles on tensile strength and stiffness,
- effect of prior fatigue cycles on creep-rupture strength, and
- effect of prior creep on tensile strength and stiffness.

The results will be discussed in the following four sections.

12.2 EFFECT OF PRIOR STATIC LOADING

A series of six 0° specimens from plaque P42 were loaded as follows: to 20% UTS and unloaded, to 40% UTS and unloaded, to 60% UTS and unloaded, and to 80% UTS and unloaded. After each unloading, the stiffness was determined. The resulting measurements are plotted in Fig. 12.1 as the change in stiffness relative to the virgin P42 average stiffness of 1.48 Msi.*

The figure indicates that loadings below 29.6% UTS do not cause any resulting stiffness loss and, presumably, produce no damage. The maximum predicted degradation, at failure, is 13.1%.

12.3 EFFECT OF PRIOR FATIGUE CYCLES ON TENSILE PROPERTIES

A series of 0° specimens from plaque P34 were subjected to tensile (R = 0.1) fatigue cycles to various fractions of the predicted cyclic life. The specimens were then monotonically tensile tested to failure. Table 12.1 shows the matrix of tests.

The resulting tensile strengths were compared with the virgin average P34 0° UTS of 22.6 ksi. The average results are shown in Fig. 12.2 as a function of cyclic life fraction. Ignoring the highest fatigue stress, which produces major damage upon the initial loading, the residual tensile strength decreases linearly with the fatigue usage factor. Note that with the recommended design margin of 20 on cyclic life,† the strength reduction will be only about 1.5%.

Plots of stiffness reduction vs cyclic life fraction, n/N_f, were given in Chap. 10 (Figs. 10.3–10.5). The room-temperature plot is reproduced in Fig. 12.3. The curves shown are from tests of 0° specimens from plaque P36. The maximum cyclic stresses reached in these R = 0.1 fatigue tests are shown as a percentage of the average 0° UTS of 26.0 ksi for plaque P36.

The curves form a relatively close band, and they are well fitted by power laws up to at least $n/N_f = 0.5$. The average of these, which do not include the upturn near $n/N_f = 1$ exhibited by some specimens, predicts an end-of-life stiffness reduction of 16.5%. This is somewhat higher than the 13.1% end-of-life stiffness loss predicted for static tensile loadings.

With the recommended fatigue design margin of 20 on cyclic life, it can be seen from Fig. 12.3 that the stiffness reduction is limited to ≤10%. A stiffness reduction of 10% has been used as a design criterion for composites.

---

*See also Chap. 3, Sect. 3.2.

†See Chap. 11, Recommended Fatigue Design.

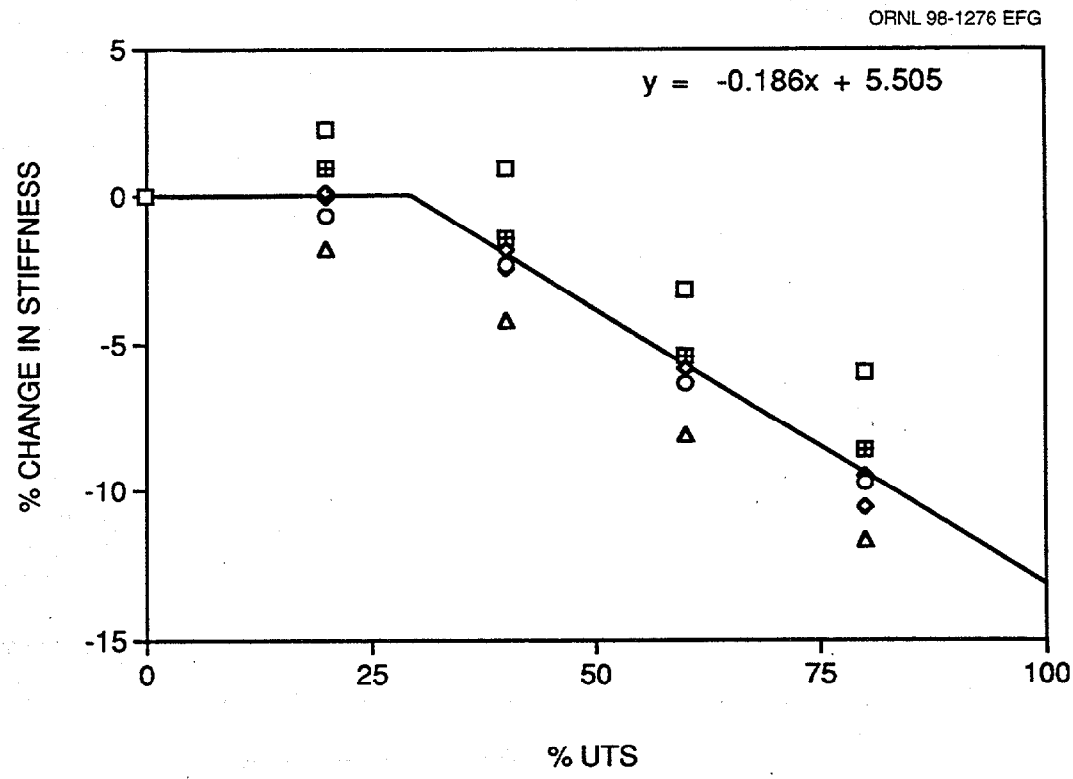

Fig. 12.1. Loss of stiffness due to prior static tensile loadings to indicated levels. Each symbol represents results from one specimen.

Table 12.1. Test matrix (number of duplicate specimens) for effect of prior fatigue on tensile properties (P34–0°)

Fatigue cycles $(n/N_f)^a$	Maximum stress (% UTS)^b			
	71.8	53.9	35.9	26.9
0.25	2	2	2	1
0.5	2	2	2	1
0.75	2	2	2	1

$^a N_f$ = 566 for 71.8% UTS.
N_f = 12,018 for 53.9% UTS.
N_f = 891,800 for 35.9% UTS.
N_f = 1.89×10^7 for 26.9% UTS.
^{b}UTS = 22.6 ksi.

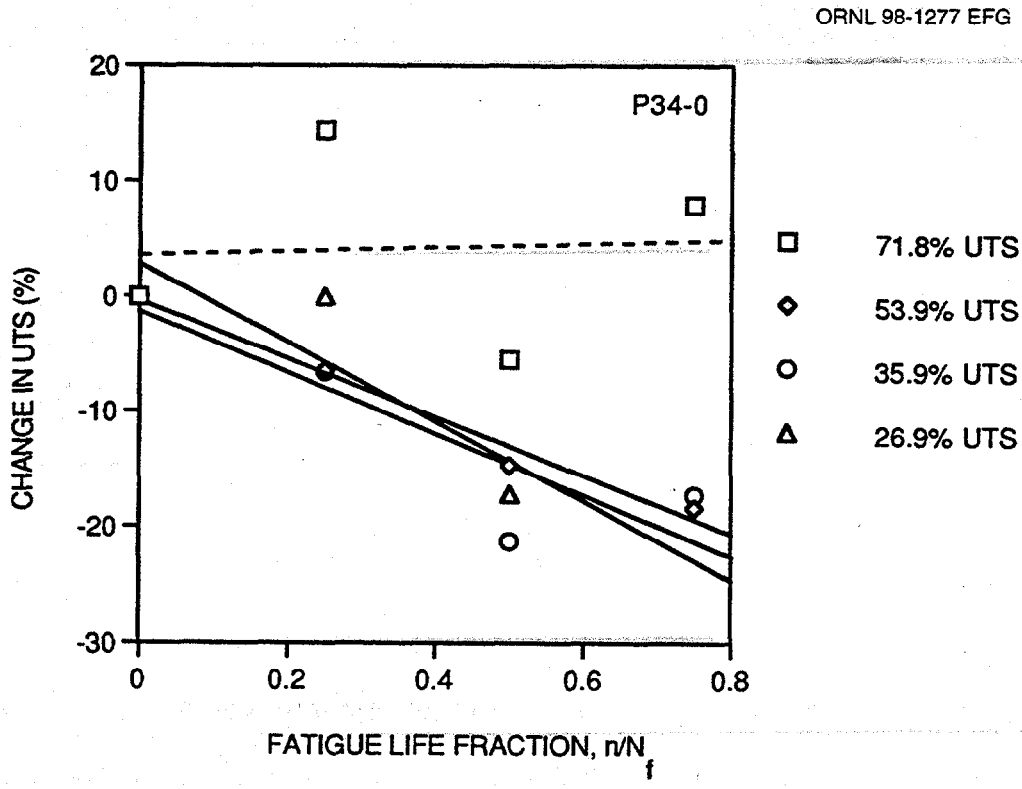

Fig. 12.2. Reduction in tensile strength vs prior cyclic life fraction.

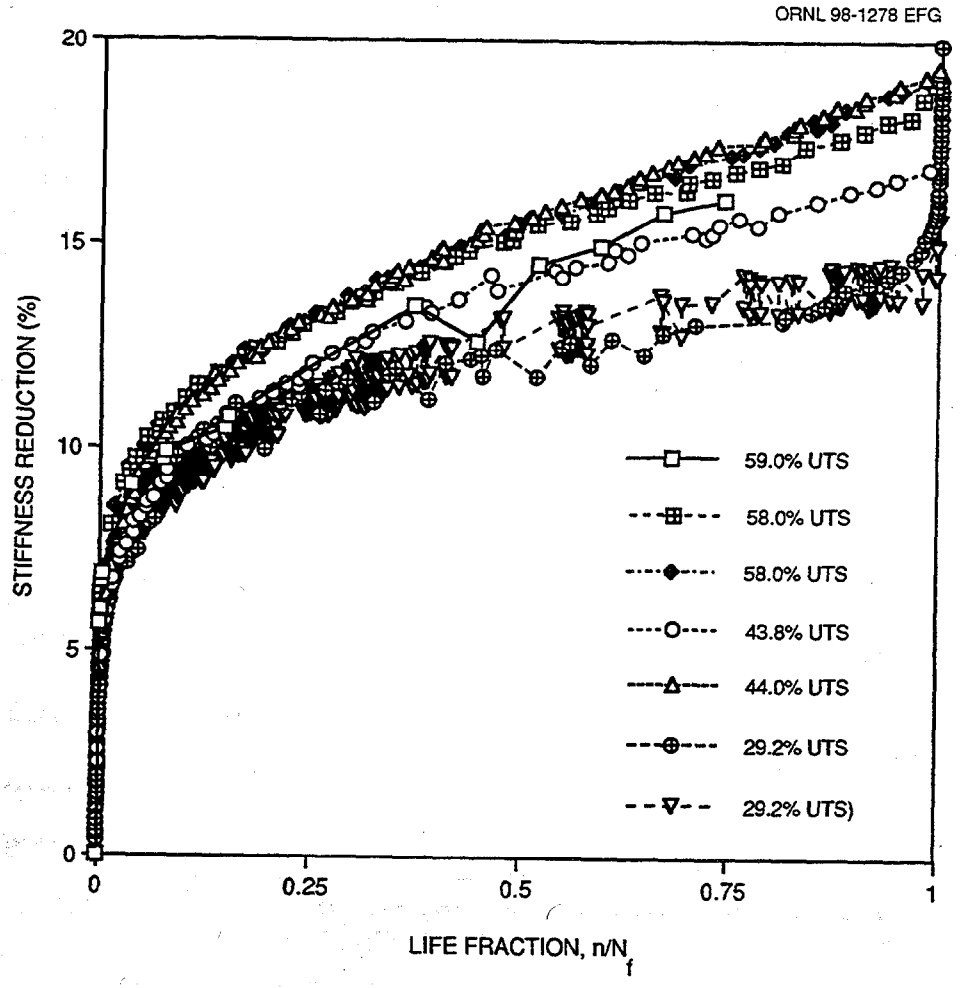

Fig. 12.3. Stiffness reduction vs cyclic life fraction.

12.4 EFFECT OF PRIOR FATIGUE CYCLES ON CREEP-RUPTURE STRENGTH

The tests described here are shown in Table 12.2 and are companions to the tests described in the previous section. The stress levels and life fractions used here were used there as well. In this case, creep tests were performed on the prefatigued specimens. The creep stress level was the same as the maximum fatigue stress—either 71.8% or 53.9% of the plaque P34 UTS of 22.6 ksi.

The creep-rupture results are plotted in Fig. 12.4. The top curve and equation are taken from Chap. 8. They represent the average creep-rupture response of several plaques in room-temperature ambient air. The

Table 12.2. Test matrix for effects of prior fatigue on creep-rupture strength (P34–0°)

Fatigue cycles (n/N_f)	Maximum stress (% UTS)	
	71.8	53.9
0.25	2	2
0.75	2	2

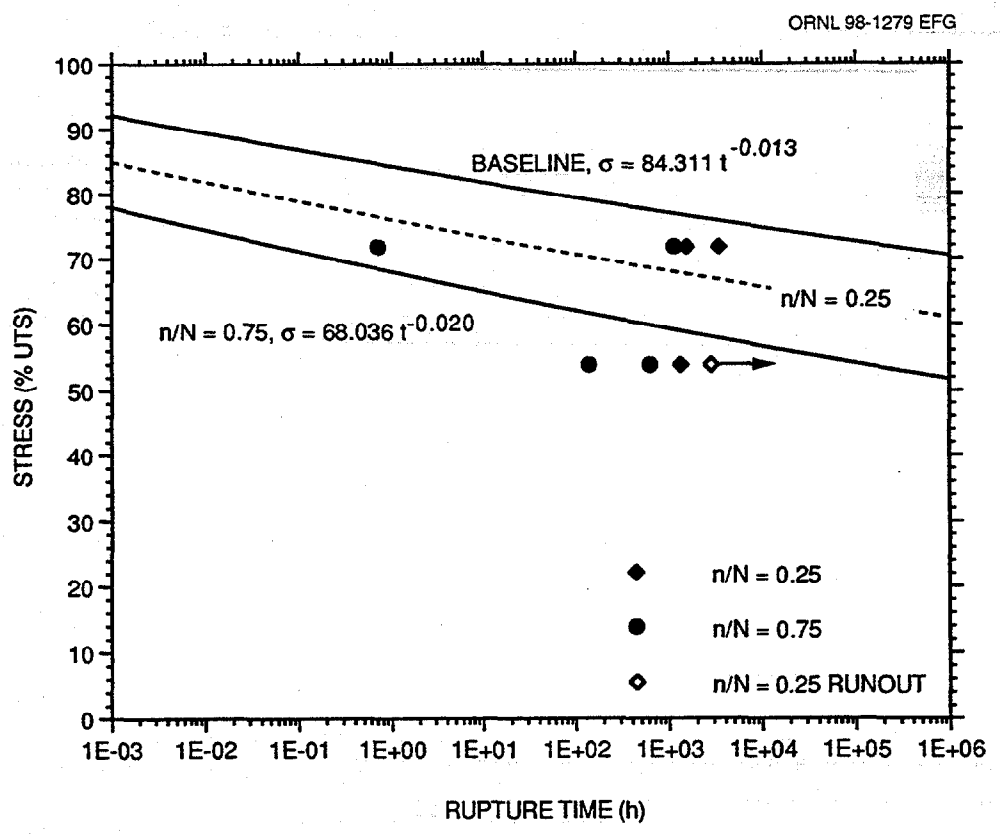

Fig. 12.4. Comparison of creep-rupture curves for various amounts of prior fatigue damage.

lower curve is a power law fit to the four disparate $n/N_f = 0.75$ data points. Although the fit looks questionable, the result is very consistent with results reported by Howe and Owen for a glass chopped strand mat/polyester resin laminate.[1] For example, at 100 h rupture time, they found the $n/N_f = 0.75$ stress rupture value to be 82% of the baseline value. Our comparable number is 78%. Our $n/N_f = 0.25$ data points are insufficient to determine a curve. The Howe and Owen results indicate the 0.25 curve is halfway between the baseline and $n/N_f = 0.75$ curves. We have drawn our dashed curve there as an educated guess.

Because the creep-rupture strength reductions increase with rupture time, the maximum values correspond to the 15-year life of a car (131,400 h). These values are as follows:

n/N_f	Maximum creep-rupture strength reduction (%)
0.25	12.9
0.75	25.7

With a fatigue design margin of 20 on life ($n/N_f = 0.05$), the creep-rupture strength reduction would be 2 to 3% at most.

Each of the eight creep deformation curves from the tests in Table 12.2 have been graphically compared with the average baseline creep representation. With the exception of the specimen that failed in less than 1 h (see Fig. 12.4), the corresponding creep curves were surprisingly similar. Some were the same, and some were up to 20% different, either way. Therefore, there is no apparent consistent effect of prior fatigue on creep deformation.

12.5 EFFECT OF PRIOR CREEP ON TENSILE STRENGTH AND STIFFNESS

Table 12.3 gives the matrix of tests carried out on 0° specimens from plaque P20 to assess the possible effects of prior creep deformation on tensile properties.

In addition to the tests in Table 12.3, three P20 specimens were creep tested to rupture at each of the three creep stress levels specified in Table 12.3. The 13-ksi tests are still in progress, but the creep failure strains at both 15 and 17 ksi averaged 0.49%. Thus, on a creep-strain fraction basis, the prior creep-strain levels of 0.1, 0.2, and 0.3% correspond to 20, 41, and 61% of rupture life.

The results are plotted in Figs. 12.5 and 12.6, which show the change from the virgin tensile strength and stiffness, respectively, for each value of prior creep strain. Each point represents the average of three tests. If there is a trend apparent in Fig. 12.5, it is toward a slight increase in subsequent tensile strength. Prior creep does not degrade tensile strength.

Table 12.3. Test matrix (number of duplicate specimens) for effects of prior creep on tensile properties

Creep strain	Creep stress [% UTS (ksi)]			
(%)	0	55.6(13)	64.1(15)	72.6(17)
0	5[a]			
0.1		3	3	3
0.2		3	3	3
0.3		3	3	3

[a]Virgin tensile tests to establish baseline properties (UTS = 23.4 ksi, E = 1.49 Msi).

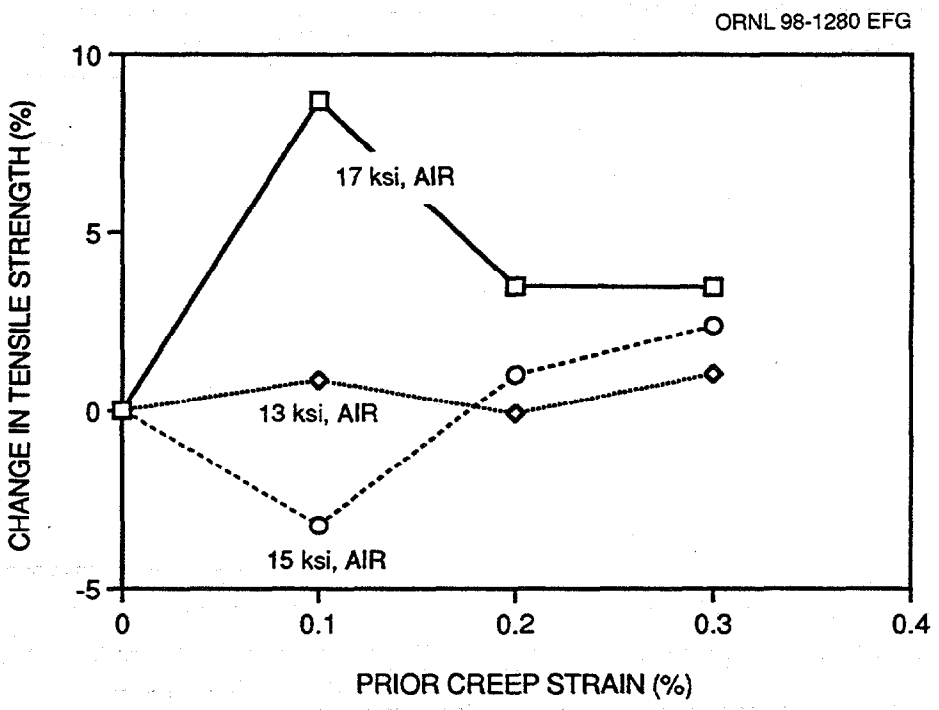

Fig. 12.5. Effect of prior creep strain on subsequent tensile strength.

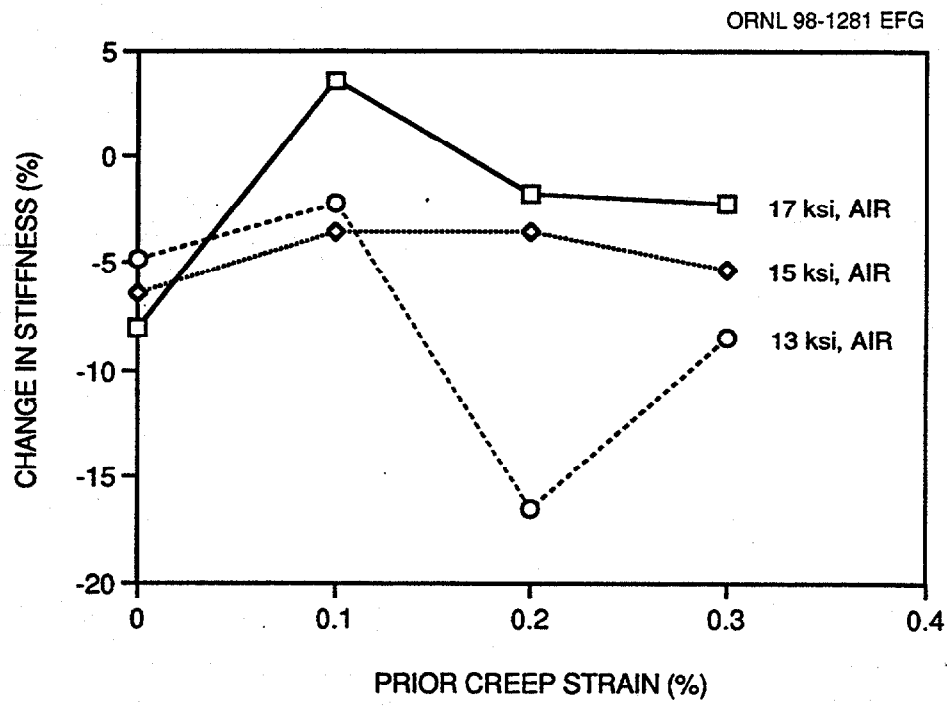

Fig. 12.6. Effect of prior creep strain on subsequent stiffness.

The zero creep strain points in Fig. 12.6 require some explanation. As was shown in Fig. 12.1, just loading to the creep stress levels produces a decrease in stiffness. To be comparable with the other points, the zero creep strain points need to reflect this loading effect. To do this, Fig. 12.1 was used with the average UTS of 23.4 ksi for plaque P20. On this basis, Fig. 12.6 shows no perceptible change in stiffness due to prior creep.

12.6 SUMMARY

The following key observations have been made:

- Static loadings above a 29.6% UTS threshold reduce the subsequent stiffness (up to 13.1% at 100% UTS).
- Residual tensile strength is reduced linearly with fatigue cycling (up to about 22% at $n/N_f = 0.8$). With a design factor of 20 on cycles to failure, the maximum reduction is negligible (about 1.5%).
- A factor of 20 on cycles to failure will limit the stiffness loss during fatigue cycling to 10% or less.
- Prior fatigue cycling has no effect on subsequent creep deformation response.
- Prior fatigue cycling does reduce subsequent creep-rupture stress levels (by 12.9 and 25.7% at n/N_f values of 0.25 and 0.75, respectively). Again, with a design factor of 20 on cycles to failure ($n/N_f = 0.05$), the loss in rupture strength due to prior fatigue is small (perhaps 2 to 3% maximum).
- Prior creep strains (up to 61% of the creep ductility) have no effect on subsequent tensile strength and stiffness.

REFERENCE

1. R. J. Howe and M. J. Owen, "Cumulative Damage in Chopped Strand Mat/Polyester Resin," pp. 137–148 in *8th International Reinforced Plastics Conference*, The British Plastics Federation, Brighton, October 1972.

13. DAMAGE TOLERANCE DESIGN FOR IMPACTS

J. M. Corum and R. L. Battiste

13.1 INTRODUCTION

This chapter focuses on the damage induced by low-energy impacts (e.g., roadway kickups and tool drops) and the resulting degradation in tensile, compressive, and fatigue properties. It is shown that damage, represented by ultrasonically determined damage areas, can be related to impactor mass and velocity for a variety of conditions. Property degradation can, in turn, be related to damage area. These relations thus provide a path for assessing the effects of low-energy impacts in design.

The following two sections review these experimentally derived relationships. After that, results from dropped-brick tests are used to validate the more general applicability of the relation between damage area and impactor mass and velocity. Finally, design assessment procedures are suggested.

13.2 BASIC IMPACT TESTS AND RESULTS

The data discussed here were all generated using a single specimen configuration: a 1/8-in.-thick × 8-in.-diam circular plate clamped on the outer edge and impacted in the center. The specimen diameter was chosen to be large enough to be representative of a plate impacted away from the vicinity of a support or stiffener, but not so large that a disproportionate amount of the impact energy would go into flexure of the plate.

Both pendulum and air-gun impact tests were conducted, the former representing tool drops and the latter representing roadway kickups. A baseline set of ambient air tests using the following parameters was performed.

	Impactor weight (lb)	Hemispherical impactor point diameter (in.)
Pendulum	25.4	0.5
Air gun	0.05	0.5

The effects of larger and smaller impactor diameters, different impactor masses (in the case of the air-gun projectile), a test temperature of –40°F, and presoaks in water and battery acid were explored and compared to the ambient air baseline. Almost all of the specimens were subsequently cut into 1-in.-wide tensile, compression, or fatigue specimens and the property degradation determined.

Table 13.1 summarizes the overall test program. In all, 65 impact tests and 414 mechanical property tests were performed. Note that residual tensile, compressive, and fatigue properties were obtained from the baseline specimens. Only tensile tests were performed for all of the other impact specimens.

For every impacted specimen, the damage area was measured from an ultrasonic C-scan image of the damaged area. Considering just the baseline results for a moment, it was found that the damage areas correlated reasonably well with the quantity impactor mass$^{0.564}$ × velocity, where mass is in pounds-second squared per foot and velocity is in feet per second. This correlation can be seen in Fig. 13.1. Both the pendulum and air-gun data result in essentially the same binomial curve fit.

Figure 13.2 shows the results of all the nonbaseline tests listed in Table 13.1 compared to the baseline correlation. All of the data, with the exception of the 180°F water soak, either lie below the baseline correlation (less damage) or well within the scatter band of the baseline data points. Thus, the baseline correlation can be used for a variety of conditions, covering significant impactor size and mass variations, as well as environments and a temperature of –40°F.

Table 13.1. List of impact tests and subsequent mechanical property tests

Impact tests	Pendulum	Air gun
Baseline	18	20
(0.5-in.-diam impactors)	(8T, 4C, 3F)[a]	(10T, 5C, 3F)
4-in.-diam impactors	2 (T)	2 (T)
0.25-in.-diam impactors	4 (T)	3 (T)
Test temperature, –40°F	2 (T)	4 (T)
Distilled water presoak, 1130 h	2 (T)	2 (T)
Battery acid pre-exposure, 24 h at 150°F	2 (T)	2 (T)
Demineralized water presoak, 1079 h at 180°F	1 (T)	1 (T)

[a]T = Tension (315 specimens).
C = Compression (63 specimens).
F = Fatigue (42 specimens, 36 tested).

Note: Numbers in parentheses in the table denote number of impact specimens devoted to each mechanical property test type. Generally, each impact specimen was cut into seven mechanical property specimens. Note that not all baseline impact specimens were cut into mechanical property specimens.

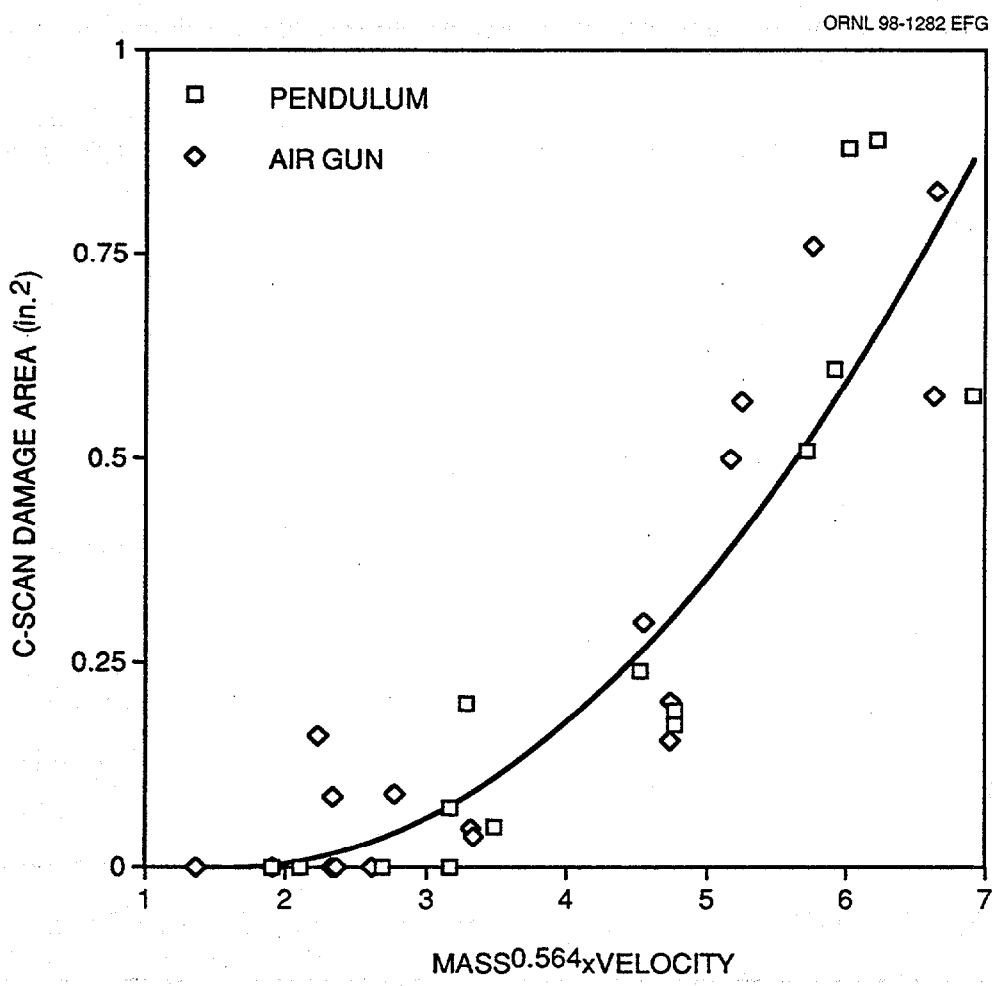

Fig. 13.1. Baseline correlation—damage area vs $m^{0.564} \times v$. Mass is in lb-s^2/ft and velocity is in ft/s.

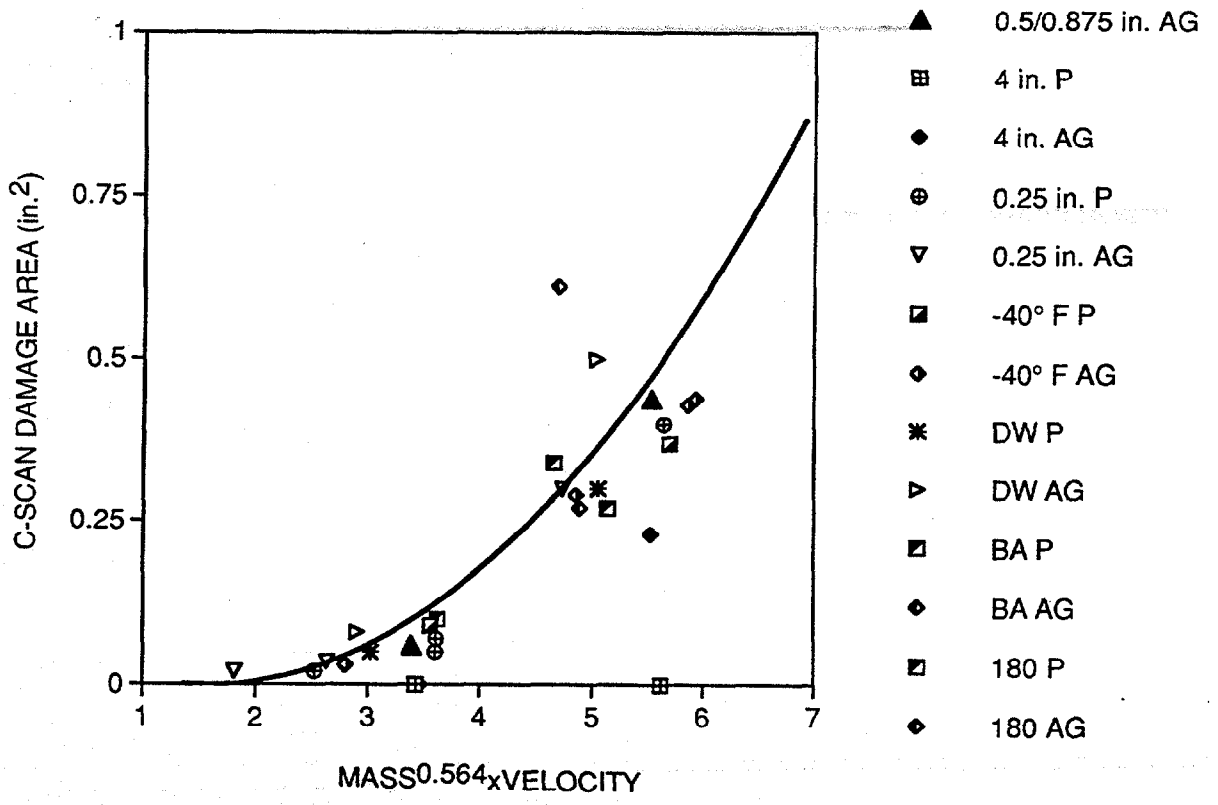

Fig. 13.2. Comparison of results for other conditions with baseline correlation. P denotes pendulum results; AG denotes air-gun results.

13.3 EFFECT ON TENSILE, COMPRESSIVE, AND FATIGUE PROPERTIES

Figure 13.3 shows typical plots of tensile properties, as determined from seven 1-in.-wide tensile specimens cut from each of two impacted plates. In all cases, the outer four specimens did not appear to be affected by the impact. Hence, average results from these four specimens were used as the reference to which the results from the center specimen were compared.

Figure 13.4 shows the resulting baseline relative strength values as a function of damage area. Tensile strength was degraded most, fatigue next, and compressive least. All of the fatigue tests were at a stress of 11.3 ksi. The resulting failure points were used to construct fatigue curves parallel to the baseline curve for the material. Strength values at 10^6 cycles were estimated from these curves and used to develop the relative values shown in Fig. 13.4. Because the fatigue correlations are assumed to be straight lines on log-log plots, the relative strength values apply to any number of cycles. Tensile stiffness degradation is shown in Fig. 13.5; compressive stiffness was not measured.

The relative properties shown in Figs. 13.4 and 13.5 are pseudoproperties. Clearly, they depend on specimen width. In fact, it has been shown that the damage areas behave like circular holes of equivalent area.*

*See Chap. 14.

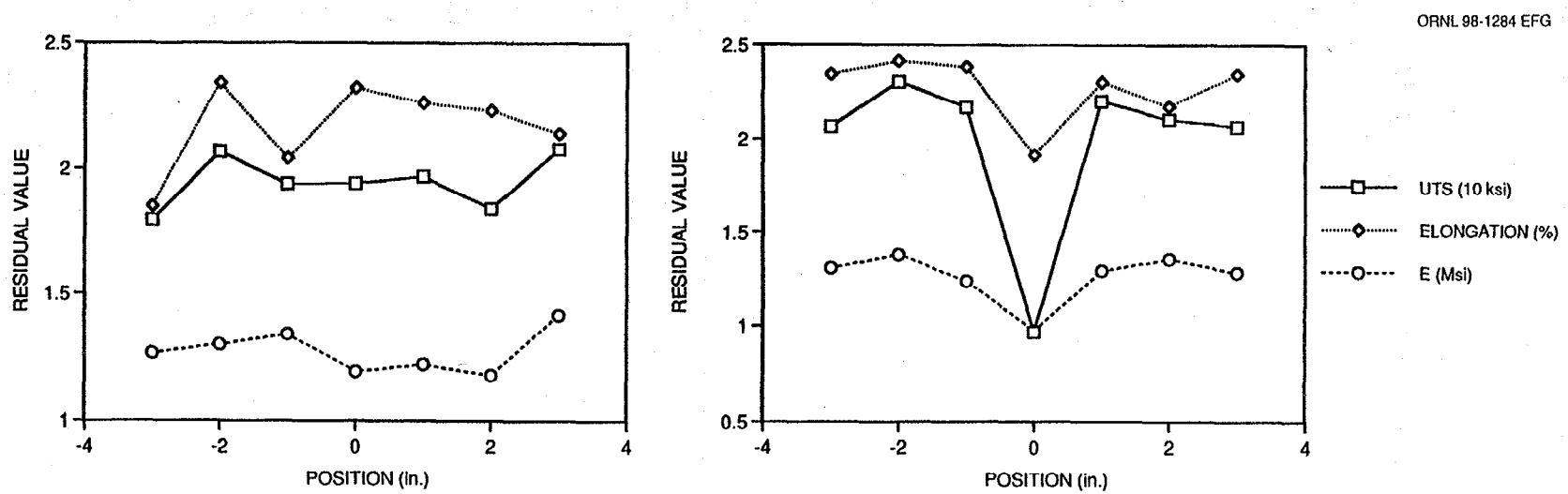

Fig. 13.3. Typical distributions of tensile properties across impacted specimens.

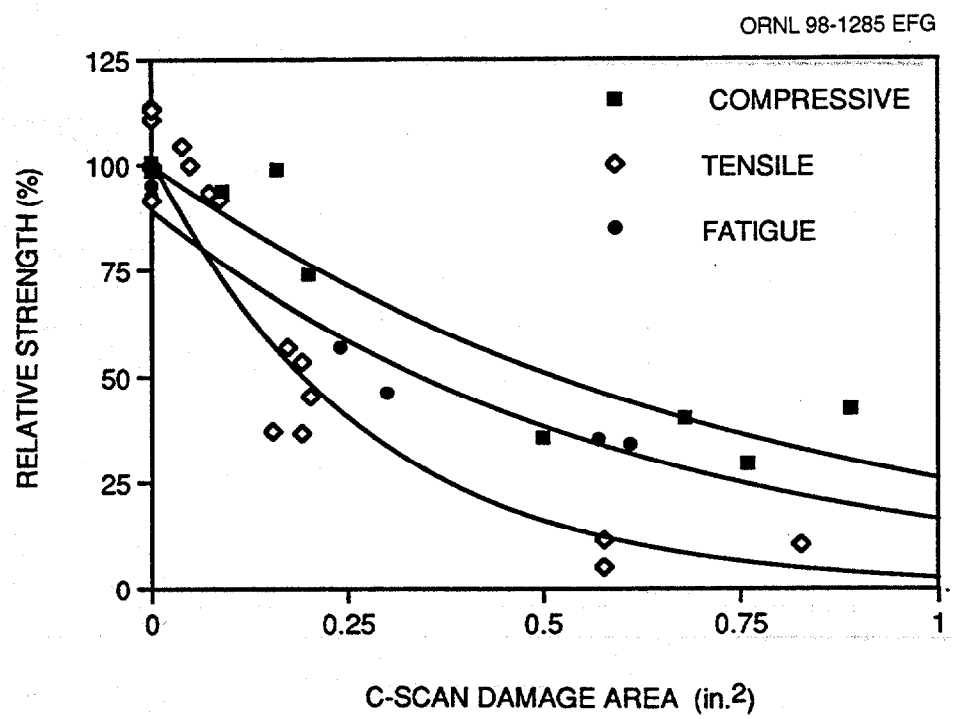

Fig. 13.4. Relative tensile, compressive, and 10^6 cycle fatigue strengths vs damage area.

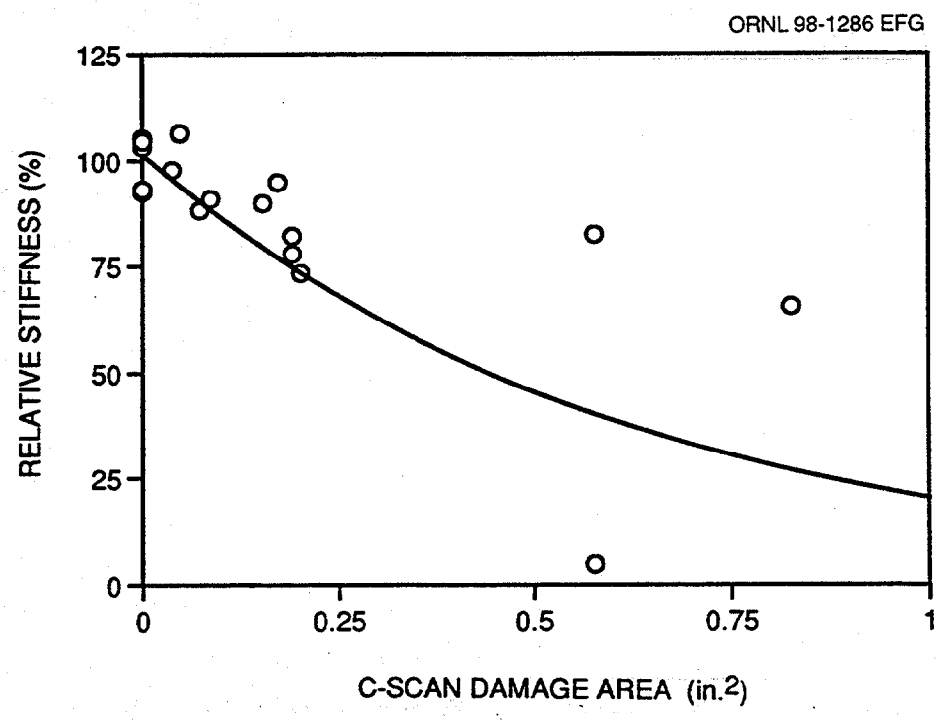

Fig. 13.5. Relative tensile stiffness vs damage area.

13.4 BRICK-DROP TESTS

The test results presented in the previous two sections are all for smooth hemispherical steel impactor points. Are they applicable to impacts from more irregular objects? To answer this question, the effects of bricks dropped on a corner were evaluated.*

The new bricks used weighed, on average, 3.7 lb. Four tests were run in which bricks were dropped from 2-, 4-, or 8-ft heights. The same clamped specimen design was used as in the previous tests. Sound, sharp corners of the bricks were chosen for the impact tests, and the corners were essentially undamaged by the impacts. The bricks were released from the diagonally opposite corner, so the center of gravity was in line with the impact point. Video footage of the drops confirmed that each brick maintained its alignment until impact.

The results of the four tests are shown in Fig. 13.6, where damage area is again plotted vs $m^{0.564} \times$ velocity. The results are in the scatter band of the previously discussed baseline data. These results add credibility to using the previous results as a basis for design.

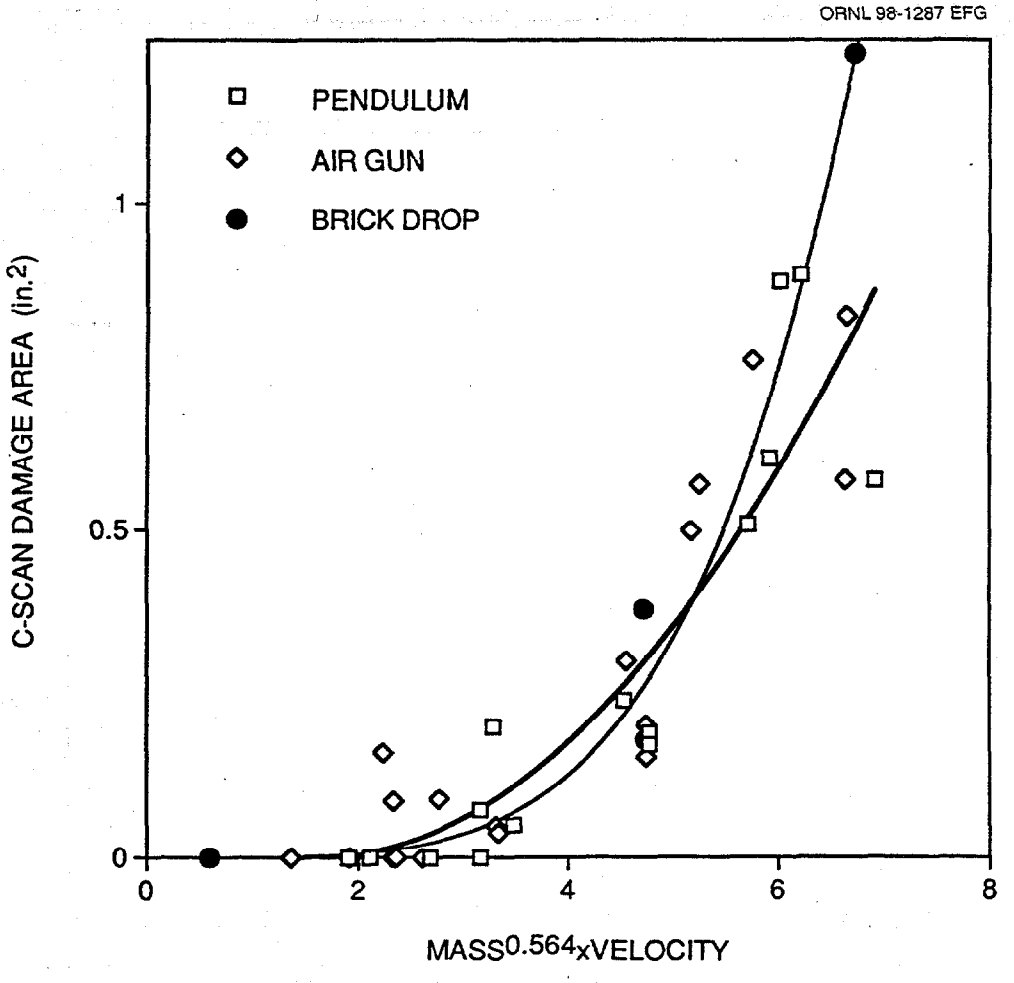

Fig. 13.6. Comparison of damage areas from brick drops with baseline data.

*Dropped bricks are one of the loadings specified for the ACC Focal Project II pickup box design.

13.5 RECOMMENDED DESIGN APPROACH

For free bodies having a known mass and impact velocity, the design curve in Fig. 13.7 is recommended for determining the damage area. The design curve is the upper limit of the scatter band of data in Fig. 13.1. No further reduction factors should be required.

Figure 13.8, which comes from Fig. 13.4, should be used to estimate strength degradation corresponding to the damage area determined from Fig. 13.7. Although localized stiffness reductions are probably not often of major consequence, a value can be estimated from Fig. 13.9, which comes from Fig. 13.5.

Conventional wisdom regarding impacts on composites states that damage areas should correlate well with the maximum contact force reached during the event, at least for larger masses. This offers an alternative way of estimating damage areas for cases where it is desired to include more of the specifics of the composite structure and of the impact event. Our analysis work demonstrated that force could be reasonably and accurately predicted by a thick-shell, dynamic time-response analysis, provided the nonlinear contact response was properly modeled.[1]

Indentation tests showed that the classical Hertzian contact law

$$F = K\alpha^{3/2}$$

described the indentation. Here, F is the indentation force (lb), and α is the indentation (in.). A value of 17.0 for K was found to be appropriate. The law can be included in a finite-element analysis by means of a nonlinear spring at the impact point.

Once the peak force in the impact is predicted, Fig. 13.10 can be used to estimate damage area. This figure is taken from Ref. 1 and comes from a correlation of predicted force vs damage area for the baseline pendulum and air-gun tests. Note that the curve in Fig. 13.10 should not be extrapolated beyond the limit shown, because the pendulum and air-gun results begin to diverge at larger damage area values.

Once the damage area is estimated from Fig. 13.10, property degradation can be estimated from Fig. 13.8.

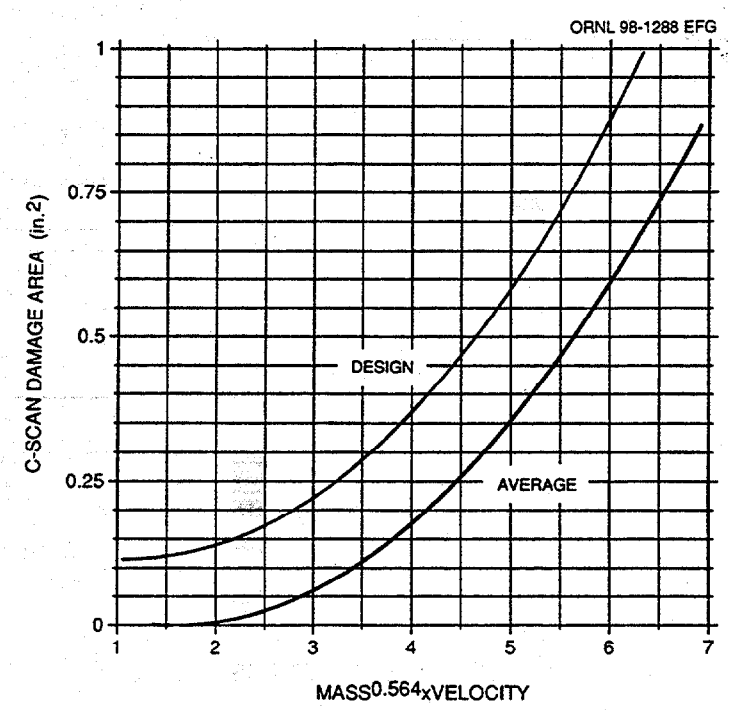

Fig. 13.7. Design curve for determining impact damage area.

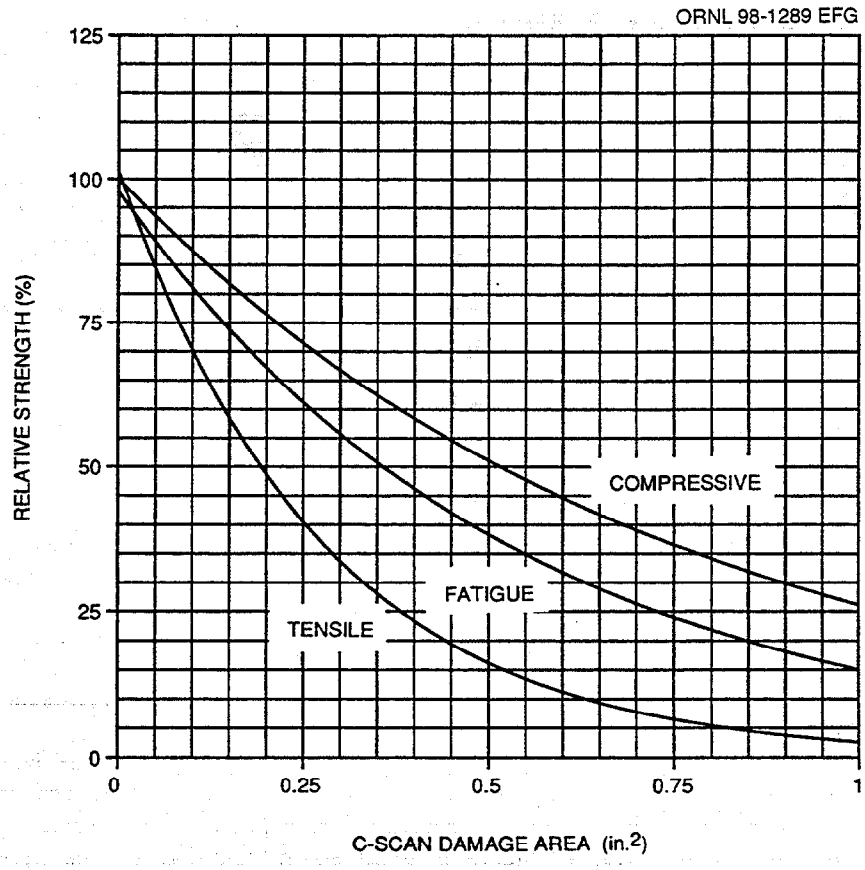

Fig. 13.8. Strength degradation as a function of damage area.

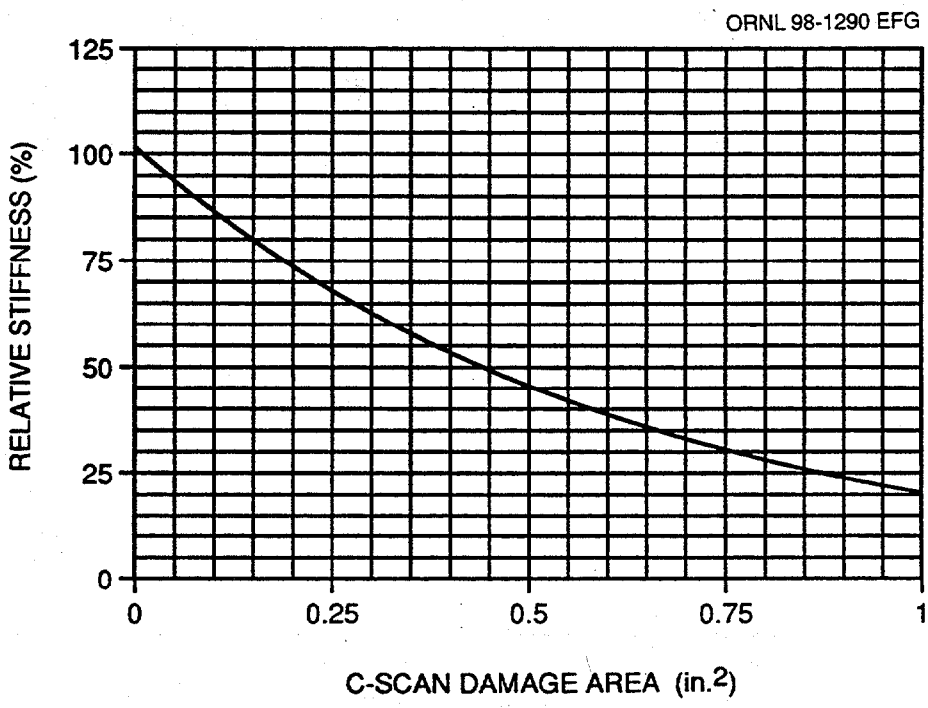

Fig. 13.9. Tensile stiffness degradation as a function of damage area.

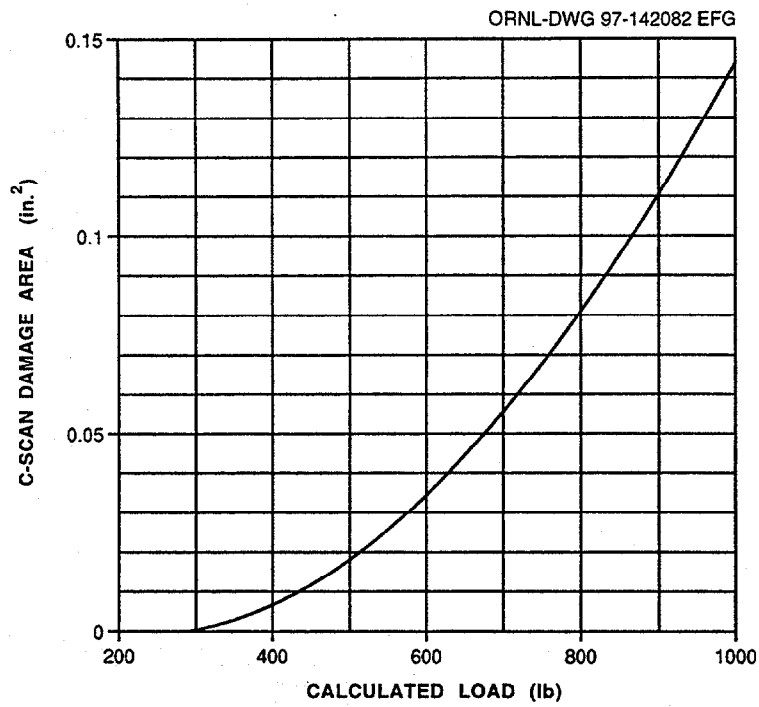

Fig. 13.10. Calculated peak contact force vs damage area.

REFERENCE

1. *Durability of Lightweight Composite Structures for Automotive Applications. Annual Progress Report for Period Ending September 30, 1996*, ORNL/TM-13345, Chap. 4, Lockheed Martin Energy Research Corp., Oak Ridge National Laboratory, December 1996.

14. SENSITIVITY TO STRESS CONCENTRATIONS—HOLES

J. M. Corum, W. Ren, R. L. Battiste, and M. B. Ruggles

14.1 INTRODUCTION

The study of the effects of circular holes on properties originated with this question: Can the reduction in tensile properties due to impacts be predicted by representing damage area as a circular hole?* A series of finite-element analyses of 1-in.-wide specimens with holes of various sizes was first carried out to determine theoretical stress concentration factors. Based on the results and on typical damage area sizes from impact studies, a hole size of 0.25-in. diameter was chosen for tensile, fatigue, and creep-rupture tests. The results are described below.

14.2 FINITE-ELEMENT ANALYSES

The finite-element grid for a 0.25-in.-diam hole together with analysis results for several hole sizes are shown in Fig. 14.1. The stress concentration factor (SCF), based on the average ligament stress, for a 0.25-in.-diam hole is 2.36. If this SCF were totally effective, the calculated strength, again based on the net area, would be 42.4% of the UTS. The calculated apparent stiffness, over a 1-in. gage length containing the hole, is 81.7% of the material modulus of elasticity, E.

14.3 TENSILE TESTS

Five tensile tests on specimens with 0.25-in.-diam holes from a single plaque, P33, were performed. The results were as follows:

- Strength = 91% UTS; $SCF_{Effect} = 1.10$
- Apparent stiffness (1-in. gage length) = 113% E

Thus, the theoretical stress concentration factor has a very weak effect (2.36 vs 1.10 actual). The stiffness was considerably greater than predicted.

Returning to the original question of impact damage, Fig. 14.2 shows a plot of relative tensile strength vs impact damage area taken from Chap. 13. Also shown on the figure are two sets of points from the above analysis results.

One set assumes no SCF at all; the other assumes that the calculated SCFs are fully effective (failure would occur when the peak stress reaches the UTS). The case of no SCF fits with the impact results very closely. Thus, in terms of strength, the degradation can be predicted by assuming the impact damage area is a circular hole with no SCF.

This observation does not extend to stiffness, as shown in Fig. 14.3. The material in the damaged area does appear to contribute to stiffness.

14.4 FATIGUE TESTS

Fatigue results of tests on P33 specimens with 0.25-in.-diam holes are compared in Fig. 14.4 with the baseline results from several plaques. At 10^6 cycles, the fatigue strength, based on average ligament stress, is 90% of normal.

---

*Volume III, "Utilization of Data," of MIL-HDBK-17-3D states that the residual strength of a damaged *laminate* with a cutout is primarily dependent on the width of the cutout and essentially independent of the cutout shape. Thus, design values reduced for a 0.25-in.-diam hole (one of the requirements for damage tolerance design) also account for an equivalent length edge cut.

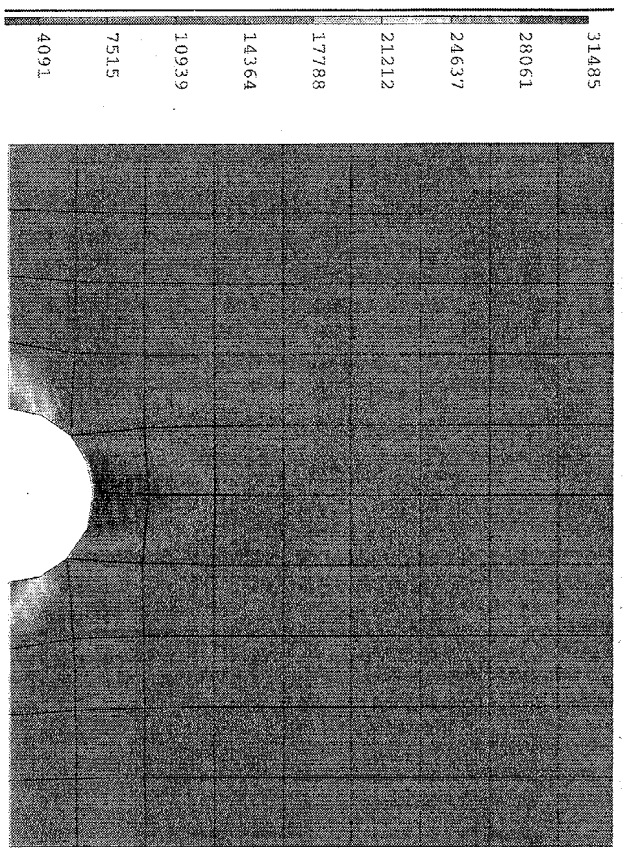

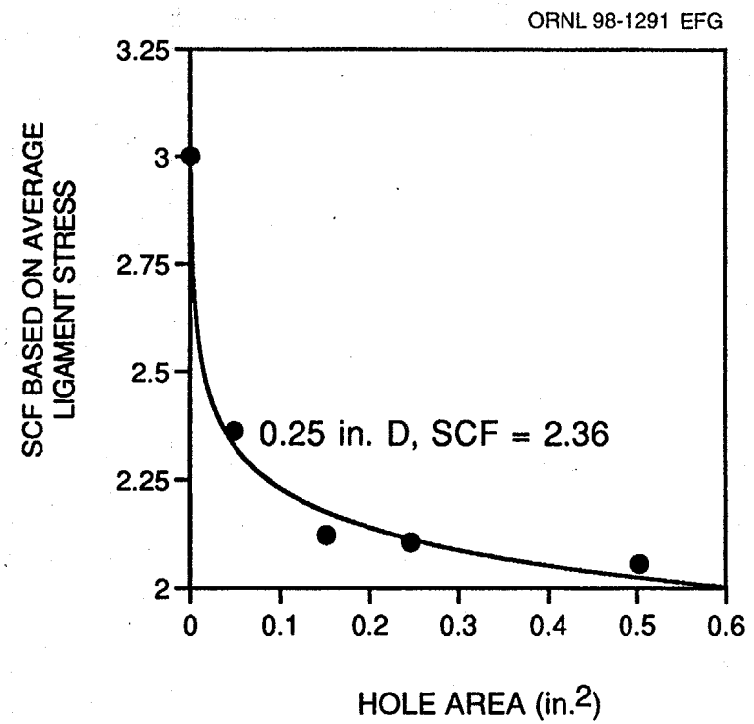

Fig. 14.1. Finite-element grid and analysis results.

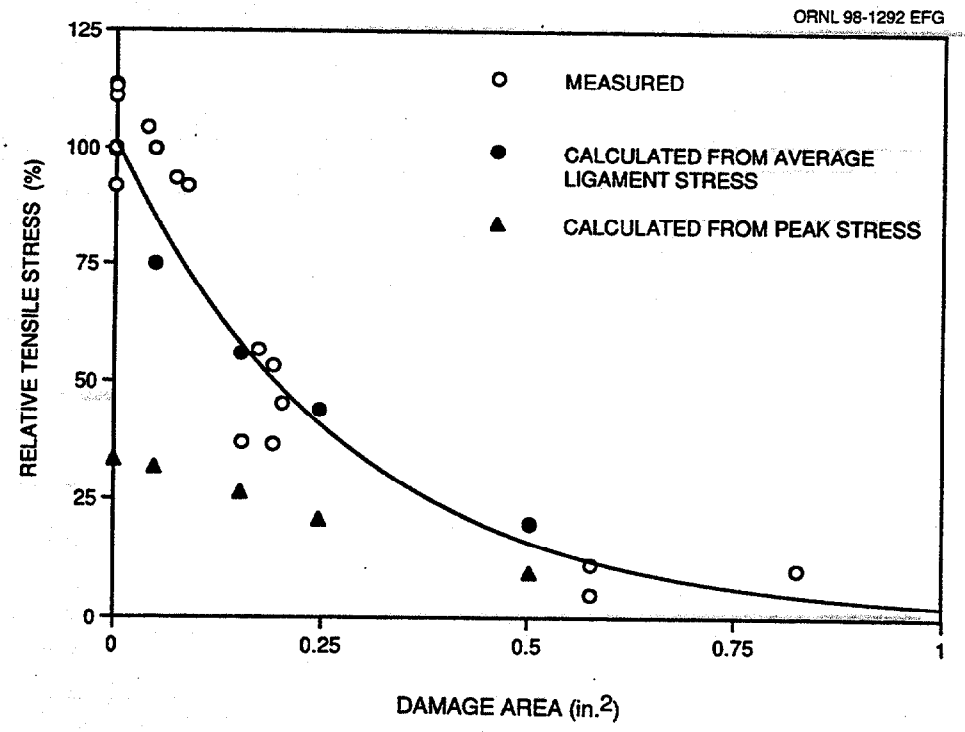

Fig. 14.2. Circular hole strength reduction predictions compared with impact strength degradation results.

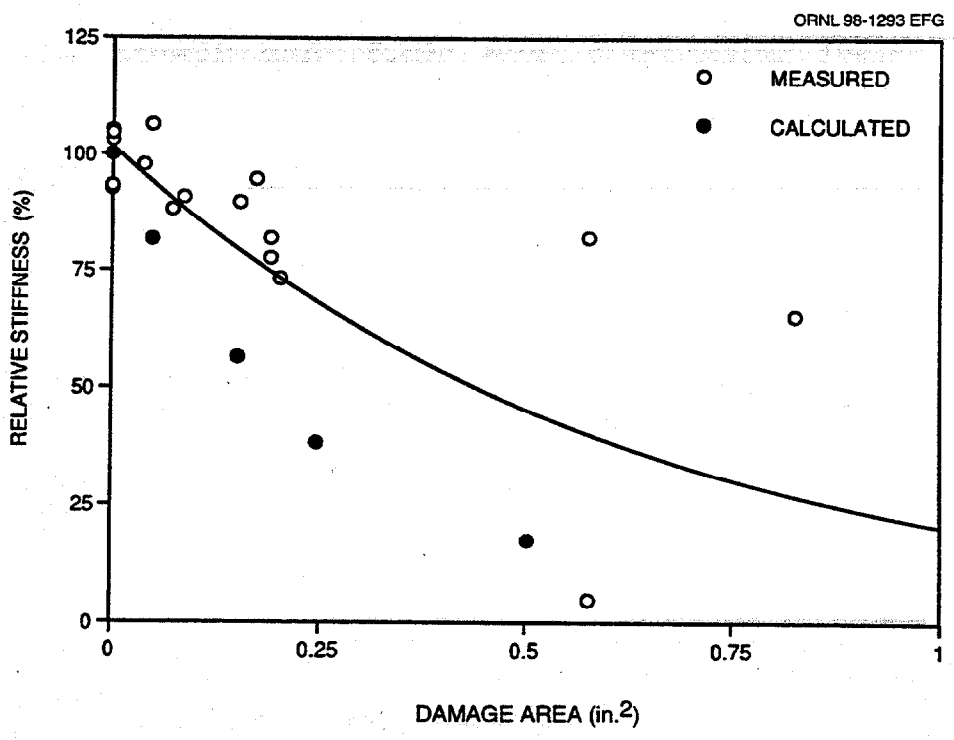

Fig. 14.3. Calculated stiffness compared to impact degradation results.

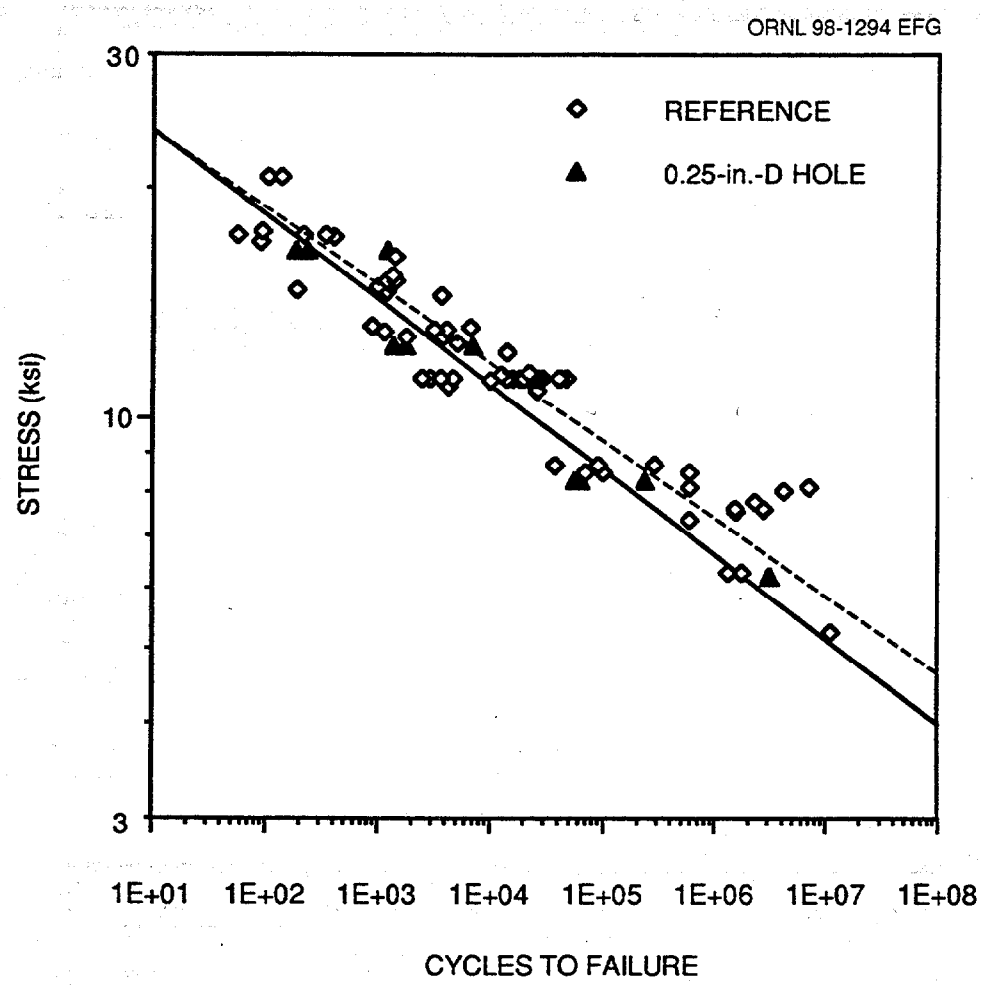

Fig. 14.4. Fatigue strength (solid line) of specimens with 0.25-in.-diam holes compared to reference fatigue curve (dashed line).

14.5 CREEP-RUPTURE TESTS

Seven creep-rupture tests were performed on specimens with 0.25-in.-diam holes. All the tests were at a single stress level of 15.5 ksi. Three specimens were from plaque P33 (with a UTS of 20.70 ksi), and four were from P42 (UTS = 23.44 ksi).

The results are compared in Fig. 14.5 with the baseline creep-rupture correlations from Chap. 8. The creep-rupture strength at 3000 h and 10^5 h is about 86% of normal (assuming parallel rupture curves as shown in the figure).

14.6 SUMMARY

The following significant observations were made.

- Tensile tests of specimens with a 0.25-in.-diam hole show that the theoretical SCF is not very effective (2.36 vs 1.10 actual).
- The fatigue strength at 10^6 cycles and the 10^5 h creep-rupture strength show about the same effective SCF as the tensile tests (1.11 and 1.16, respectively).

- Tensile strengths calculated for specimens with circular holes, using just the average ligament stress, agree well with residual strengths from specimens with impact damage. On this basis, strength degradation due to impact can be estimated by representing the damage area by a circular hole.
- The stiffness degradation is, however, overestimated on this basis.

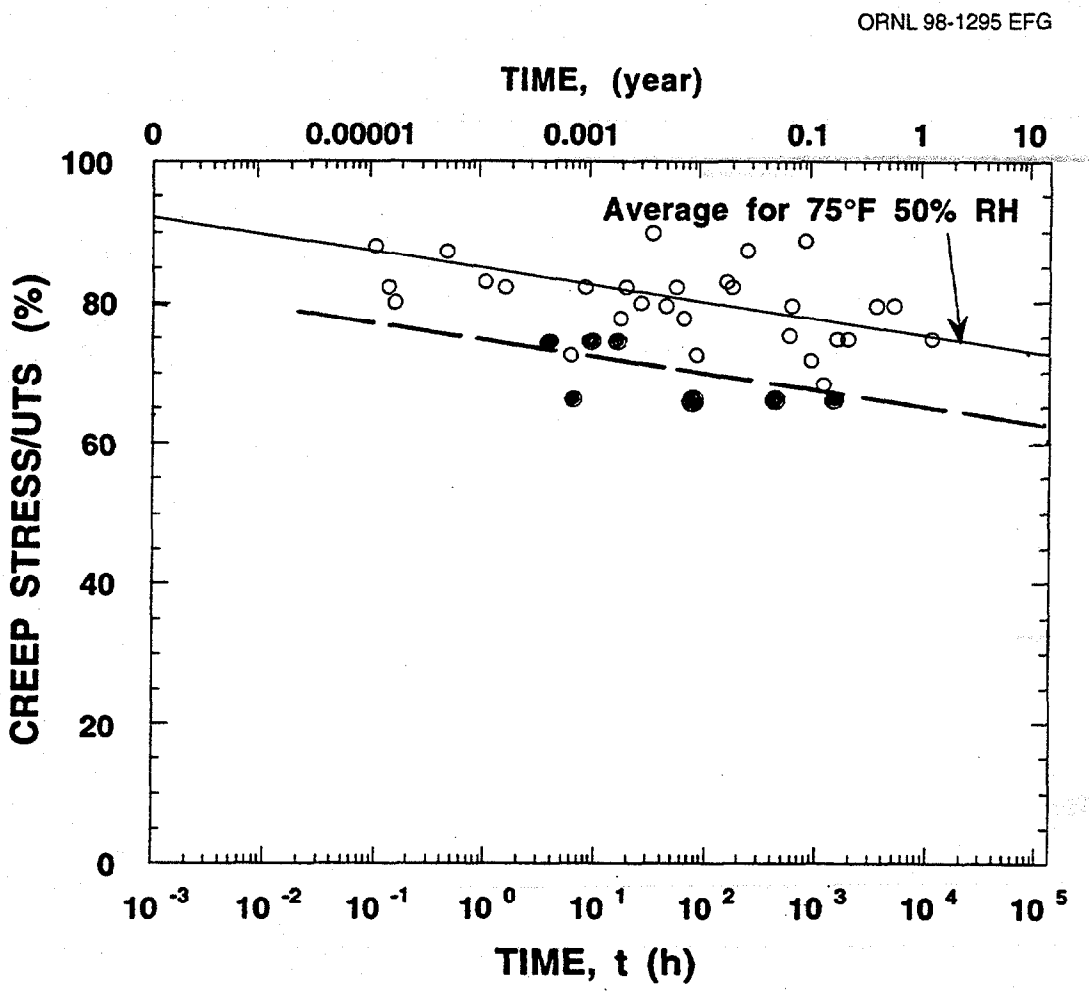

Fig. 14.5. Creep-rupture strength of specimens with 0.25-in.-diam holes (solid points, dashed line) compared to reference creep-rupture curve (open points, solid line).

15. HAT SECTION FRACTURE TESTS—IMPLICATIONS FOR DESIGN CRITERIA

G. T. Yahr, R. L. Battiste, J. M. Corum, and C. R. Luttrell

15.1 INTRODUCTION

Application of composites to automotive structures will involve three-dimensional geometries. The "hat sections" shown in Fig. 15.1 have geometrical discontinuities (bends) representative of three-dimensional products. Specimens were cut from the hat sections and tested to provide an insight into how well the design criteria might apply at such discontinuities.

Tensile and out-of-plane flexure tests on coupon specimens from the hat sections indicated that the strength of the hat section is 77% of the reference material flat plaques.*

15.2 MONOTONIC TESTS

One-inch-wide pieces of the hat section were subjected to monotonic and cyclic tension or compression in the 90° direction as shown in Fig. 15.2. The specimens shown in Fig. 15.3 were twisted about the shear center monotonically and cyclically. Monotonic out-of-plane flexure tests were run on small beams in the 90° direction.

ORNL 98-1296 EFG

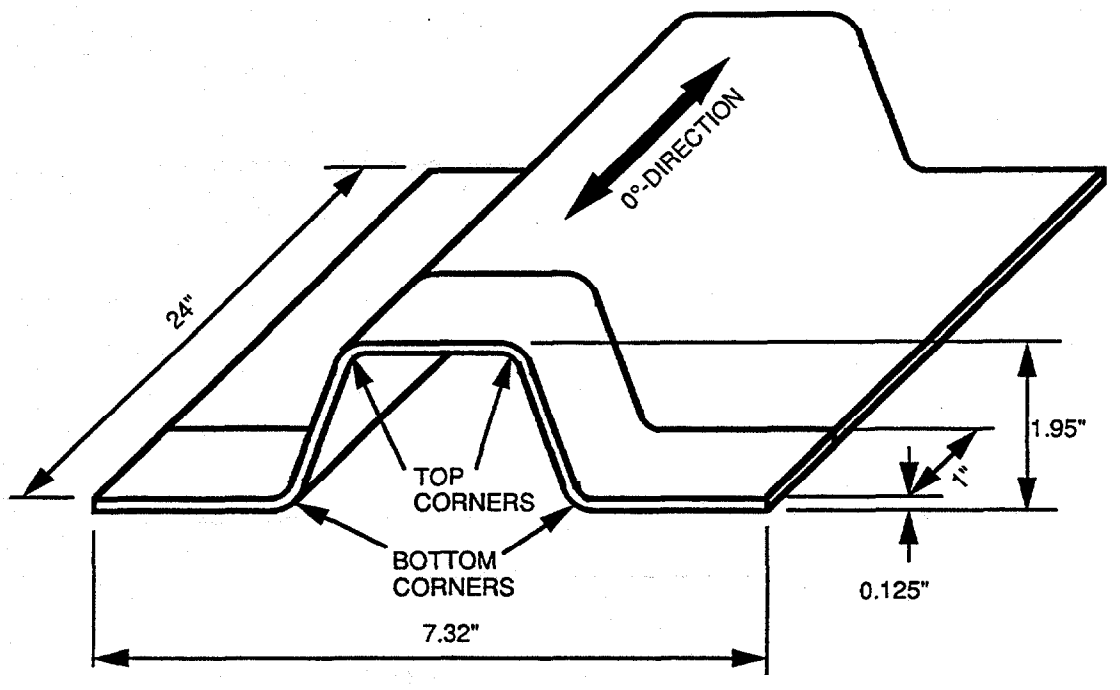

Fig. 15.1. Hat section. Specimens for tension and compression hat section tests are made by cutting 1-in. pieces as shown.

*The hat sections have the same continuous-strand mat reinforcement as the reference material, but the urethane matrix is different (Baydur STR-400-CA vs MM364 for the reference material).

ORNL 98-1297 EFG

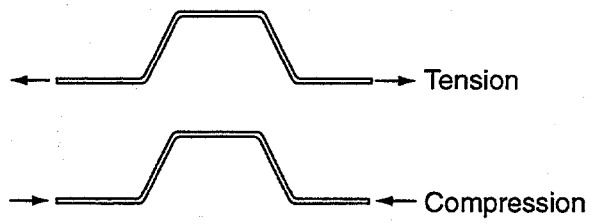

Fig. 15.2. Application of load in the tension and compression hat specimens.

ORNL 98-1298 EFG

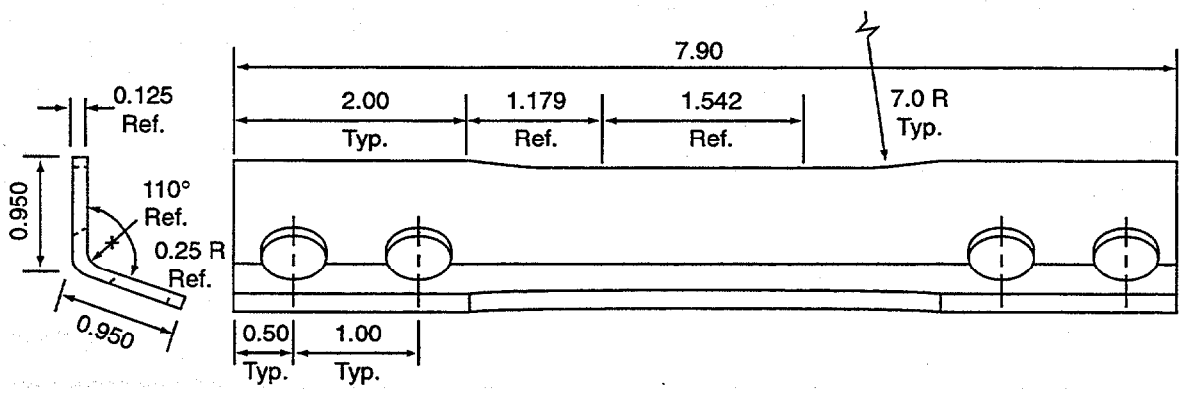

Fig. 15.3. Hat section torsion specimen. Dimensions are in inches.

Except for tensile and flexure tests, the average peak stress intensity for each test series at failure was determined by finite-element analysis.

Tests	Failure stress intensity (ksi)
Flexure	39.04
Hat tensile	17.39
Hat compressive	34.28
Hat torsion	61.89
Average tensile strength (90° direction)	21.90
Average tensile strength (0° direction)	16.40
150% tensile strength	24.60

It was expected that the tensile and compressive hat section tests would correlate well with the flexure tests because the specimens are subjected to a high bend stress. The compressive hat section test did correlate reasonably well. Those specimens broke at the outside of one of the top corners at an average stress intensity of 34.28 ksi, which was 88% of the flexure strength. A typical failed compressive hat specimen is shown in Fig. 15.4.

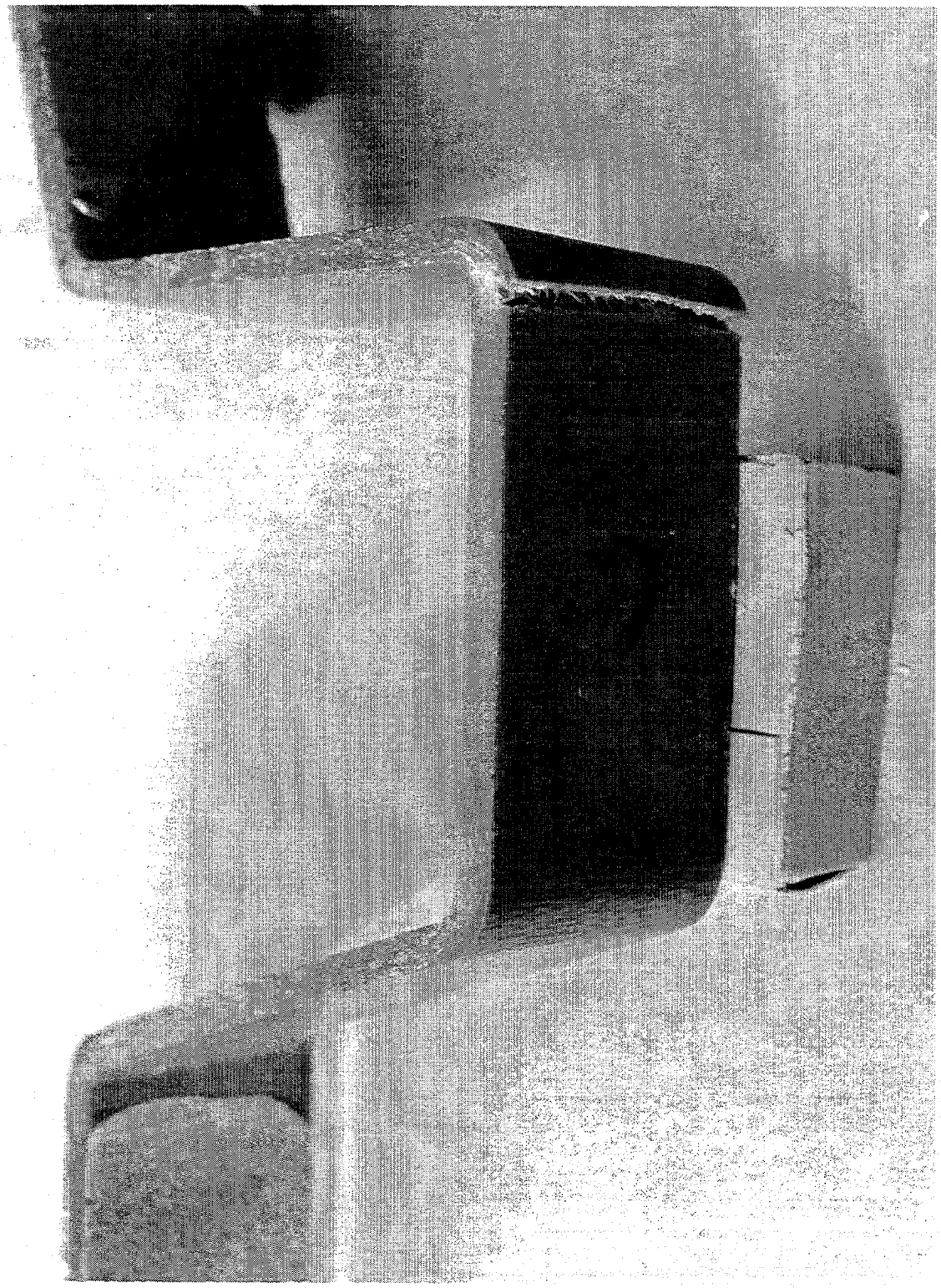

Fig. 15.4. Compressive hat section specimen. Sudden fracture occurred at the outside of a top corner, as shown.

Examination of the hat sections revealed that the fiberglass was pulled toward the inside of the corners during fabrication. This explains the slightly low failure stress in the compression specimens. If the distribution of the fiberglass in the corners cannot be improved, allowable stress values must be reduced by 20% in such regions.

The tensile hat section specimens never really broke. They delaminated in the corners as the tensile stress surface tended to be pulled inward, as shown in Fig. 15.5, and the load dropped briefly at an average stress intensity of 17.39 ksi, which was 44.5% of the flexure strength. The load resumed increasing after delamination as the pull on the specimens continued until the machine stroke limit of 2 in. was reached. The average stress intensity at that time was 29.95 ksi. Although this stress intensity is 72% higher than the load when delamination occurred, it is still only 77% of the flexure strength. The delamination is a failure mechanism that was not experienced in the tensile, compressive, and shear tests that were done to characterize this material.

The stress intensity, at the first load drop in the tensile hat tests, is 79.4% of the average tensile strength in the 0° direction. A factor of 1.5 on the allowable stress intensity is suggested for out-of-plane bending in a flat plate. However, a factor of 0.8 on the allowable stress intensity must be used for out-of-plane bending in the region of tight bends in the plate.

The hat torsion specimens broke at a calculated stress intensity that was 3.7 times the average tensile strength in the 0° direction. This is not unexpected because these specimens were subjected to shear, and the maximum shear theory was quite conservative relative to the Iosipescu shear test results. Two typical failed hat torsion specimens are shown in Fig. 15.6.

15.3 APPLICATION OF DESIGN GUIDE

The hat section tests provide an opportunity to evaluate the design guide analysis methods and criteria (Part 1). Small deformation, elastic, finite-element analyses of the compressive hat section bend, tensile hat section bend, and torsion hat section specimens were performed according to the design guide. The elastic predictions are compared to the experimental results in Figs. 15.7–15.9. The maximum allowable load based on the maximum allowable stress intensity is indicated by a horizontal line in each figure. It is important to note how well the deformation is predicted because in many applications it is expected that operational requirements on deformation may be more limiting than the maximum allowable stress intensity. These hat section tests are especially good for evaluating the ability to predict deformation because the deformations are large compared to the specimen thickness. The relative deflection of the grips of the tensile specimens was 3 to 3.25 times the thickness. The predicted deflection was within the scatter from the six specimens.

The relative deflection of the grips on the compressive specimens was 3.6 to 4.0 times the thickness. Here the deflection was accurately predicted at low loads but was underestimated by 5 to 14% when the load was large enough to produce the maximum allowable stress intensity.

The grips on the torsion specimens rotated 14.3 to 16.9° when pieces of the composite were used to prevent the steel grips from cutting into the specimen. The rotation increased to 20 to 22° when rubber was used to cushion the grips.

Proper modeling of the boundary conditions at the grips in the finite-element analysis for the hat section torsion specimens was difficult. The range of elastic analysis results shown in Fig. 15.9 bounds the experimental results.

The allowable stress intensity levels depicted in Figs. 15.7–15.9 seem to provide an adequate design margin against excessive deformation and failure in all cases.

15.4 FATIGUE TESTS

Three tension and two compression hat section fatigue tests were conducted at an R ratio of 0. The maximum stress intensity in the specimens all exceeded the maximum allowable stress intensity. The tension hat specimens delaminated but continued to support the applied loads until the cycling was discontinued. Their stiffness continually decreased throughout the cycling. The stiffness of the specimens when the tests were terminated was 44 and 80% of the original specimen stiffnesses.

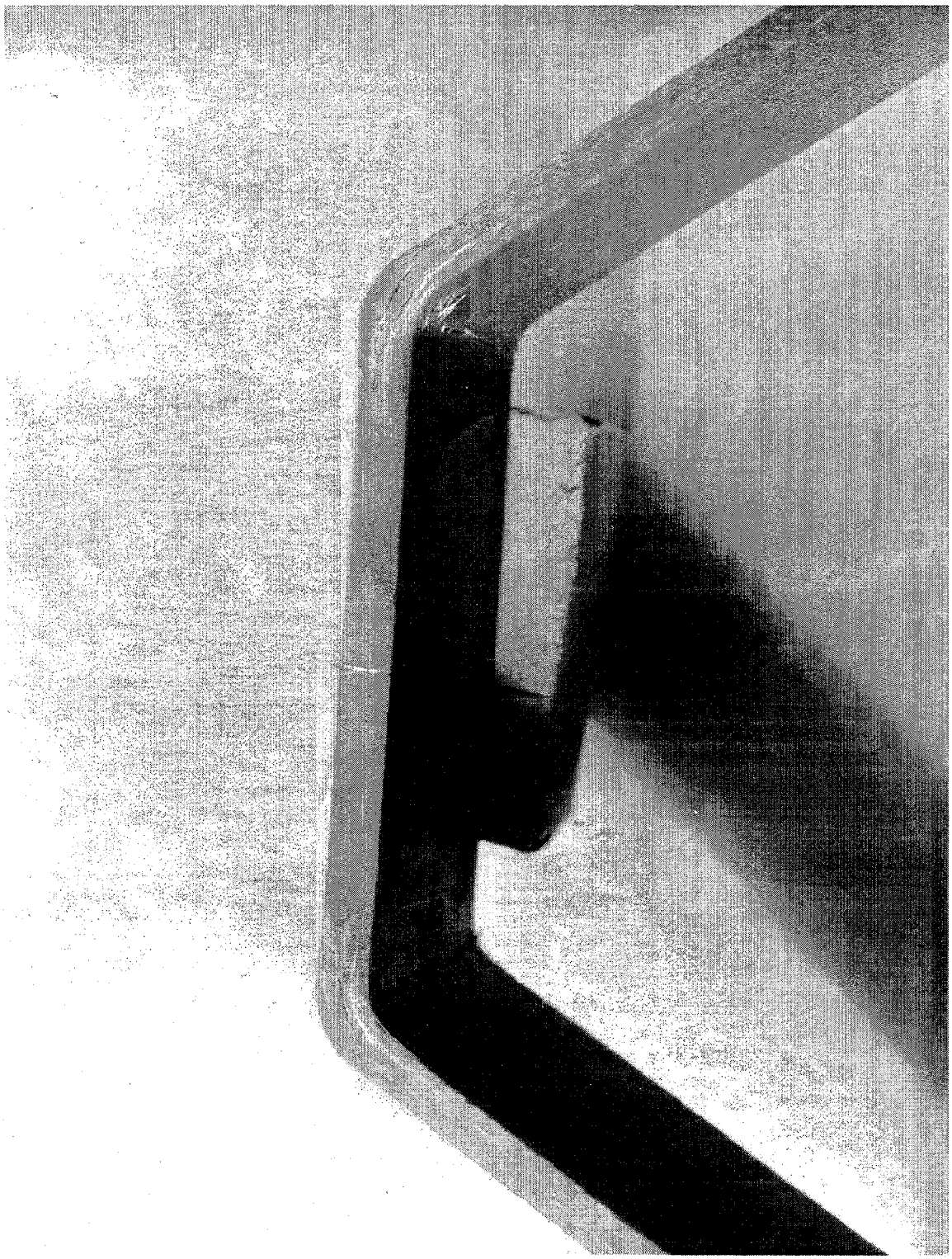

Fig. 15.5. Delamination occurred in the corners when tension was applied to the hat section specimens.

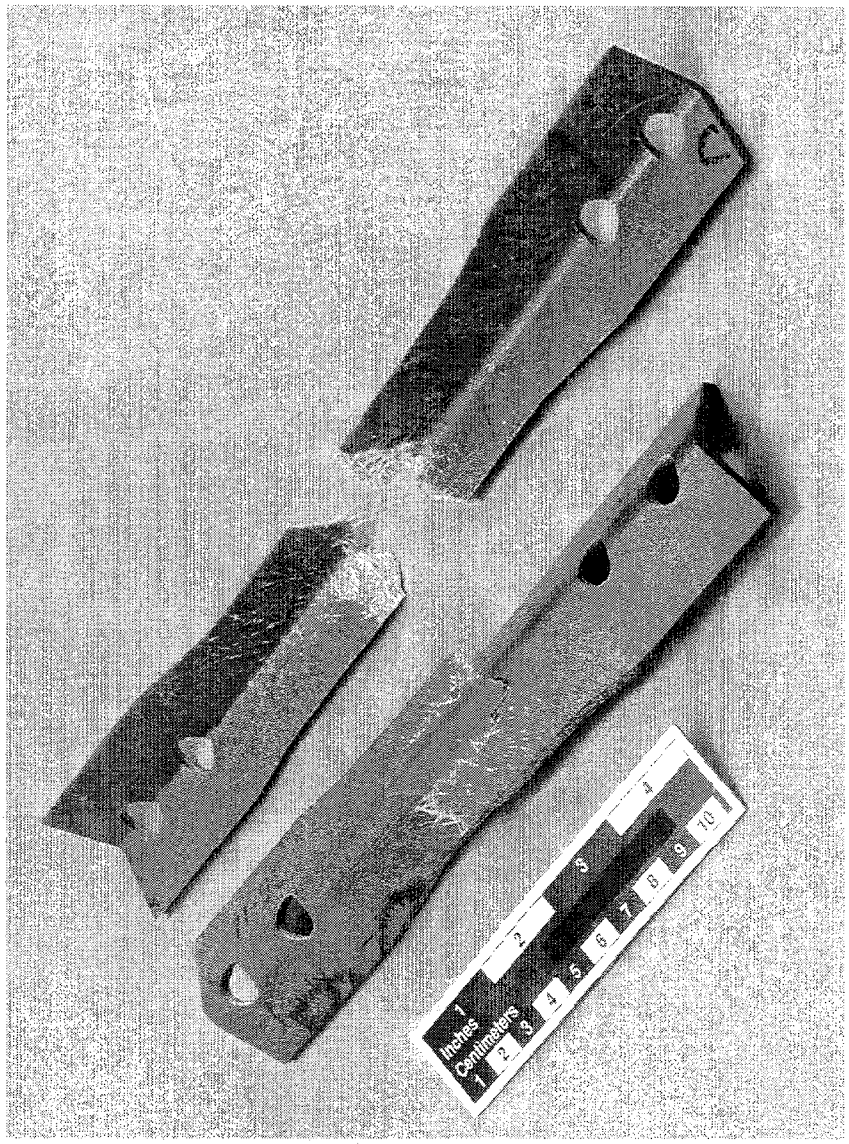

Fig. 15.6. Hat section torsion specimens broke as shown, starting at the edges.

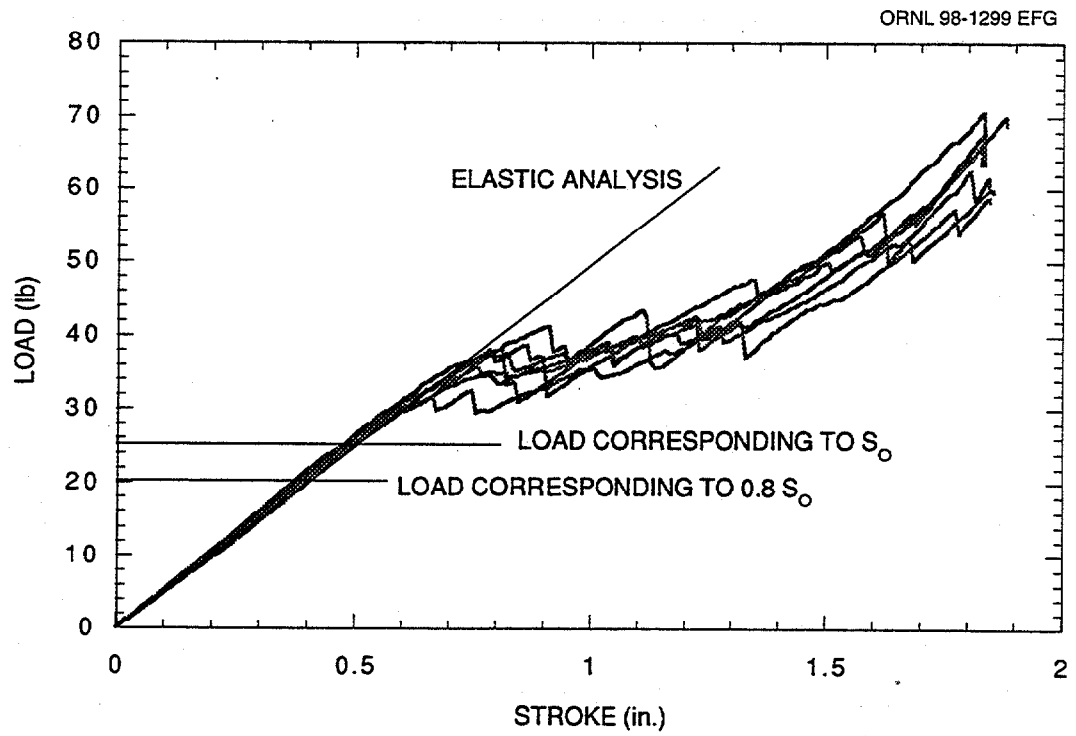

Fig. 15.7. Elastic analysis results agreed well with hat section tensile tests beyond the load that produced the maximum allowable stress intensity.

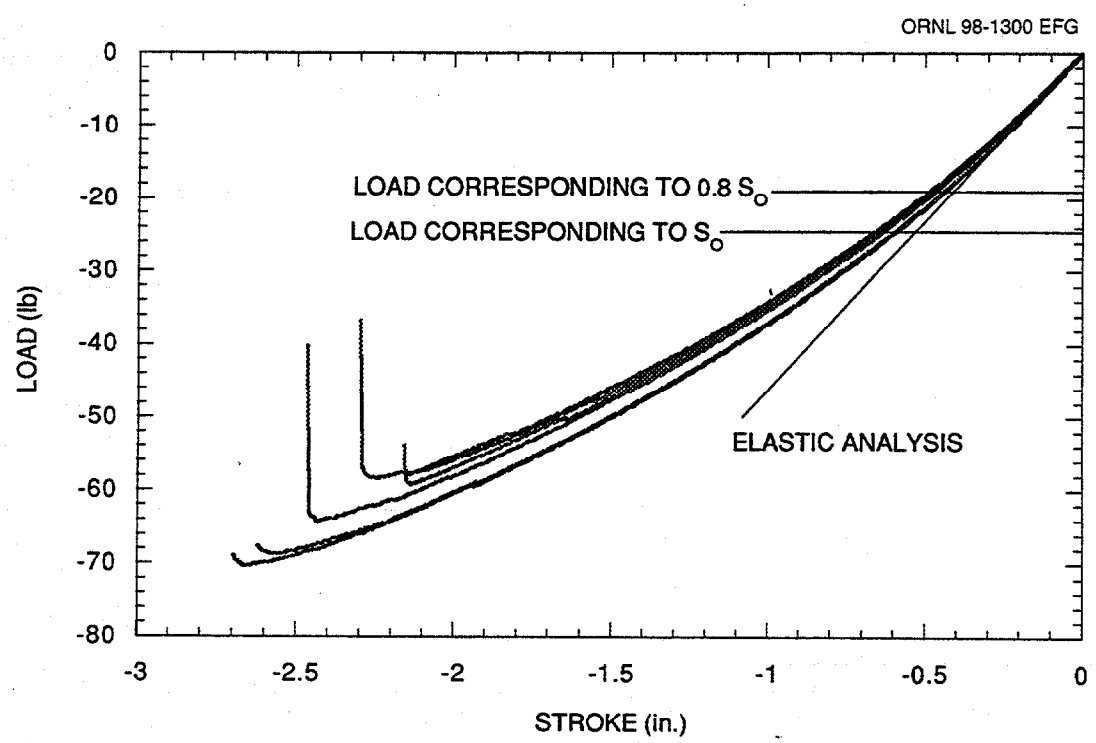

Fig. 15.8. Elastic analysis agreed well with hat section compressive test results at low loads.

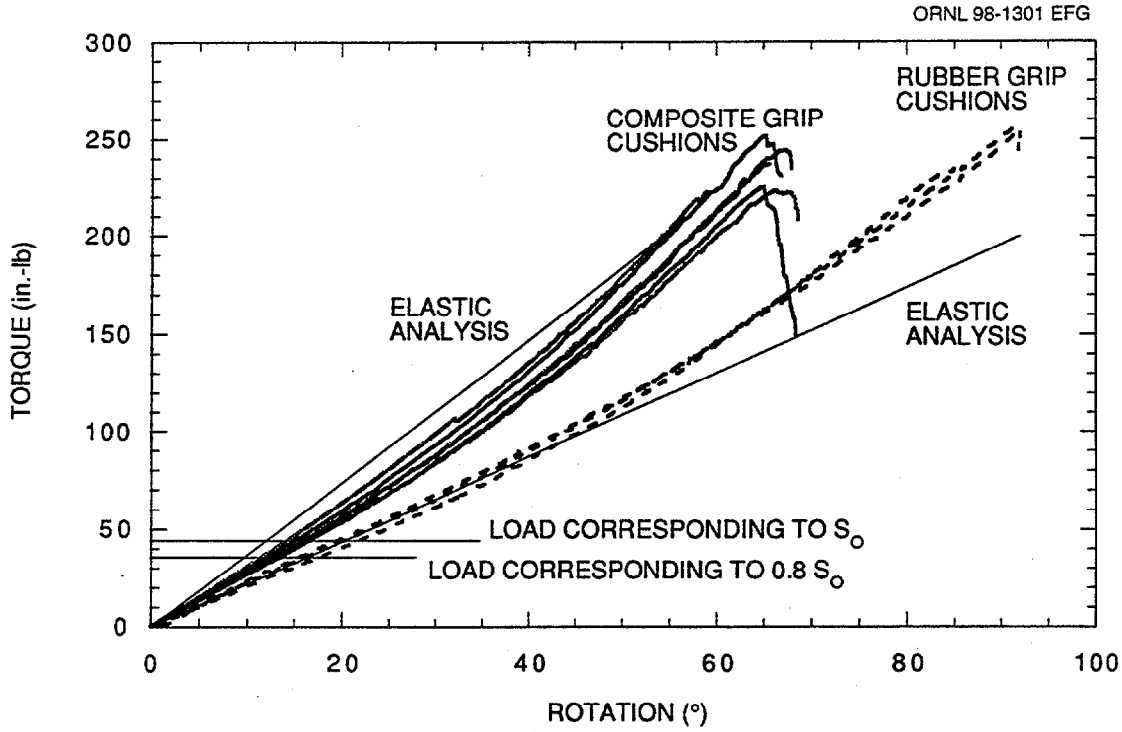

Fig. 15.9. Range of elastic analysis results for torsion hat section specimens bounds the measured rotations.

The cycles to delamination and total cycles were compared to allowable lives based on the fatigue design curves given in Chap. 11. The design life was determined using the ratio of the maximum stress intensity to the 0°-direction tensile strength to enter the fatigue curve. One of the tension specimens delaminated at 6.5 times the allowable design life, and the other one delaminated at 18.8 times the allowable design life. The design fatigue curves have a built-in factor of 20 on cycles to failure.

The maximum stress intensity in the two compressive hat section fatigue specimens exceeded the 0°-direction tensile strength. Therefore, the predicted fatigue life was zero. However, one of the specimens failed after 957 cycles, and the other failed after 17,800 cycles.

Eleven torsion hat specimens were tested at an R ratio of zero, and three were tested at R = –1. The maximum stress intensity was higher than the 0°-direction tensile stress in every test. Therefore, the predicted life was zero. The predicted life was extremely conservative because the minimum cycles to failure was 347 cycles. Remember that the monotonic torsion hat section strengths were also much higher than predicted.

The design lives were also predicted by using the ratio of the maximum torque in the fatigue tests to the average failure torque in the monotonic tests to enter the design fatigue curve. The allowable design life was less than the actual cycles to failure for every test. However, the ratio of actual life to design life was less than 13 for all the tests with an R ratio of 0 and greater than 24 for all the tests with an R ratio of –1.

15.5 SUMMARY

The following key observations came from the hat section tests:

- When this material is molded into complex shapes, care must be taken to ensure proper distribution of the fiberglass, especially at corners.
- The delamination that occurred in the tensile hat section tests points to the need for recognizing that there are competing failure modes.

- The monotonic strengths of the compressive hat section and torsion specimens were conservatively predicted.
- Based on the compressive hat section results, a factor of 0.8 on the allowable stress should be used in the region of tight bends to account for the poor fiber distribution.
- The delamination observed in the tensile hat section test decreased the stiffness but did not result in catastrophic failure.
- Fatigue lives of the hat section and torsion specimens all exceeded the allowable lives predicted using the design fatigue curves.
- The fatigue design curve for $R = -1$ gave more conservative predictions than the fatigue design curve for $R = 0$.
- The deformations predicted by finite-element analysis, using the recommended design analysis guidelines, agreed well with test results on the hat section specimens at loads up to the load that resulted in the maximum stress intensity reaching the maximum allowable value.

16. PREDICTIVE MODEL FOR TIME-DEPENDENT DEFORMATION

Y. J. Weitsman, M. Elahi, J. Gao, and L. V. Smith

16.1 GENERAL

In this chapter, a predictive model for the deformation of the reference composite under load, temperature, and in the presence of distilled water is established on the basis of an extensive amount of short-term characterization data. The formulations were proven to be consistent with a constitutive model, based on fundamental principles of irreversible thermodynamics and continuum mechanics, that was purposely developed for the material at hand.

The main purpose of the modeling effort is to quantitatively relate deformation to underlying mechanisms that occur in the reference material. Consequently, specimens were deliberately selected from a limited number of plaques to exclude the effects of plaque-to-plaque variability, which would mask the effects of stress, temperature, and distilled water. Nevertheless, the experimental program used replicate coupons for each circumstance to ascertain the validity of the data and identify the range of remaining scatter. In this manner, this chapter should establish a fundamental methodology that applies to material systems akin to the reference material, which should accelerate the time required in future investigations.

In view of the aforementioned limitation on the number of plaques employed, the data collected here differ from the average values presented in other sections of this report.

16.2 DATA AND MODEL

On the basis of overwhelming experimental evidence, it was determined that the response of the swirl-mat composite at hand exhibits features that correspond to viscoelastic behavior compounded by the presence and growth of a multitude of microcracks. The latter aspect is best described by a continuum distribution of damage. The expressions presented below conform with a constitutive formulation based on fundamental principles of continuum mechanics and irreversible thermodynamics.

16.2.1 Linear Range ($0 \le \sigma < 5.2$ ksi)

Up to a stress level of about 5.2 ksi, which is about 25% of the ultimate failure stress, the response is linearly viscoelastic, with the time-dependent strain proportional to stress and compliance expressed in power-law form.

Thus, under constant stress σ ($0 \le \sigma < 5.2$ ksi), the strain is related by $\varepsilon(t) = D(t)\,\sigma$, where

$$D(t) = D_0 + D_1 t^n \ , \tag{16.1}$$

where t is time in minutes.

At room temperature, the parameters in Eq. (16.1) are bounded by 5.8×10^{-7} psi^{-1} $< D_0 < 7.4 \times 10^{-7}$ psi^{-1}, $7.7 \times 10^{-8} < D_1 < 1.4 \times 10^{-7}$, and $0.05 < n < 0.08$. The above ranges of values stem from the inherent inhomogeneity of the composite.

16.2.2 Nonlinear Range ($\sigma > 5.2$ ksi)

In the nonlinear range, it was possible to relate strain to stress through a stress-dependent amplification factor, $K_\sigma(\sigma)$. Thus, strain under constant stress $\sigma > 5.2$ ksi is given by

$$\varepsilon(t) = K_\sigma(\sigma)\,(D_0 + D_1 t^n)\sigma \ , \tag{16.2}$$

where

$$K_\sigma(\sigma) = 1 + K_d\,(\sigma - \sigma_d)\,H(\sigma - \sigma_d)\ . \tag{16.3}$$

In Eq. (16.3), $K_d = 0.024\ \text{ksi}^{-1}$, $\sigma_d = 5.2$ ksi, and H (•) denotes the unit step function.

It was further noted that in the nonlinear range, strains do not recover completely even at long times after load removal. The nonrecovered, permanent, strain $\in_p$ can be related to the largest strain $\in_{max}$ attained during the loading stage, namely

$$\varepsilon_p = K_p\,[\varepsilon_{max}(t) - \varepsilon_d]\,H(\varepsilon_{max}(t) - \varepsilon_d)\ , \tag{16.4}$$

where, in Eq. (16.4), $K_p = 0.051$, $\varepsilon_d = 4100\ \mu\varepsilon$, and $\varepsilon_{max}(t)$ denotes the largest strain attained prior to load removal.

16.2.3 Temperature Effects

Temperature was shown to enhance deformation within both linear and nonlinear ranges of stress. For temperatures 75°F < T < 190°F and stress $0 < \sigma < 8$ ksi, strain under constant stress can be related by

$$\varepsilon(t) = f(T,\sigma)(D_0 + D_1 t^n)\ , \tag{16.5}$$

where

$$f(T, \sigma) = K_\sigma(\sigma)\{1 + (T - T_R)\,H(T - T_R)\,[1 + 2.6 \times 10^{-3}\,(T - T_R) + 4.5 \times 10^{-4}\,(\sigma - \sigma_d)\,H(\sigma - \sigma_d)]\}\ . \tag{16.6}$$

In Eq. (16.6), $\sigma_d = 5.2$ ksi, $T_R = 75$°F, and T is in degrees Fahrenheit. Note the synergism between stress and temperature implied by Eq. (16.6). This synergistic effect is absent in the curve-fitting procedure used in Chap. 7.

16.2.4 Effects of Distilled Water

These effects were recorded in the linear stress range ($0 \le \sigma < 5.2$ ksi) and for specimens pre-exposed to distilled water at 72, 125, and 180°F. All strain data were recorded at room temperature.

Strain could be related to stress by means of an amplification factor, g_m, namely for constant stress σ:

$$\varepsilon(t) = g_m\,(D_0 + D_1 t^n)\,\sigma\ , \qquad 0 \le \sigma < 5.2\ \text{ksi}\ .$$

In this expression, the factor g_m depended strongly on the temperature T employed during preimmersion, with no clear trend in relation to fluid content.

Furthermore, various observations on fluid weight gain during immersion, and weight loss during subsequent drying, indicate that the reference swirl-mat composite should not be subjected to sustained exposures to distilled water at temperatures exceeding 120°F if permanent damage is to be avoided.

Sorption data of distilled water into the composite depart from predictions of classical diffusion, with departures increasing markedly with immersion temperature. In view of the foregoing departures, it is possible to obtain only approximate values for the diffusion coefficient. Estimated values suggest about a

tenfold acceleration of the diffusion process between 70 and 190°F. In addition, the diffusion process in the swirl-mat composite appears to proceed up to about ten times faster than in laminated composites.

16.2.5 Cyclic Loading

Short-time stress-controlled cycling experiments, ranging up to 2000 cycles, indicated that compliance enhancement (i.e., stiffness reduction) can be related to the levels of σ_{max} and σ_{min} employed during stress cycling. A sawtooth wave form was used.

Compliance enhancement could be expressed in a power law form, namely

$$w_i = C_i/D_0 = 1 + \left(\Delta w^* + \Delta\hat{w} \bullet i^m\right) H\left(\sigma - \sigma_d\right) , \tag{16.7}$$

where in Eq. (16.7) the index i denotes cycle number, C_i is the compliance obtained during the down-loading stage of the ith cycle, D_0 is the initial compliance, and σ_d = 5.2 ksi as before. The parameters Δw^*, $\Delta\hat{w}$, and m depend on σ_{max} and σ_{min} (or $\bar{\sigma}$ and the ratio R) employed during cycling. Employing data for R = 0.1 and R = 0.3, with σ_{max} = 4, 8, 12, and 16 ksi made it possible to represent the compliance enhancement data by the empirical expressions:

$$\begin{aligned} \Delta w^* &= \left[-3\times10^{-4}\left(\sigma_{max}\right)^2 + 14.2\times10^{-3}\sigma_{max} - 5.372\times10^{-2}\right](R+0.9) \\ \Delta\hat{w} &= \left[-0.86\times10^{-4}\left(\sigma_{max}\right)^2 + 3.08\times10^{-3}\sigma_{max} - 1.204\times10^{-2}\right](1.08-0.8R) \\ m &= \left(95\times10^{-4} - 8\times10^{-3}R\right)\sigma_{max} + 0.1833 \ . \end{aligned} \tag{16.8}$$

16.2.6 Generalizations

The strain under time-varying stress, $\sigma = \sigma(t)$, can be evaluated by means of the convolution integral:

$$\varepsilon(t) = D_0 K_\sigma[\sigma(t)]\sigma(t) + D_1 \int_0^t (t-\tau)^n \frac{d}{d\tau}\left\{K_\sigma[\sigma(\tau)]\sigma(t)\right\} d\tau \ . \tag{16.9}$$

Similarly, the strain under cyclic stress is given by

$$\varepsilon(t) = D_0 w(t)\sigma(t) + D_1 \int_0^t (t-\tau)^n \frac{d}{d\tau}\left[w(\tau)\sigma(\tau)\right] d\tau \ . \tag{16.10}$$

Equations (16.9) and (16.10), which stem from the fundamental model, are applicable only during times of increasing strain. These expressions provided very good predictions for deformations under two-step loads and cyclic inputs. If $\varepsilon(t)$ decreases over a certain timespan, it is necessary to employ values of $K_\sigma(\sigma)$ and w that correspond to the largest value of past strain. These fixed values of K_σ and w are to be employed until $\varepsilon(t)$ regains its previous maximal value. As in all nonlinear circumstances, computations may require an iterative procedure.

The maximal and minimal strains during cyclic loading, which were predicted in accordance with Eqs. (16.7), (16.8), and (16.10), employed $D_0 = 5.329 \times 10^{-7}$ psi, $D_1 = 3.533 \times 10^{-8}(\text{psi})^{-1}(\text{sec})^{-n}$, and n = 0.086. These values correspond to the averages recorded for the specimens employed in the cyclic testing program. Very good correlation was noted between data and predictions based on expressions in Eqs. (16.7) and (16.10).

Complete information will be provided in report ORNL/TM-13521, titled *Some Aspects of the Deformation Response of Swirl-Mat Composites*.

16.3 ISOCHRONOUS STRESS-STRAIN CURVES

Stress-strain response at distinct values of load durations are shown in Fig. 16.1, and strain recovery for distinct durations of prior loading are shown in Figs. 16.2(*a*)–16.2(*e*). These plots are based on $D_0 = 6.2 \times 10^{-7}$ (psi)$^{-1}$, $D_1 = 7.7 \times 10^{-8}$(psi)$^{-1}$(min)$^{-0.08}$, and n = 0.08. All of the above plots are based on Eqs. (16.1)–(16.4) and terminate at locations corresponding to the failure times reported in Chap. 8. The curves shown in Fig. 16.1 for room temperature can be used for elevated temperatures when scaling the strain by the factor $f(T,\sigma)/K_\sigma(\sigma)$.

Note again that the isochronous curves presented here differ from those shown in Chap. 7 because they were purposely derived from a limited selection of plaques and extrapolate short-term data.

16.4 DETAILED RESULTS

Detailed information regarding room-temperature creep was reported in report ORNL/TM-13281 (September 1996). Details regarding the remainder of this chapter will be reported in ORNL/TM-13251.

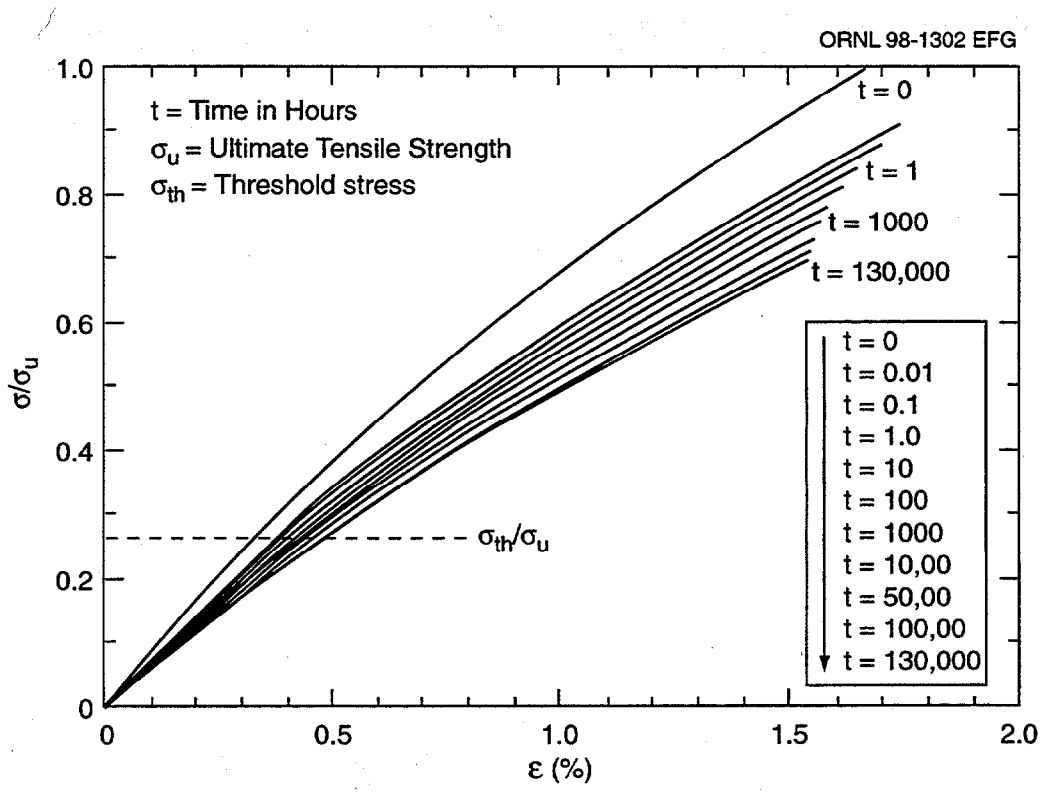

Fig. 16.1. Isochronous stress-strain curves. Time t in hours. Curves terminate at failure.

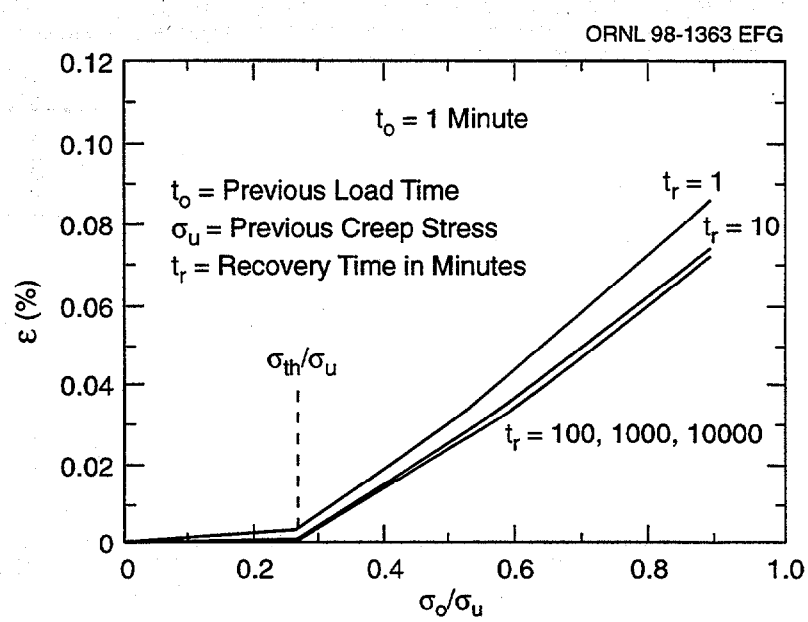

(a) **σ_0/σ_u held for the duration of t_0 = 1 min.**

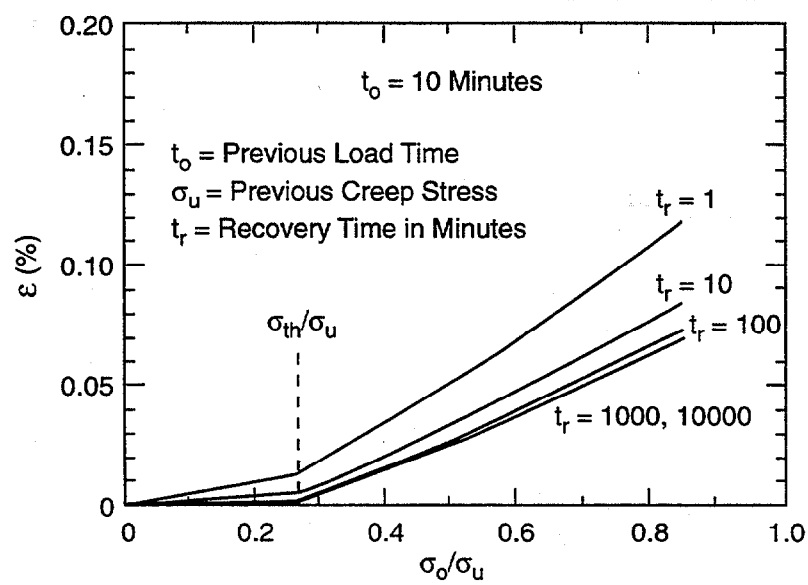

(b) **σ_0/σ_u held for the duration of t_0 = 10 min.**

Fig. 16.2. Isochronous curves of recovery strain ∈ vs previously applied stress. (t_r denotes recovery time, in minutes, elapsed since unloading.)

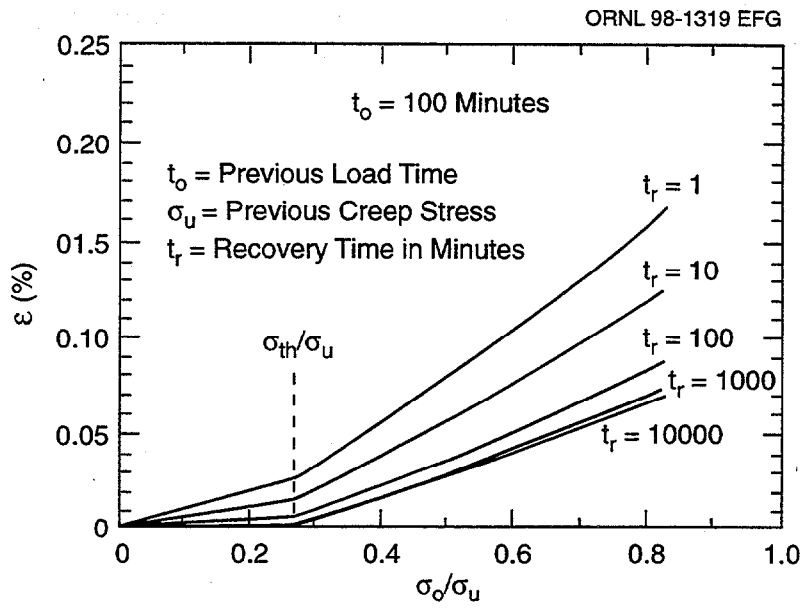

(*c*) **σ_0/σ_u held for the duration of t_0 = 100 min.**

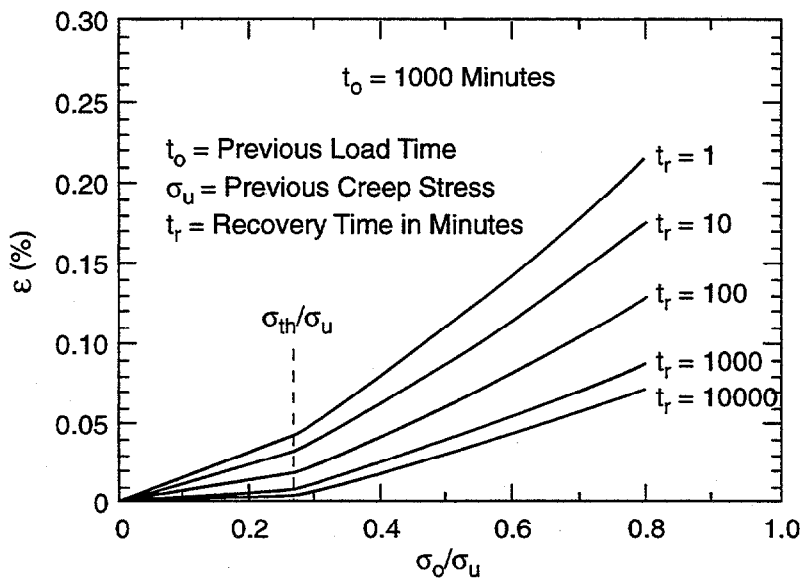

(*d*) **σ_0/σ_u held for the duration of t_0 = 1000 min.**

Fig. 16.2. (cont.) Isochronous curves of recovery strain ∈ vs previously applied stress. (t_r denotes recovery time, in minutes, elapsed since unloading.)

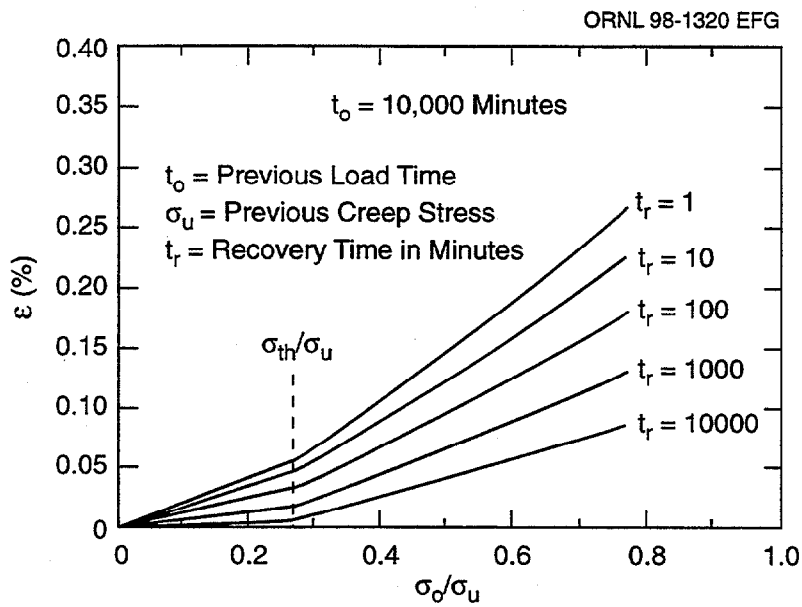

(*e*) **σ_0/σ_u held for the duration of t_0 = 10,000 min.**

Fig. 16.2. (cont.) Isochronous curves of recovery strain ∈ vs previously applied stress. (t_r denotes recovery time, in minutes, elapsed since unloading.)

17. DAMAGE DEVELOPMENT AND GROWTH

D. C. Worley III, R. S. Benson, H. M. Herring, and P. K. Liaw
(The University of Tennessee, Department of Materials Science and Engineering)

17.1 INTRODUCTION

Through a subcontract, the Department of Materials Science and Engineering at The University of Tennessee undertook a study of damage initiation and propagation in the reference CSM/isocyanurate composite using specimens tested at ORNL. Methods of examination included ultrasonic C-scans, light microscopy, and scanning electron microscopy (SEM). Tensile, creep, and fatigue loadings were addressed, and specimens were examined prior to loading, at interruption points during loading, and after failure. Environmental effects (distilled water and windshield washer fluid) were also examined. The following sections briefly summarize the observations and damage mechanisms.

17.2 DAMAGE INITIATION

For short-time tension and time-dependent creep loadings, damage initiation is widespread, occurring at multiple locations throughout the composite. Damage or microcrack initiation sites include (1) voids, (2) fiber/matrix debonding, (3) fiber/fiber debonding, and (4) irregularities or flaws in the specimen edges.

The widespread nature of damage initiation sites is illustrated by Fig. 17.1, which shows a series of C-scans of a single tensile specimen after being incrementally loaded to various percentages of the UTS. A noticeable darkening occurs between 20% and 40% of the UTS, indicating the widespread initiation of damage. Figure 3.1 in Chap. 3 was a plot of the percent change in stiffness vs percent UTS for a series of tensile specimens similarly incrementally loaded. Damage, as reflected by a loss of stiffness, begins to occur at a threshold of about 30% UTS, which agrees well with the C-scan images.

It has been found that by using computerized image analysis of each C-scan picture, an average gray-scale value can be determined that correlates with prior loadings. The darker the image, the greater the sound-wave attenuation, and the greater the microdamage.

Damage initiation in fatigue, although involving to some degree the same four mechanisms, appears to be much more dominated by matrix cracking—from voids and surface defects—in the early stages. The

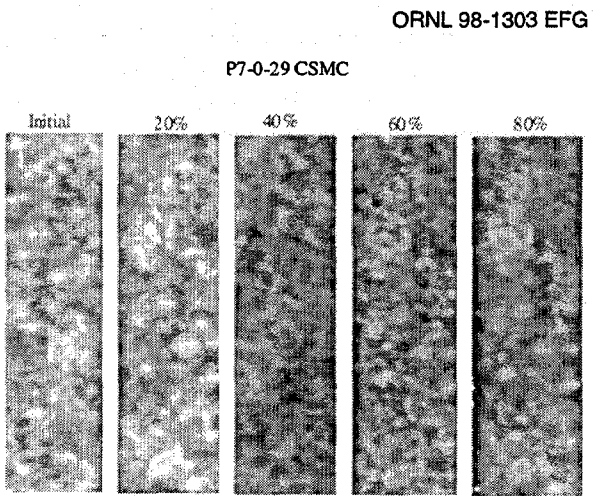

Fig. 17.1. C-scan images of a tensile specimen incrementally loaded to 20, 40, 60, and 80% of the UTS.

fatigue plots in Chap. 10, showing maximum cyclic strain vs log cycle number (e.g., Fig. 10.7), exhibit a linear range and then, later in the cyclic life, an upswing. Based on light microscope observations of interrupted fatigue test specimens, it is believed that the linear portion corresponds to a preponderance of matrix microcracking. The upswing indicates a transition to fiber-dominated damage. The debonding leads to an increase in strain.

17.3 DAMAGE PROPAGATION

As microcracks grow at multiple sites, a dominant crack eventually develops. Generally, this dominant crack is one that has encountered a path of least resistance characterized by few dense junctions of fiber bundles and multiple voids at or near the bundle junctions encountered. Propagation in the majority of cases follows fiber matrix interfaces, unless the crack is diverted toward voids lying near the interface. Voids tend to lure the crack into the matrix; it then returns to the fiber/matrix interface, perhaps along a different bundle. This behavior is illustrated in Fig. 17.2, where a large void directs a crack from one bundle to another.

Figure 17.3 follows the progression of a crack as it propagates across a tensile specimen. The loading direction is horizontal. In Fig. 17.3(*a*) the crack is propagating to the upper left along a fiber bundle, A. In Fig. 17.3(*b*) a second bundle, B, is encountered. As seen in Fig. 17.3(*c*), two bundles lie beneath B, one going toward the upper left and one going vertically (perpendicular to the load). The crack went under bundle B, along the bundle going to the upper left, and then it went vertically along the bundle lying perpendicular to the load [see Fig. 17.3(*d*)]. Figure 17.3(*e*) shows the crack encountering other bundles at D, and Fig. 17.3(*f*) depicts debonding and fiber breakage in these bundles (light areas).

Whereas the crack in Fig. 17.3 propagated with increasing load, fatigue cracks propagate with increasing cycle number, as shown in Fig. 17.4. The specimen in this case contained a 0.25-in.-diam circular hole, and the views in Fig. 17.4 are of the side of the hole where the tensile stresses are largest (the loading is horizontal). The specimen had a dark coating, so the microcracks show up as light lines. As can be seen, the crack density increases with cycles.

In some cases, fracture surfaces were examined using SEM. Commonly observed characteristics include matrix cracking, fiber/matrix interfacial debonding, fiber pull-out, and fiber breakage. Figures 17.5 and 17.6 display some of these features. In Fig. 17.5, the fracture surface and face of the specimen are viewed. Fiber breakage, matrix cracking, and some debonding can be seen. Matrix cracking, in the form of river patterns typical of brittle failure, can be seen in Fig. 17.6 emanating from a fiber bundle. Figure 17.7 exhibits all of these fracture characteristics.

Figure 17.8 is a simplified representation of the failure process. Region A represents fibers oriented in the loading direction, B represents fibers normal to the loading direction, and C represents those fibers that are at some angle to the load. The A fibers carry the largest load and undergo fiber pull-out under tensile loads. The B fibers are least favorably oriented and undergo fiber/matrix debonding. The C fibers can undergo tensile and shear failures, producing fiber/matrix debonding and fiber pull-out. For tensile loading, the initial crack, whether in the matrix, around the fiber bundle, or in the fiber bundle, propagates until it comes in contact with a fiber/matrix interface. As shown in both Fig. 17.8 and the SEM images, the crack then follows the interfaces until complete failure.

17.4 ENVIRONMENTAL EFFECTS

A series of companion creep and fatigue tests, using a single stress level for each, was carried out in three environments:

- ambient air,
- distilled water, and
- methanol-based windshield washer fluid.

The fatigue specimens were preexposed for 100 h and then tested in the environment. The creep specimens were not preexposed; average failure time for the distilled water creep specimens was 166 h, and

ORNL 98-1304 EFG

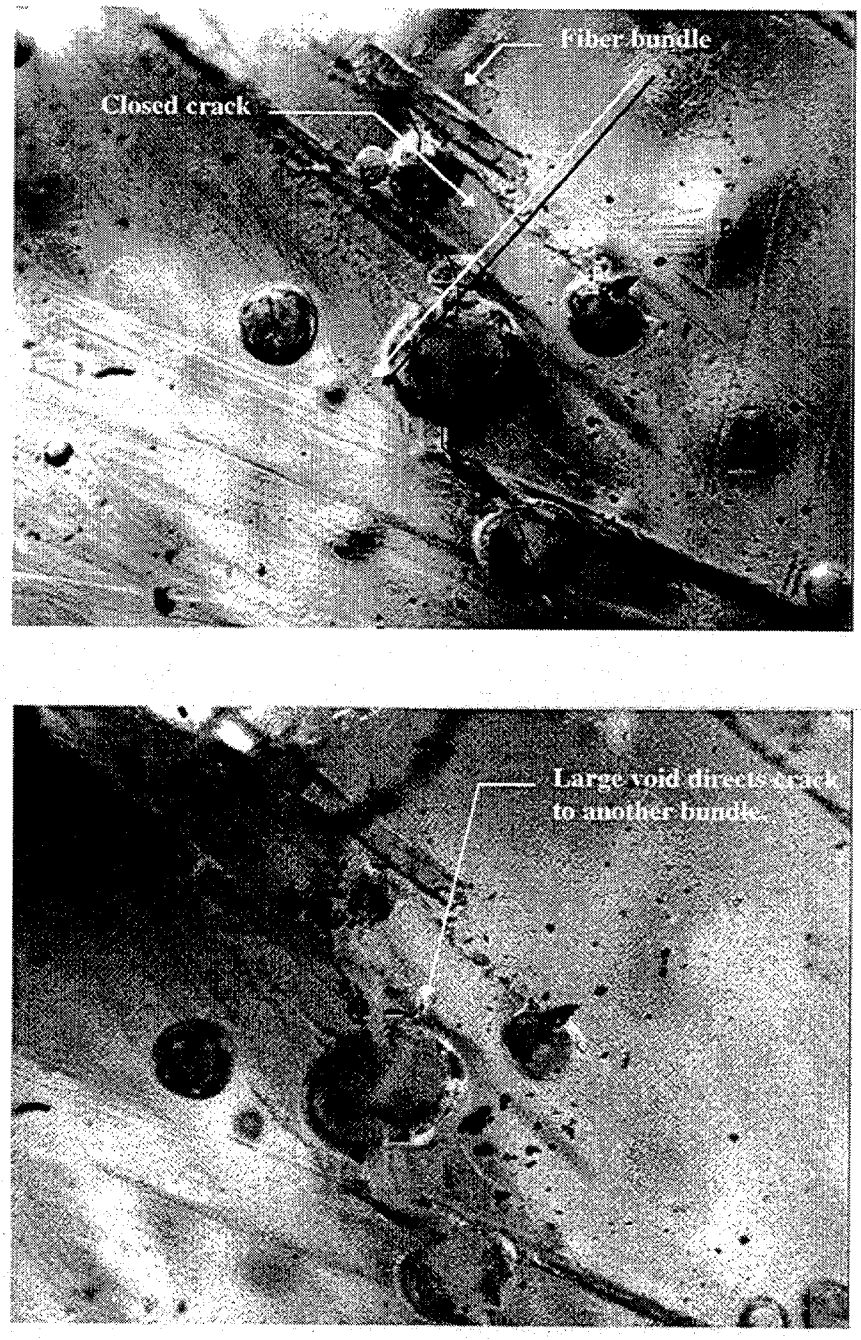

Fig. 17.2. Crack propagation through a large void. The upper image shows the crack closed; the lower image of the same area shows the crack open. The loading is horizontal.

ORNL 98-1305 EFG

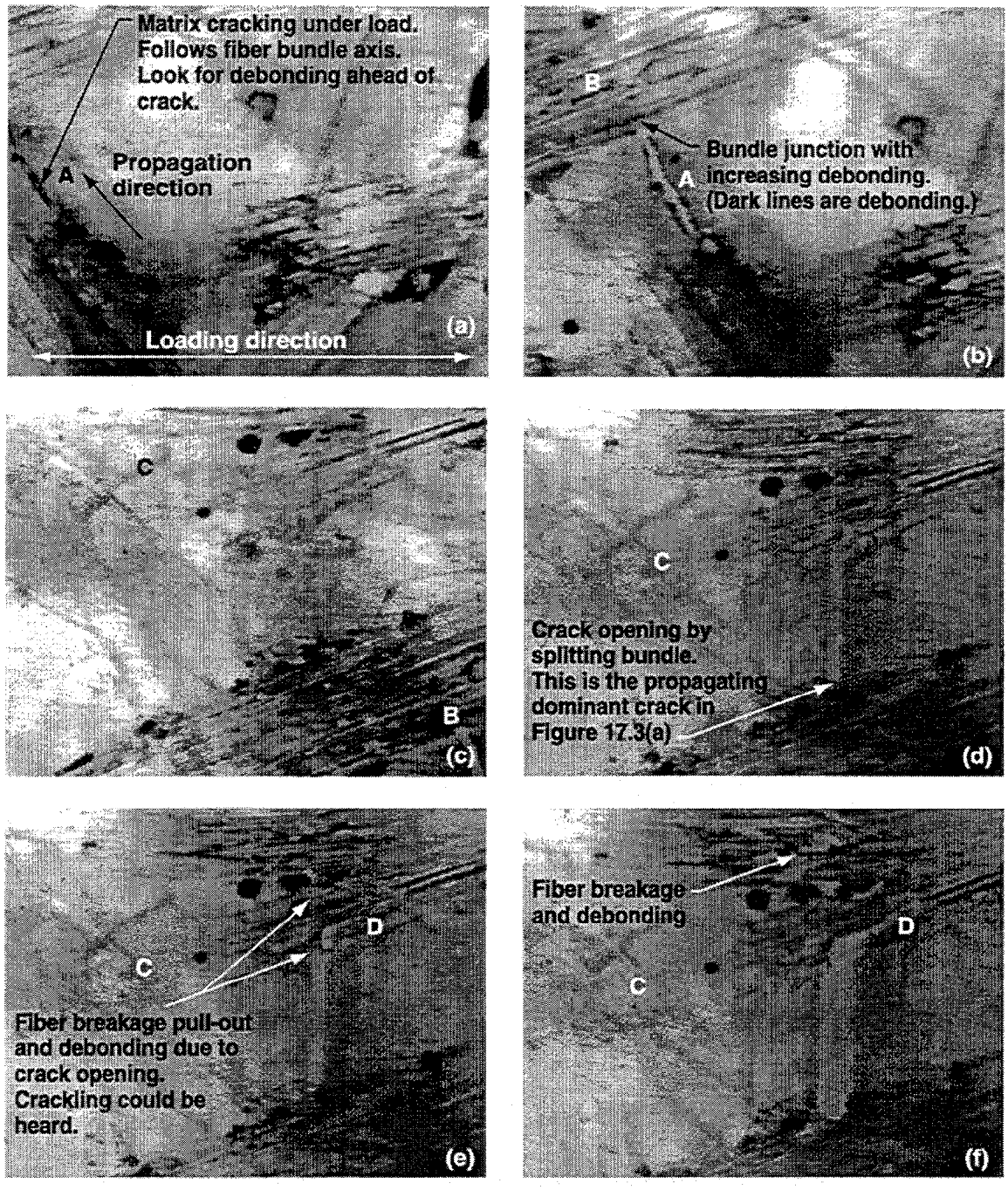

Fig. 17.3. Propagation of a crack across a tensile specimen.

ORNL 98-1306 EFG

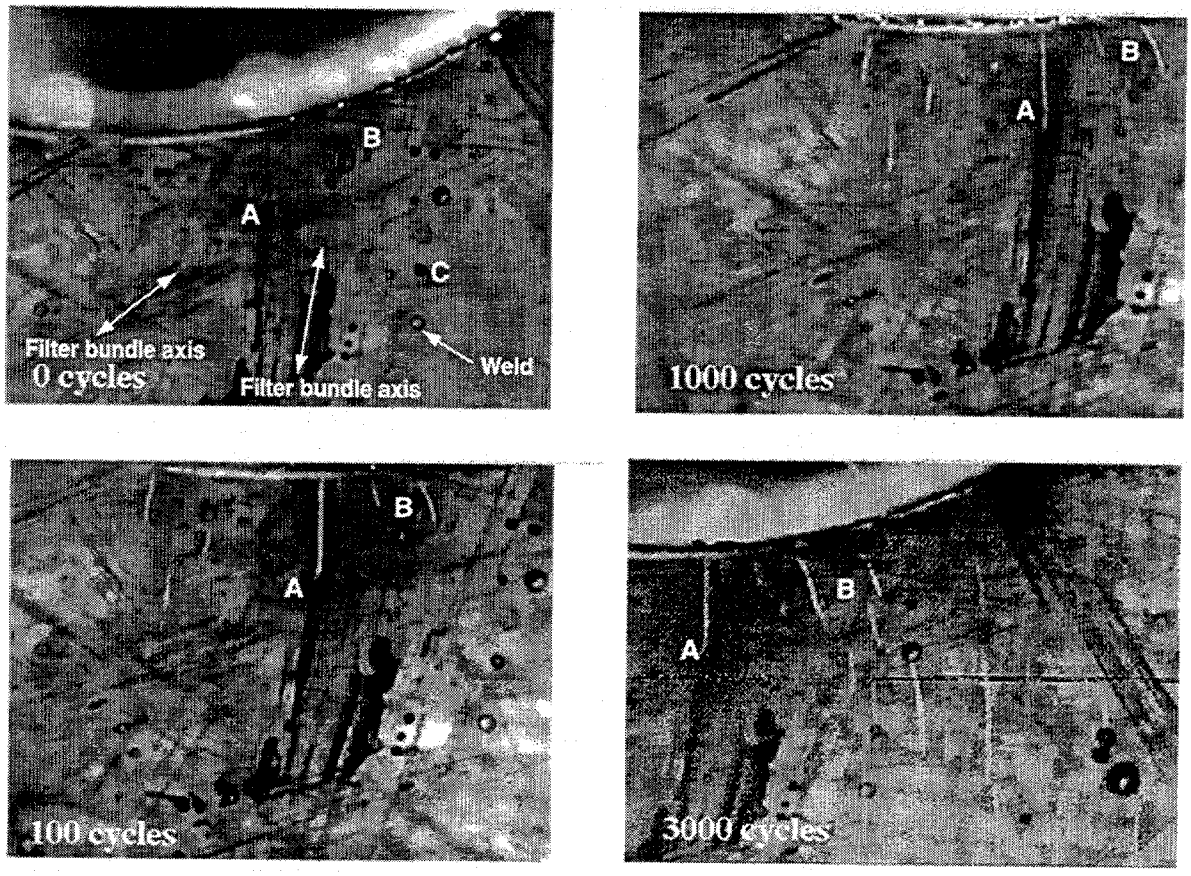

Fig. 17.4. Progression in observable damage as a function of cycles.

ORNL 98-1307

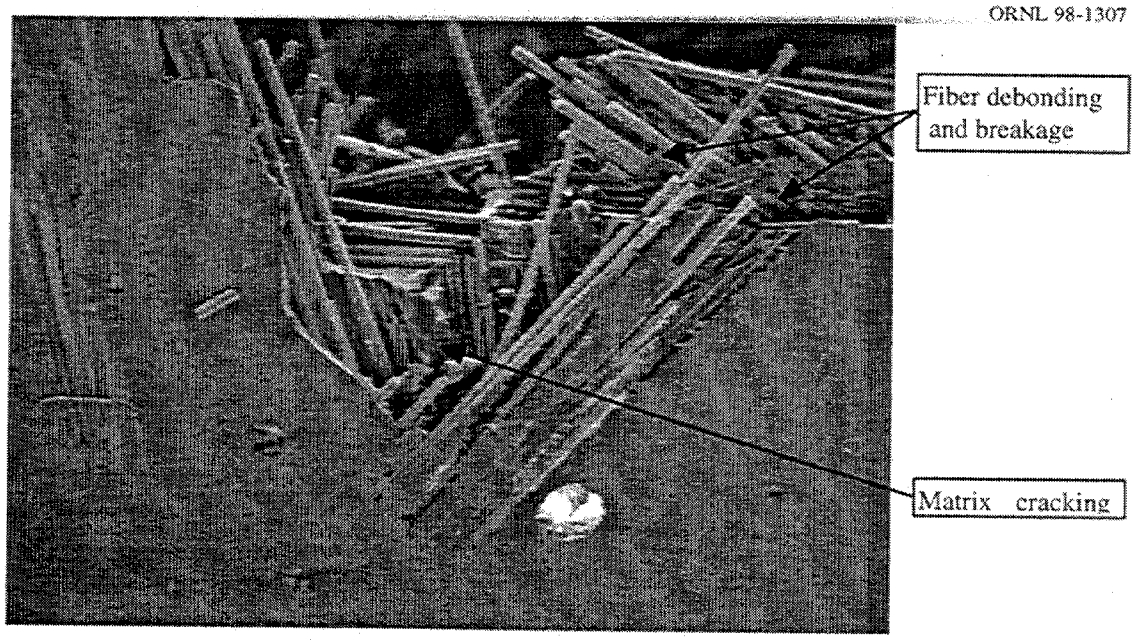

Fig. 17.5. Fracture surface viewed from the side and top (70×).

ORNL 98-1308 EFG

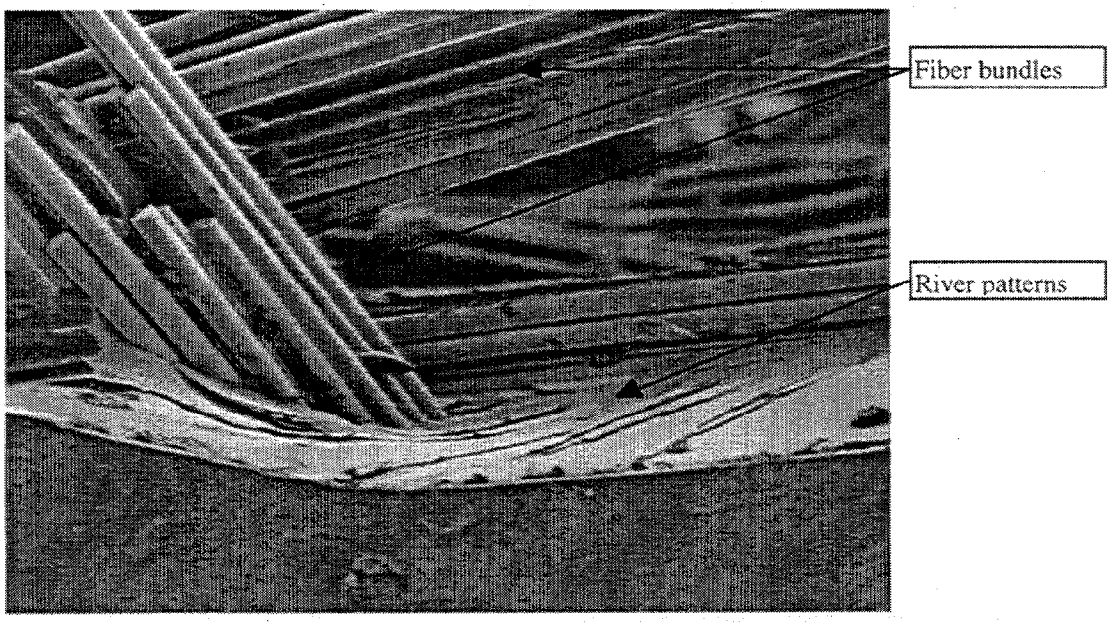

Fig. 17.6. River patterns on a fracture surface (300×).

ORNL 98-1309 EFG

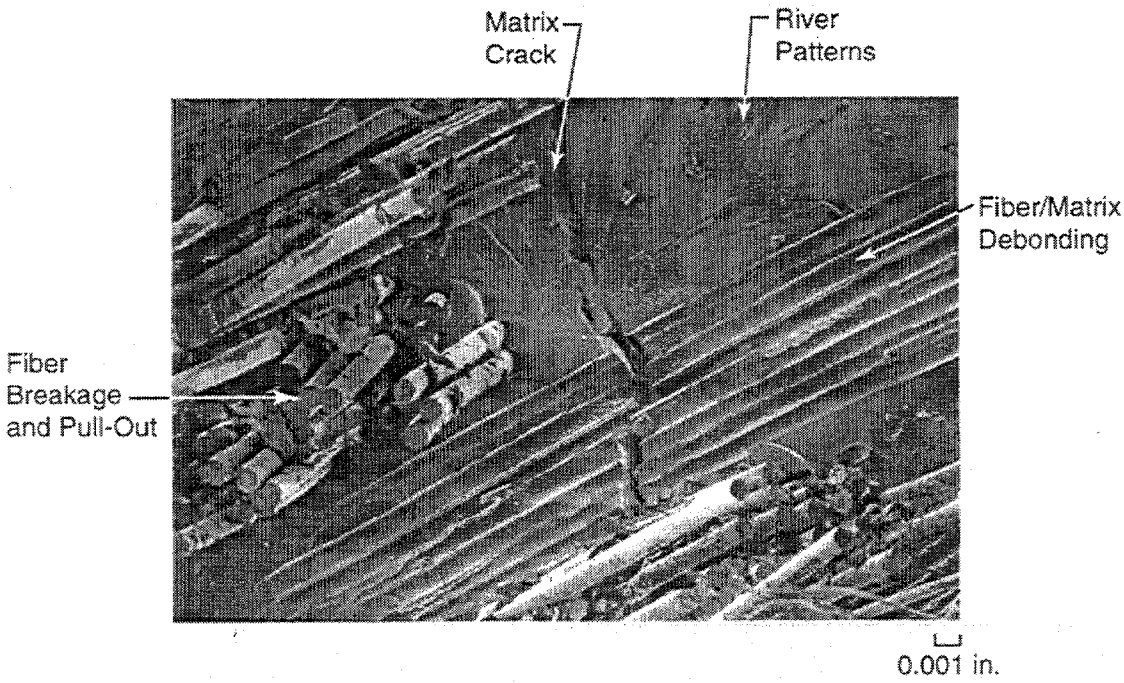

Fig. 17.7. Fracture surface of a failed creep specimen.

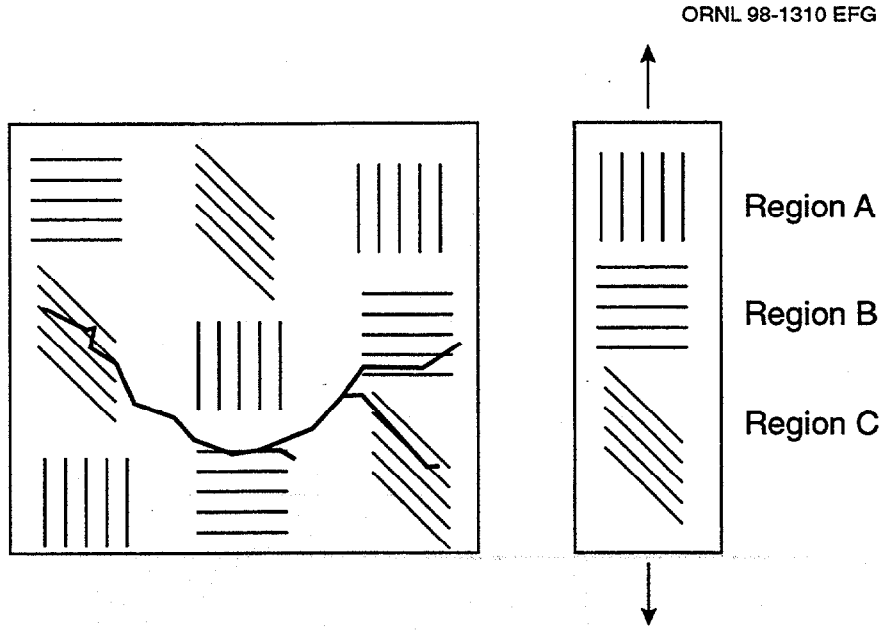

Fig. 17.8. Schematic of failure mechanism.

for the windshield washer specimens, 451 h. The specimens were examined before and after testing by the three methods previously described.

As has been described in previous chapters, exposure to distilled water and windshield washer fluid caused an increase in creep strain (Chap. 7) and decreases in creep-rupture strength (Chap. 8) and fatigue strength (Chap. 11). Creep strains, for both fluids, were increased 50 to 60% over the in-air strains, creep-rupture strengths were about 55 to 60% of the in-air strength, and fatigue strengths were 85 to 90% of the in-air value.

Typical creep fracture surface SEMs are shown in Fig. 17.9. Note that in the distilled water case the matrix surface shows brittle fracture bands (more than in the in-air case), whereas in the windshield washer fluid case the surface is relatively smooth. This difference was typical.

Figure 17.10 similarly shows fatigue SEM fracture surfaces. In the distilled water case, there are again river patterns. Note the clean fibers. In the windshield washer fluid case the surface is smooth. Generally, clean fibers were observed for distilled water, whereas in the windshield washer fluid case (and in-air case) the fibers had pieces of matrix clinging to them, indicating that a good bond was maintained.

It is postulated that these differences result from the fact that (1) windshield washer fluid has a much larger plasticizing effect on the matrix (because the solubility parameter of the methanol in the windshield washer fluid is relatively close to that of polyurethane), and (2) the distilled water tends to attack the fiber/matrix interface. Greater plasticization of the matrix means it is somewhat less brittle—thus the decrease in river patterns. Greater interface attack means the fibers pull out more cleanly.

ORNL 98-1311 EFG

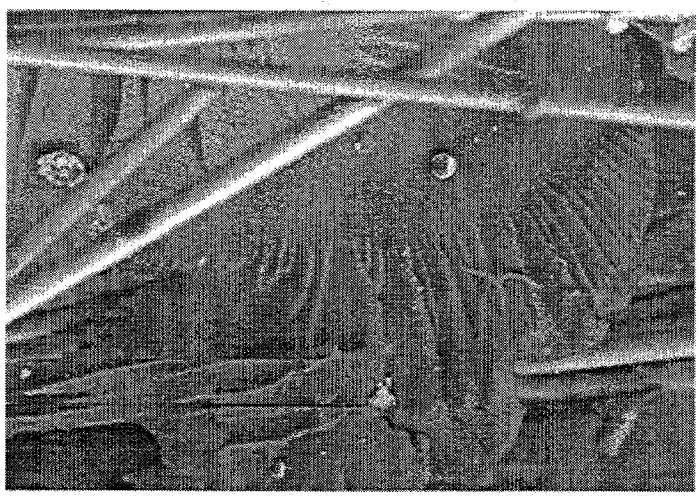

0.13

(*a*) **Distilled water.**

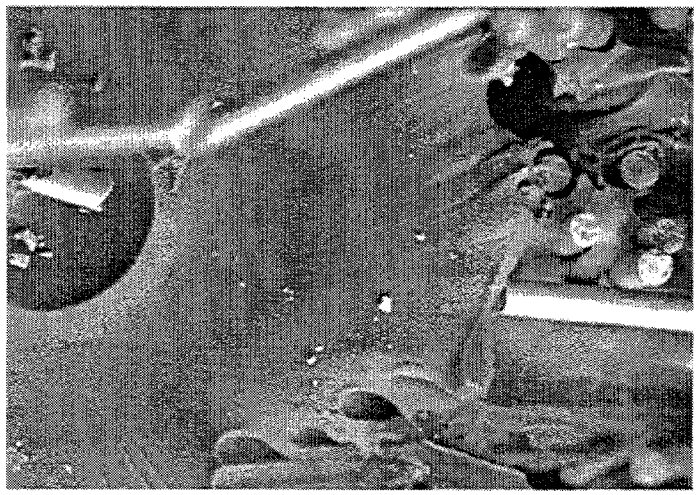

0.1

(*b*) **Windshield washer fluid.**

Fig. 17.9. SEM images of creep specimen fracture surfaces.

ORNL 98-1312 EFG

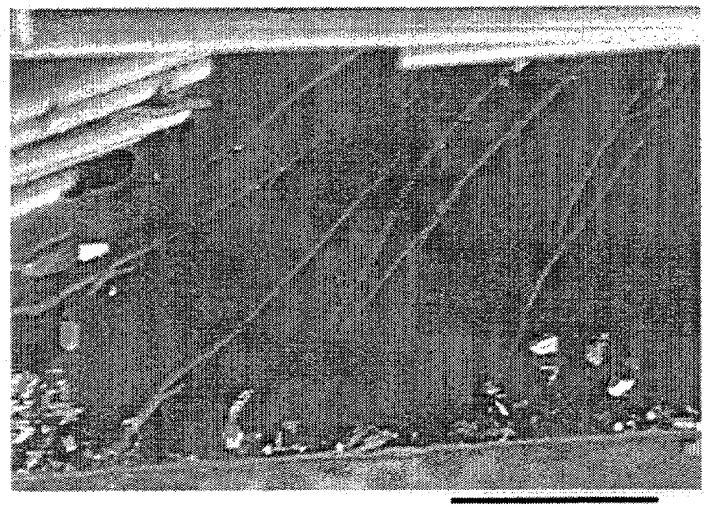

(*a*) **Distilled water.** 0.1

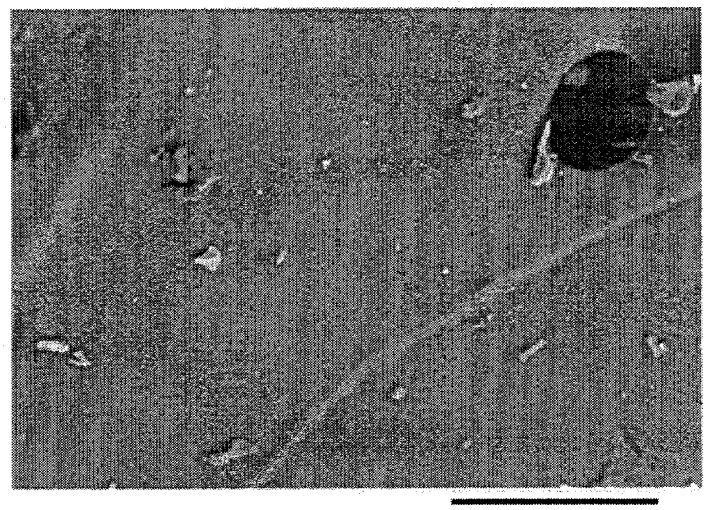

(*b*) **Windshield washer fluid.** 0.1

Fig. 17.10. SEM images of fatigue specimen fracture surfaces.

INTERNAL DISTRIBUTION

1. R. L. Battiste
2. H. W. Blake
3. R. G. Boeman
4. C. R. Brinkman
5–14. J. M. Corum
15. W. G. Craddick
16. M. Elahi
17. D. L. Erdman
18. J. G. Hansen
19. H. W. Hayden, Jr.
20. W. K. Kahl
21. L. D. Klett
22. C. R. Luttrell
23. R. N. McGill
24. D. J. Naus
25. R. E. Norris
26. W. Ren
27. M. B. Ruggles
28. W. A. Simpson, Jr.
29. P. A. Sklad
30. J. M. Starbuck
31. C. D. Warren
32. Y. J. Weitsman
33. G. T. Yahr
34. T. Zacharia
35. R. E. Ziegler
36. ORNL Patent Section
37. Laboratory Records, ORNL-RC
38–39. Laboratory Records, OSTI

EXTERNAL DISTRIBUTION

40. R. S. Benson, Department of Materials Science and Engineering, The University of Tennessee, 427-C Dougherty Engineering Building, Knoxville, Tennessee 37996-2200.
41. R. A. Bergen, MSX International, 255 Rex Boulevard, Auburn Hills, Michigan 48326.
42. K. Fielder, The Dow Chemical Company, 2301 N. Brazosport Blvd., B-1608, Freeport, Texas 77541-3257.
43. R. B. Freeman, The Budd Company, 1515 Atlantic Boulevard, Auburn Hills, Michigan 48326.
44. R. Gjerde, Textron Automotive Company, 100 Brady Road, Americus, Georgia 31709.
45–74. E. M. Hagerman, Automotive Composite Consortium, General Motors, 30500 Mound Road, I-6, Box 9055, Warren, Michigan 48090-9055.
75. J. M. Henshaw, Department of Mechanical Engineering, The University of Tulsa, 600 S. College Avenue, Tulsa, Oklahoma 74104-3189.
76. G. A. Holmes, National Institute of Standards and Technology, Bldg. 224, Room B116, MS: Room B108, Gaithersburg, Maryland 20899.
77. D. Kossak, Cambridge Industries, 29333 Stephenson Highway, Madison Heights, Michigan 48071.
78. F. G. Krautz, Vetrotex Certainteed, 4515 Allendale Road, Wichita Falls, Texas 76310-2199.
79. P. K. Liaw, Department of Materials Science and Engineering, The University of Tennessee, 427-B Dougherty Engineering Building, Knoxville, Tennessee 37996-2200.
80. K. Liechti, Engineering Mechanics Research Laboratory, Department of Aerospace Engineering and Engineering Mechanics, The University of Texas at Austin, Austin, Texas 78712.
81. G. R. Miesel, Ashland Chemical Company, 900 Wilshire Drive, Suite 110, Troy, Michigan 48084.
82. L. M. Ojanen, Decona International, 50 Casmir Court, Concord, Ontario, Canada L4K 4J5.
83. D. Oplinger, AAR-431, FAA William J. Hughes Technical Center, Atlantic City International Airport, New Jersey 08405.
84. T. A. Reinhart, The University of Dayton Research Institute, 300 College Park Drive, Dayton, Ohio 45469-0130.
85. D. N. Robinson, Department of Civil Engineering, The University of Akron, Akron, Ohio 44325-3905.

86. G. Sandgren, Owens Corning Science & Technology Centre, 2790 Columbus Road, Route 16, Granville, Ohio 43023-1200.
87. C. R. Schultheisz, National Institute of Standards and Technology, Building 224, Room A209, Gaithersburg, Maryland 20899.
88. T. D. Seagrave, Bayer Corporation, 100 Bayer Road, Pittsburgh, Pennsylvania 15205.
89. L. V. Smith, Washington State University, School of Mechanics and Materials Engineering, Pullman, Washington 99164-2920.
90. C. T. Sun, Purdue University, School of Aeronautics and Astronautics, 1282 Grissom Hall, West Lafayette, Indiana 47907-1282.
91. R. Talreja, School of Aerospace Engineering, Georgia Institute of Technology, Atlanta, Georgia 30332-0150.
92. D. C. Worley, Department of Materials Science and Engineering, The University of Tennessee, 427-B Dougherty Engineering Building, Knoxville, Tennessee 37996-2200.
93–95. J. A. Carpenter, U.S. Department of Energy, 1000 Independence Avenue, SW, Washington, DC 20588.
96. H. E. Clark, U.S. Department of Energy, Oak Ridge Site Office, Oak Ridge, Tennessee 37831.
97. P. G. Patil, U.S. Department of Energy, 1000 Independence Avenue, SW, Washington, DC 20588
98. M. R. Rawlins, U.S. Department of Energy, Oak Ridge Site Office, Oak Ridge, Tennessee 37831.